



HAL
open science

Search for gamma-ray bursts with SVOM/MXT space telescope: Development and characterization of the onboard scientific software

Shaymaa Hussein

► **To cite this version:**

Shaymaa Hussein. Search for gamma-ray bursts with SVOM/MXT space telescope: Development and characterization of the onboard scientific software. Instrumentation and Methods for Astrophysics [astro-ph.IM]. Université Paris-Saclay, 2022. English. NNT : 2022UPASP100 . tel-03869731

HAL Id: tel-03869731

<https://theses.hal.science/tel-03869731>

Submitted on 24 Nov 2022

HAL is a multi-disciplinary open access archive for the deposit and dissemination of scientific research documents, whether they are published or not. The documents may come from teaching and research institutions in France or abroad, or from public or private research centers.

L'archive ouverte pluridisciplinaire **HAL**, est destinée au dépôt et à la diffusion de documents scientifiques de niveau recherche, publiés ou non, émanant des établissements d'enseignement et de recherche français ou étrangers, des laboratoires publics ou privés.

Search for gamma-ray bursts with
SVOM/MXT space telescope:
Development and characterization of the
onboard scientific software

*Recherche de sursauts gamma avec le télescope spatial
SVOM/MXT: Développement et caractérisation du logiciel
scientifique embarqué*

Thèse de doctorat de l'université Paris-Saclay

École doctorale n° 576, Particules, Hadrons, Énergie, Noyau:
Instrumentation, Imagerie, Cosmos et Simulation (PHENIICS)

Spécialité de doctorat: Astroparticules et Cosmologie

Graduate School: physique, Référent: Faculté des sciences d'Orsay

Thèse préparée dans l'unité de recherche **IJCLab** (Université Paris-Saclay, CNRS), sous la direction de **Florent ROBINET**, Chargé de recherche, et la co-direction de **Nicolas LEROY**, Chargé de recherche

Thèse soutenue à Paris-Saclay, le 03 octobre 2022, par

Shaymaa HUSSEIN

Composition du jury

Sophie HENROT-VERSILLÉ

Directrice de recherche, Université Paris-Saclay,
Laboratoire de Physique des 2 Infinis Irène Joliot
Curie, (UMR9012)

Présidente

Jean-Luc ATTEIA

Astronome (HDR), Institut de recherche en astro-
physique et planétologie

Rapporteur & Examineur

Paul O'BRIEN

Professeur des universités, University of Leicester

Rapporteur & Examineur

Adam GOLDSTEIN

Chargé de Recherche, Universities Space Re-
search Association

Examineur

Florent ROBINET

Chargé de Recherche, Université Paris-Saclay,
Laboratoire de Physique des 2 Infinis Irène Joliot
Curie, (UMR9012)

Directeur de thèse

Titre: Recherche de sursauts gamma avec le télescope spatial SVOM/MXT: Développement et caractérisation du logiciel scientifique embarqué

Mots clés: Sursauts gamma, Astronomie X, SVOM, MXT, Instrumentation spatiale, Localisation en temps-réel

Résumé: Les sursauts gamma (GRB) sont des sursauts lumineux, puissants et courts de rayons gamma suivis d'une rémanence moins lumineuse des rayons gamma jusqu'aux énergies radio. Leur extrême luminosité, qui les rend visibles dans tout l'Univers, en fait des outils précieux pour sonder l'aube de l'Univers. Dans ce contexte, SVOM, qui est une mission sino-française, vise à détecter et caractériser les GRBs à partir de fin 2023. A bord, le télescope MXT est conçu pour détecter la rémanence des rayons X mous et les localiser avec une précision inférieure à 2 arcmin en quelques minutes. Le MXT est composé d'une optique basée sur le principe des "yeux de homard" pour focaliser les photons X, d'une caméra basée sur un pnCCD pour détecter les photons X, et d'une unité de traitement de données qui gère le traitement scientifique en temps réel. Au cours de cette thèse, les algorithmes scientifiques embarqués ont été développés, testés et caractérisés.

Les algorithmes scientifiques étudiés dans cette thèse sont de trois types. Tout d'abord, j'ai développé un traitement d'image pour caractériser le niveau de bruit dans le détecteur et identifier les photons au-dessus du niveau de bruit. Deuxièmement, j'ai conçu l'algorithme de localisation pour localiser le GRB mieux que 2 minutes d'arc en quelques minutes d'observation. Enfin, j'ai mis en place le calcul du rapport signal sur bruit de la source en temps réel. De plus, une simulation a été construite pour étudier les performances scientifiques du MXT dans l'observation et la localisation de vrais GRBs. MXT localise environ 80% de GRBs mieux que 2 minutes d'arc après 10 minutes d'observation. Le MXT est capable de caractériser les propriétés temporelles et spectrales de la rémanence des rayons X. Le modèle de vol du MXT a été minutieusement testé lors d'essais sur rayons X en Allemagne. Ces tests a Panter ont montré que l'algorithme scientifique embarqué peut fonctionner de manière fiable et sur le long terme.

Title: Search for gamma-ray bursts with SVOM/MXT space telescope: Development and characterization of the onboard scientific software

Keywords: Gamma Ray Burst, X-ray astronomy, SVOM, MXT, space-instrumentation, real-time localization

Abstract: The Gamma-ray Bursts (GRBs) are luminous, powerful, and short flashes of gamma rays followed by a less luminous afterglows from gamma-ray up to radio energies. Their extreme luminosity, which makes them visible across the entire Universe, makes them valuable tools to probe the dawn of the Universe. In this context, SVOM, which is a Sino-French mission, aims at detecting and characterizing GRBs starting at the end of 2023. Onboard, The MXT telescope is designed to detect the soft X-ray afterglows and localize them with a precision below 2 arcmin within a few minutes. The MXT is composed of optics based on the "lobster eyes" principle to focus the X-ray photons, a camera based on a pnCCD to detect the X-ray photons, and a data processing unit that manages the scientific processing in real-time. During this thesis, I developed, tested, and characterized the onboard scientific

algorithms. The scientific algorithms studied in this thesis are divided into three parts. First, I designed the image analysis to characterize the noise level in the detector and identify the photon signal above the noise level. Second, I developed the algorithm to localize the GRBs better than 2 arcmin in a few minutes of observation. Finally, I implemented a method to compute the source signal-to-noise ratio in real-time. Furthermore, a simulation has been built to study the scientific performance of the MXT in observing and localizing real GRBs. MXT localizes about 80% of the GRBs better than 2 arcmin after 10 minutes of observation. MXT is able to characterize the temporal and spectral properties of the X-ray afterglow. The flight model of the MXT has been thoroughly tested in the Panther X-ray test facility in Germany. The Panther test results have shown that the onboard scientific algorithm can be operated reliably and in a long run.

”لا يُنْبَلُ الرَّجُلُ بِنَوْعِ مِنَ الْعِلْمِ؛ مَا لَمْ يُزَيِّنْ عِلْمَهُ بِالْأَدَبِ.“ عبد الله بن المبارك.

“No category of knowledge will make a person noble, if his knowledge does not beautify his conduct” Ibn Mubarak.

Do not go where the path may lead; go instead where there is no path and leave a trail.

لا تذهب حيث يقودك الطريق لكن اذهب حيث يمكنك أن تصنع طريقك الخاص وتترك اثرا.

أنا دون الله لم أكن شيئاً على الإطلاق

فالحمد لله الذي لا يُؤدِّي شكر نعمةٍ من نعمه إلا بنعمة منه

إلى أبي و أمي ... نبع العطاء الذي لا ينضب،، مصدر قوتي وسبب ابتسامتي

إلى حبيبي محمد ... زوجي الذي كان وسيكون دوماً إلى جانبي

إلى الذين شاركوني أجمل الذكريات لأكثر من سبع وعشرين عام:

إلى هشام،،

إلى منار،،

إلى روح حنان الطاهرة

إلى ملاك

إلى سراب

إلى محمد

إخوتي،،، شكراً، لأنني ما كنت لأفعلها لو لم تكونوا في حياتي.

إلى الأصدقاء الذين نقابلهم بنفس وهج الروح مهما طالت مدة الغياب... إلى عاطفة، ثراء، منار،

ماسة و إلى ريما و رنا.

أنا أعيش في نعمة كبيرة لوجودكم جميعاً في حياتي

أحبكم ..

شيماء

باريس، أيلول 2022

To those who did not know a sound except the sound of bombardment above their heads, to those who have never seen a light but the glow of bombs in their sky..to the patient and steadfast people of Palestine ...

To the thousands of youth whose dreams were shattered and unjustly denied travel at the Israeli occupation checkpoints ...

To the thousands of unjustly and oppressively imprisoned in the Israeli occupation prisons ...

To the millions of children who have been prevented from going to their schools in all the countries that suffer from wars for long years and no one cares about their educations or lives because simply they are from the point of view of the world: "uncivilized." ...

TO YOU, AND ONLY BECAUSE OF YOU, I WILL CONTINUE MY WAY, HOPING TO BUILD A BETTER FUTURE FOR YOU.

Shaymaa
Paris, September, 2022

Contents

Acknowledgments	4
Acronyms	7
Résumé étendu en français	9
Introduction	15
1 Gamma Ray Bursts	17
1.1 Observational history	17
1.1.1 The discovery and early times	17
1.1.2 The afterglow era	19
1.1.3 Current missions	22
1.2 Phenomenology	28
1.2.1 GRB progenitors and emission mechanism	28
1.2.2 The prompt emission	31
1.2.3 The afterglow emission	35
1.3 Motivation for GRB study and prospects	37
1.3.1 GRBs and the early universe	38
1.3.2 GRB and the inter-stellar medium	38
1.3.3 GRB and multi-messenger astronomy	39
2 The SVOM mission	43
2.1 Scientific instruments	44
2.1.1 Space-based instruments	44
2.1.2 Ground-based instruments	50
2.1.3 The VHF alert network	51
2.2 Scientific programs	52
2.2.1 The <i>Core</i> program	53
2.2.2 The <i>General</i> program	54
2.2.3 The <i>Target of Opportunity</i> program	55
2.3 Orbit and observation scenario	56
2.3.1 Satellite orbits and profile	56
2.3.2 Observation scenario and alert system	58
3 The Micro channel X-ray telescope	61
3.1 The MXT features and scientific objectives	61
3.2 The MXT reference frames and system of coordinates	63
3.2.1 The reference frames	63

3.2.2	The system of coordinates	64
3.3	The MXT subsystem	66
3.3.1	The MXT optics	68
3.3.2	The MXT camera	72
3.3.3	The MXT data processing unit	78
3.4	The MXT onboard science software	79
3.4.1	The scientific algorithm	80
3.4.2	Development workflow	82
3.5	Simulation of the MXT telescope	84
3.5.1	Satellite simulation	85
3.5.2	Source simulation	85
3.5.3	Camera simulation	88
3.5.4	Telescope simulation	89
4	Camera images processing	91
4.1	The MXT dark algorithm	92
4.1.1	Ground dark algorithm	93
4.1.2	Onboard dark algorithm	94
4.1.3	Results and characterization	98
4.2	Photon identification	105
4.2.1	Energy gain table	106
4.2.2	Pixel clustering	106
4.2.3	Photon reconstruction	107
4.2.4	Pixel veto and insensitive columns	109
4.2.5	Monitoring and configuration of photons identification	110
5	Source localization in real time with the MXT	113
5.1	Source localization method	113
5.1.1	The point spread function formatting	114
5.1.2	Cross-correlation	114
5.1.3	Source position angles	117
5.1.4	Signal-to-noise ratio	119
5.1.5	Multi-source detection	126
5.1.6	Configuration of localization algorithm	128
5.2	Results and characterization	130
5.2.1	The source intensity	130
5.2.2	The photon map resolution	131
5.2.3	Edge bias	133
5.2.4	Insensitive columns	135
5.2.5	Multiple sources	139
5.2.6	Signal-to-noise ratio	140
5.3	The MXT flight model test at Panter	145
5.3.1	Test overview	145

5.3.2	Localization performance	148
5.3.3	Edge bias characterization	149
5.3.4	Insensitive columns	150
6	Observation of GRBs with the MXT	153
6.1	Simulation of realistic GRB scenarios	154
6.1.1	Simulation features and validation	154
6.1.2	Simulation of MXT observations	160
6.1.3	Localization of real GRBs sample with the MXT	165
6.2	Short GRBs study	167
6.2.1	Selection criteria	168
6.2.2	The luminosity in the rest frame	171
6.3	Multi-messenger astronomy with the MXT	176
	Conclusion	181
	A Swift GRBs detected by ECLAIRs	187
	B publications	235
	List of Figures	235
	List of Tables	249

Acknowledgment

These three years have been a rich adventure, full of invaluable research and personal experience. I am pleased to express my gratitude to those who made it possible.

First, I would like to thank the jury members: Paul O'Brien, Jean-Luc Atteia, François Gonzalez, Sophie Henrot-Versille, and Adam Goldstein for their acceptance to evaluate my work and for giving me moments from their valuable time to read and comment on my manuscript.

My sincere thanks to my supervisor, Florent Robinet, for giving me the opportunity to be part of the SVOM space mission. Thanks Florent, for every skill you taught me, for every knowledge you transferred to me, for your availability always to discuss and to answer my questions, and for your patience especially when I was asking stupid questions!

I am so grateful to two people, without whom I would not have been able to continue my way in France, Marie-Hélène and Nicolas. Marie-Hélène, my advisor and my friend, you guided me from the beginning, since my first days in France, during the master, the internship, and during the Ph.D. Your support and advice during the good and hard times helped and motivated me to continue. Nicolas "le roi," the best boss ever! thank you for integrating me within the gravitational wave group in IJCLab and within the SVOM collaboration, thank you for giving me the opportunity to travel and meet many scientists in several labs. Thank you for your availability to help in any time, you never told me I am busy I can not help now. Your door was always open to me and to all group members.

The gravitational wave group, Thanks to all of you! During three years, you let me feel that I am within my family. In my first year, I was the only non-French member in the group, but you never let me feel that I am excluded; you always tried to integrate me within you, helped me with the French administrative, and tried to teach me French "without success! I am sorry!". Thank you, Patrice, Tito, Nicolas Arnaud, Angélique, Aymeric, Manuel, Pierre Alexandre, Roman, and Marion. Thanks also to the former member of the group: Sarah, Fabien, Marie-Anne, Jean-Gregoire, David, Imene, and Julia. I also thank the MXT software team at IJCLab, Antoine, Marc, and Charles.

Warm thanks to Achille Stocchi the director of the IJCLab and the great couple Ahmed & Hadil, who are leading the collaboration between Paris Saclay university and my home university, An Najah. Thanks to this collaboration I got the opportunity to come to France to do an internship and then I continued my way. Thank you for our deep and valuable discussions, and support.

Sincere thanks to CNES for funding half of my thesis and allowing me to work on a space instrument. I would like to thank the MXT manager, thank you Karine for giving me the opportunity to participate in several tests for MXT in France and in Germany, and for encouraging me during this thesis. I also would like to thank Martin, who shared a lot of knowledge and information with me; you taught me several skills. Thanks to all of the CNES team, your trust in me to achieve the work always motivated me.

My deep appreciation goes to the scientific PI of the MXT, Diego Gotz. I learned a lot from you, and I am sure I will learn more. I would also like to thank the all MXT team at

CEA: thanks, Bertrand, Aleksandra, Aline, Eric, Diana, Philippe, Nicolas, and all the others. Thanks also to Vadim Burwitz from MPE in Germany.

One of the best moments during my thesis was in Italy with the Swift/XRT team in the Brera Astronomical Observatory. I especially thank Maria-Grazia and Paolo for the valuable knowledge and tools you taught me and for the lots of joy and pleasant moments I spent at the observatory.

Finally, Thanks to all scientists, engineers and the administrators in IJCLab and in the SVOM collaboration who shared their experiences with me.

Thanks to my family, beloved, and friends. Thank you, Mom and Dad, for the trust you gave me, for believing in me since the beginning, for your wishes, and for your encouraging words. Sisters and brothers: Hisham, Manar, Malak, Sarab, Mohammed, thanks for standing with me during this long way; thanks for the joy, for fun, for all the lovely memories that we lived and will live together. My brother Mohammed, the third physicist in our family, we shared the same place last year, and we had lots of adventures together, and I know that we will have more. You supported and helped me a lot. Thanks!

I would like to say a few words to my sister Hanan, who passed away during my last year in the thesis. I know you are still close to us, and you are now in a better place. I would like to tell you that I would not do it without you. You were the first one who inspired, supported, and encouraged me to study physics. I am so grateful for the nice moments we shared together and with your daughter Lea in France, Germany, and sure in Palestine.

I would like to express my warm emotions and love to my second family, Al Maa' آل ماع : Theraa, Manar, Masa, Afnan, and Oula, thank you my dears, for the craaaazzy times we had together in the same apartment, especially during COVID, and for all cooking and parties that we had for no reason!! I love you all!!! Thanks also, and good luck to the "Palestinian family" in France; we were literally a family: Tasneem, Sally & Omer, Reema & Yahya, Afnan, kholoud, and all the others.

Last but not least, getting married was the greatest thing that happened during my Ph.D. studies. To the love of my life, my husband Mohammad, warm emotions and thanks. You were always by my side, supporting and caring for me.

Acronyms

ADU Analog-digital units. 88

AGN Active Galactic Nuclei. 25, 27

BAT Burst Alert Telescope. 22

BATSE Burst And Transient Source Experiment. 18

CAMEX Complementary metal-oxide-semiconductor Amplifiers and MultipLEXer. 73

CCD Charged-Coupled Device. 15

CGRO Compton Gamma Ray Observatory. 17

CNES Centre national d'études spatiales. 43

CNSA China National Space Administration. 43

COMPTEL Compton Telescope. 18

EGRET Energetic Gamma Ray Experiment Telescope. 18

FEE Front End Electronics. 72

FEEM Front End Electronics Module. 78

FWHM Full width at half maximum. 70

GBM Gamma-ray Burst Monitor. 25

GFT Ground Follow-up Telescope. 10, 43

GRB Gamma Ray Burst. 9, 15

GRBM Gamma Ray Burst Monitor. 19

GRD Gamma-Ray Detector. 46

GRM Gamma-Ray Monitor. 43

GWAC Ground-based Wide Angle Camera. 10, 43

HESS High Energy Stereoscopic System. 27

-
- HETE** High Energy Transient Explorer. 21
- IACT** Imaging Atmospheric Cherenkov Telescope. 27
- IHEP** Institute of High Energy Physics. 46
- INTEGRAL** International Gamma-Ray Astrophysics Laboratory. 26
- LAT** Large Area Telescope. 25
- LIGO** Laser Interferometer Gravitational-Wave Observatory. 25
- LRIS** Low Resolution Imaging Spectrometer. 20
- MAF** MAjor time Frame. 79
- MDPU** MXT Data Processing Unit. 67
- MPE** Max-Planck institute for extraterrestrial physics. 47
- MXT** Micro-channel X-ray Telescope. 10, 15
- NAOC** National Astronomical Observatories of China. 48
- OSSE** Oriented Scintillation Spectrometer Experiment. 17
- PSF** Point Spread Function. 69
- SCSW** Scientific software. 78
- SVOM** Space Variable Object Monitor. 10, 15
- SXC** Soft X-ray Camera. 21
- ToO** Target of Opportunity. 10, 43
- UVOT** UV/Optical Telescope. 22
- VHF** Very High Frequency. 21
- VT** Visible Telescope. 43
- WFC** Wide Field Camera. 20
- WXM** Wide field X-ray Monitor. 21
- XIOPM** Xi'an Institute of Optics and Precision Mechanics. 48
- XRT** X-Ray Telescope. 22

Résumé étendu en français

Les sursauts gamma (GRBs) [1, 2] sont des éclairs intenses de rayons gamma avec une gamme d'énergie comprise entre ~ 100 keV et 1 MeV. Ces flashes de rayons gamma sont appelés *prompt* émissions [3] et durent généralement de quelques millisecondes à plusieurs minutes. Les émissions prompt sont suivies d'une émission *afterglow* de longue durée des rayons X aux énergies radio.

Selon leur durée, les GRBs sont classés en GRBs de longue durée ($\lesssim 2$ s) et en GRBs de courte durée ($\gtrsim 2$ s) [4]. Les GRBs longs et les GRBs courts ont également des propriétés spectrales différentes: les GRBs courts ont un spectre plus dur que les GRBs longs. De plus, les deux classes de GRBs ont des propriétés de galaxies hôtes différentes. Cette différence indique que les deux classes proviennent d'au moins deux générateurs différents ; les GRBs longs (ou un pourcentage significatif d'entre eux) sont associés à l'effondrement du cœur des étoiles supermassives [5, 6], tandis que les GRBs courts (ou un pourcentage significatif d'entre eux) sont associés à la fusion d'étoiles binaires objets compacts impliquant au moins une étoile à neutrons [7, 8, 9]. Les progéniteurs GRBs sont des émetteurs multi-messagers [10]. En plus des rayonnements électromagnétiques, les progéniteurs GRBs émettent un rayonnement non électromagnétique sous la forme de neutrinos de haute énergie [11] et d'ondes gravitationnelles [12], des ondulations dans l'espace-temps causées par l'accélération d'objets compacts, prédites par la Théorie de la relativité générale d'Einstein [13, 14, 15].

La haute luminosité des GRBs [16, 17] en fait des outils précieux pour sonder l'univers primordial [18] et tester notre compréhension de la physique dans les conditions les plus extrêmes [19].

Les GRBs sont étudiés et observés depuis plus de cinquante ans. Après des décennies d'observation, notre connaissance générale des GRBs est bien établie. Par contre, de nombreux détails restent en suspens et doivent être abordés comme la dissipation d'énergie interne à l'émission prompt [20].

La clé pour résoudre les mystères des GRBs est d'observer simultanément le rayonnement électromagnétique dans une large gamme spectrale et les messagers non électromagnétiques des mêmes progéniteurs. Une telle observation multi-messagers s'appuie sur un ensemble de télescopes spatiaux et terrestres de suivi et sur un ensemble de détecteurs sensibles aux rayonnements

nements non électromagnétiques [21, 22].

Dans ce contexte, le Space Variable Object Monitor (SVOM) [23], un satellite franco-chinois, commencera à fonctionner en 2023 pour observer les GRBs [24]. Le satellite SVOM dispose d'un ensemble complémentaire de télescopes embarqués et au sol, offrant une large couverture spectrale des émissions GRB *prompt* et *afterglow*.

À bord, SVOM dispose de quatre instruments, deux instruments à large champ de vision pour détecter les émissions promptes de GRB : l'instrument ECLAIRS (4 - 250 keV) qui est le déclencheur du satellite et le Gamma Ray Monitor (GRM) (15 keV - 5 MeV). SVOM est également équipé de deux instruments à champ de vision étroit : le télescope à rayons X à micro-canaux (MXT) (0,2 - 10 keV) [25] pour détecter les rémanences GRB dans la gamme des rayons X, et le télescope visible (VT) (450 - 1000 nm) pour détecter les rémanences GRB dans les gammes visible et proche infrarouge.

Au sol, il y a la caméra grand angle (GWAC) et les télescopes de suivi au sol (GFTs) pour suivre la source, et un réseau d'alerte d'antennes VHF pour une transmission rapide des informations entre le satellite et le sol.

Grâce à cette large gamme d'énergie unique, SVOM est capable d'observer les GRBs et leur rémanence dans une large gamme spectrale, permettant une meilleure compréhension de la physique qui les sous-tend. La mission SVOM est étendue au-delà de l'étude GRB, qui est le programme *Core* de la mission. Profitant de la large bande d'énergie de SVOM, plusieurs objets astrophysiques à haute énergie sont ciblés lors des programmes SVOM *General* et *Target of Opportunity (ToO)*.

Au cours de ma thèse, j'ai étudié principalement les observations du programme de base avec le MXT, où le MXT observe et localise la rémanence des rayons X des GRBs dans la gamme d'énergie de (0,2 - 10 keV) et communique rapidement les informations de la source au sol pour suivre la source. Dans le programme général, le MXT observe les rayons X d'autres types d'objets astrophysiques sur la base de propositions. Dans le programme ToO, le MXT observe les contre-parties X des sources multi-messagers, notamment la fusion de systèmes binaires, avec au moins une étoile à neutrons émettant des ondes gravitationnelles en plus du GRB.

Le MXT vise à localiser les GRBs avec une précision inférieure à deux minutes d'arc en moins de 10 minutes d'observation. La localisation rapide et précise de la source en temps

quasi réel est nécessaire pour favoriser le suivi de la source depuis le sol à des énergies plus basses [26], mesurer les décalages vers le rouge de la source, et ainsi étudier les propriétés GRB dans le repère au repos de la source [27], étudier la galaxie hôte [28] et le milieu environnant [29].

Le MXT a été conçu pour garantir le résultat scientifique attendu. Il se compose principalement de trois parties : l'optique [30], la caméra [31] et l'unité de traitement des données. Les optiques MXT sont des optiques à micro-canaux basées sur la géométrie des yeux de homard résultant en une PSF particulière avec un point central et de deux bras orthogonaux. Ce système optique est fixé à la caméra sur la base d'un détecteur pnCCD à faible bruit. Le MXT est équipé d'une unité de traitement de données (MDPU) pour analyser les images capturées par la caméra et effectuer un traitement scientifique.

Les traitements scientifiques gérés par le MDPU sont divisés en 4 catégories: la caractérisation du bruit, la reconstruction des photons et la localisation des sources, la gestion du paquet de télémétrie à envoyer au sol, et le suivi des données en produisant des résultats intermédiaires des trois traitements précédents. Au cours de ma thèse, j'ai conçu et mis en œuvre les deux premières catégories.

La première catégorie est la caractérisation du bruit, dans laquelle le niveau de bruit intrinsèque dans le détecteur est mesuré. Le bruit intrinsèque dépend de la température. Ainsi, le bruit doit être fréquemment caractérisé à bord pour correspondre aux conditions d'observation. Le bruit est caractérisé en calculant le niveau de bruit moyen et les cartes de seuil (les cartes dites sombres) pour tous les pixels. Nous avons développé une méthode pour calculer la carte de bruit moyen en prenant la valeur moyenne pixel par pixel sur N images et la carte de seuil comme plusieurs écarts type de la fluctuation du bruit autour de la valeur moyenne. Un seuil de valeurs aberrantes est inclus pour rejeter les pixels aberrants de l'analyse et pour garantir de ne pas biaiser les cartes sombres. L'évaluation des cartes sombres s'est avérée robuste en présence de valeurs aberrantes et équivalentes aux cartes de référence calculées avec l'analyse au sol.

Lors des observations, les cartes sombres sont utilisées pour sélectionner les pixels au-dessus du bruit. Le MDPU traite les pixels sélectionnés pour reconstruire les photons X et les accumuler dans la carte de photons. La carte de photons est utilisée pour localiser la source et calculer ses coordonnées dans le ciel avec précision et rapidité, ce qui est la principale exigence scientifique du MXT.

Durant ma thèse, j'ai conçu et testé l'algorithme de localisation MXT. L'algorithme tire parti de la forme de la PSF du MXT (point central + bras) pour guider la recherche du pic de la source. La carte de photons (le signal détecté) est corrélée avec la PSF (la forme du signal attendu). La position du pic dans le détecteur MXT est ensuite donnée par le barycentre 2D autour de la valeur de corrélation maximale. Cette méthode s'est avérée plus performante qu'un simple barycentre sur la carte de photons, en particulier dans le cas d'un faible flux de photons. La méthode de corrélation est calculée dans l'espace de Fourier à bord car elle est plus rapide que de la calculer dans le domaine spatial.

Pour répondre aux exigences de précision de localisation < 2 arcmin après 10 min, le MXT doit détecter au moins 200 photons. Le nombre typique de photons reçus pendant les premières secondes de la rémanence des rayons X varie entre quelques centaines et quelques milliers, ce qui signifie que MXT répondra aux exigences dans la plupart des observations.

J'ai étudié l'impact de plusieurs effets sur les performances de la localisation. Nous avons testé l'effet de la réduction de la résolution de la carte de photons, qui s'avère sans effet si elle est réduite à la moitié de la taille d'origine. De plus, nous avons caractérisé le biais causé par l'observation des sources dans le champ de vue du MXT, et nous avons corrigé ce biais. De plus, nous avons caractérisé et corrigé l'effet de la limitation matérielle, comme la présence de colonnes insensibles.

L'algorithme de localisation à bord du MXT doit être capable de détecter jusqu'à trois sources dans le champ de vision. Le MXT dérive la coordonnée du ciel, le nombre de photons et le rapport signal sur bruit pour chaque source. Afin de calculer le rapport signal sur bruit à bord, une méthode est développée en utilisant les données d'intercorrélation. La méthode est basée sur la sélection de deux valeurs de corrélation croisée pour calculer le nombre de photons et le nombre de bruits de fond dans le détecteur pour calculer le rapport signal sur bruit pour chacune des trois sources. La méthode pour calculer le rapport signal sur bruit à bord s'est avérée fonctionnelle et rapide.

Le modèle de vol du MXT, y compris les algorithmes scientifiques embarqués, a été minutieusement testé dans l'installation de test de rayons X Panter en Allemagne d'octobre à novembre 2021. Le test prouve que les algorithmes scientifiques embarqués du MXT peuvent être utilisés de manière fiable et à long terme. Les cartes sombres embarquées se sont avérées caractériser le bruit intrinsèque du détecteur et sélectionner les pixels avec un signal au-dessus

du bruit pendant l'observation. Avec les cartes embarquées, les photons d'énergie jusqu'à 0,08 keV peuvent être identifiés au-dessus du niveau de bruit. Les algorithmes de localisation se sont avérés donner une localisation précise du faisceau source injecté, même lorsqu'il est placé au bord du champ de vision du MXT. L'algorithme de localisation a montré de la robustesse en présence de colonnes insensibles. Enfin, le test sur modèle de vol du logiciel scientifique embarqué a été livré au CNES.

Les performances du MXT sont testées à l'aide de scénarios réalistes de GRB basés sur l'observation de Swift/XRT. Le logiciel SATANLIGHT a été développé pour simuler de tels scénarios. SATANLIGHT simule l'optique du MXT, la caméra, la géométrie, les sources dans le champ de vue et l'observation MXT. De plus, un GRB réaliste avec un spectre physique et un modèle de courbe de lumière peut être simulé sur la base d'observations précédentes par des missions similaires comme Swift. Durant ma thèse, j'ai participé au développement et à la caractérisation de cette simulation pour le MXT.

Le MXT a montré qu'il était capable d'étudier et de caractériser l'évolution temporelle de la rémanence X. De plus, le MXT est capable de caractériser le spectre des rémanences X, en particulier l'absorption des photons X à basse énergie (<1 keV). Les performances de localisation sont testées à l'aide de la population GRB du XRT. Les GRBs observés par le XRT sont convertis en observations MXT, et ils sont localisés par l'algorithme embarqué. Le MXT localise $\sim 80\%$ des GRBs XRT à mieux que 2 minutes d'arc après 10 min d'observation.

J'ai également commencé une étude des observations du programme Target of Opportunity avec le MXT, dans lequel le MXT suivra l'alerte des ondes gravitationnelles (OGs) pour rechercher les contre-parties X de la même source. Avec la sensibilité actuelle des détecteurs OG, les progéniteurs de GRBs courts sont plus susceptibles d'être observés avec les OGs. Pour cela, j'effectue une sélection d'échantillons courts de GRBs avec un décalage vers le rouge calculé. Plusieurs études peuvent être réalisées avec cet échantillon, j'effectue une étude des propriétés dans le référentiel des sources. Parmi les propriétés étudiées figurent les luminosités X. Enfin, l'échantillon a été utilisé pour tester l'observation avec MXT pendant le programme ToO. La détection de la contrepartie avec le MXT dépend de la vitesse à laquelle le télescope pointe vers la source et si le MXT a trouvé la source dès les premières observations ou non.

Comme résultat préliminaire de cette étude, le MXT doit pointer vers la source en moins de 4 heures pour localiser une source multi-messagers avec une précision inférieure à 2 minutes

d'arc. Pour les sources lointaines $z \approx 0.1$, le MXT n'est pas capable de les localiser avec une telle précision, mais, il pourra observer et localiser ces sources avec moins de précision.

Introduction

Gamma-Ray bursts (GRBs) [1] [2] are intense flashes of gamma-rays with energy range from ~ 100 keV-1 MeV. These gamma-ray flashes are called *prompt* emissions [3] that typically last from a few milliseconds to several minutes, followed by long-lasting *afterglow* emission from X-ray to radio energies.

According to their duration, GRBs are classified into long-duration GRBs with a duration of more than ~ 2 s and short-duration GRBs lasting less than ~ 2 s [4]. long-GRBs and short-GRBs originate from at least two different progenitors; long-GRBs are associated with the core collapse of supermassive stars [5] [6], while short-GRBs are associated with the merger of binary compact objects involving at least one neutron star [7] [8] [9]. GRB progenitors are multi-messenger emitters [10]. In addition to electromagnetic radiations, GRB progenitors radiate non-electromagnetic radiation in the form of high-energy neutrinos [11] and gravitational waves [12], ripples in space-time caused by acceleration of compact objects, predicted by Einstein's theory of general relativity [13] [14] [15]. The GRBs high luminosity [16] [17] makes them valuable tools to probe the early universe [18] and test our understanding of physics under most extreme conditions [19].

GRBs have been studied and observed for more than fifty years. After these observational decades, the general picture of GRBs has been well established. On the other hand, many details remain outstanding and must be addressed like the internal energy dissipation to the prompt emission [20].

The key to resolving the GRB mysteries is to observe the electromagnetic radiation in a broad spectral range and the non-electromagnetic messengers simultaneously from the same progenitors.

Such an observation relies on a set of space and ground follow-up telescopes and a set of sensitive detectors for the non-electromagnetic radiations [21] [22].

In this context, the Space Variable Object Monitor (SVOM) [23], a Franco-Chinese satellite, will start to operate in 2023 to observe GRBs [24]. The SVOM satellite has a complementary set of onboard and ground-based telescopes, providing broad spectral coverage of GRB *prompt* and *afterglow* emissions. Onboard SVOM, the Micro-channel X-ray Telescope (MXT) [25] will detect GRB afterglows in the X-ray range. MXT aims at localizing GRBs with an accuracy below two arcmin in less than 10 minutes of observation. The rapid and precise source localization in near real-time is necessary to foster the source follow-up from the ground at lower energies [26], measure the source redshifts, and thus study GRB properties in the source rest frame [27], study the host Galaxy [28] and the surrounding medium [29].

The MXT has been designed to guarantee the anticipated scientific outcome. It is equipped with a Charge-Coupled Device (CCD) detector [31], micro-pore optics [30], and a data pro-

cessing unit to manage scientific processing onboard. The data processing unit is responsible for detector noise characterization and analyzing in real-time the images captured by MXT to retrieve the GRB precise sky coordinates.

During my thesis, I designed and implemented the scientific software responsible for the noise characterization of the MXT detector and the software responsible for the source rapid localization onboard of the MXT. Tight constraints are set to the onboard software due to limited resources in space, the space conditions, and the limitations from the hardware subsystem. Despite these constraints, the MXT science software proved to match the scientific requirements during several tests.

This manuscript begins with a detailed description of the GRBs in the Chap. 1, where the evolution of our understanding of GRBs physics, the progenitors theoretical models, the *prompt* and *afterglow* emission mechanism and their properties, prospects, and motivation for GRBs studies are discussed. Chapter 2 describes the SVOM mission, where onboard and ground instruments are presented. The targeted astrophysical objects by SVOM and the observation programs are explained. The MXT instruments onboard of SVOM satellite is explained in Chap. 3, where the scientific objectives, features, coordinates, subsystems and simulation are described. Chapter 4 is devoted to the image processing performed by the MXT, including the MXT's detector noise characterization and the photon reconstruction. The development and characterization of the MXT algorithm to localize GRBs in real time and to compute the GRB signal-to-noise ratio are explained in Chap. 5. Finally, the MXT performance of observing real scenarios of GRBs is tested in Chap. 6. In addition, a sample of short GRBs with reliable redshift is studied and it is used to test the MXT observation in the context of multi-messenger astronomy.

1 - Gamma Ray Bursts

In this chapter, GRBs are discussed and explained from the observational and phenomenological points of view. Section 1.1 presents the historical aspects of the GRB discovery and observations through different space missions. The physical properties of GRB progenitors and emissions are explained in Sec. 1.2. Prospects and motivations for GRB study and building new instruments to detect them are presented in Sec. 1.3.

1.1 . Observational history

This section outlines the watershed discoveries that revolutionized our understanding of GRB physics. The observational history of GRB can be divided into three distinguished eras: the discovery and early era are presented in Sec. 1.1.1. The era of detecting the GRB afterglow is presented in Sec. 1.1.2. Finally, the current era is presented in Sec. 1.1.3. During each era, GRB missions are discussed regarding their capabilities and progress in understanding the nature of GRBs.

1.1.1 . The discovery and early times

1.1.1.1 The discovery of GRBs

The GRBs were first discovered by the Vela American military satellites [32] in the late 1960s [33]. Vela had been built to monitor the gamma radiation pulses emitted by nuclear weapons. Vela consisted of 12 satellites, each equipped with X-ray (3-12 keV) and gamma-ray (0.2-1.5 MeV) detectors.

On July 2, 1967, Vela detected a gamma radiation flash (see Fig. 1.1) that was not likely to come from nuclear weapons as it exponentially decays with time. Supernovae [34] [35] or solar flares [36] were two other possible explanations for such an event, but neither had occurred on that day. Later on, improved versions of Vela with higher time resolution were launched to determine the direction from which the gamma-rays were arriving. By analyzing the arrival times of sixteen detected events, rough sky positions were estimated, and they excluded terrestrial or solar origin and revealed a new type of gamma-ray flashes of cosmic origin later called GRBs. [37].

Each detected GRB is named based on its observation date, GRB YYMMDD. If more than one GRB is detected on the same day, an alphabetical counter is added, for example, GRB YYMMDDA, GRB YYMMddb.

1.1.1.2 The Compton Gamma Ray Observatory

Since the serendipitous discovery of GRB, several satellites have been launched to observe GRBs and study their properties. The Compton Gamma Ray Observatory (CGRO) [38] was one of the first missions dedicated to the physics of GRBs. CGRO was launched in 1991 equipped with four instruments: the Oriented Scintillation Spectrometer Experiment (OSSE), the Imaging

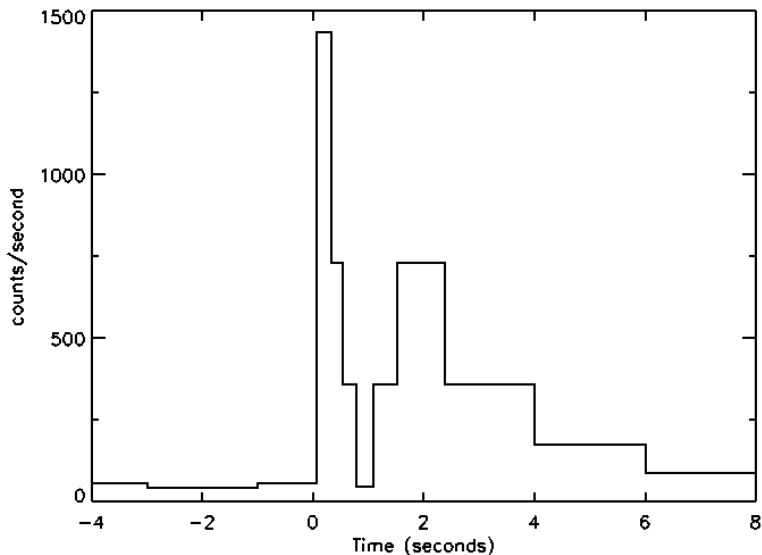


Figure 1.1: Light curve of the first GRB detected by Vela showing the intensity of the photons as a function of time, about 1500 photons were detected in the first second. The GRB’s duration is less than 10 s. Credit: NASA

Compton Telescope (COMPTEL), the Energetic Gamma Ray Experiment Telescope (EGRET), and the Burst And Transient Source Experiment (BATSE), as shown in Fig. 1.2.

The BATSE instrument [39] was in charge of detecting the GRBs in the energy range of (0.02 - 1 MeV). The BATSE consists of eight detectors mounted at each of the eight corners of the main structure of CGRO to cover the whole sky (see Fig. 1.2). After 9 years mission of CGRO, BATSE observed 2704 bursts (roughly one per day) and this led to highlighting several characteristics of GRBs.

The angular distribution of the detected bursts shows that GRBs are distributed all over the sky [40]. Figure 1.3 shows the sky map for the bursts detected by BATSE in the galactic coordinates as a function of their fluence (a measure of photon flux). It shows an isotropic distribution regardless of the source intensity, indicating an extra-galactic origin of GRBs.

GRBs from the BATSE first catalogue [42] show a bimodal distribution of their duration as shown in Fig. 1.4. First, the GRB duration is parametrized by the T_{90} value representing the time during which the 5% to 95% of GRB counts are accumulated at a given energy range. The T_{90} is measured in the observer (redshifted) frame. The bimodal distribution of the T_{90} indicates two classes of GRBs based on their duration with a separation at $T_{90} \sim 2$ s. The short-GRBs have average duration of $T_{90} \sim 0.5$ s, where the long-GRBs have average durations of $T_{90} \sim 30$ s [4]. These values are instrument-dependent according to the instrument sensitivity: as an instrument is less sensitive at a given energy band, it measures lower T_{90} .

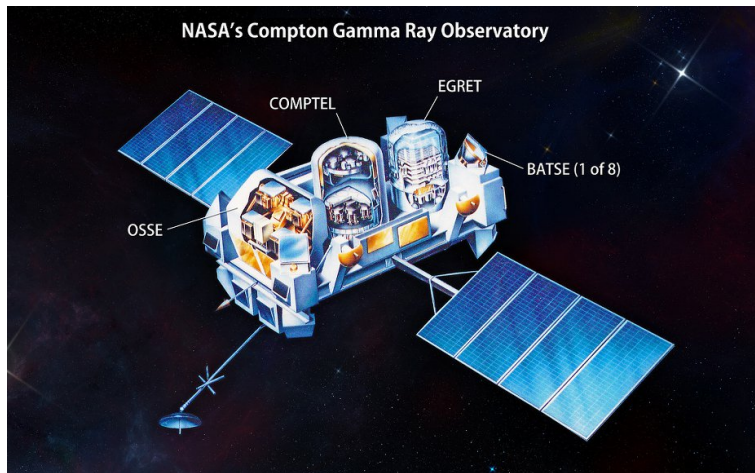


Figure 1.2: Structure of the CGRO satellite with its instruments: OSSE, COMPTEL, EGRET, BATSE. the BATSE 8 detectors are placed at each corner of CGRO structure

The hypothesis of different classes of GRBs is also supported by looking at their spectral properties. In terms of spectrum hardness ratio r_h , which is the ratio of the counts in two separated energy bands: $r_h = C_{E_2}/C_{E_1}$, where C_{E_2} (resp. C_{E_1}) is the number of counts with energy in E_2 (resp. E_1) band, with $E_2 > E_1$. short-GRBs have on average a harder spectrum, i.e., higher r_h than long-GRBs. The different properties of long-GRBs and short-GRBs pointed towards the possibility to have at least two different progenitors of GRBs.

Despite thousands of GRB observations by BATSE, the source of GRBs remained unknown. Astrophysicists proposed many theoretical predictions to validate the GRB extra-galactic origin demonstrated by CGRO mission. According to theories [44], the GRB source must be very compact to emit high-energy fluxes in a short time. The compact source releases the energy as relativistic outflow [45] [46]. As the relativistic outflow interacts with the surrounding media, it decelerates and loses energy so that one can predict synchrotron radiations [47] follow the GRB due to this interaction. This synchrotron radiation is the afterglow.

1.1.2 . The afterglow era

At that time, the obstacle to know the GRB origin was the lack of GRB distances information. Detecting the possible GRB counterpart allows for a better source localization and spectroscopic measurement of the redshift and hence the GRB's distance, which is not achievable with gamma-ray detectors. Later missions were designed to have the capability to detect the GRB afterglows.

1.1.2.1 The BeppoSAX satellite

The BeppoSAX [48] satellite, launched in 1996, was dedicated to the detection of the GRB afterglows. It had a set of instruments with a small field of view, including four X-ray telescopes operating in the 0.1 - 10 keV energy range to detect the afterglow. It had a set of a wide field-of-view instruments: the Gamma-Ray Burst Monitor (GRBM) instrument (50-700 keV) and

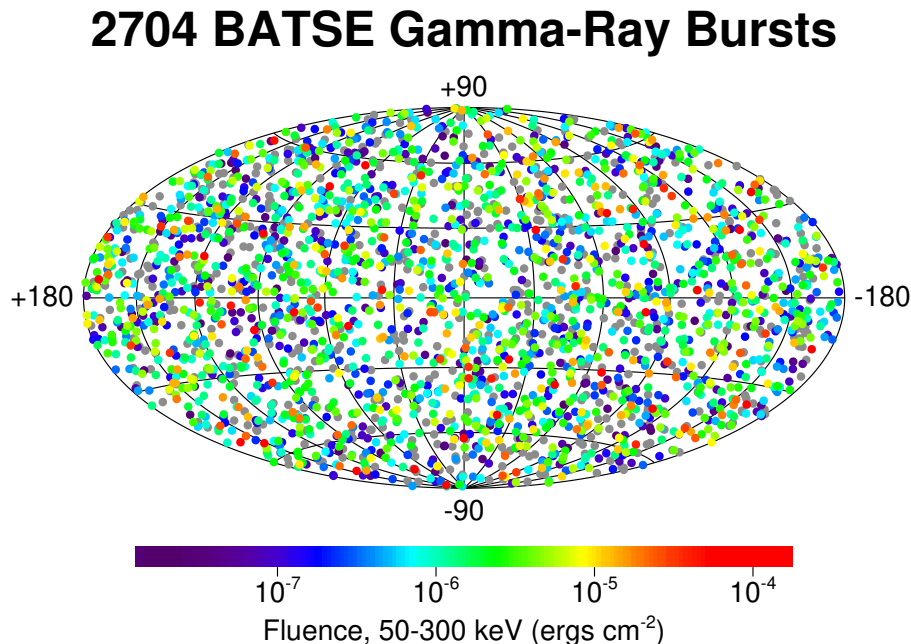


Figure 1.3: The angular distribution of 2704 GRBs recorded with BATSE. The projection is given in galactic coordinates. The GRBs locations are color-coded based on the fluence. This figure shows an isotropic distribution of GRBs that reveals an extra-galactic origin. Credit: [41].

the Wide Field Camera (WFC) (2 - 30 keV) to detect the GRB prompt emissions.

On 1997 Feb. 28, the GRBM detected the prompt emission from GRB 970228 [49]. About eight hours later, the X-ray narrow field instruments followed up the observation of GRB 970228 to search for counterparts at different energies. A bright X-ray emission was detected [50], and the first X-ray afterglow was discovered with a power-law decaying intensity with time as seen in Fig. 1.5.

Observing GRB X-ray afterglows led to retrieving a precise location of the source (~ 1 arcmin). The GRB coordinates were transmitted to the ground to observe the source in lower energy ranges. Thanks to the small localization error box of the X-ray instruments, the optical telescopes on the ground could point toward the source and follow up the observation. The optical afterglow was discovered, but no spectral lines were identified in the optical spectrum, so the redshift of the GRB 970228 was not measured [52]. A few months later, BeppoSAX GRBM detected GRB 970508 [53]. The afterglow was detected in X-ray by onboard X-ray telescopes and in optical energy ranges by the Low-Resolution Imaging Spectrometer (LRIS). The spectral lines were identified in the optical spectrum as shown in Fig. 1.6.

Hence, the redshift for a GRB was determined for the first time as in the following:

$$z = \frac{\lambda_{obs} - \lambda_0}{\lambda_0}, \quad (1.1)$$

where λ_{obs} is the observed wavelength of a spectral line, and λ_0 is its wavelength in the

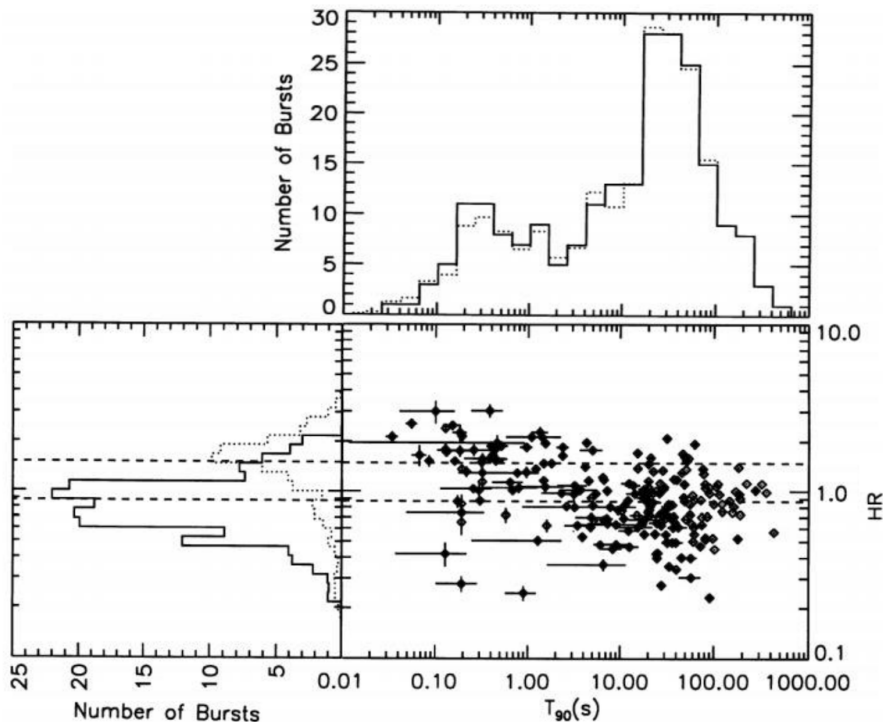


Figure 1.4: Distribution of GRB T_{90} and r_h , taken from the BATSE first catalog [41]. The plot shows a bimodal distribution for the T_{90} and r_h (HR in the plot), indicating two different classes of GRBs with different progenitors. Credit [43].

rest frame. The GRB 970508 redshift was constrained to $z=0.835\pm 0.001$ by comparing the wavelength of spectral lines in Fig. 1.6 to their corresponding rest wavelengths, which confirm a cosmological origin of the GRB.

BeppoSAX observed 1082 GRBs over seven years. The optical afterglow was observed for a few of BeppoSAX GRBs. The main limitation for not detecting the optical afterglow was the long time needed to transmit the source location to the ground, so the afterglow faded before being observed. The rapid data transmission was improved with later missions.

1.1.2.2 The High Energy Transient Explorer satellite

The High Energy Transient Explorer (HETE-2) satellite [54] was launched on October 9, 2000, to observe the prompt and X-ray afterglow emissions. HETE-2 had three instruments onboard, the FREGATE gamma-ray spectrometers with an energy range of 4-600 keV, the Wide-field X-ray Monitor (WXM) (2-25 keV) that locates GRBs with accuracy ~ 10 arcmin, and a set of Soft X-ray Cameras (SXC) (0.5-14 keV) to detect the X-ray afterglow and determine its location with accuracy < 10 arcsec. HETE-2 transmitted the coordinates of the source computed onboard, via a Very-High Frequency (VHF) network, to the ground only within a few minutes compared to a few hours in the previous missions. This rapid transmission of the source

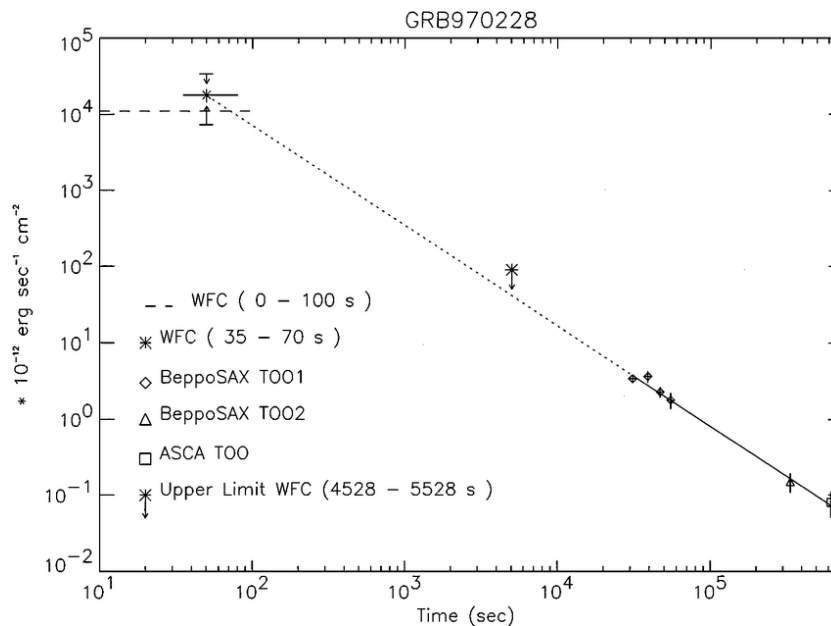


Figure 1.5: X-ray light curve of the first detected GRB afterglow. The light curve was constructed from data collected by several instruments onboard the BeppoSAX satellite. Credit: [51].

information allowed following up the source from the ground with lower energy ranges.

In 2003, HETE-2 observed bright GRB 030329, which is a long-GRB lasting more than 25 s. The X-ray afterglow was detected, and thanks to the rapid transmission of the GRB coordinates, the early optical afterglow was observed by the Siding Spring Observatory in Australia less than two hours after the burst. The spectral analysis of the optical afterglow at different times after the burst [55] shows supernova features in the optical spectrum as seen in Fig. 1.7. GRB 030329 spectrum confirmed the association of some long-GRBs to the death of a massive star or the supernova. [56].

1.1.3 . Current missions

1.1.3.1 The Neil Gehrels Swift Observatory

The Neil Gehrels Swift Observatory or Swift [57] is a multi-wavelength space satellite dedicated to the study of GRBs prompt and afterglow emissions. It was launched in November 2004 and is still in operation today. Swift has three instruments onboard, the Burst Alert Telescope (BAT) (15-150 keV) to detect the prompt emission [58], the X-ray Telescope (XRT) (0.3-10 keV) to detect the X-ray afterglow [59], and the Ultra-Violet/Optical Telescope (UVOT) (170-600 nm) to detect the ultra-Violet and the optical afterglow [60].

The Swift satellite outperforms its predecessors in its rapid and auto-slew capability. The BAT instrument detects the GRB's prompt emission, then the satellite auto slews to place the GRB in the field of view of the XRT and UVOT instruments, that in their turn, observe the source afterglow. The XRT localizes the source more precisely than BAT and transmits this

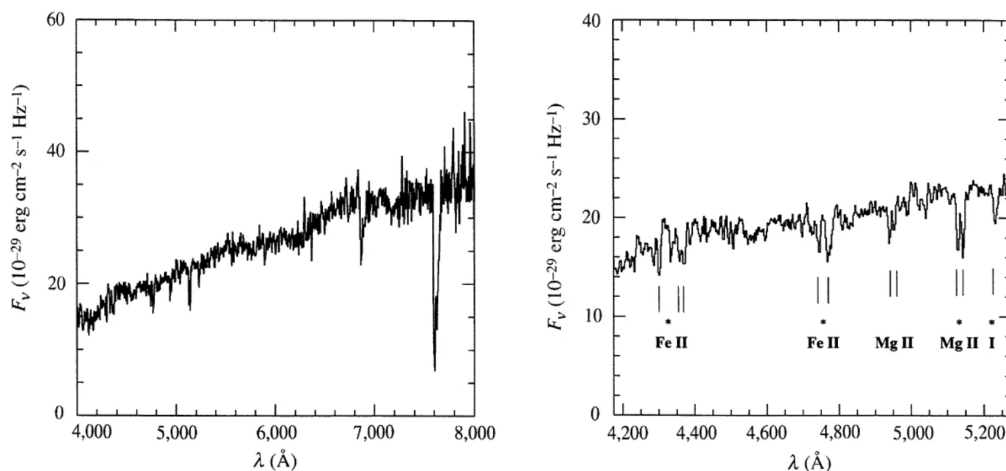


Figure 1.6: The spectrum of GRB 970508 optical afterglow as it is detected by LRIS (left). The Fe and Mg spectral lines are identified and constrained the GRB redshift to $z=0.835\pm 0.001$ (right). Credit: [53].

location to the ground to quickly follow up the source in the visible and infrared energy ranges. Thanks to the precise (1 - 4 arcmin, $\sim 2 - 5$ arcsec, ~ 0.5 arcsec for the BAT, XRT, UVOT, respectively) and rapid localization and multi-wavelength follow-up capabilities, Swift has made several breakthroughs in the science of GRBs [61].

The Swift accurate localization and rapid transmission of the position allowed for the determination of the redshift for $\sim 30\%$ of GRBs. Figure. 1.8 shows the distribution of the measured redshift values before and after Swift measurement. The mean value of redshift measured for Swift GRBs is $z \sim 2.2$. By estimating the redshift of GRBs, one can roughly measure the GRB distances according to the Hubble:

$$d = \frac{z \times c}{H_0} \quad (1.2)$$

where c is the speed of light, H_0 is the Hubble constant today, and d is the proper distance from the source galaxy at z redshift to the observer. Equation 1.2 is correct for low redshift, for further redshift the equation becomes more complicated but the distance is still proportional to the redshift. In 2009, Swift detected the most distant observed GRB, GRB 090423, with a redshift of 8.3 [62]. Such a high redshift proves that GRBs are a unique probe of the early universe.

Swift and HETE-2 discovered the first afterglow of a short GRB, allowing for the measurement of redshift for short GRBs.

Measuring the distance of GRBs allows to perform statistical studies of GRB properties at the source rest-frame which give clues about the GRB progenitors and their host galaxies. Long-GRBs and short-GRBs show different host galaxies properties, supporting that short-GRBs have a different progenitor than long-GRBs [65]. The association of long-GRBs to

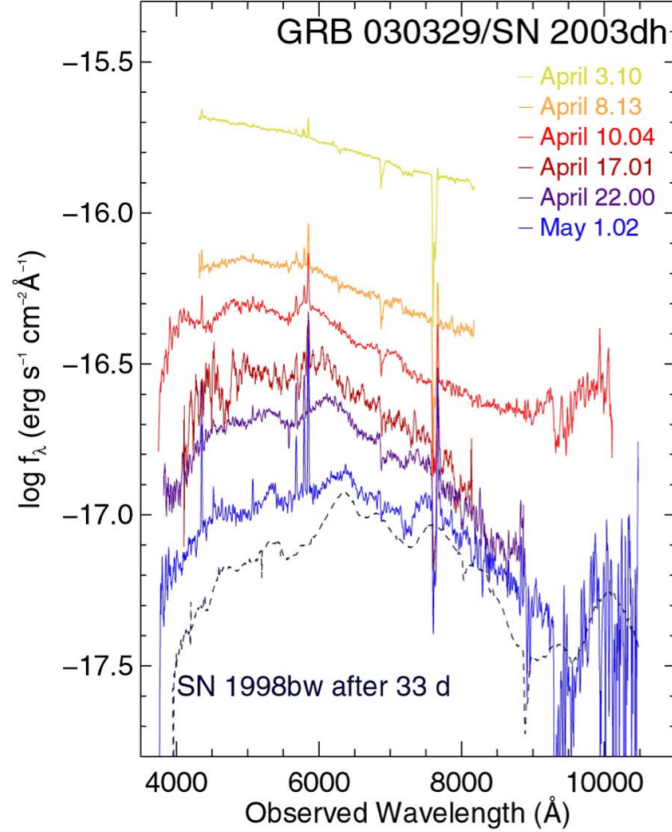


Figure 1.7: Spectral evolution of the GRB 030329 optical afterglow flux. The spectrum five days after the burst (April 3.10) shows a typical power-law spectrum. The supernova-like features appear 12 days after the burst (on April 10.04) and continue to develop in the weeks after. (May 1.02), SN2003dh dominates the spectrum with a spectrum similar to SN1998bw (dashed line) after 33 days. Credit [55].

supernovae was already confirmed, but there was no observational evidence for the short-GRB progenitors. Several short-GRBs are found to be located in early-type galaxies [66] that have low star-formation rate¹ ($< 0.1 M_{\odot} \cdot \text{yr}^{-1}$) and old stellar population (≥ 1 Gyr). [67]. The same properties are expected for the compact objects merger, supporting the hypothesis of an association of short-GRBs to the merger of two compact objects: two neutron stars (NS-NS) [7] or a neutron star and a black hole (NS-BH) [9] [68] [69]. This hypothesis was confirmed later by the coincident detection of a short-GRB and a gravitational wave from NS-NS merger in 2017 [70].

Although Swift has made several breakthroughs in the physics of GRB afterglows, it did not progress in prompt emission due to its limited coverage at high energies (150 keV for BAT instrument).

¹the total mass of stars formed per year, given in solar masses M_{\odot} per year

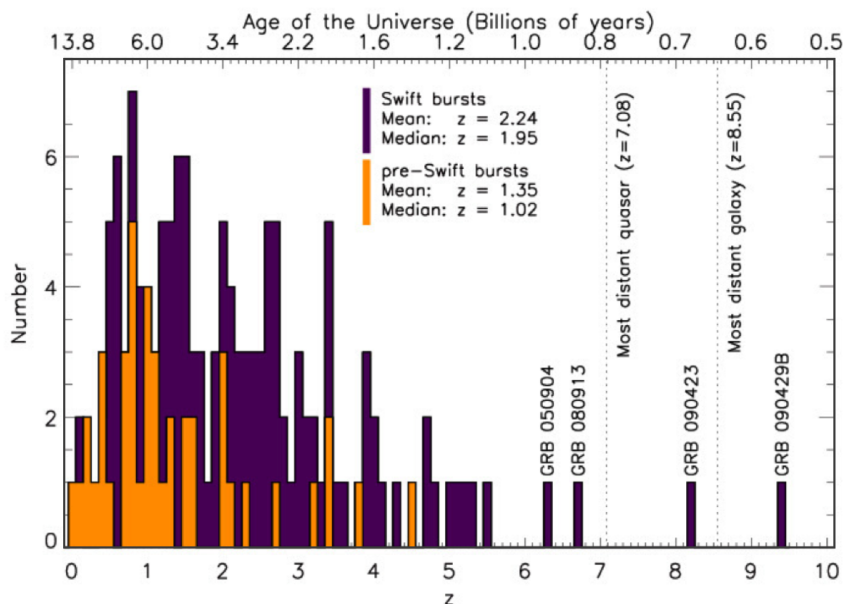


Figure 1.8: The distribution of GRB redshift z measured by Swift (in dark purple) and before swift (in orange). The Swift mission increased the number of GRBs with measured redshift and observed a far-distant GRB with redshift $z=8.3$. GRB 090429B has a photometric redshift $z=9.06$ with large error bars with a lower limit of $z > 7$ [63]. No spectral lines have been identified in the afterglow spectrum of GRB 090429B, so GRB 090423 is the most distant GRB with confirmed redshift. Credit: [64].

1.1.3.2 Fermi Gamma-ray Space Telescope

The Fermi Gamma-ray Space Telescope or Fermi satellite [71] is an American satellite developed by NASA to detect high-energy gamma rays with energy coverage of (15 keV - 300 GeV). This extended energy range complements Swift satellite observations (Sec. 1.1.3.1). The Fermi satellite was launched in June 2008 and is still in operation today. Fermi has two instruments onboard: the Gamma-ray Burst Monitor (GBM) [72] to detect GRBs with an energy range of 15 keV - 20 MeV, it consists of 14 scintillation detectors providing a large field of view covering the whole sky except the points occulted by Earth. The Large Area Telescope (LAT) [73] is sensitive to very-high-energy gamma rays (20 MeV - 300 GeV) from objects like active galactic nuclei (AGN), with an effective detection area of $\sim 0.9 \text{ m}^2$ for GeV energies. The LAT field of view covers 20% of the sky.

Fermi has increased the statistics of burst observations at very-high energy. During three first years of its mission [74], the Fermi satellite detected 12 GRBs with energies above the GeV [75]. Fermi detected the most energetic GRB ever recorded: GRB 080916C, with a total energy of 8×10^{54} erg [76].

On August 17, 2017, Fermi/GBM recorded a short-GRB, GRB 170817A [77] [78], in coincidence with a detection by the LIGO [79]/Virgo [80] of a gravitational-wave signal GW170817 [70]

from a NS-NS merger [7] [70]. Figure 1.9 shows the gravitational-wave signal recorded by LIGO/Virgo interferometers and the short-GRB emission light curves detected by Fermi/GBM and the International Gamma-Ray Astrophysics Laboratory (INTEGRAL) [81] telescopes. The short-GRB was observed with a delay of ~ 2 s after the merger [82].

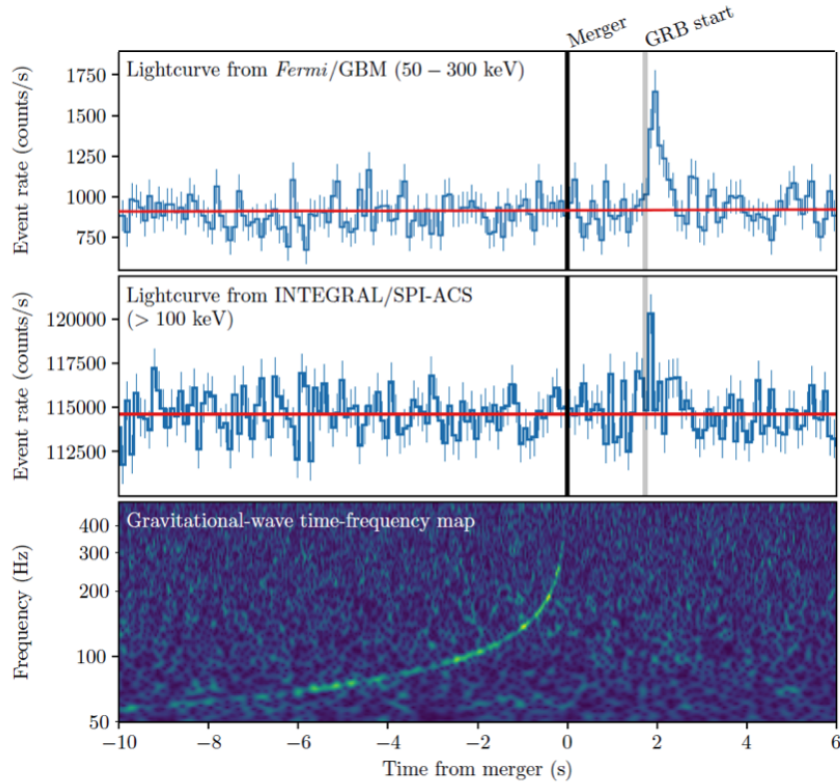


Figure 1.9: The simultaneous detection of GRB 170817A and GW170817 from an NS-NS merger. Top: GRB light curve observed by Fermi/GBM, middle: GRB light curve observed by INTEGRAL. Bottom: gravitational-wave signal as observed by LIGO interferometers. The three signals are co-aligned in time, the black line indicates the time of the merger, and the gray line indicates the beginning of the GRB emission with a delay of about 2 seconds after the merger. Credit: [70].

This event revolutionized our understanding of the physics of GRBs, in particular the GRB progenitors. It was the first time that the GRB source was observed with a non-electromagnetic radiation. It confirmed the compact binary merger model as a progenitor for at least a fraction of short-GRBs (see Sec. 1.1.3.1). This simultaneous detection of gravitational-wave and GRB radiations from a single source opened a wide window of multi-messenger astronomy as more events are expected to occur in the future. The prospects for GRBs in the context of multi-messenger astronomy are discussed in Sec. 1.3.

1.1.3.3 High Energy Stereoscopic System

The High Energy Stereoscopic System (HESS) [83] is a set of five ground telescopes dedicated to the very-high-energy gamma-rays (0.03 - 100 TeV) from a cosmic origin: gamma rays from supernova remnants, active galactic nuclei (AGN) [84] and GRBs [85]. Figure 1.10 shows the array of HESS telescopes, consisting of four 12 m telescopes and one telescope of 28 m with a total detection effective area of $> 600 \text{ m}^2$ for a few tens of GeV energies. The five telescopes are Imaging Atmospheric Cherenkov Telescopes (IACTs) that detect the very short flash of Cherenkov radiation generated by the relativistic charged particles produced when a very-high-energy gamma ray hits the atmosphere.



Figure 1.10: The five-telescope H.E.S.S. array located in Namibia. Credit: HESS collaboration.

Fermi/LAT has shown that a fraction of GRBs has GeV gamma-ray features in their emission (see Sec. 1.1.3.2). One explanation of very-high-energy gamma rays is the inverse Compton scattering. The particles in the relativistic outflow up-scatter the afterglow photons or photons from neighboring star clusters to higher energies up to more than 100 GeV. GRBs with a confirmed high-energy ($>10 \text{ GeV}$) gamma-ray emission are rare, about $\sim 1\%$ with the sensitivity of present days instruments [86].

The Major Atmospheric Gamma Imaging Cherenkov (MAGIC) telescope [87] is another telescope dedicated to the very-high-energy gamma-ray. The MAGIC telescope has the same working principle as the HESS. It consists of two IACTs sensitive to gamma rays with energies between 25 GeV and 30 TeV.

The Cherenkov Telescope Array (CTA) is a future telescope consisting of IACTs and has same working principle of the HESS and MAGIC telescopes. The CTA will extend the energy range of the observed gamma-ray up to 300 TeV.

Studying GRBs at very high energy would constrain the emission mechanisms and provide insight into particle acceleration in the GRB's outflow. HESS, with its large detection area, is aiming at increasing the sample of very-high-energy GRBs [88]. HESS receives alerts from experiments like Swift and Fermi to follow up GRBs, searching for very-high-energy gamma rays. Although numerous follow-ups have been carried out with HESS, only 2 GRBs have been

observed with very-high-energy gamma-rays: GRB 190829A [89] observed between ($\sim 0.18 - 3.3$ TeV), and GRB 190114C observed between ($\sim 0.1 - 0.5$ TeV) [90], GRB 190114C is also observed by the MAGIC telescope. Thanks to the broad energy and large detection area of the HESS telescopes, more very-high-energy GRBs are expected.

1.2 . Phenomenology

As discussed in Sec. 1.1.1.2, GRBs are classified into two classes based on their duration, long-GRBs, and short-GRBs (Fig. 1.4). The classification is supported by the spectral properties and environment properties. Long-GRBs have a softer prompt emission spectrum than short-GRBs, and short-GRBs are found in galaxies on average older than the host galaxies of long-GRBs. These properties form substantial evidence of at least two different types of progenitors. Long-GRBs (or a fraction of them) are believed to be associated with the core collapse of massive stars (the supernovae) as seen in Sec. 1.1.2.2. Meanwhile, short-GRBs (or a fraction of them) are believed to be associated with the merger of NS-NS or NS-BH as seen in Sec. 1.1.3.2. This section discusses the most accepted model for the GRB progenitors, their prompt and afterglow emission mechanisms, and their temporal and spectral properties.

1.2.1 . GRB progenitors and emission mechanism

The short-GRBs and long-GRBs show similar spectral evolution. The long-GRBs during the first 2 s have similar properties to short-GRBs, indicating a common emission mechanism for both classes regardless of their different progenitors. This section first discusses the emission mechanisms for a GRB regardless of its progenitors. Then the two models of GRB progenitors are discussed, along with hints to other possible GRB progenitors.

1.2.1.1 The fireball model

The fireball model is the most accepted model that describes how the energy from a GRB central engine is turned into radiation. In this model, a stellar-mass object (the progenitor) undergoes a catastrophic event that releases a large amount of energy in a small region (the central engine) of size D , containing a mass M_0 , most likely a black hole [1]. In this compact region, a fraction of the energy is converted into gravitational waves, another fraction is carried by neutrinos [10], and a small fraction goes to a fireball of hot thermal photons γ , leptons e^\pm and baryons [91].

From the observed prompt emission fluence, one can deduce the total prompt emission energy (known as the isotropic energy) of $E_{iso} \sim 10^{51}$ erg. The observed average prompt photon energy is $E_\gamma \sim 1$ MeV, and the time between two successive photon pulses is Δt . This time variability Δt is short and could be as short as milliseconds [92].

The short-time variability implies a very compact emitting region with a size of $D \leq c \times \Delta t \sim 300$ km. Otherwise, the emission would be smeared out in time, wiping out any short-timescale variability.

Consequent to the central engine compactness and high energy, the central engine is optically thick, i.e. a significant fraction f_e of photons with initial density n_γ would have enough energy

to go through pair production process: $\gamma\gamma \rightarrow e^\pm$ [93]. The density of produced electrons is $n_e = f_e \times n_\gamma$.

The optical depth ² (τ) of the central engine is given by:

$$\tau = n_e \sigma_T D = f_e \times n_\gamma \sigma_T D = f_e \frac{E_{iso}}{E_\gamma D^3} \sigma_T D, \quad (1.3)$$

where σ_T is the Thomson cross-section. Substituting the typical values of E_{iso} , E_γ in Eq. 1.3 gives an optical depth of $\tau \sim 10^{15}$. With such a high optical depth, the central engine is opaque and does not radiate electromagnetic emission; thus, it has a thermal spectrum inconsistent with the observation [94].

However, the source luminosity deduced from energies and timescales discussed above is $\sim 10^{50}$ erg/s, it is larger than the Eddington luminosity ($\sim 10^{38} \frac{M}{M_\odot}$ erg/s), above which radiation pressure exceeds self-gravity, so that the fireball expands. In order to explain the observed non-thermal spectrum, the fireball must expand with an ultra-relativistic speed with a Lorentz factor Γ , which implies two modifications. First, the photon energy in the source frame is reduced by a factor Γ : $E_{\gamma,emit} = \Gamma E_{\gamma,obs}$. Second, the timescale in the source frame Δt_{emit} is larger by a factor Γ^2 than the timescale in the observer frame Δt_{obs} : $\Delta t_{emit} = \Gamma^2 \Delta t_{obs}$. Consequently, the source has a size of $D = c \times \Gamma^2 \Delta t_{obs}$, and the optical depth is reduced by a factor of Γ^{-6} . From Eq. 1.3 the Lorentz factor must be $\Gamma > 100$ to have an optical thin region with $\tau < 1$, [93].

The fireball expands adiabatically in a particular direction due to the pressure from the accretion disk around the central object, forming a jet with an initial $\Gamma \sim 1$. The initial thermal energy is converted into kinetic energy carried by the particles in the jet $E \sim \Gamma M_0 c^2$, thus the jet is accelerated, and Γ evolves linearly until it reaches the saturation value of $\Gamma = \frac{E}{M_0 c^2}$ at a distance r_s from the central engine, as shown in Fig. 1.11. When $\Gamma > 100$, only a small fraction of photons are energetic enough to create e^\pm pairs, and the fireball engine becomes transparent, but most of the radiant energy was converted to kinetic energy of particles in the jet. The jet continues to expand with constant Lorentz factor $\Gamma = \frac{E}{M_0 c^2}$ [95].

As the source initially released its energy sporadically, the particles inside the jet move as shells with different speeds and different Γ but with the same order of magnitude. The differentially moving shells of particles collide inside the jet (at a distance r_{is} from the central engine, see Fig. 1.11), producing internal shocks [96] that convert the kinetic energy into high-energy photons (the prompt emission) most likely by the synchrotron and synchrotron self-Compton mechanisms [47].

As the jet travels outward from the central engine, the particles interact with the interstellar medium around the progenitor (at a distance r_{es} from the central engine as shown in Fig. 1.11), producing external shock [96]: forward shock toward the inter-stellar medium and reverse shock from the inter-stellar medium toward the jet. The external shock radiates synchrotron radiations in the range of X-ray, UV, optical, infrared, and radio energies (the afterglow emission). Afterward, the jet is decelerated into the non-relativistic regime. Afterglow emission is observed until all kinetic energy is converted into synchrotron emission, and then

²Optical depth is a measure of a medium absorptivity where a completely transparent medium has an optical depth of zero.

the emission fades. The brightness of the afterglow depends on the fireball kinetic energy and on the density of the inter-stellar medium. In a denser medium, more particles from the jet interact with the inter-stellar medium, so more synchrotron radiation is emitted.

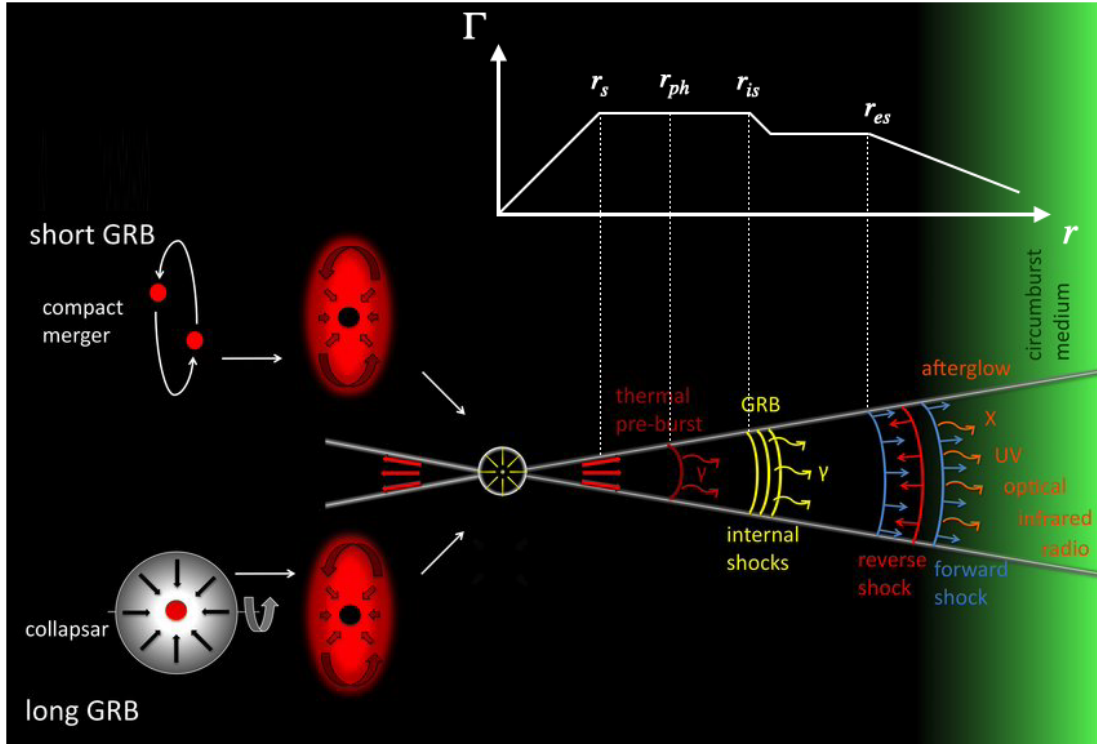


Figure 1.11: The fireball model showing how the energy from a GRB progenitor is turned into radiation. Credit NASA.

1.2.1.2 Long-GRB progenitor: the collapsar model

This model associates long-GRBs with the core-collapse of massive stars into a rapidly rotating black hole. Residual stellar matter swirls into a high-density accretion disk or torus [97]. Due to the fast rotating black hole, the accretion of matter in the polar regions becomes less intense, since the matter forms an accretion disk around the black hole and perpendicular to its poles. The e^\pm , γ fireball expands relativistically, and the expansion is collimated by the pressure from the accretion disk, forming a jet orthogonal to the accretion disk.

Unlike the ordinary supernova that only requires the star to be massive enough, to evolve to a GRB a star has to satisfy three conditions [98]. The star must be massive enough ($\sim 30M_\odot$) to form a central black hole. In addition, it must be rapidly rotating to develop an accretion disk capable of launching jets. Moreover, it must have a low metallicity so the jets can reach the star surface and to prevent high opacity driven mass loss. These three conditions make a GRB a rare event.

The connection between the long GRBs and the core collapse of massive stars has been confirmed by observing GRBs immediately followed by a supernova [99], like GRB 060218 (SN 2006aj) [100], and GRB 030329 (SN 2003dh) [101], as seen in Sec. 1.1.2.2.

The collapsar model is confirmed as a long-GRB progenitor, but it is not the only model. Some long-GRBs like GRB 060505 [102] and GRB 060614 [103] have been detected with no sign of supernova, which gives a clue to diversity in long-GRBs progenitors which could also include luminous magnetars.

1.2.1.3 Short-GRB progenitor: the merger model

The generally preferred model for short-GRB progenitors is the merger of binary compact objects involving at least one neutron star. The two compact objects lose energy in the form of GWs and gradually spiral inward. Once compact objects approach within a few stellar radii, tidal interaction disrupts the star, and the two compact objects merge, forming a black hole. A massive accretion disc surrounds the newly formed black hole. Hence, the fireball expands similarly as in the collapsar model along the rotational axis of the black hole. The merger could also produce a kilonova, a near-infrared/optical transient powered by the radioactive decay of heavy nuclei produced by the r-process in the ejecta during the mergers [104].

Several observations support the merger model. First, the observed short-GRB rate [105] is similar to the binary neutron stars estimated rate [106]. Second, short-GRBs are located in areas with an old stellar population; therefore, short-GRB progenitors are most likely related to old objects, like neutron stars and black holes [107]. Finally, kilonova emissions have been associated with some short-GRBs [108], such as GRB 130603B, where a faint object is observed in the optical and infrared range after one day and rapidly faded [109].

In 2017, the merger model was confirmed to be a progenitor of a fraction of short-GRBs by coincidentally detecting a gravitational wave signal (GW170817) a short-GRB (GRB 170817A) and a Kilonova from a merger of two neutron stars [70].

However, the merger model fails to describe some features observed in a subset of short-GRBs light curves, like the X-ray flares, which are an unpredictable increase in brightness of X-ray afterglows for a short time [111]. X-ray flares are thought to be related to the reactivation of the central engine [112], where magnetic energy stored in the magnetic field around the progenitors can be converted to kinetic energy carried by e^\pm , γ fireball [113]. This kind of progenitor, called a magnetar, is a neutron star with a powerful magnetic field around it (see Fig. 1.12). The magnetar could be generated when two neutron stars are not massive enough to form a black hole; hence the merger leads to a more massive neutron star. The magnetic fields of the two neutron stars are substantially amplified during the merger forming a strong magnetic field around the newly formed neutron star [114].

1.2.2 . The prompt emission

Observationally, the prompt emission is the phase in which the emission of gamma-rays/hard X-rays (~ 100 keV - 1 MeV) is detected. It typically lasts from a few milliseconds to a few seconds with variable light curves and no clear feature of spectral properties. In the following, the spectral and temporal properties are discussed in detail.

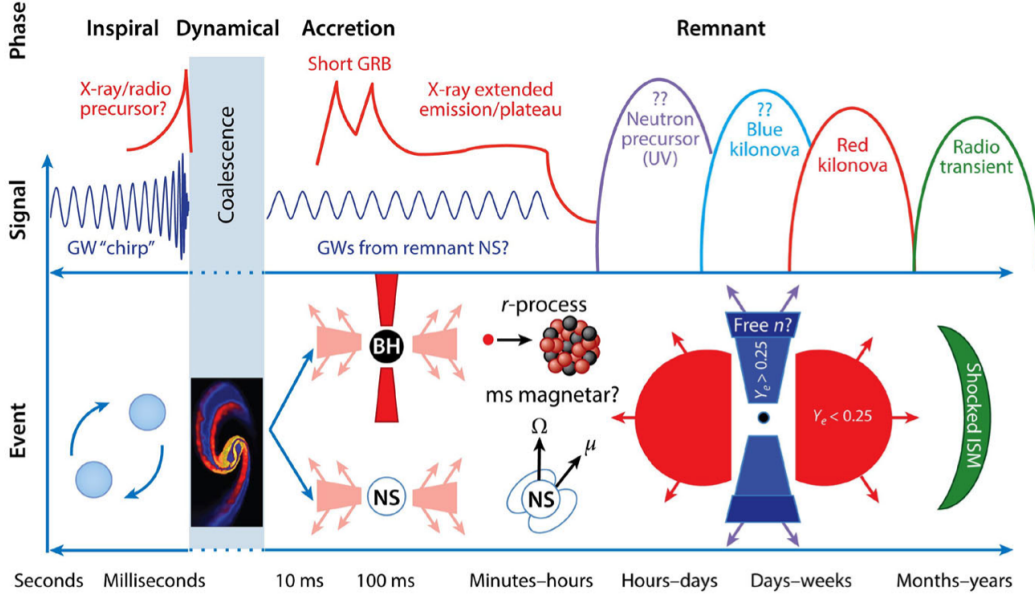


Figure 1.12: The scenario of a neutron star merger as a function of time. The expected gravitational wave and electromagnetic signatures from minutes before until years after the merger are illustrated on top. A merger of two neutron stars could produce a black hole (BH) and a Kilonova. The merger forms a more massive neutron star with a strong magnetic field if the two neutron stars are not massive enough. Credit: [110].

1.2.2.1 Spectral properties

The spectrum of GRB prompt emission is crucial to understand the radiation mechanisms involved in the GRB events. It provides clues about the burst energy, the characteristics of the outflow, as well as the particle acceleration mechanisms.

The spectrum can be expressed intrinsically or as observed by an instrument with $\mathcal{S}(E)$ effective area. The $\mathcal{S}(E)$ of an instrument is less than the total detection surface. The effective area $\mathcal{S}(E)$ depends on the photons energy, since the detector does not have the same detection efficiency for all energies. By convention, the spectrum can be expressed in the following ways [91] depending on the topic of study:

- photon number spectrum $N(E)$: it is the number of emitted photons per unit energy.
- flux density spectrum $F_\nu(E) = EN(E)$: it is the photon energy per unit energy. This spectrum is used when the photons can not be counted directly. The energy spectrum $\nu F_\nu(E)$ or the spectral energy distribution (SED) can be obtained from the flux density spectrum: $\nu F_\nu(E) = E^2 N(E)$. It shows the distribution of the source energy as a function of the frequency.
- photon count spectrum $C(E)$: it displays the number of detected photons by an instrument as a function of energy. It changes depending on the effective area of the instrument:

$$C(E) = N(E) \times \mathcal{S}(E)$$

For GRBs, the spectrum is usually expressed by the photon number spectrum $N(E)$. GRBs show non-thermal spectra with most of the energy ejected in the range of 0.1-2 MeV. The radiative process responsible for prompt emission has not been identified yet [115]. However, the most likely processes are the synchrotron, and self-Compton mechanisms [116]. From the observations, the GRB prompt emission spectrum is fitted with different functions [117] depending on the internal characteristic of the GRB, like the energy of the event or the particle distribution in the jet. The majority of GRBs (67% of Fermi/GBM GRBs) [116] are well fitted by the *Band function* [118], which is a smooth joint broken power-law given by:

$$\begin{cases} AE^\alpha \exp(-\frac{E}{E_0}) & E < (\alpha - \beta)E_0, \\ A[(\alpha - \beta)E_0]^{\alpha-\beta} \exp(\beta - \alpha)E^\beta & E \geq (\alpha - \beta)E_0, \end{cases} \quad (1.4)$$

where A is the normalization, α is the low photon spectrum index with typical values between 0 and -2, β is the high photon spectrum index with typical values between -2 and -4. Consistent results were also obtained by later missions. E_0 is the break energy between the two spectral regimes. An important parameter is the peak energy that can be computed from the energy spectrum $E^2N(E)$ as in Fig. 1.13. The peak energy is related to the break energy as the following:

$$E_p = (2 + \alpha)E_0. \quad (1.5)$$

The E_p characterizes the "hardness" of the spectrum and represents the energy at which most photons are emitted. E_p ranges from several keV to several MeV. The Band model is an empirical formula, and the physics behind the spectrum is not well understood. It can be interpreted in terms of the progenitor energy: how energy is dissipated and ejected to the fireball or what particles dominate. For example, the soft spectrum can be explained by the sporadically ejected energy to the particles moving in shells at a given rate. The interactions of the shells produce internal shock waves that emit synchrotron radiation. Later the ejected energy is slowed down to give the hard decay spectrum.

Some other GRBs show different spectra with power-law and exponential cutoff given by:

$$N(E) = AE^\alpha \exp(-\frac{(\alpha + 2)E}{E_p}). \quad (1.6)$$

This spectrum could be associated with an electron-dominated outflow and when the electrons slow down, they emit radiation via Compton scattering. This model is a subset of the Band function in the limit that $\beta \rightarrow -\infty$.

A subset of GRBs has a power-law prompt emission spectrum given by:

$$N(E) = AE^\lambda, \quad (1.7)$$

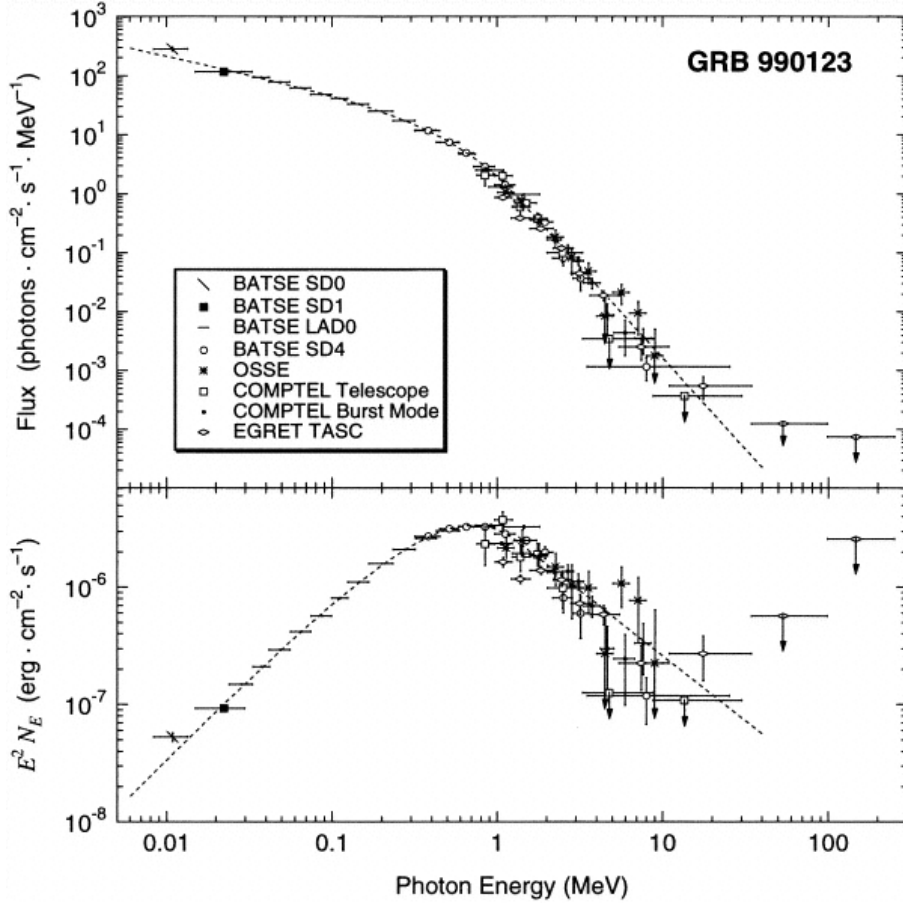


Figure 1.13: The spectrum of GRB 990123, taken from CGRO detectors and well fitted by the Band function given in Eq. 1.4. Top: the photon number spectrum $N(E)$. Bottom: the energy spectrum $E^2 N(E)$ with peak energy $\sim 1470 \pm 110$ keV. Credit: [119].

where λ is the photon index with a negative value. This model is used to fit the spectrum of faint GRBs or when the detector has a narrow energy band.

More observations are required to build a concrete understanding of the energy dissipation and the ejecta composite that could explain the observed spectrum.

1.2.2.2 Temporal properties

The prompt emission light curve is quite irregular in shape. Most of the GRBs show a time variability Δt over scales much smaller than the burst duration T like GRB 920221 in Fig. 1.14. In contrast, some GRBs have no observed variability during the burst $\Delta t \sim T$ such as GRB 920216B in Fig. 1.14. This temporal variability is explained by the multiple internal shocks, as the central engine can be active for the whole duration of the burst. Hence, the particle shells are spread out at different radii.

Figure 1.14 shows a sample of 12 GRBs from the BATSE archive, where the irregular shape

of their light curves can be seen. The sample includes short and long-duration events (from milliseconds to minutes), events with single peaks, and events with many peaks.

One more temporal property is the "spectral lag," in which the arrival time of the pulses in the softer energy band is delayed with respect to the pulse in a harder band. This spectral lag is visualized clearly for long-GRBs. Meanwhile, the short-GRBs show no spectral lag.

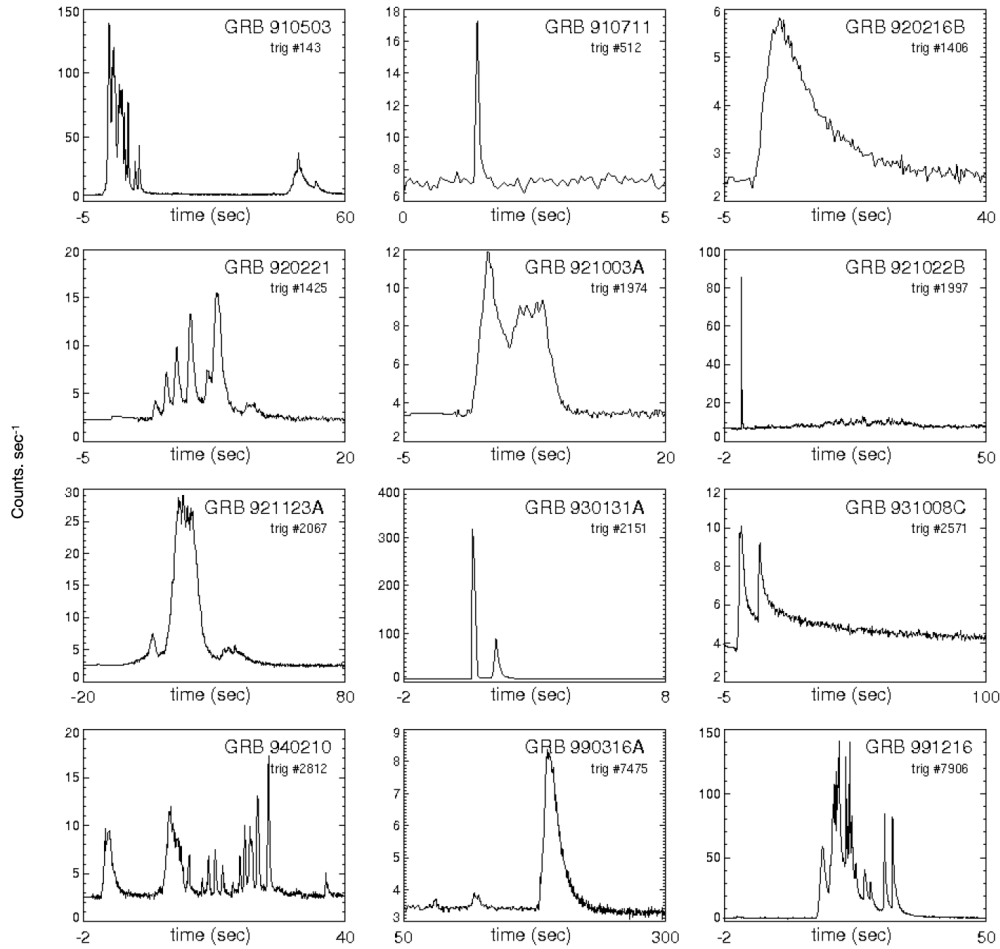


Figure 1.14: Sample of 12 GRBs light curves from the BATSE database showing their irregular shape. Credit: NASA

1.2.3 . The afterglow emission

The afterglow phase is defined as the emission (X-ray, UV, optical, infrared, and radio) released due to the interaction between the outflow particles and the inter-stellar medium producing external shocks: a forward shock that propagates in the surrounding medium and a reverse shock that propagates back to the outflow. The shock strength reduces as the outflow slows down, so the afterglow emission softens and fades with time.

The X-ray afterglows typically last for a few hours requiring a fast follow-up, while the

optical afterglows fade within days and radio afterglows last weeks to months. In the following, I will focus on the X-ray afterglow, that is the most related to the topics discussed in this thesis.

1.2.3.1 X-ray afterglow spectrum

The spectrum of the X-ray afterglow can be modelled with a simple power-law as in Eq. 1.7, λ taking typical values between ~ -1 and -3 .

The afterglow spectrum in the X-ray range suffers from several absorptions, as the radiation emitted by a distant source could be absorbed in the host galaxy, in our galaxy, and along the line of sight by diffuse matter [120]. In particular, X-ray photons (< 1 keV) are energetic enough to ionize neutral interstellar hydrogen gas completely, and they are absorbed by losing their energy via the photoelectric effect. For higher energy photons (> 1 keV) [121], the absorption probability decreases.

This absorption causes a characteristic bending of the power-law spectrum at low energies depending on the amount of material along the line of sight, as shown in Fig. 1.15. The X-ray afterglow spectrum is corrected as the following:

$$N(E) = A \times E^\lambda \times \exp(-N_H^{int} \sigma(E)) \times \exp(-N_H^{Gal} \sigma(\frac{E}{(1+z)})), \quad (1.8)$$

where $\sigma(E)$ is the cross section of the photoelectric effect, N_H^{int} is the intrinsic column density, N_H^{Gal} is the galactic column density.

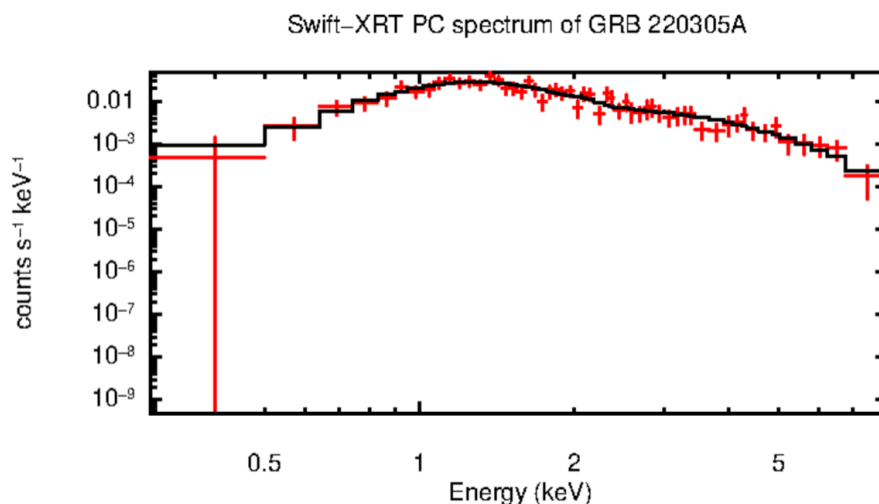


Figure 1.15: GRB 220305A X-ray afterglow spectrum, taken from the Swift/XRT database. The effect of galactic and extra-galactic absorption is visible for energies < 1 keV. Credit: [122]

1.2.3.2 X-ray afterglow light curve

Generally, the afterglow emission does not have a high temporal variability like the prompt emission, and its temporal behaviour should follow a simple power-law decay. However, one of the most remarkable discoveries of Swift is that indeed the X-ray afterglow from minutes to hours after the trigger shows many possible features, illustrated in Fig. 1.16:

0. This phase represents the end of the prompt emission.
- I. Steep decay phase: it is the first phase after the prompt emission. It is smoothly connected to the end of the prompt emission phase and appears in most X-ray afterglow light curves. It has a very steep slope $\propto t^{-3}$ and could reach $\propto t^{-10}$. In this phase, the spectrum evolves and becomes softer than the prompt emission phase. The spectrum photon index (λ) is ~ -1 to -1.5 .
- II. Plateau phase: it is observed in $\sim 50\%$ of GRBs $10^2 - 10^3$ s after the prompt emission. It has a shallow decay $\propto t^{-0.5}$. This plateau phase could be explained by the energy injected continuously in the outflow due to the long-lasting central engine. So the outflow loses energy by interacting with the surrounding medium, and the central engine compensates for the energy loss. The spectrum in this phase is similar to the previous phase with a photon index ~ -1 .
- III. Normal decay phase: happens around $10^3 - 10^4$ s after the prompt emission. It is called "the normal phase" because it has the typical decay slope ($\propto t^{-1}$) that the external forward shock model predicts. This phase can be explained by stopping injecting energy, so the outflow keeps losing energy in the form of synchrotron radiation by interacting with the circumburst medium. The typical spectrum remains unchanged with a photon index ~ 1 .
- IV. Fast decay phase: the normal phase shows a steepening to a slope of $\propto t^{-2}$. This occurs after the so-called jet break, due to the outflow deceleration and the consequent decrease of the relativistic beaming, the outflow visible area reaches the border of the jet. No spectral evolution is observed during this phase.
- V. X-ray flare: this phase is seen in $\sim 30\%$ GRBs afterglow light curves. They could occur $10^2 - 10^5$ s after the prompt emission (they are superimposed on any previous phases). They are thought to be related to the reactivation of the central engine, as they show high temporal variability like the prompt emission.

Figure 1.17 shows an example of the X-ray afterglow light curve, taken from the Swift/XRT database. It shows the first steep decay, the plateau, the normal decay, and the X-ray flare. The fast decay phase is not seen in the light curve as the photon flux decreases rapidly.

1.3 . Motivation for GRB study and prospects

This section discusses how GRBs play an essential role in different fields in Astrophysics.

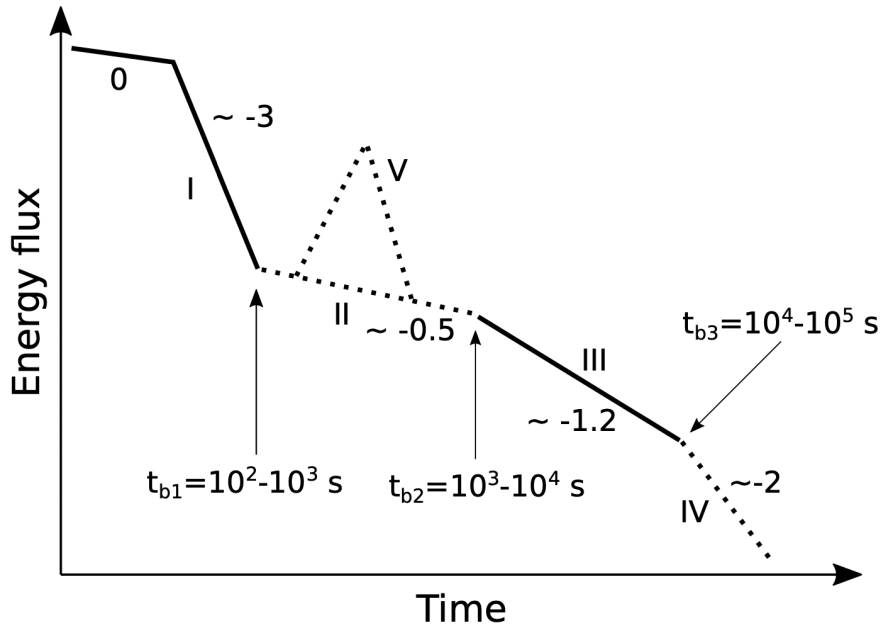


Figure 1.16: A canonical model for the X-ray afterglow light curve, showing all possible phases that can be seen in the light curve based on the Swift/XRT observation. Credit: [123]

1.3.1 . GRBs and the early universe

The GRBs are unique tools to probe the early universe, particularly the star formation evolution. Long-GRBs have massive stars as progenitors, where the massive star can be found in star-forming regions with a wide range of redshift up to $z \approx 9$.

Furthermore, GRBs can be used to study the cosmological parameters at a given redshift in a complementary to the type Ia supernovae "the standard candle" [124]. GRBs can be observed with high redshifts contrary to the Ia supernovae that can only be observed up to redshift $z \sim 1.7$.

So far, the sample of GRBs with measured redshift is still limited, so more GRBs observation and redshift measurements are required to use the GRB as a definite tool to probe the early universe and study the cosmological parameters.

1.3.2 . GRB and the inter-stellar medium

The afterglow emission travels through the inter-stellar medium. Therefore, by studying The afterglow emission spectral and temporal properties we can get detailed information about the density profile of the inter-stellar medium

Spectral (absorption or emission) lines in the afterglow spectrum give clues about the metallicity and the chemical abundance of the inter-stellar medium, the host galaxy, and the intergalactic medium along the line of sight.

1.3.3 . GRB and multi-messenger astronomy

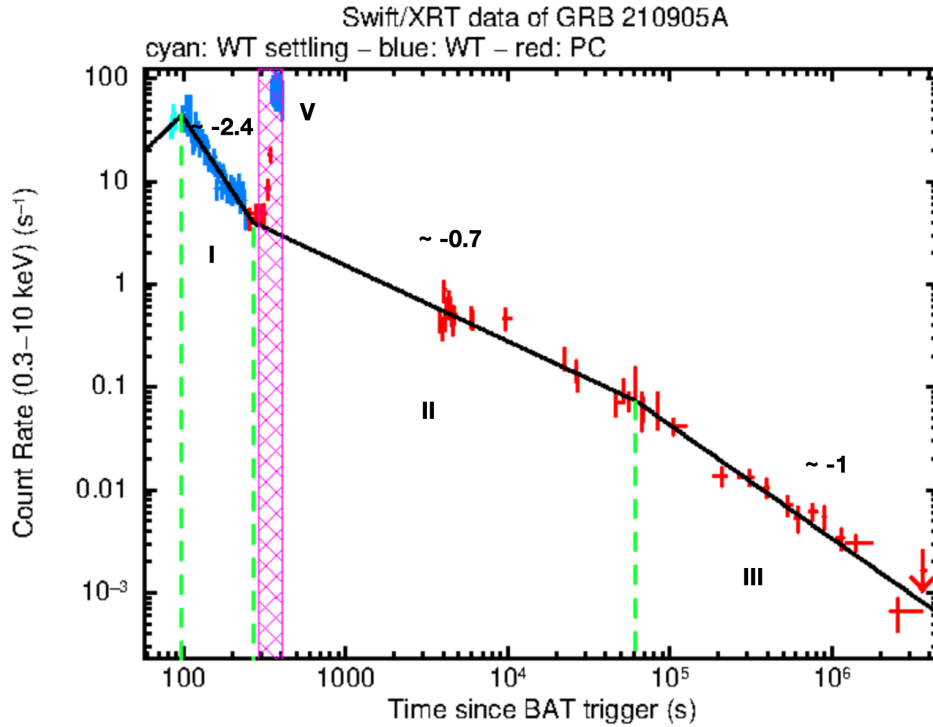


Figure 1.17: GRB 210905A light curve as observed by the Swift/XRT telescope. Four phases have occurred in this light curve, with the slope noted on top of each phase segment, and the index of each decay step is noted bottom of the light curve line. Credit: [122]

GRB sources emit radiation across the electromagnetic spectrum, high-energy neutrinos, and gravitational waves. As seen in Sec. 1.2.1.1 the internal shock and so the prompt emission occur at a distance of $\sim c\Gamma^2\Delta t \sim 10^{11} - 10^{13}$ m with $\Gamma > 100$ and $\Delta t \sim 100$ ms. This far distance from the central engine prevents studying the property of the central engine and the early phase of energy dissipation. In order to probe the GRB central engine and progenitors, it is essential to detect the radiation emitted during the first moments, such as the gravitational waves and the high-energy neutrinos.

In 2017, a gravitational wave and a short-GRB signal were observed simultaneously by LIGO/Virgo and Fermi (respectively) from a merger of two neutron stars (see Sec. 1.1.3.2). LIGO/Virgo and Fermi transmitted the alert with the source coordinates to the scientific community to follow the source in different wavelengths. After 11 hours from the merger time, an optical transient was identified by 6 collaborations with rapidly fading flux. The first spectrum of the transient shows a thermal spectrum evolving rapidly from blue to the near infrared. The absence of absorption lines (standard in supernova-like transients spectrum) excluded the possibility of a supernova. The observation of the radioactive decay of r-process elements confirmed the transient as a kilonovae and it is given a name (AT2017gfo) [125]. Chandra Observatory de-

tected the X-ray counterparts nine days after the gravitational wave detection [126]. VLA also observed the radio afterglow about sixteen days after the gravitational wave detection [127], discovering for the first time the afterglow of an off-axis GRB. No high-energy neutrino radiation was detected in coincidence with the merger. However, an upper limit of the neutrino flux is set by the *iceCube* experiment [128]. Figure 1.18 shows the follow up sequence of the two neutron stars merger on August 17, 2017.

This detection is unprecedented and yields a scientific wealth not possible from either radiation alone. First, it confirms the association of a subset of short-GRBs with binary mergers. The detection leads to constraint the equation of state for the neutron star by comparing the binary mass measured from the gravitational wave signal with the two possible objects after the merger remnant: a rotating black hole with an accretion disk and a magnetar. The joint detection also gave clues about the energy of the explosion. The kilonova and the optical afterglow provide information about the energy of the outflow and the inter-stellar medium. For a complete picture of the scientific outcome of this detection, refer to [129]. So far, GW170817/GRB 170817A is the only joint observation we have. More observations are required to understand how the GRB properties depend on the progenitor properties (masses, spins, structure ..etc) which is only possible with tens of joint observations.

More multi-messenger events are expected in the future due to improved sensitivity of the LIGOs/Virgo detectors during the following observation run O4 [130], and due to the join of the KAGRA detector the detection of gravitational waves. The expected detection of two neutron stars increases from 1_{-1}^{+12} during last observation run O3 run to 10_{-10}^{+52} during the following run O4. Regarding the black hole and neutron star binaries, the expected detection rate increases from 0_{-0}^{+19} during O3 to 1_{-1}^{+92} during O4 [130].

Swift and Fermi are still operating, but, they could reach the end of their missions in any moment. SVOM will complement and then take over the detection of GRBs prompt and afterglow emission in a wide spectral range and a long temporal window. Many new and advanced instruments sensitive to messengers like neutrinos and gravitational waves will be in operation at the same time as SVOM (Fig. 1.19). SVOM will receive alerts from these instruments to follow up the source and observe the electromagnetic radiation. The joint observation by SVOM and these new facilities will make real advances in multi-messenger astronomy. The next chapter 2 presents the SVOM mission and its detection strategy for the multi-messenger detection of GRBs sources.

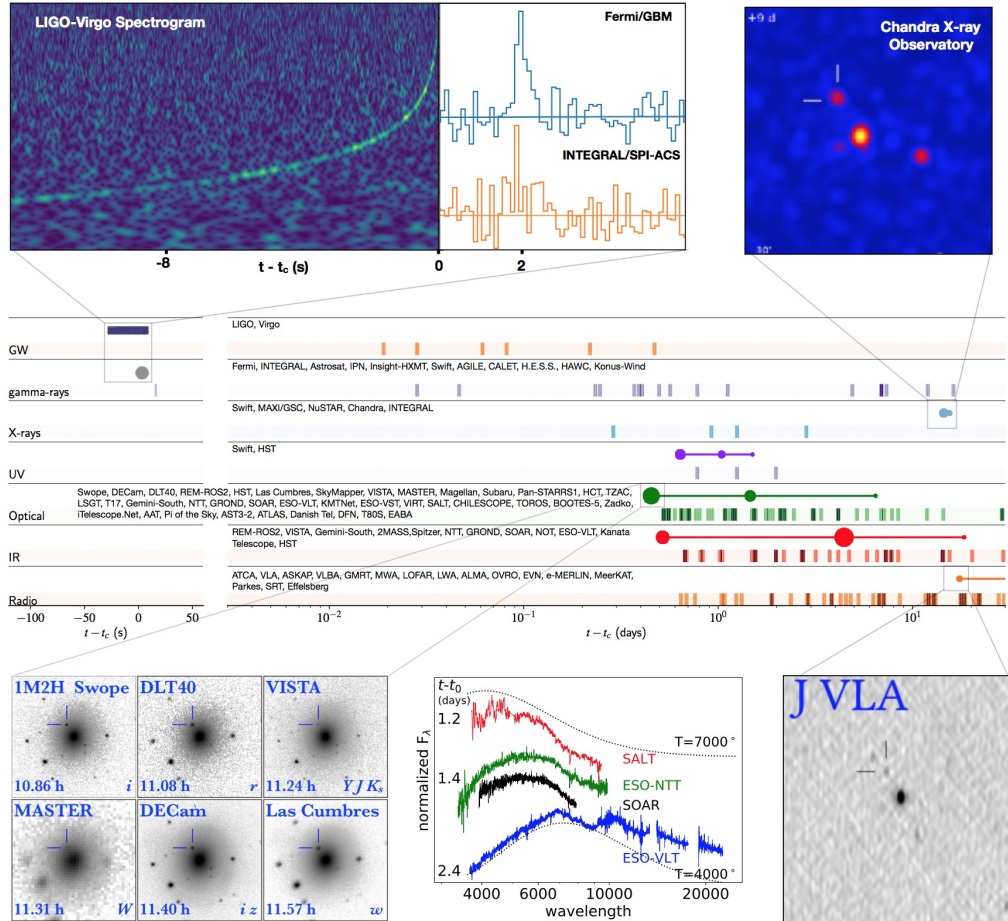


Figure 1.18: Timeline of the GW170817, GRB 170817A, and AT2017gfo signals. Top: LIGO/Virgo spectrogram of GW170817 (left), the Fermi and INTEGRAL observed light curves of GRB 170817A (center), and the Chandra observation of the X-ray counterpart (right). Middle: The observations sequence of the multi messengers. Two types of information are shown for each band/messenger. The shaded dashes represent the times when information was reported for each wavelength. The names of the relevant instruments are indicated at the beginning of the row. Solid circles represent observations in each band, circles areas scaled by brightness. The solid lines indicate when the source was detectable by at least one telescope. Bottom: the optical afterglow observations by different 6 telescopes (left), the Kilonova spectrum (center), and the radio afterglow observation by VLA (right). Credit. [70]



Figure 1.19: The observational panorama in the SVOM era. The simultaneous observations with SVOM and these facilities will be important to understand many transient phenomena like GRBs. Credit: [19].

2 - The SVOM mission

Contents

1.1	Observational history	17
1.1.1	The discovery and early times	17
1.1.2	The afterglow era	19
1.1.3	Current missions	22
1.2	Phenomenology	28
1.2.1	GRB progenitors and emission mechanism	28
1.2.2	The prompt emission	31
1.2.3	The afterglow emission	35
1.3	Motivation for GRB study and prospects	37
1.3.1	GRBs and the early universe	38
1.3.2	GRB and the inter-stellar medium	38
1.3.3	GRB and multi-messenger astronomy	39

SVOM [19] [131] is a Franco-Chinese mini-class satellite with a total weight of 930 kg and a set of ground-based instruments. The SVOM instruments were developed under the responsibility of the French space agency: Centre national d'études spatiales (CNES), and the Chinese space agency: China National Space Administration (CNSA). It is dedicated mainly to the study of GRB physics and to be launched in 2023. SVOM has four instruments onboard. Two of them are wide field of view instruments: the ECLAIRs telescope and the Gamma-Ray Monitor (GRM), and two are narrow field of view instruments: the Micro-channel X-ray Telescope (MXT) and the Visible Telescope (VT).

The space payload is complemented by a set of ground-based instruments to follow up the source: the Ground-based Wide Angle Camera (GWAC) and the Ground Follow-up Telescopes (GFTs), and by an alert network of VHF antennas for rapid transmission of the information between the satellite and the ground.

With unique wide-energy range, SVOM is able to observe GRBs and their afterglow in a broad spectral range, allowing a better understanding of the physics behind them. The SVOM mission is extended beyond the GRB study, which is the *Core* program of the mission. Taking the advantage of the wide-energy band of SVOM, several high-energy astrophysical objects are targeted during SVOM *General* and *Target of Opportunity (ToO)* programs. The nominal SVOM mission is planned up to three years. After that, the extended mission will start.

Section 2.1 explains the space and the ground instruments in terms of their properties and the detection role. The SVOM observational programs and the targeted astrophysical objects are explained in Sec. 2.2. The orbit and altitude followed by SVOM are explained in Sec. 2.3 together with the observation strategy.

2.1 . Scientific instruments

SVOM has a complementary set of ground-based instruments, space-based instruments, and a network for communication between ground and space. Some of these instruments have been developed in France and others in China with contributions from other countries: Germany, UK, Switzerland and Mexico. Figure 2.1 shows SVOM space-, ground-based instruments, with the flag of the countries that contributed to the development.

In this section, the construction and the function of each instrument are discussed.

2.1.1 . Space-based instruments

Four instruments compose the SVOM space payload as shown in Fig. 2.1. This is presented in the following sections and the characteristics are summarized in Tab. 2.1.

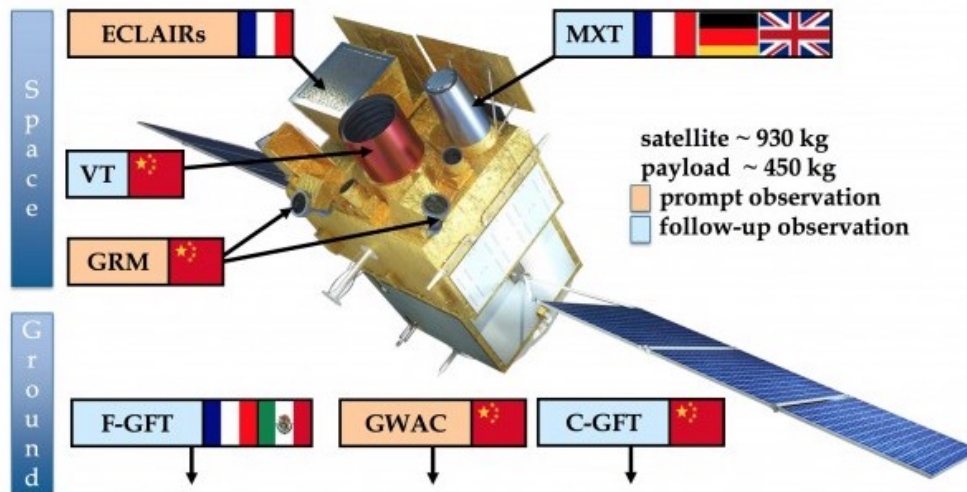


Figure 2.1: Graphical picture showing the SVOM components with its space- and ground-based instruments. The flag for each country contributing to the development of the instruments is indicated. Credit: SVOM collaboration.

2.1.1.1 ECLAIRs

ECLAIRs is a wide field of view (~ 2 sr) hard X-/gamma-ray coded-mask imager [132] [133], in charge of detection and fast localization in near real-time of GRB prompt emission (see Sec. 1.2.2). It is a French instrument developed by the French space agency CNES in collaboration with APC, CEA/IRFU-Saclay, and IRAP French laboratories.

ECLAIRs images the sky in an energy range of 4-120 keV. ECLAIRs, with a low energy threshold of 4 keV, is able to detect highly redshifted bursts, as well as extra-galactic soft X-ray transients, like X-ray flashes or supernova shock breakouts, which have not been well studied till today [134].

Figure 2.2 shows the components of the ECLAIRs telescope, where, at the top, there is the coded mask (54×54 cm²) that covers a significant fraction of the sky (2 sr). The mask consists

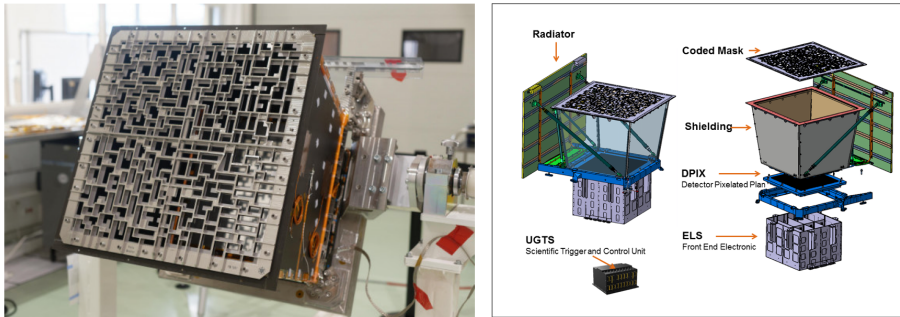


Figure 2.2: The flight model of the ECLAIRS coded mask (left). A schematic of the ECLAIRS telescope, showing its subsystem (right). Credits: SVOM collaboration.

of opaque and transparent regions. The photons can only pass through the transparent region that is 40% of the coded mask total region. The flight model of the coded mask is shown in Fig. 2.2. When photons pass through the coded mask, they interact with the detector (called DPIIX), located 46 cm below the coded mask.

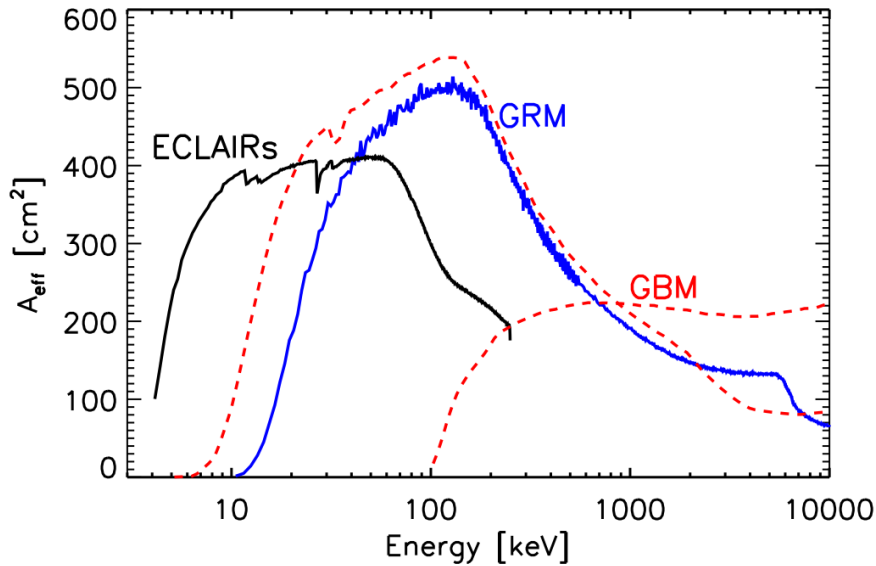


Figure 2.3: ECLAIRS total effective area for on-axis sources (black line), and the GRM effective area for 30 ° off-axis source (blue line). The Fermi/GBM effective area corresponds to four NaI and one BGO detectors (red dashed lines). Credit [135]

The detector consists of 80×80 CdTe pixels of 4×4 mm² each and 1 mm thickness, giving a total detection area of 1024 cm². The detector has a sensitivity of 2.5×10⁻⁸ erg.cm⁻².s⁻¹ for 1 s observation and an energy resolution of less than 1.6 keV at 60 keV. The effective area $\mathcal{S}(E)$ of ECLAIRS is more than 200 cm² at 6 keV and more than 340 cm² in the (10-70 keV) energy

range, which gives an advantage to ECLAIRs over the previous mission in low energy ranges. For example, the Fermi/GBM instrument (see Sec. 1.1.3.1) has an effective area $< 100 \text{ cm}^2$ at 10 keV. Figure 2.3 shows the effective area of ECLAIRs, GRM, and Fermi/GBM instruments. With this sensitivity, ECLAIRs is expected to detect more than 70 GRBs per year.

The image resulting from the interaction of the photons with the detector is called the shadow-gram, shown in Fig. 2.4. The data processing unit processes the shadow-gram image to search for new GRBs in the ECLAIRs field of view and to retrieve GRB positions onboard using a deconvolution algorithm (see Fig. 2.4). ECLAIRs has a localization accuracy better than 12 arcmin within a few minutes of observation [136]. The onboard computed position is then sent to the payload data processing unit that send the coordinates to the ground and to the other instruments onboard to follow-up the source in lower energy ranges. The MXT receives the trigger from ECLAIR, and improves the source localization. The complete observation sequence by all instruments is explained in the Sec. 2.3.2.

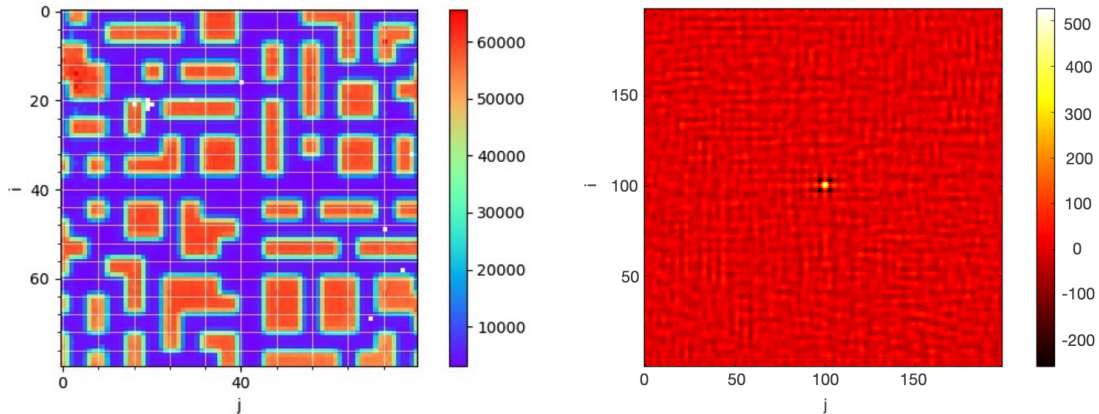


Figure 2.4: Example of the ECLAIRs shadow-gram image showing the number of counts recorded by the detection plane through the coded mask (left). A sky image reconstructed using the deconvolution algorithm, showing the source in the center of the ECLAIRs field of view (right). Credit: SVOM collaboration.

2.1.1.2 GRM

The Gamma-Ray Monitor (GRM) [137] is a wide field gamma-ray detector developed by the the Institute of High Energy Physics (IHEP) in China. It is operating in the energy range of 15 keV - 5 MeV and consists of three identical Gamma-Ray Detectors (GRD), spaced by 120° from each other in the perpendicular plane, with a total field of view of 2.6 sr, overlapping the ECLAIRs field of view as shown in Fig. 2.5.

Figure 2.5 shows the subsystems of one GRD, each GRD detector is composed of a sodium iodide (NaI) crystal scintillator, a plastic scintillator, a photo multiplier, readout electronics, and a calibration detector. In order to protect the detector from the low-energy electrons, a plastic scintillator is placed on top of the NaI scintillator.

As a gamma-ray photon passed through the plastic scintillator, the photon interacts with the scintillation material of the NaI scintillator, depositing its energy that is converted to blue light. The photo multiplier detects the blue light and amplifies it, and the readout electronics count the detected photons. The calibration detector is installed at the edge of each GRD to monitor the energy gain and calibrate the energy.

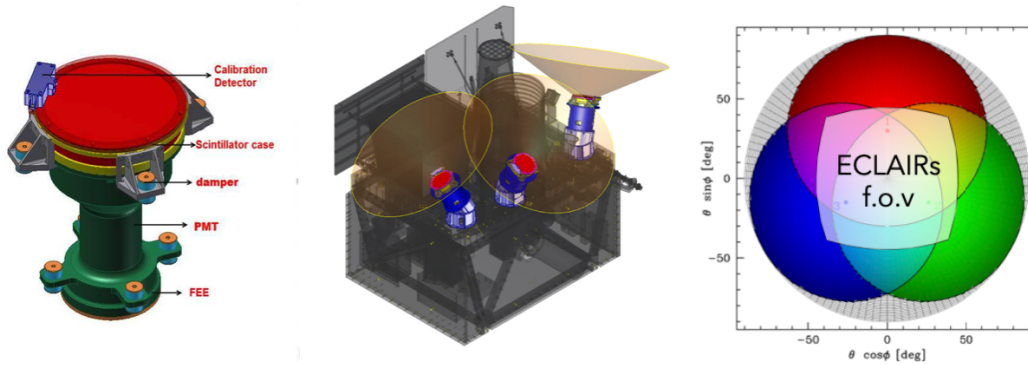


Figure 2.5: A graphical image of a single GRD detector composing the GRM instrument showing the subsystems of the detector (left). A graphical photo showing the arrangement of the three GRD detectors onboard the SVOM satellite (center). The combined field of view of the three GRD detectors (the red, blue, and green circles), superimposed with ECLAIRs field of view. The figure shows that the GRM covers the field of view of ECLAIRs completely (right). Credit: SVOM collaboration.

Thanks to its high-energy range, the GRM plays a vital role in characterizing the prompt emission properties, in particular the spectral parameters like the peak energy (see Sec. 1.2.2.1), which can not be studied by the ECLAIRs instrument alone (4 - 120 keV). The GRM also participates in the search for coincidental events with gravitational-wave sources detected by the LIGO and Virgo detectors (see Sec. 2.3.2).

Combining the information from the three GRD detectors, the GRM localizes the source with an accuracy better than 5° . GRM has its own trigger to enhance the ECLAIRs trigger. GRM is expected to detect > 90 GRBs per year.

By combining the data from ECLAIRs and GRM [19], SVOM is able to cover both Swift/BAT and Fermi/GBM energy ranges, and perform a complete study from a few keV up to a few MeV of prompt emissions and their spectral shape.

2.1.1.3 The MXT

The Micro-channel X-ray Telescope (MXT) [138] is a narrow field of view (58×58) arcmin² X-ray telescope, under the responsibility of CNES in collaboration with CEA/IRFU and IJCLab French laboratories, the University of Leicester in the United Kingdom, and the Max-Planck institute for extraterrestrial physics MPE in Germany.

The MXT is dedicated to studying and characterizing the afterglow emission in the soft X-ray energy range (0.2 - 10 keV). The MXT has scientific requirements of rapidly refinement

of the GRB position computed by ECLAIRs with better precision, and transmitting the GRB coordinates to the ground segment for the follow-up in lower energy ranges. The MXT also studies and characterizes the spectral and temporal properties of the X-ray afterglow. Moreover, with its low-energy threshold, the MXT is able to give information about the absorption of the afterglow emission in both the intergalactic medium and in host galaxies.

Figure 2.6 shows a schematic view of the MXT with its subsystems: the camera, the optics, the structure, and the radiator. The MXT subsystems, characteristics, scientific requirements and functions, are discussed in details in Chap. 3.

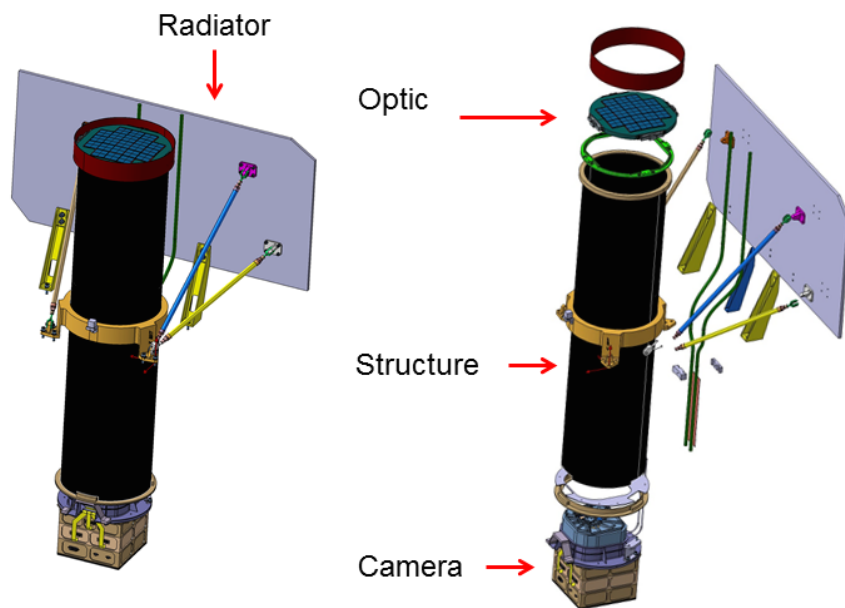


Figure 2.6: A graphical photo showing the MXT with its subsystems. Credit: SVOM collaboration.

2.1.1.4 VT

The Visible Telescope (VT) [139] is a narrow field of view (26×26 arcmin²) visible telescope, developed by the National Astronomical Observatories (NAOC) and Xi'an Institute of Optics and Precision Mechanics (XIOPM) in China, aiming at detecting GRB afterglows in the visible energy range.

The VT subsystems are sketched in Fig. 2.7. It is designed following the Ritchey–Chrétien telescope design [140] with primary (40 cm diameter) and secondary mirrors. The visible light is splitted into two channels using a dichroic mirror: the blue channel (450 - 650 nm) and the red channel (650 - 1000 nm) as seen in Fig. 2.8.

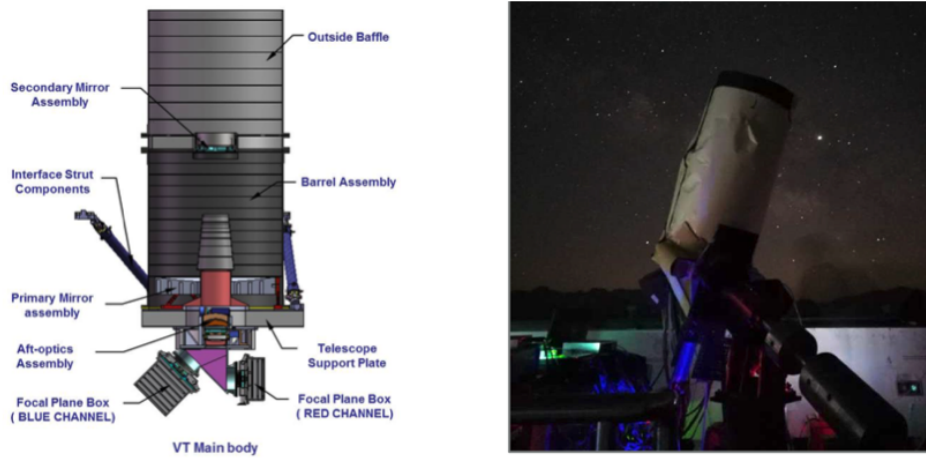


Figure 2.7: A graphical photo showing the different subsystems of the VT telescope (left). The qualification model of the VT telescope during the performance test at NAOC Beijing (right). Credit: SVOM collaboration

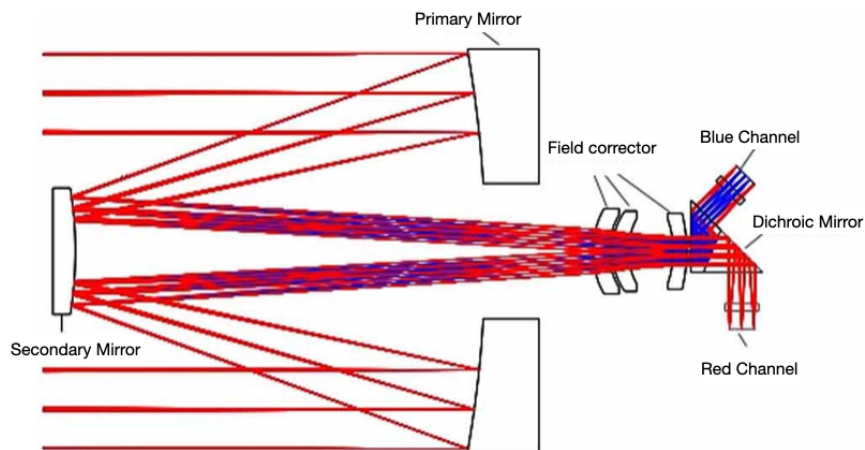


Figure 2.8: The optical path through the VT showing both the red and blue channels. Credit: SVOM collaboration

For each channel, a CCD detector is placed at the bottom of the focal plane to record photons and construct the image. Thanks to the high efficiency of the CCD detectors ($> 50\%$ for the red channel CCD) and sensitivity up to magnitude of $M_v = 22.5$ ¹ for an exposure of 300 s. With this sensitivity, the VT is able to observe the optical afterglow even for a far-distant GRBs with redshift $z > 6.5$.

The VT has its own data processing unit to process the images centered on the location

¹The magnitude M_v is a measure of the flux of an astrophysical object in a given wavelength interval

provided by the MXT. The VT refines the position computed by the MXT to achieve a localization accuracy < 1 arcsec and transmits the position in near real-time to allow the ground follow-up.

With its sensitivity, localization accuracy, and rapid pointing to the source, the VT is expected to increase the percentage of observed GRBs with confirmed high redshift up to $\sim 67\%$ compared to $\sim 30\%$ for Swift/UVOT.

2.1.2 . Ground-based instruments

2.1.2.1 GWAC

The Ground-based Wide Angle Camera (GWAC) system [141] is a set of 40 cameras, each of them with a diameter of 18 cm operating in the visible range (500 - 850 nm). Figure 2.9 shows a picture of the system prototype. The system's total field of view is around 5000 degree squared, providing a wide coverage of the sky regions observed by SVOM. Each camera is attached to a 4096×4096 CCD detector with sensitivity up to a magnitude of $M_v = 16$ in the new moon and to $M_v = 15$ during the full moon (for 10 s exposure). Three additional telescopes (two of 60 cm diameter and one of 30 cm) are installed to follow-up the source. The main goal of the GWAC system is to observe in the visible range during the prompt emission (in which most of the energy is emitted in the gamma range). A few GRBs have been observed from visible to gamma during their prompt emission phase. With the GWAC, the sample of GRBs observed in optical range during the prompt emission phase is expected to be increased by observing from 5 minutes before to 15 minutes after the trigger of more than 12% of SVOM GRBs. Such observations give clues about the different processes during the prompt emission phase, like the energy dissipation, radiation mechanisms, and particle acceleration in the jet.



Figure 2.9: Panorama for the GWAC system prototype installed at Xinglong Observatory in China. Credit: SVOM collaboration.

The GWAC receives GRB coordinates first from ECLAIRS, and then it receives the improved coordinates from the MXT, and the VT. The GWAC searches for the optical afterglow around the received coordinates with a localization accuracy of around 11 arcsec after 13 s. The system also has its own trigger that gives the system the ability to detect the source in an autonomous way. It also participates to follow-up multi-messenger events during the SVOM ToO program [142] (see Sec. 2.2).

The GWAC has been installed at the Ali observatory in China, it has been operating since 2019, and it responded to gravitational-wave alerts from LIGO and Virgo detectors during the O3 run (2019 - 2020).

2.1.2.2 GFTs

The Ground Follow-up Telescopes (GFTs) consist of two robotic telescopes shown in Fig. 2.10: the French GFT or COLIBRÍ [143] that has a field of view of 26×26 arcmin² and a diameter of 1.3 m operating in the visible to near infrared energy range (400 - 1800 nm), installed at the national observatory of San Pedro Mártir in Mexico, under the responsibility of France in collaboration with Mexico. The second robotic telescope is the Chinese GFT (21×21 arcmin²) with a diameter of 1.32 m operating in the visible band (400 - 900 nm) [19], installed at the Jiling observatory in China.

The two telescopes are dedicated to following up the detected sources by SVOM in less than a minute as a response to the alert transmitted by ECLAIRs. They compute the precise coordinates of the source with an accuracy of less than one arcsec and send it to the French science center, which communicates it to larger telescopes for visible light (NTT [144], VLT [145]) and radio waves (ALMA observatory [146]). GFTs also provides information about the redshift of the sources by studying the spectrum of the observed optical afterglow.

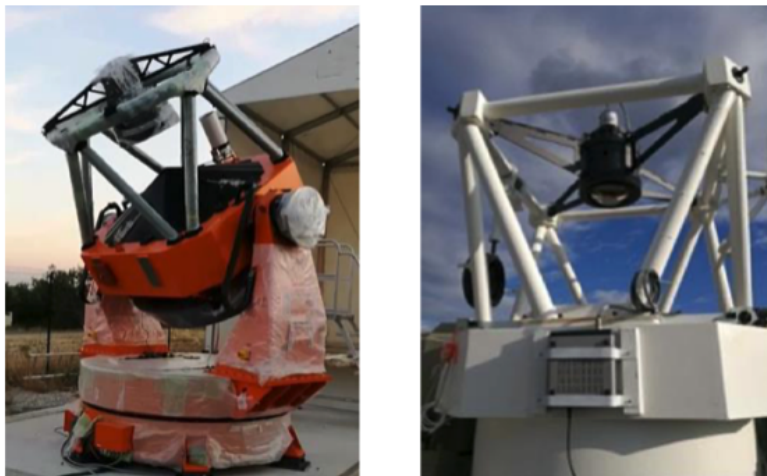


Figure 2.10: The two Ground Follow-up Telescopes. Left: the French telescope. Right: the Chinese telescope at Jilin observatory. Credit: The SVOM collaboration.

2.1.3 . The VHF alert network

What distinguishes SVOM from previous missions, is the rapid transmission of the information between the satellite and the ground segment; thanks to the Very-High Frequency (VHF) emitter onboard and the set of 45 VHF antennas that are installed homogeneously between latitudes -30° and $+30^\circ$ as seen in Fig. 2.11.

Table 2.1: Scientific and technical characteristics of the SVOM space payload and ground segment.

Instrument	Type	Field of view	Energy range	Sensitivity
ECLAIRs	Hard X-/gamma-ray coded mask imager	2 sr	4-120 keV	2.5×10^{-8} erg cm ⁻² s ⁻¹ in 1s
GRM	Set of three gamma-ray detector	2.6 sr	15 - 5000 keV	
MXT	X-ray telescope based on Lobster Eye optics	$1.1^\circ \times 1.1^\circ$	0.2 - 10 keV	8×10^{-11} erg cm ⁻² s ⁻¹ in 10s
VT	Ritchey-Chrétien telescope	26×26 arcmin ²	450 - 1000 nm	22.5 magnitude in 300 s
GWAC	Set of 40 camera and two optical telescopes	5000 degree squared	500 - 850 nm	16 magnitude in the new moon, and 15 magnitude in the full moon in 10 s
French GFT		26×26 arcmin ²	400 - 1800 nm	
Chinese GFT		21×21 arcmin ²	400 - 900 nm	

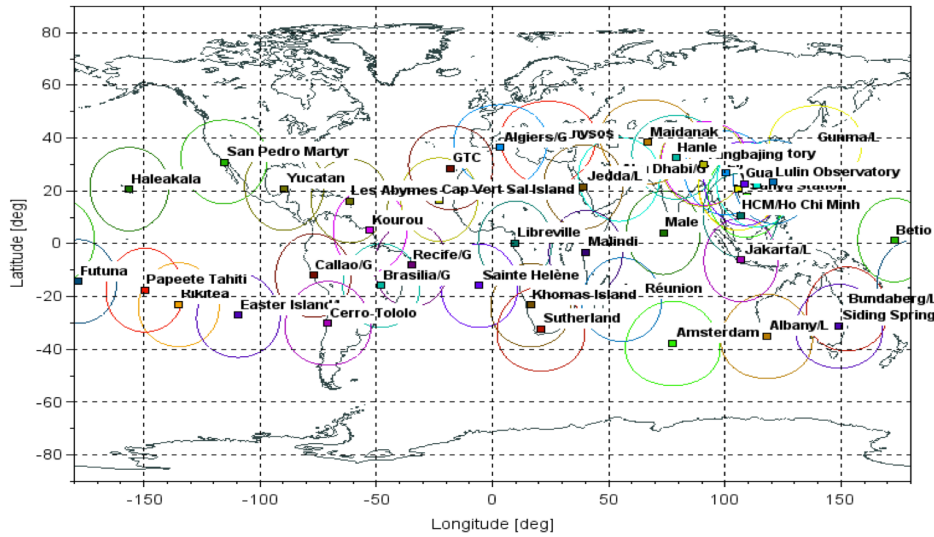


Figure 2.11: distribution of the VHF antennas between -30° and $+30^\circ$ around the equator.

When a GRB is detected, the alert is transmitted in a VHF packet to the ground. The VHF packet is received by one of the antennas, which in turn sends it to the French science center that communicates it to the ground facilities in less than 30 seconds after the alert time.

2.2 . Scientific programs

SVOM is a mission dedicated mainly to GRBs. In addition, SVOM observes a wide variety of astrophysical objects taking advantage of its wide energy band detection range. The astrophysical sources targeted by SVOM are distributed in three programs: the *Core* program (CP), the *General* program (GP), and the Target of Opportunity (*ToO*) program. Each program has an identified percentage of the mission time that will evolve during the extended mission to match the interests of the astrophysical community. Figure 2.12 shows the distribution of mission time over the three programs for the nominal and the extended mission.

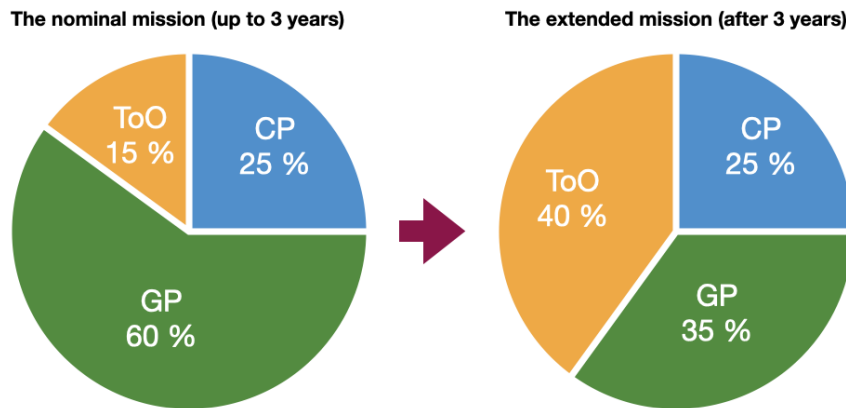


Figure 2.12: The observation time percentage planned for the different scientific programs of SVOM during the nominal mission (left), and the extended mission (right) after 3 years.

In the following, the three scientific programs of SVOM are explained. In each program, the targeted sources and the scientific objectives are presented.

2.2.1 . The *Core* program

As a *Core* program, SVOM is designed to study the physics of the GRB phenomenon in all its diversity. Both the prompt and afterglow emissions are studied and characterized, thanks to the wide spectral and temporal coverage of the emissions and the optimized follow-up strategy.

As seen in Fig. 2.12, the *Core* program spans 25% of the mission useful time, in which SVOM enriches the field of GRBs with many new observations that will improve our understanding of GRBs physics, in particular, their progenitors, host galaxies, jet production.

First, SVOM will study the prompt emission from gamma to optical energy range. SVOM will build a sample of GRBs with well-measured spectral and temporal properties thanks to the wide coverage of ECLAIRS and GRM (4 keV - 5 MeV). Having such a sample is required for a better understanding of the physics behind the prompt emission: the physical mechanism behind the GRB ultra-relativistic jet [147], the composition of the jet (electromagnetic or matter-dominated) [148], the internal dissipation mechanism responsible for the prompt emission [149], and many other debating topics are constrained and characterized.

Observing the prompt emission in the X-ray range will enable to the characterization of the spectrum and the identification of the dominant radiative process (see Sec. 1.2.2.1).

With the GWAC (see Sec. 2.1.2.1) optical observations, SVOM is expected to increase the number of GRBs with observed optical prompt emission, which provides clues about the internal dissipation mechanism.

Another scientific objective during the *Core* program is to study the afterglow emission from X-ray to radio energies. The MXT fast re-pointing to the GRB makes it possible to detect the early afterglow, which contains essential information about the end of the prompt emission phase and its connection to the afterglow phase.

The joint energy coverage of the ECLAIRS and the MXT in the (4 - 10 keV) energy range is

expected to provide crucial information on the relation between the prompt emission and the afterglow, for long GRBs lasting several minutes.

The wide coverage of GRB afterglows by the MXT and VT and by the ground telescopes will provide clues about the GRB distance, the nature of the interaction of the jet with the inter-stellar medium, and the nature of the host galaxy.

SVOM also will transmit the detection information to other experiments operating at the same time with SVOM in order to extend the afterglow observation. For example, SKA experiment (see Fig. 1.19) may observe the radio afterglow of a large number of SVOM GRBs, providing information about the surrounding environment density.

Along its mission, SVOM will detect all known types of GRBs: the typical GRBs ($E_p > 50$ keV) including short-GRBs, long-GRBs, and ultra-long GRBs, the softer GRBs: X-Ray Rich GRBs (XRR) ($30 \leq E_p \leq 50$ keV), and X-Ray Flashes (XRFs) ($E_p < 30$ keV) that are poorly studied till today. ECLAIRs with its low threshold energy is able to detect the XRR and the XRFs GRBs, and study their spectral properties.

SVOM is expected to increase the sample of GRBs with confirmed redshift up to 67%, thanks to the VT sensitivity and the rapid source localization by the MXT that allows the rapid follow up by the ground telescopes. As a reference, the Swift sample of GRBs confirmed redshift is about 30%.

Among SVOM confirmed redshift GRBs, the number of very-far distant GRBs with high redshift ($z > 5$) is expected to increase, opening a wide opportunity to probe the early universe. Figure 2.13 shows the expected distribution of redshift of ECLAIRs GRBs detected over SVOM nominal mission, showing a detection of 3 - 4 GRBs per 3 years with redshift $z > 5$.

2.2.2 . The *General* program

This program has 60% of the nominal mission useful time and is reduced to 35% during the extended mission as seen in Fig. 2.12. During the *General* program, the SVOM satellite monitors several astrophysical transients from the optical up to hard X-ray energies; trying to reveal the not well understood processes like the jet evolution and the disk accretion.

scientist can apply for an observation proposal every year. Proposals are evaluated and accepted by the time allocation committee based on the scientific value. Some interesting objects that can be monitored during this program are explained in the following:

- Active Galactic Nuclei (AGN): They are galaxies with an active super-massive black hole at their center. They are divided into different classes, based on the angle of the line of sight with respect to the accretion disk [150] as seen in Fig. 2.14.

During its general program, SVOM will monitor these objects. ECLAIRs, with its unprecedented sensitivity, especially in the range of (10 -20 keV), will study the inverse Compton scattering spectra of the scattered photons (emitted by the disk around the central supermassive black hole) by the relativistic electron plasma in the vicinity. ECLAIRs is expected to observe 250 AGN [19] during one year of observation, GWAC will study their light curves, and they will be followed by the MXT and the VT telescopes to monitor the X-ray and optical counterparts.

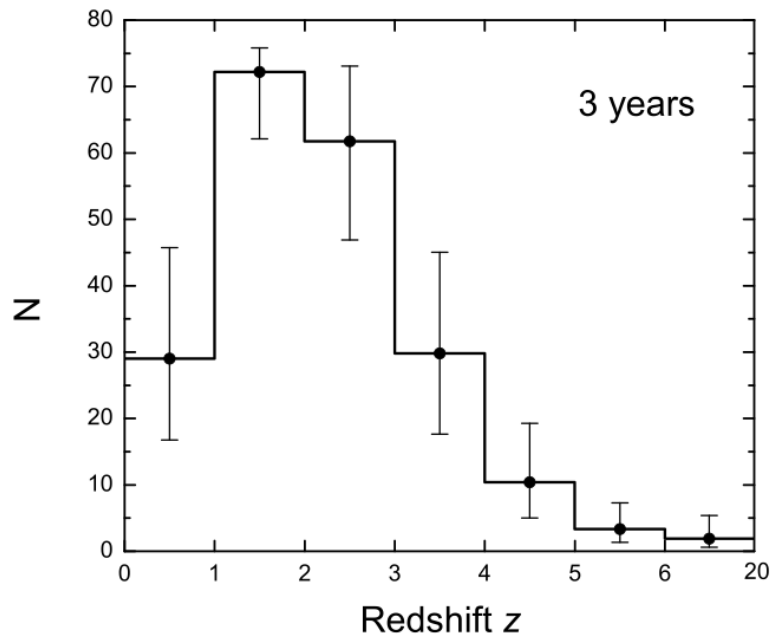


Figure 2.13: Simulation of the expected distribution for GRBs detected by ECLAIRs during the SVOM nominal mission (3 years), plotted as a function of their redshift. Credit: [19].

- Galactic accreting systems: the (0.1 - 5000 keV) energy coverage of SVOM gives the ability to study the galactic accreting objects like X-ray binaries [151], black hole binaries [152], and the cataclysmic variables [153]. In these systems, a compact object (white dwarf, neutron star, black hole) attracts matter forming an accretion disk. SVOM will observe these objects from the early stages of their outbursts, trying to shed light on the interaction of the matter in the accretion disk under extreme conditions of gravity.
- Flaring stars [154]: variable stars that go through dramatic increase in brightness for a few minutes. By observing the X-ray emission with the MXT, SVOM can study the geometry of the magnetic loop reconnection causing these events.
- The cosmic X-ray background [155]: is an isotropic X-ray emission from a combination of unresolved X-ray sources outside of the Milky Way. It is tracked by ECLAIRs and the MXT telescopes.

2.2.3 . The *Target of Opportunity* program

The *ToO* program is devoted to the unplanned observation of transient sources [156]. During the nominal mission, 15% is saved for this program, raised to 40% during the extended mission. During this program, the SVOM science center receives alerts from other facilities to follow transient astrophysical sources. GWAC can observe directly after receiving the alerts, and the

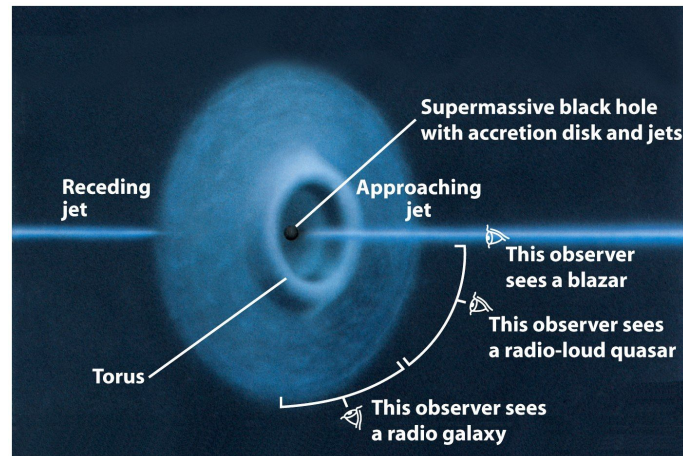


Figure 2.14: An AGN with an accretion disk and a relativistic jet [84]. The different classes based in the viewing angle are shown. Credit:UCSP

GFTs confirm the GWAC observations with their narrow field of view. The alerts are sent to the satellite, and the satellite starts observing in less than 12 hours after the alert.

The targeted astrophysical objects are classified into three categories: the nominal ToO (ToO-NOM), the exceptional ToO (ToO-EX), and the the multi-messenger ToO (ToO-MM).

The ToO-NOM includes follow up of known transient astrophysical objects, GRB revisits, or follow up of GRBs detected by other facilities.

The exceptional ToO (ToO-EX) to observe exceptional astrophysical events requiring rapid observation and follow-up.

Concerning the multi-messenger ToO (ToO-MM), SVOM follows up sources detected by other experiments in other radiation type, like the gravitational-wave and neutrino radiation. As mentioned in Sec. 1.3, SVOM will be operating at the same time with the advanced LIGO/Virgo/KAGRA, and it will coincide with advanced neutrino detectors like the *iceCube-Gen2*. The instruments and facilities that will be operating during the SVOM mission are shown in Fig. 1.19. SVOM will send and receive alerts to and from these instruments to detect the multi signatures from the astrophysical sources.

2.3 . Orbit and observation scenario

2.3.1 . Satellite orbits and profile

In order to match the scientific requirements of the mission, SVOM follows a specific orbit [157]. First of all, SVOM is placed in the low-Earth orbit to protect the instrument from the charged particles in space [158]. The spacecraft is placed at an altitude of ~ 625 km with an inclination of about 30° as illustrated in Fig. 2.15. As a result, SVOM has an orbit period of ~ 96 min (~ 15 orbit/day). Second, to provide protection against the sunlight, the satellite follows a so-called B1-law orbit, in which it points about 45° from the anti-solar direction (as shown in Fig. 2.16). With this pointing, the galactic plane [159] and bright sources like the

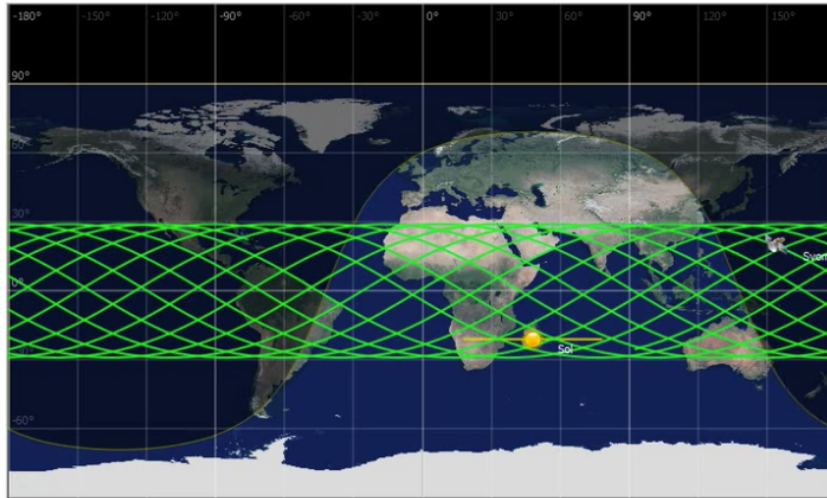


Figure 2.15: The orbit of SVOM over several revolutions (green lines) where the SVOM inclination is about $\pm 30^\circ$ with respect to the equator. Credit:CNES.

Sco-X1 (which is bright in (4-20 keV)) are excluded from the ECLAIRs field of view.

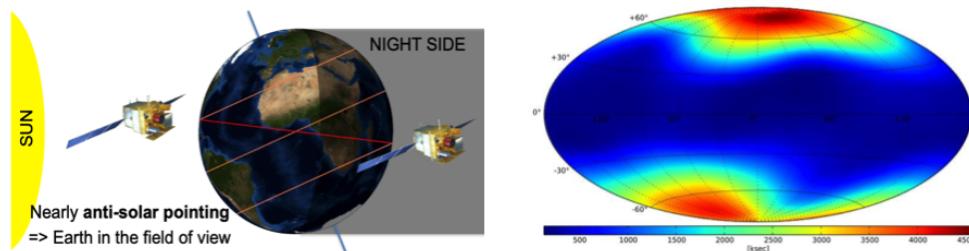


Figure 2.16: An illustrate of the B1 law orbit followed by SVOM (left), where the satellite points toward the anti solar direction. A simulation for ECLAIRs exposure in galactic coordinates (right), where most ECLAIRs observation time is spent near the galactic poles avoiding the galactic plane. Credit: SVOM collaboration

As a consequence of the low-Earth orbit and the B1 law orbit, SVOM will always detect GRBs in the night hemisphere, increasing the probability of the rapid follow up from the ground instruments and the measurement of GRB redshift, which is one of the primary requirements from the mission. Another consequence from the combination of the B1 and low-Earth orbits is that the Earth will occult the satellite several times per day which reduces the duty cycle of ECLAIRs to 65% and of the MXT and the VT to 50%. Furthermore, the satellite will pass by the South Atlantic anomaly [160] that has a high flux of trapped protons and electrons, which requires a shutdown of the satellite, resulting in a dead time of 13% - 17%.

2.3.2 . Observation scenario and alert system

The connection within the space payload and the ground segment has been optimized to ensure rapid information communication and get the maximum benefit from the unique complementary set of SVOM instruments.

The data from and to the satellite is communicated via three different frequencies: X-band (8 - 12 GHz), S-band (2 - 4 GHz), and VHF (30 - 300 MHz) based on their priority to the mission. The information that is required to be communicated in near real-time is sent by VHF packets (see Sec. 3.4.1), like the GRB observation alert, and the most crucial information about the GRB, for example, its location. This requires having 45 VHF ground station on Earth, at the footprint of the SVOM orbit (see Fig. 2.11). The complete scientific data set is later (in one hour typically) sent via X-band packets for deep analysis on the ground. The S-band is mainly used for the regular sanity checks of the instruments onboard. The observation scenarios and alert system differ according to the scientific program.

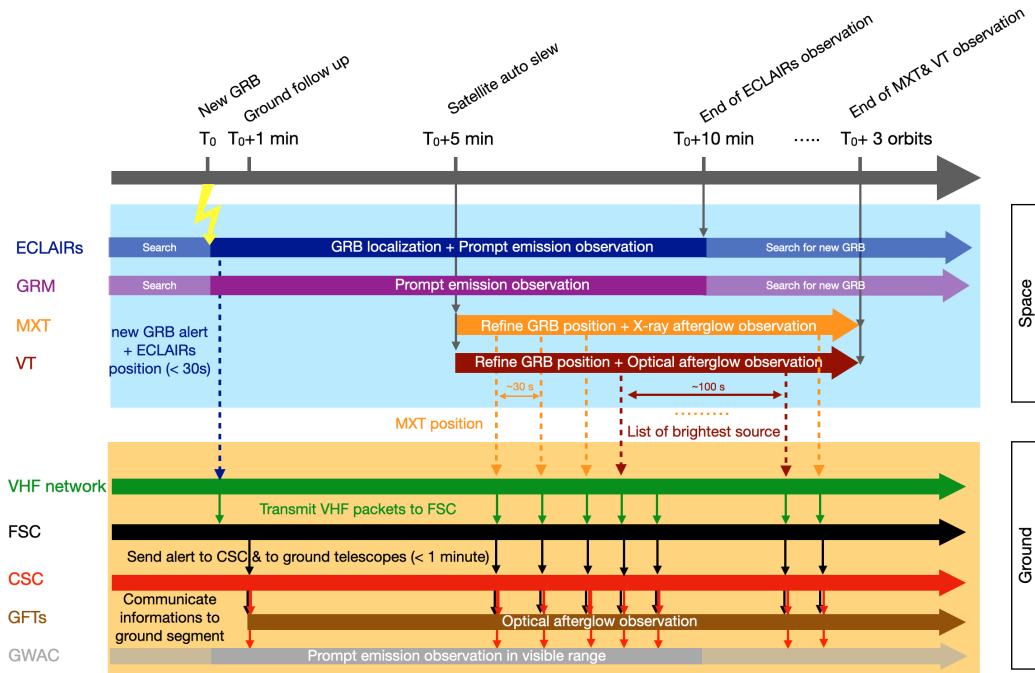


Figure 2.17: SVOM observation scenario during the core program. The observation starts when ECLAIRs detects a new GRB within its field of view at T_0 . ECLAIRs sends an alert with the GRB coordinates to the ground, and the GRB follow-up at lower energy starts at $T_0 + 1$ min by the GFTs and GWAC system. If the GRB is bright enough (in term of the signal-to-noise-ratio), the satellite auto slew and the observation with the narrow field of view telescopes start at $T_0 + 5$ min. The MXT and the VT refine the GRB position and transmit it to the French science center (FSC) that communicates it to the Chinese science center (CSC) and the ground segment.

The observation scenario during the *Core* program is illustrated in Fig. 2.17. First, ECLAIRs

detects a new GRB within its field of view at time T_0 as indicated in Fig. 2.17. ECLAIRs computes the GRB sky location with accuracy less than 12 arcmin, and the GRB signal-to-noise-ratio. The signal-to-noise-ratio gives a measure of how much the source is brighter than the noise level in the detector. The GRB is also observed by GRM in the same time as its field of view overlaps the one of ECLAIRs. If the signal-to-noise-ratio is above the trigger threshold ρ_{alert} , ECLAIRs sends an alert via the VHF emitter in the satellite. The alert is received by one of the VHF antennas on the ground and is transmitted to the French science center in less than 30 s (for 60 % of the alerts). The French science center communicates the alert and the ECLAIRs position to the Chinese science centre. The two centers send the information in less than 1 minute to the SVOM ground segment for rapid follow-up.

A slew threshold is defined ρ_{slew} to control the auto slew of the spacecraft, and it is defined to be higher than the alert threshold: $\rho_{slew} > \rho_{alert}$ to reduce the probability of false slew alerts. If the signal-to-noise-ratio $> \rho_{slew}$, and the slew is allowed, the satellite auto-slews in 5 minutes to place the GRB in the field of view of the MXT and the VT. The MXT (the orange arrow in Fig. 2.17) observes the X-ray afterglow, aiming at better localizing the GRB. Thanks to its onboard localization algorithm (see Chap. 5), the MXT localizes ~ 80 % of the GRBs better than 2 arcmin in less than 10 minutes. The MXT sends the GRB position information in a VHF packet, known as the VHF position packet. As more photons are detected, the MXT better estimates the source location and keep sending the position packets every 30 s for 3 orbits. The VT observes the optical afterglow to refine the GRB sky position computed by the MXT to arcsec accuracy. The VT also sends VHF packets regularly with the brightest source in its field of view.

If the GRB detection is confirmed, the GRB information is communicated to the scientific community via GRB networks like the GCN (Gamma-ray Burst Coordinates Network) [161] to follow up the GRB with very large telescopes and other satellites.

About one hour later, all the GRB data observed by space telescopes are sent to the ground scientific centers via X-band for further investigations and studies.

During the *General* program, the observation scenario changes depending on the observation proposal that is selected by the time allocation committee. When the proposal is accepted, a command is sent to the satellite, and the satellite slews to put the source in the field of view of the desired instrument. The observation of the source lasts for about a single orbit (~ 45 min). During the nominal mission, the majority of the general program observations follow the attitude law of the SVOM. Up to 10% of observations are allowed to deviate from the attitude law of SVOM to keep the favorable observation condition for the core program. This percentage is raised to 50% during the extended mission.

Regarding the *ToO* program, the observation depends on the targeted source, so the satellite slews to put the source in the field of view of the desired instrument. In the case of ToO-EX and ToO-MM, they can interrupt the GRB observation and start observing the target of opportunity source. The observation lasts for 1 orbit for the ToO-NOM and up to 14 orbits for the ToO-EX and the ToO-MM. Figure 2.18 shows a simulation of the astrophysical objects detected during the three scientific programs for one year.

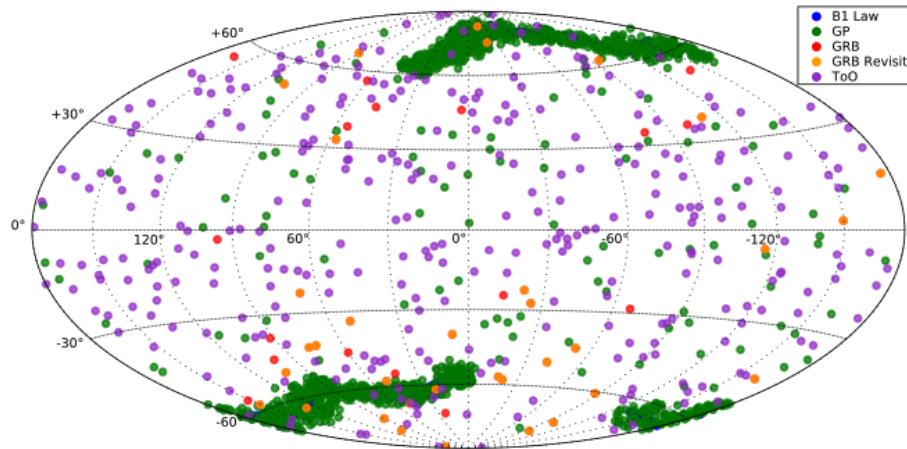


Figure 2.18: A scenario of one year of observation for the three scientific programs showing the sky map in galactic coordinates with 65 simulated GRBs and one ToO per day. Red points are the GRB observation (*Core* program), green points are the *general* program observation, orange points are the *ToO-Nom* observations, and purple points are the *ToO-Exp* and *ToO-MM* observations. Credit: SVOM collaboration.

3 - The Micro channel X-ray telescope

Contents

2.1	Scientific instruments	44
2.1.1	Space-based instruments	44
2.1.2	Ground-based instruments	50
2.1.3	The VHF alert network	51
2.2	Scientific programs	52
2.2.1	The <i>Core</i> program	53
2.2.2	The <i>General</i> program	54
2.2.3	The <i>Target of Opportunity</i> program	55
2.3	Orbit and observation scenario	56
2.3.1	Satellite orbits and profile	56
2.3.2	Observation scenario and alert system	58

This chapter discusses the scientific objectives of the MXT and its subsystems. Section 3.1 presents the features and the scientific goals of the MXT. The system of coordinates of the MXT is explained in Sec. 3.2. The MXT subsystems are discussed in detail in Sec. 3.3. The scientific software implemented onboard the MXT is introduced in Sec. 3.4. Section 3.5 explains the simulation tool developed to simulate an observation with the MXT.

3.1 . The MXT features and scientific objectives

As mentioned in Sec. 2.1.1, the MXT is a narrow field-of-view X-ray telescope that covers an area of 58×58 arcmin² of the sky. It is a light and compact telescope with a total mass of 42 kg and a focal length of 1.13 m. For comparison, the Swift/XRT telescope, which is similar to the MXT in terms of scientific objectives, has a total mass of ~ 200 kg. The small mass of the MXT sets tight constraints on its design, as explained in Sec. 3.3.

The MXT is based on square micro-pore optics [30] to focus the X-ray photons attached to a low-noise CCD detector [138], with an angular resolution of about 10 arcmin and sensitivity of $\sim 2 \times 10^{-10}$ erg.cm⁻².s⁻¹ in 10 s of exposure which is about 10 mCrab¹, and sensitivity of $\sim 4 \times 10^{-12}$ erg.cm⁻².s⁻¹ in 10⁴ s of exposure (~ 150 μ Crab) [31].

The MXT is designed to detect the X-ray afterglow emission in the soft X-ray energy range (0.2 - 10 keV) with an automatic, rapid, and precise localization of GRBs. As mentioned in

¹A Crab is a standard unit used to measure the intensity (flux density) of astrophysical X-ray sources. A Crab is defined as the intensity of the Crab Nebula at the considered X-ray photon energy [162].

Sec. 2.3.1, the ECLAIRs instrument localizes the source with uncertainty < 12 arcmin. Afterward, the satellite auto-slews to put the source in the field of view of the MXT. The MXT covers the localization error box provided by ECLAIRs with its 58×58 arcmin² field of view and refine the GRB coordinates. The MXT is expected to localize $\sim 80\%$ of GRBs with accuracy better than two arcmin after 10 minutes of observation, which increases up to a few arcsec in the case of very bright GRBs [25]. The first GRB coordinates obtained onboard are immediately communicated to the VT and transmitted to the ground via the VHF network to ensure the follow-up of the afterglow in lower energy ranges. As the MXT accumulates more photons, the source localization is improved, and the new coordinates are periodically sent to the payload data processing unit that sends the information to the ground instruments.

In addition, the MXT allows to study the spectral properties of the X-ray afterglow with an energy resolution of ~ 0.08 keV at 1.5 keV [31]. The MXT sensitivity enables the determination of the spectral index λ (see Sec. 1.2.3.1), which is the form of the energy distribution of the emission. Determining the spectral index permits the reconstruction of the distribution of energetic particles responsible for the X-ray emission and obtaining information on the shock waves physics. Moreover, the MXT soft operational band (0.2 - 10 keV) allows measuring the absorption of the X-ray emissions [138], which occurs both in the intergalactic medium and in the host galaxies, as discussed in Sec. 1.2.3.1.

Table 3.1: Scientific and technical characteristics of the MXT compared to the requirements.

Characteristic	Design	Value
Total mass	< 45 kg	42 kg
Focal length	> 1.1 m	1.13 m
Field of view	$> 50 \times 50$ arcmin ²	58×58 arcmin ²
Energy	0.2 - 10 keV	0.2 - 10 keV
Sensitivity	2×10^{-10} erg cm ⁻² s ⁻¹ in 10 s 4×10^{-12} erg cm ⁻² s ⁻¹ in 10 ⁴ s	2×10^{-10} erg cm ⁻² s ⁻¹ 4×10^{-12} erg cm ⁻² s ⁻¹
Angular resolution	10 arcmin at 1.5 keV	11 arcmin
Spectral resolution	0.08 keV at 1.5 keV	0.08 keV
Temporal resolution	< 100 ms	100 ms
Localization accuracy	85% < 2 arcmin in 10 min	80% < 2 arcmin
Detector type	pnCCD 256×256 pixels	pnCCD 256×256 pixels
Optics type	Micro-pore optics	Micro-pore optics

The MXT is also able to study the temporal properties of the X-ray afterglow. The rapid slew of the satellite (< 5 minutes) allows the MXT to detect the end of the prompt emission phase and the very beginning of the X-ray afterglow phase. Furthermore, MXT is able to follow the evolution of the afterglow emission for up to a whole day after the initial prompt signal. [25]

Table 3.1 summarizes the general features and characteristics of the MXT. It shows that the current characteristics match the design requirements, except for the angular resolution,

which is 1 arcmin above the designed value. Degradation of the angular resolution affects the localization accuracy that becomes less than the requirements by 5%. Where $\sim 80\%$ of GRBs are localized with the desired accuracy instead of 85%.

3.2 . The MXT reference frames and system of coordinates

This section explains the notation, convention, and reference frames defined for the MXT. In addition, the notation and coordinates for the sources and the detector plane are explained. List of notations and conventions explained during this section will be used until the end of this manuscript.

3.2.1 . The reference frames

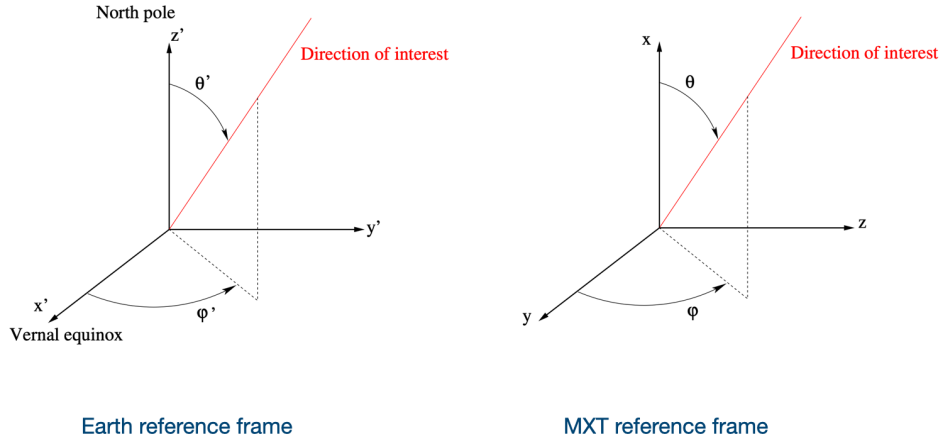


Figure 3.1: The Earth reference frame \mathcal{R}' and its celestial coordinates (x', y', z') , where the rotation axis is the z' -axis (left). The MXT reference frame \mathcal{R} and its associated coordinates, where the telescope pointing direction is toward the x -axis, by convention (right). The spherical coordinates are used to describe an astrophysical object in the sky (in red), where all quantities in the Earth reference frames are primed.

Two systems of coordinates are defined. First, the Earth reference frame \mathcal{R}' , where the Earth celestial coordinates are (x', y', z') . The z' axis is the rotation axis of the Earth and points to the North pole. The $x'y'$ plane is the equatorial plane, and the x' axis points to the vernal equinox. The second reference frame is the MXT reference frame \mathcal{R} , and is given a system of coordinates (x, y, z) . By convention, the x -axis is the pointing direction of the telescope, and the focal plane is the yz plane. The two reference frames are shown in Fig. 3.1.

To transform from one reference frame to the other, a three dimensional rotation is performed using the Euler angles (α, β, γ) [163], as shown in Fig. 3.2.

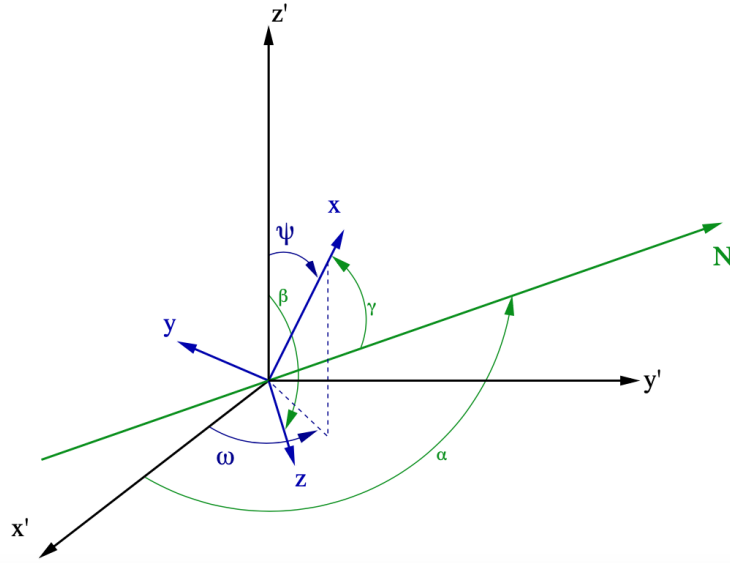


Figure 3.2: The rotation to change the system of coordinates between \mathcal{R} and \mathcal{R}' , performed using the Euler angles is represented in green. N is the line of nodes which is a common perpendicular line to the z and z' axes.

3.2.2 . The system of coordinates

3.2.2.1 The detector coordinates and notations

The MXT detector is placed in the focal plane, which is contained in the yz plane, as explained above. Two systems of coordinates are defined for the detector. The first coordinates are the pixel coordinates, where the detector consists of N columns in the y -direction and N rows in the z -direction, forming a matrix of $N \times N$ pixels. Pixels are indexed by i and j in the y - and z -directions, running from 0 to $N - 1$ respectively, where $N = 256$. Each pixel covers 13.6 arcsec of the field of view.

The second system of coordinates is the intrinsic coordinates where the detector plane is contained in $0 \leq y < 1$ and $0 \leq z < 1$. The pixel with index (i, j) is centred at $(\frac{i+0.5}{N}, \frac{j+0.5}{N})$. In addition the camera is given a physical size in the three dimensions, $L \times L$, and e , as seen in Fig. 3.3.

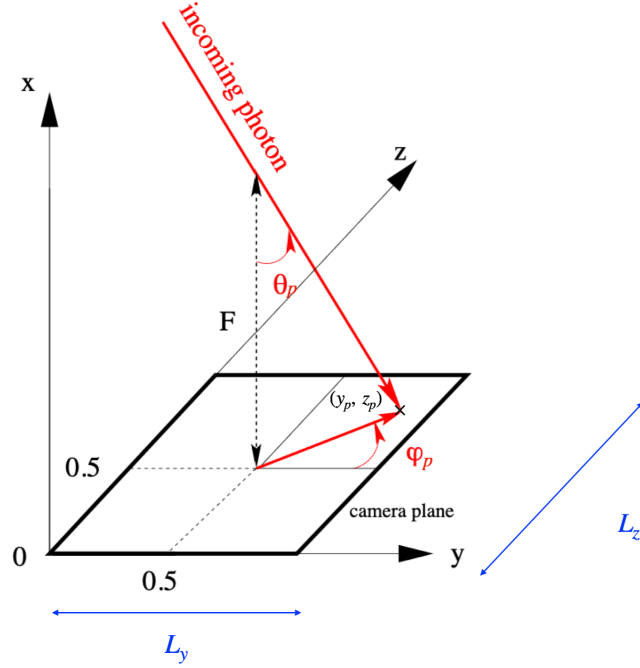


Figure 3.3: System of coordinates used to describe the MXT camera plane and the astrophysical source direction.

3.2.2.2 The source coordinates and notations

In both reference frames \mathcal{R} and \mathcal{R}' , an astrophysical object in the sky is described using spherical coordinates. For \mathcal{R}' (resp. \mathcal{R}), θ' (resp. θ) is the polar angle between the z' -axis (resp. x -axis) and the direction of interest (the red line in Fig. 3.1), where $0 \leq \theta' \leq \pi$ (resp. $0 \leq \theta \leq \pi$). Meanwhile ϕ' (resp. ϕ) is the azimuth angle between the x' -axis (resp. y -axis) and the projection of the direction of interest on the $x'y'$ (resp. yz) plane, where $0 \leq \phi' \leq 2\pi$ (resp. $0 \leq \phi \leq 2\pi$).

Alternatively the astrophysical objects in the sky can be described in the \mathcal{R}' reference frame by the the right-ascension ($= \phi'$) and the declination ($= \pi/2 - \theta'$) as shown in Fig. 3.4. The right ascension is the celestial equivalent of terrestrial longitude. It is measured as the angle from the vernal equinox. The declination is comparable to terrestrial latitude, and it is measured north (positive values) or south (negative values) of the celestial equator.

An astrophysical object is also parametrized by an opening angle ι_s as seen in Fig. 3.5. The ι_s angle represents the spread of the particles out from the source. Particles generated by the object has an incoming direction (θ_p, ϕ_p) within the opening angle.

Once a particle with spherical coordinates (θ_p, ϕ_p) hits the detector, as represented by Fig. 3.3, the particle hit position in the detector is given by the Cartesian coordinates (y_p, z_p) :

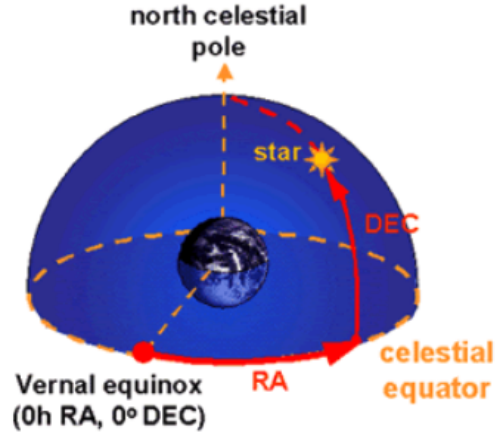


Figure 3.4: The right-ascension (RA) and declination (DEC) of a star derived from the Earth celestial coordinates.

$$\begin{aligned} y_p &= 0.5 + \frac{F}{L} \times \tan \theta \cos \phi, \\ z_p &= 0.5 + \frac{F}{L} \times \tan \theta \sin \phi, \end{aligned} \quad (3.1)$$

where F is the MXT focal length. The pixel index (i_p, j_p) that contains the hit position is given by:

$$\begin{aligned} i_p &= \lfloor (y_p \times N + 0.5) \rfloor, \\ j_p &= \lfloor (z_p \times N + 0.5) \rfloor. \end{aligned} \quad (3.2)$$

3.3 . The MXT subsystem

The MXT consists of a light tube structure made of Carbon Fiber Reinforced Polymer combined with titanium reinforcements to comply with the mission requirements in terms of mass [164]. The structure provides stability to the telescope under thermal and mechanical stresses that it is exposed to in orbit. The structure has been developed and tested thermally and mechanically at CNES.

On top of the structure, an optical module consisting of square micro-pores is installed to focus X-ray photons. The other end of the structure is attached to a low-noise camera (pnCCD

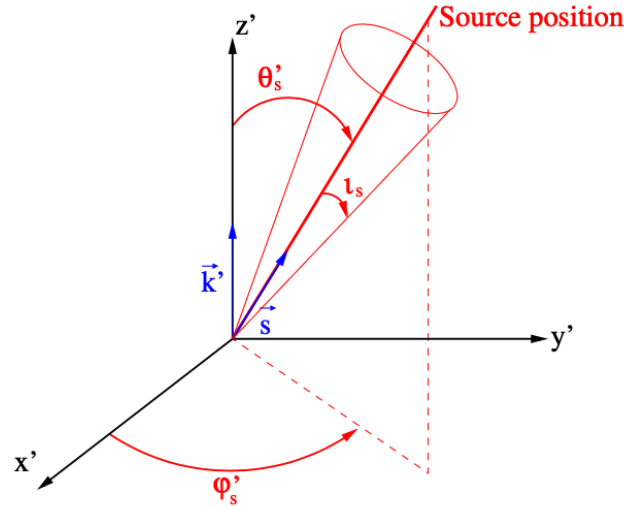


Figure 3.5: An astrophysical object as seen from the Earth reference frame. The object central position is given (θ'_s, ϕ'_s) . The source has an opening angle l'_s .

detector) to image X-ray photons. In addition, the MXT is equipped with a data processing unit called the (MDPU), to analyze the images captured by the camera in real time.

Furthermore, the MXT has a radiator to dissipate the heat produced by the cooling system of the subsystems, particularly the camera, and keep the instrument at a stable temperature. The radiator consists of a six-fold Constant Conductance Heat Pipe with propylene fluid [165], and is developed and tested at CNES. Figure. 3.6 shows the flight model of the MXT installed in the integration room at CNES. Metal foils cover the MXT for protection before delivery to China.

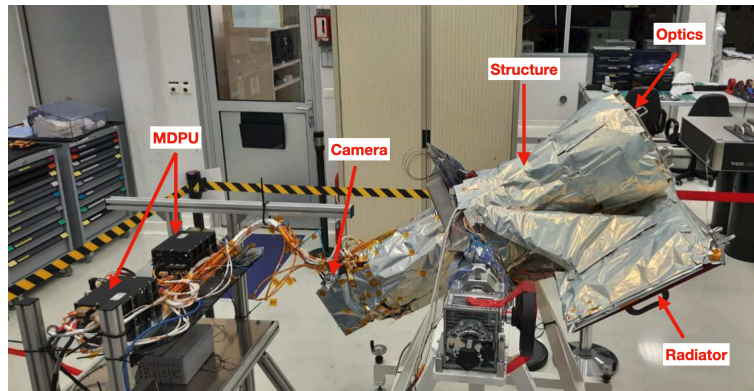


Figure 3.6: The MXT flight model at CNES integration room, covered with protection layers. The subsystems are labeled in red. Credit:CNES

In the following, the MXT optics, camera, and MDPU are explained. Since the MXT is analog to the Swift/XRT telescope in terms of scientific function and objectives, a comparison

between their subsystems is held in Sec. 3.3.2.

3.3.1 . The MXT optics

The principle of X-ray telescope optics is based on grazing incidence mirrors [166], in which the X-ray photon is reflected twice with a very small angle ($<2^\circ$) on two coaxial surfaces such as a hyperboloid and a paraboloid. These grazing optics were introduced in 1952 by Hans Wolter (the design carries his name) [167], who outlined three ways to build these optical modules; an example of Wolter I design [168] is shown in Fig. 3.7.

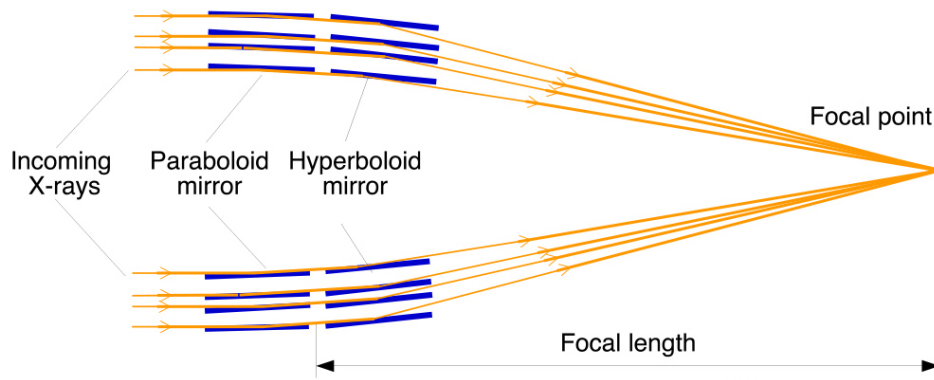


Figure 3.7: Cross-section of a typical Wolter type space telescope showing the light path in grazing incidence optics before it is focused on a detection plane. Credit: [169].

This optical design was used by several X-ray space telescopes like XRT [170]. Wolter design telescopes require a long focal length to focus the X-ray photons, which is incompatible with the mass constraint for the MXT; thus, the Wolter design is not used for the MXT.

However, another optical configuration for grazing-incidence mirrors can be implemented. For this purpose, the MXT optics is designed following a lobster eye optic configuration that is used for the first time by a narrow field-of-view X-ray telescope. The lobster eye optics is inspired by the eye of the lobster, and were first introduced by Roger Angel in 1979 [171].

The lobster eye consists of square channels arranged on a spherical plane (as seen in Fig. 3.8) with a radius of curvature $R = 2F$, where F is the focal length of the optics. The incident light beams are reflected by the smooth sides of the square channels and focused on the focal plane.

Grazing reflections with lobster eye optics require the length of the square side to be greater than the incident photon wavelength and the depth of the channel to be ~ 100 times greater than the square length [171]. Knowing that the wavelength of soft X-rays in the energy range of 0.2 - 10 keV is a few nanometers, the MXT optics has a square channel of the depth of 1.05 mm to 2.4 mm, and a length of the order of a few tens of micrometers ($40 \mu\text{m}$) [172]. This is why the telescope carries the name of a micro-channel X-ray telescope.

The square channels are grouped in 40×40 mm plates. Each plate consists of 600625 square channels [30]. The inner square walls are coated with a 25 nm Iridium layer to boost the reflectivity, and the plates are coated at the top with 70 nm of Al for thermal protection.

The MXT has a set of 25 plates (see Fig. 3.9), designed by the University of Leicester and built by Photonis company in France [173].

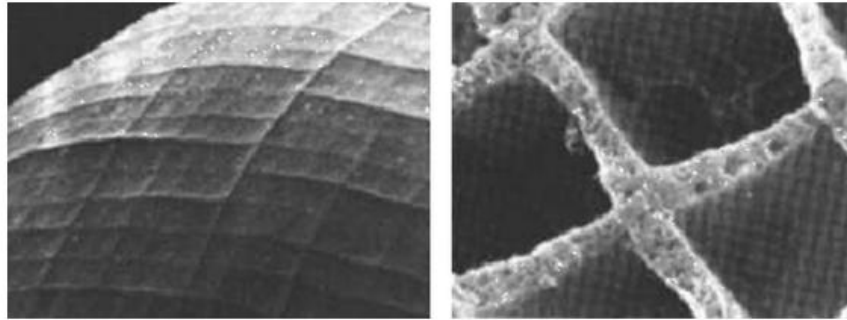


Figure 3.8: The eye of a lobster as viewed by the microscope. Left: the square channels arranged on a spherical plane. Right: closer view for the square channels of the lobster eye. Credit: NASA.

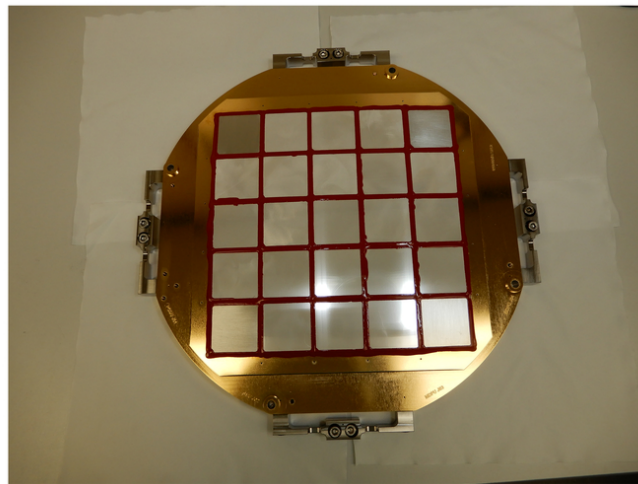


Figure 3.9: Flight model assembly of the MXT optics, showing the 25 plates. Credit: University of Leicester.

The advantage of this optic is its uniform response over the entire field of view. Indeed, the micro-channels that make up the lobster eyes allow them to capture light even at the edges of their eyes, which leads to increase the field of view.

The response of an optic to light from a point source is called the Point Spread Function (PSF); the shape of the PSF depends on the deflection of the incident light by the optics.

In the lobster eye configuration, the incident light can be reflected twice and focused on a central spot, reflected once and focused on cross arms, or not reflected and form a diffuse

patch as seen in Fig. 3.10. For the MXT optical system, $\sim 50\%$ of the incident X-ray flux is focused in the central spot, $2 \times 22\%$ in the cross arms, and the rest in a diffuse patch [174]. These percentages vary from one energy to another. As the photon energy increases, fewer photons are focused on the central spot, and more photons are focused on the arms or form diffuse patch.

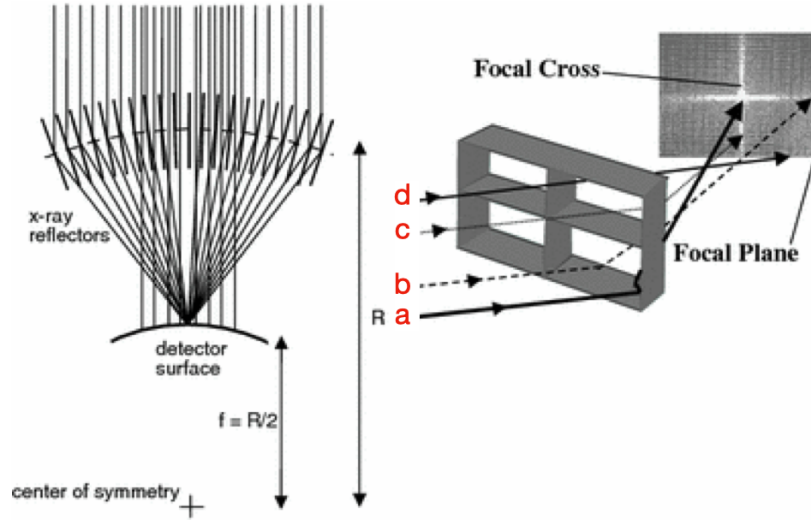


Figure 3.10: The spherical plane and the focal length of the optics (left). The reflection of photons by the optics (right), photons labeled by (a) undergoing two reflections are focused on the central spot, whereas those reflected only once are focused on the cross-arms (b and c), and photons (d) passing straight through without any reflection form the diffused background. Credit: [175].

The PSF of the MXT optics can be modeled using a real data as an intensity probability discrete function. The PSF function depends on the incident photons position (y, z) and the energy E_{ph} : $\mathcal{P}(y, z, E_{ph})$. For a fixed photon energy the PSF model is given by:

$$\mathcal{P}(y, z) = \frac{A}{(1 + \eta)^2} \left(\frac{1}{1 + (2y/G)^2} + \eta(1 - (y/H)^2) \right) \left(\frac{1}{1 + (2z/G)^2} + \eta(1 - (z/H)^2) \right), \quad (3.3)$$

where A is a normalization value, G is the full width at half maximum (FWHM), η is the peak brightness of cross arms with respect to the central spot, and H is length of cross-arms.

The PSF is modeled twice the size of the detector in order to cover all possible directions of incoming photons. Figure 3.11 shows the MXT PSF model at Al-K energy (1.49 keV) and at Fe-K energy (6.4 keV), where the intensity on the central spot at Al-K energy is about twice the intensity on the central spot at Fe-K energy.

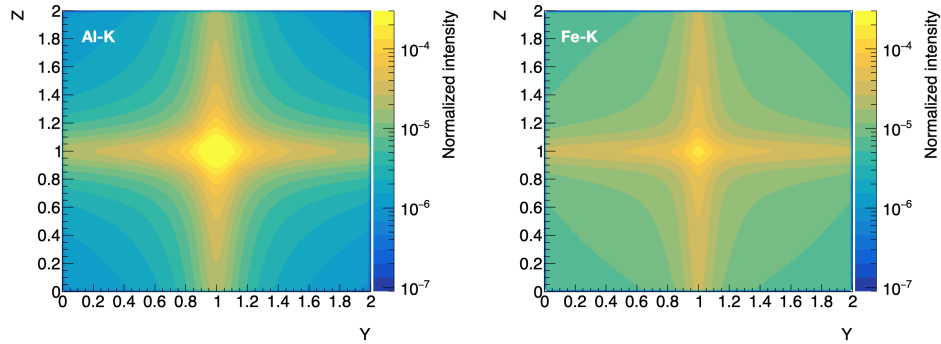


Figure 3.11: The PSF model of the final configuration of the optics. It is composed of a central spot and cross arms, where the intensity of photons on the central spot changes with energy. Left: at Al-K energy (1.49 keV). Right: at Fe-K energy (6.4 keV).

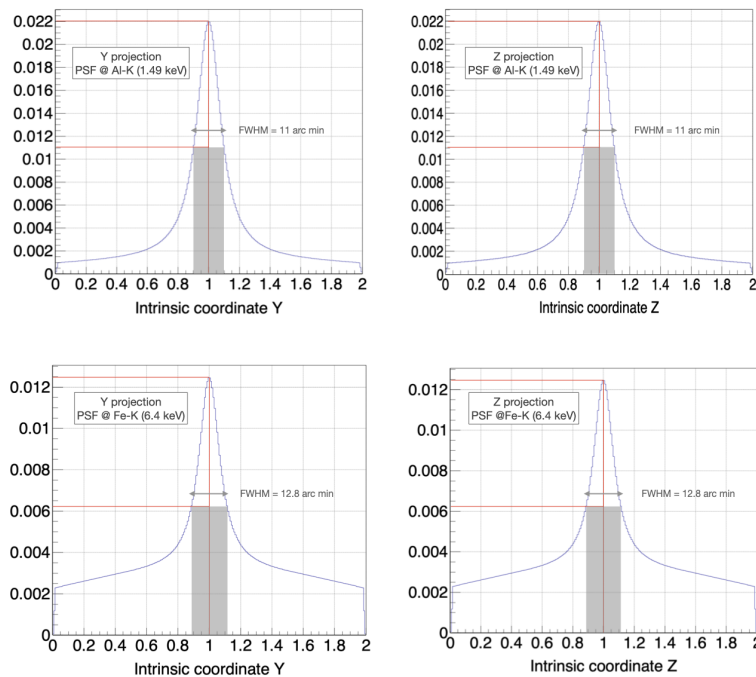


Figure 3.12: The one dimensional projection of the PSF model. Top: the y projection of the PSF model at Al-K energy with a FWHM of 11 arcmin (left). The z projection of the PSF model at Al-K energy with the same FWHM as the y projection one: 11 arcmin (right). Bottom: the y projection of the PSF model at Fe-K energy with FWHM of 12.8 arcmin (left). Bottom: the z projection of the PSF model at Fe-K energy with the same FWHM as the y projection one: 12.8 arcmin (right).

Consequent to the energy dependence, the FWHM of the PSF changes with the photon energy. The smaller the FWHM, the better the angular resolution and *vice versa*. Figure 3.12 shows the y and z projection of the PSF at Al-K and Fe-K energies and the corresponding FWHM at both energies. The FWHM of the PSF at 1.49 keV is 11 arcmin, while it increases to 12.8 arcmin at 6.4 keV. However, the plots show that the shape of the PSF remains symmetrical around the central spot in both directions regardless of the photon energy.

The variance of the optics grazing incidence efficiency with energy affects the effective detection area of the telescope. Figure 3.13 shows how the effective area changes with energy, the best detection efficiency occurs when the photons energy is about 1.5 keV, with an effective area of $\sim 38 \text{ cm}^2$.

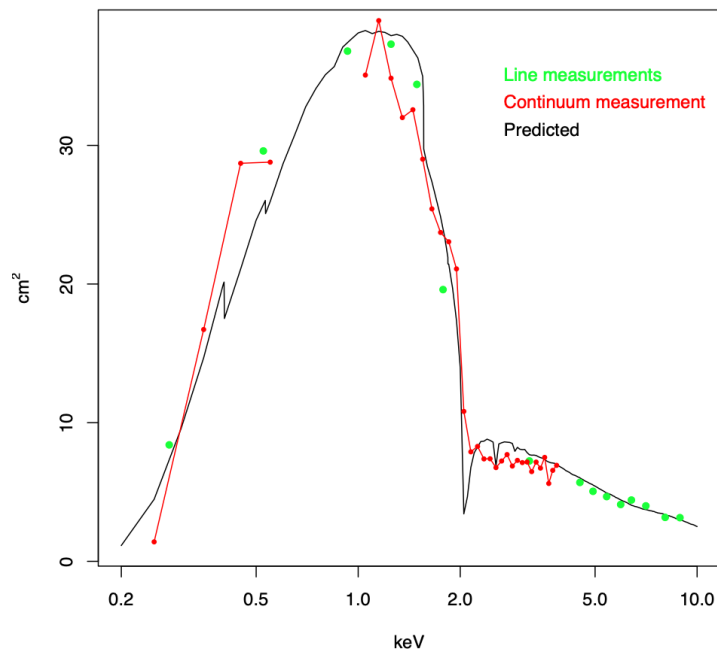


Figure 3.13: The effective area of the MXT telescope corresponds to the case in which only the central spot is considered. The black line is the designed effective area based on simulation. The green and red points are the measured effective area of the flight model telescope. It perfectly matches the predicted one. Credit: the University of Leicester.

3.3.2 . The MXT camera

The MXT camera is designed and integrated at CEA. The camera assembly consists of three units, the detector, the calibration wheel, and the Front End Electronics (FEE). The whole camera assembly with the different components is presented in Fig 3.14.

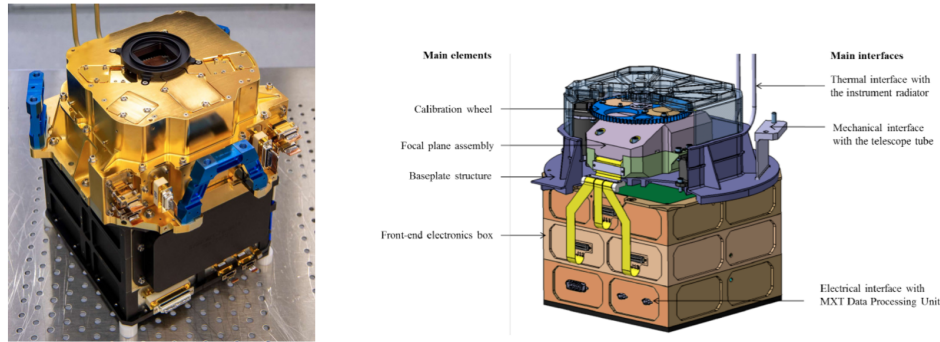


Figure 3.14: The flight model of the camera (left). A schematic of the camera showing the different components, the calibration wheel, the detector and the FEE (right). Credit: CEA.

3.3.2.1 The MXT detector

The detector is a CCD based on pn-junctions (pnCCD) and composed of a matrix of 256×256 pixels. The pnCCD detector is read out in parallel by two Complementary metal-oxide-semiconductor Amplifiers and MultipLEXer (CAMEX), each reads 128 columns of pixels (see Fig. 3.15).

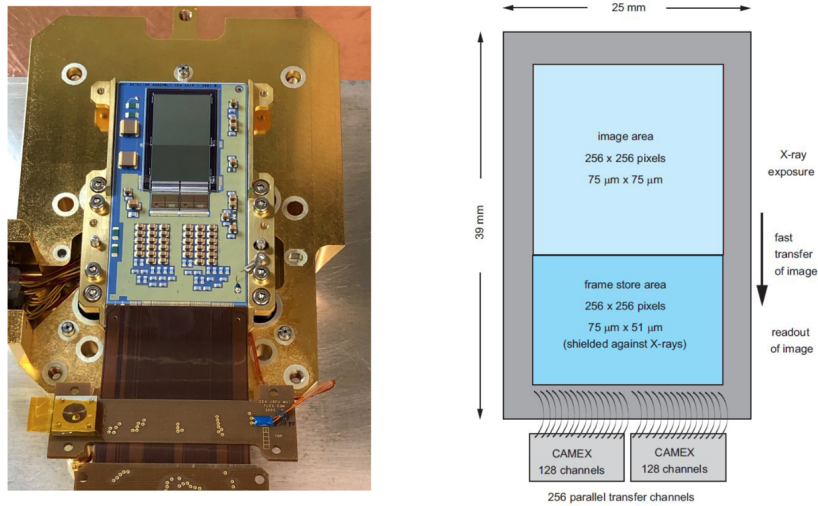


Figure 3.15: Cross sectional view of the MXT pnCCD detector. Left: is the flight model of the detector. Right: Schematic of the detector showing the image area composed of 256×256 pixels, each of size $75 \mu\text{m} \times 75 \mu\text{m}$; a frame store area is at the bottom of the image area with shielding against X-ray photons. The detector readout system (the two CAMEX) is attached to the frame store area. Credit: CEA.

The pnCCD and the two CAMEX were developed by MPE in Germany. The detector provides a high-energy resolution of ~ 0.08 keV at 1.5 keV and a high quantum efficiency: 92% at 1 keV, 27% at 0.28 keV, and 99% at 4.5 keV [31]. The quantum efficiency affects the effective detection area (Fig. 3.13) of the telescope in addition to the optics properties (see Sec. 3.3.1).

The best detector performance is achieved when the operating temperature is $< -60^\circ$ C [176]. To keep the detector operating at this temperature and to provide thermal stability, the focal plane is equipped with a cooling system. The cooling system keeps the detector at a temperature of $-65 \pm 1^\circ$ C to have the detector at a stable temperature during the mission. A metal shielding is added on top of the detector in order to provide protection against high-energy particles, especially once the satellite crosses the south atlantic anomaly.

The detector working principle

The detector is divided into two active regions, as seen in Fig. 3.16: the image region and the frame store region. The front side of the detector is divided into electrodes (cathodes) grouped in pixels. The detector is back-illuminated, i.e., photons can hit the detector only from the back side of the detector, and the other sides are depleted [31], as seen in Fig. 3.16. Once an X-ray photon enters the back side of the detector, it deposits its energy via the photoelectric effect creating electron-hole clouds in the silicon. The cathodes absorb the hole while the electron moves to local potential minima under the pixels. Every δt integration time, the electrical potential of cathodes changes periodically, allowing the electrons packets to be moved pixel by pixel towards the frame store region to be read out by the electronics column by column.

The detector intrinsic noise

Two kinds of intrinsic noise $I = \mathcal{D} + R$ arise in the detector: the dark noise \mathcal{D} and the read noise R .

- The dark noise: all materials with a temperature above absolute zero suffer from thermal noise within. Thermal agitation of the material (the silicon in the MXT case) causes the electrons to be freed from the material and collected under the potential well of a pixel. When the electronics read out the detector, these noisy electrons become part of the signal, indistinguishable from electrons induced by astronomical photons. The electrons current due to thermal agitation is called the dark current or dark noise because it is not caused by the photons. The generation of the dark current is strongly dependent on the temperature.
- The read noise: arises from the measurement process and consists of two inseparable components. The first one is due to converting an analog signal to a digital number, which is not perfectly repeatable. Each CAMEX produces a statistical distribution of possible answers centered on a mean value. Thus, a slightly different value may be produced even for the hypothetical case of reading out the same pixel twice with an identical charge. Second, the electronics themselves introduce bogus electrons into the entire measurement, resulting in unwanted random fluctuations in the final output. Combining these two effects produces an additive uncertainty in the final output value for each pixel. The read noise is the average level of this uncertainty and is limited by the electronic properties of

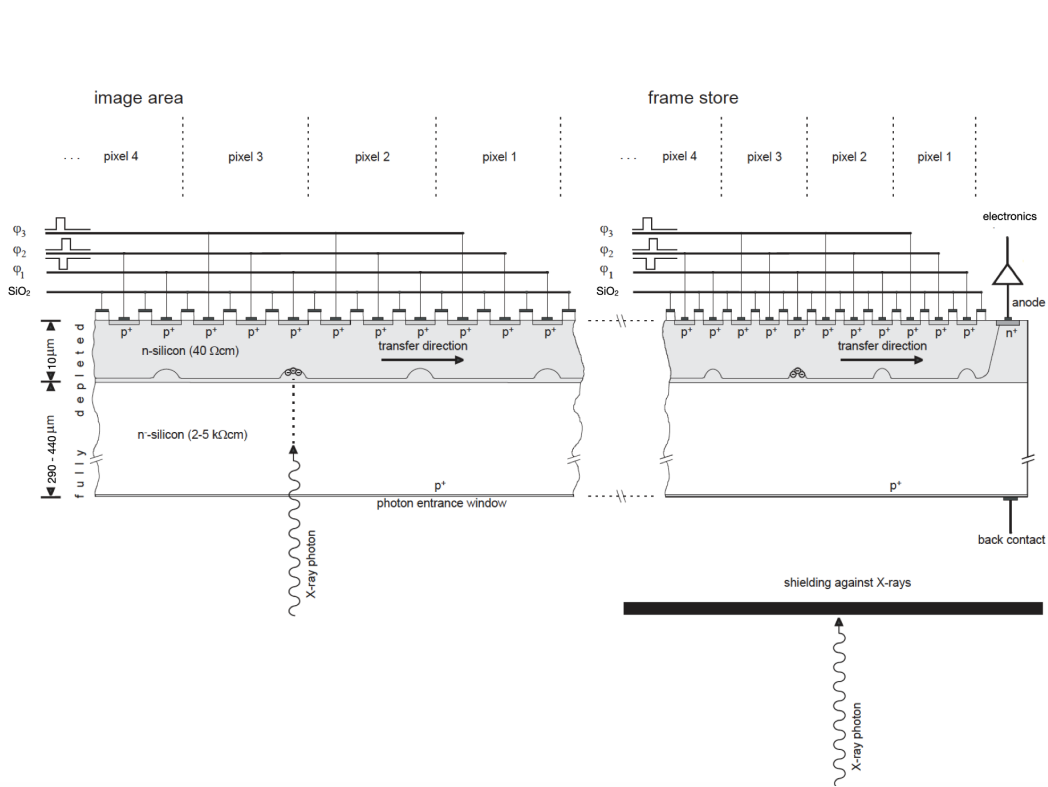


Figure 3.16: Schematic views of a CCD detector based on a pn-junction. Credit [177].

the two CAMEX.

Moreover, as the two CAMEX read out the image in parallel, the common-mode noise fluctuations affect all the pixels in a row and vary from one row to another. An example of a camera frame with only intrinsic noise is shown in Fig. 3.17: the structure of columns can be seen as each column has a different average noise value due to the parallel read-out process.

An example of a camera picture taken with only intrinsic noise is shown in Fig. 3.17: the structure of columns can be seen as each column has a different average noise value due to the parallel read-out process.

The MDPU characterizes the detector intrinsic noise I to compute the noise offset (the average) value $O[i][j]$ and sets a noise threshold (the fluctuation around the average) T_{ij} for each pixel in order to distinguish signals from noise, as explained in Sec. 4.1.2. Since the intrinsic noise depend on the temperature, the noise must be characterized in the same thermal environment as the observation.

3.3.2.2 The calibration wheel

A calibration wheel shown in Fig. 3.18 is added on top of the detector to account for different observation scenarios. It is made of 126 mm of aluminum and has four positions [165]:

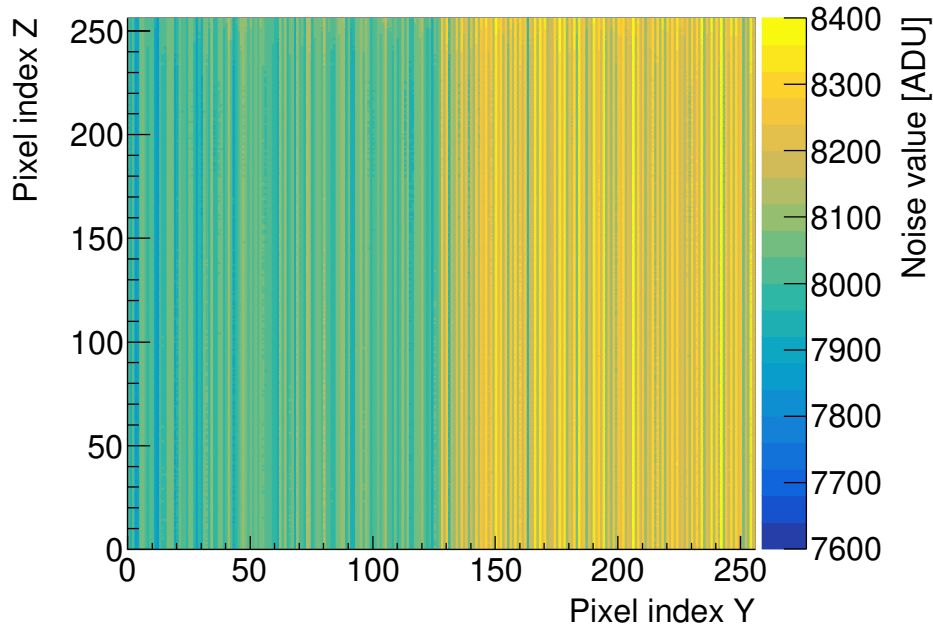


Figure 3.17: Example of a frame taken by the MXT detector with intrinsic noise only. The effect of the read-out process is clearly seen where the structure of the columns appears with a distinction between the two CAMEX.

- Closed position: where a shutter is used to protect the detector from high energy radiations and to characterize the detector noise.
- Open position: used during sky observations.
- Filter position: where an Ultra-Violet (UV) filter is used to limit the straylight in the field of view of the MXT before and after the earth occultation. Straylight is the light from the sun reflected by the atmosphere. However, this position will not be used since the UV filter was broken during a mechanical test for the camera.
- Source position: where a ^{55}Fe (5.9 keV) calibration source is used for energy calibration of the detector and to measure the energy resolution evolution with the aging of the detector.

3.3.2.3 The Front-End Electronics

A FEE is placed at the bottom of the focal plane to control and power the detector. The detector converts photon energy into charges (electrons) by the photoelectric effect, the CAMEX collects these charges, and the FEE digitizes the signals and communicates the pixels information in two modes.

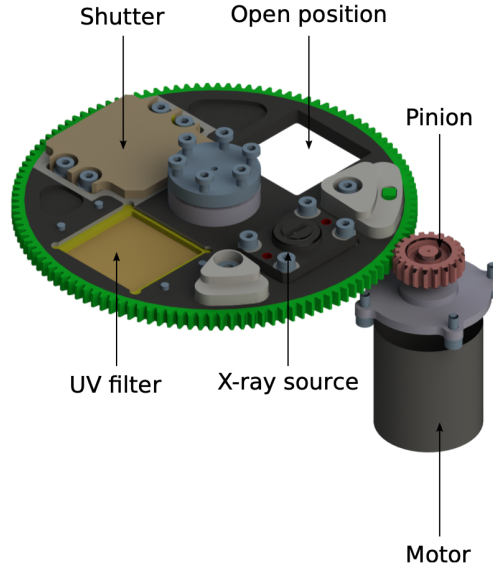


Figure 3.18: The MXT calibration wheel shows the four positions and the motor that turns the wheel. Credit: [178].

The first mode is called the **FULL-FRAME**, where the camera captures an image every 200 ms. In this mode, the FEE communicates the raw amplitude $A_r[i][j]$ without treatment for the 256×256 pixels. This mode is used for the detector noise characterization, as explained in Chap. 4, and for the energy calibration. The second mode is the **EVENT** mode, in which the camera captures an image every 100 ms. In this mode, The FEE computes the amplitude deviation from the noise offset value: $A[i][j] = A_r[i][j] - O[i][j]$ and communicates the pixel indices (i, j) and $A[i][j]$ if $A[i][j] > T[i][j]$. This mode is used during observations to process only pixels that contain a signal. In addition, the FEE is operated in the **CONF** mode, in which the FEE does not communicate any information and the camera does not take pictures. The features of each mode are summarized in Tab. 3.2. The image processing performed during each mode is discussed in detail in Chap. 4.

Table 3.2: Comparison between the three operating modes of the FEE.

	FULL-FRAME	EVENT	CONF
Information	$A_r[i][j]$ for 256×256 pixels	(i, j) and $A[i][j]$, if $A[i][j] > T[i][j]$	No information
Image rate	5 images/s	10 images/s	No images
Usage	For noise characterization and energy calibration	For astrophysical observations	while passing by South Atlantic anomaly

The MXT global mode is defined as a combination of the wheel position and the FEE mode. The list of MXT global modes is given in Tab. 3.3. The South Atlantic anomaly configuration is selected if the satellite passes by the anomaly, the Earth occultation configuration is selected if the Earth is in the field of view of the MXT, and the operation configuration is selected

otherwise.

Table 3.3: List of global modes of the MXT that are a combination of the wheel position and the FEE mode.

Global mode	wheel position	FEE operating mode
South Atlantic anomaly	Closed	CONF
Earth occultation	Closed/Source	FULL-FRAME/EVENT
Operation/dark	Closed	FULL-FRAME
Operation/observation	Open/Filter	EVENT
Operation/calibration	Source	FULL-FRAME/EVENT

3.3.3 . The MXT data processing unit

The MDPU manages the power distribution for the MXT subsystems, provides the interface of the MXT subsystems to the PDPU, manages the telemetry packets, manages the data received from the FEE through a space-wire link, measures and controls the temperature of the MXT camera and optics, and manages the real-time data processing.

In order to handle the tasks mentioned above, six software are coded in the MDPU. Each uses a specific part of the memory; hence, each software is called a partition. The list of the MDPU partitions is given in the following:

- The command control software (CCSW) manages all mode transitions and the telecommands.
- The input/output server (IOS) is a communication link to the PDPU.
- The navigation software (NAV) detects Earth occultation and gives information to other partitions about the spacecraft slew.
- The FEE module (FEEM) manages the camera and its temperature.
- The scientific software (SCSW) manages the data processing onboard.
- The Hardware Software Event Manager (HSEM) verifies that the previous softwares are working.

The MDPU configuration is based on two cores to run all the partitions. The architecture of the MDPU is shown in Fig. 3.19.

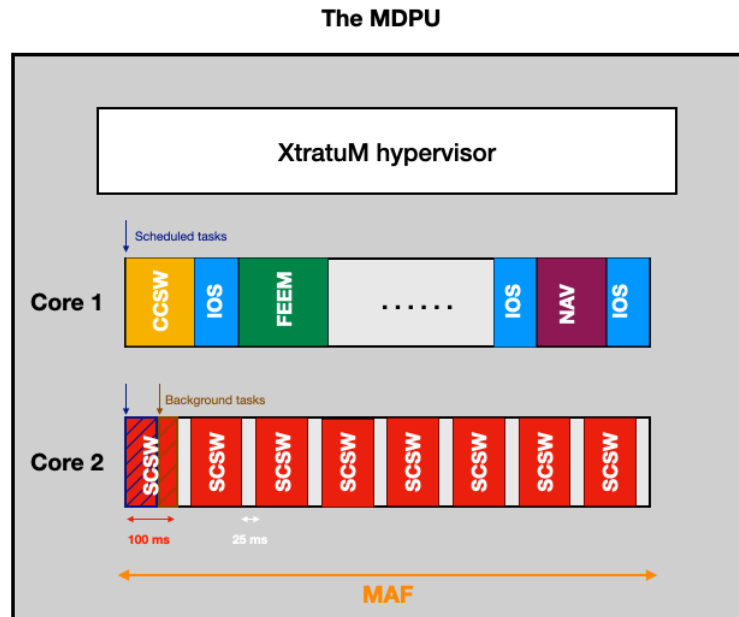


Figure 3.19: The MDPU architecture consists of two cores, one of which (core 2) is reserved for the science partition. Partitions are scheduled by the XtratuM hypervisor in a periodically repeated MAF. The MAF is divided into time slots used by a given partition to perform scheduled or background tasks.

One out of two cores is reserved for the science partition. All the partitions are integrated in the real-time XtratuM hypervisor [179] that schedules the partitions in a fixed cyclic plan consisting of a MAjor time Frame (MAF) of 1 s which is periodically repeated. For the science partition, the MAF is divided into eight time slots of 100 ms triggered every 125 ms.

In each time slot, two analysis tasks could be executed. First, the sequentially scheduled tasks must be executed like getting the current camera mode. The second type of analysis is the background tasks that are performed using the remaining time in a slot when all the scheduled tasks are completed. When the slot ends, the background analysis is interrupted and resumes at the next slot if there is some spare time.

3.4 . The MXT onboard science software

The SCSW partition manages the autonomous onboard scientific processing of data recorded by the telescope and formats the output data to be sent to the ground via VHF and X-band packets for the ground processing. The IJCLab is in charge of developing and characterizing the onboard SCSW under the responsibility of CNES. Section 3.4.1 presents briefly the algorithm coded in the SCSW partition to manage the data science processing and formatting. Sec. 3.4.2 shows the workflow of the development and test of the SCSW partition.

3.4.1 . The scientific algorithm

In order to fulfill the MXT scientific requirements, four analyses must be performed onboard. Each analysis is performed with a specific FEE mode and wheel position. Figure 3.20 illustrates the scientific algorithm implemented onboard the MXT.

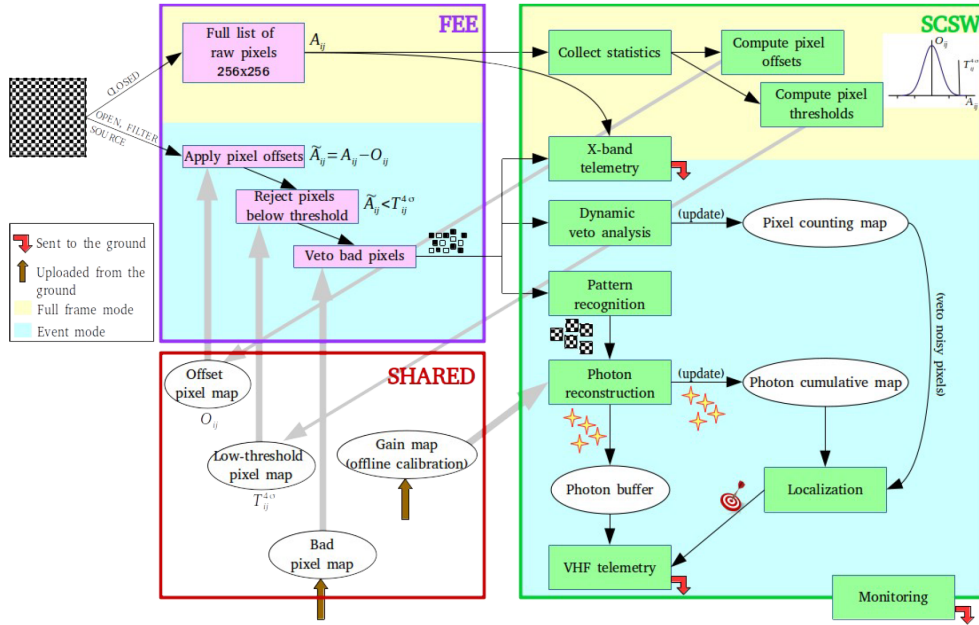


Figure 3.20: Onboard data processing flowchart. The purple box represents the FEEM partition, the green box represents the SCSW partition, and the red one is shared memory between the two partitions. The analysis during the FULL-FRAME and EVENT modes are shadowed in yellow and blue, respectively. Four analyses are performed, the noise characterization that is performed with the FULL-FRAME mode, the source localization that is performed during the EVENT mode, the telemetry packets formatting, and the data monitoring in both modes.

The first analysis is the detector noise characterization, in which the detector intrinsic noise I is characterized to compute the offset $O[i][j]$ and the threshold $T[i][j]$ for each pixel (see Sec. 3.3.2). These values are communicated to the FEEM partition to select only pixels above noise level during the observation. The noise characterization is performed with a closed wheel position to ensure that no photons are hitting the detector. The noise characterization algorithm is called the dark algorithm. The dark algorithm is performed when the selected FEE mode is the FULL-FRAME mode, because the information of all pixels is needed to characterize the noise in each, and it is performed as a background analysis. The dark algorithm is explained more in Chap. 4

The second analysis is the source localization, which is performed with an open-wheel position and EVENT FEE mode, because only pixels containing a signal above noise are required, and it is performed as a background analysis. During this analysis task, the SCSW partition analyzes the camera images to search for a source within the field of view of the MXT and

compute its coordinates. More details are given in Chap. 4 and Chap. 5.

The third analysis is the telemetry packets formatting, in which the data is sent to the ground via X-band or VHF packets. The camera images are sent via X-band packets, and the image analysis results are sent via VHF packets. The X-band packets are formatted and sent in both FEE modes. Meanwhile, the VHF packets are sent only during an observation, where the FEE is operating in the **EVENT** mode.

The last analysis is the data monitoring, in which the SCSW partition computes some intermediate results of the three analyses above to monitor and check that the analysis is running as expected.

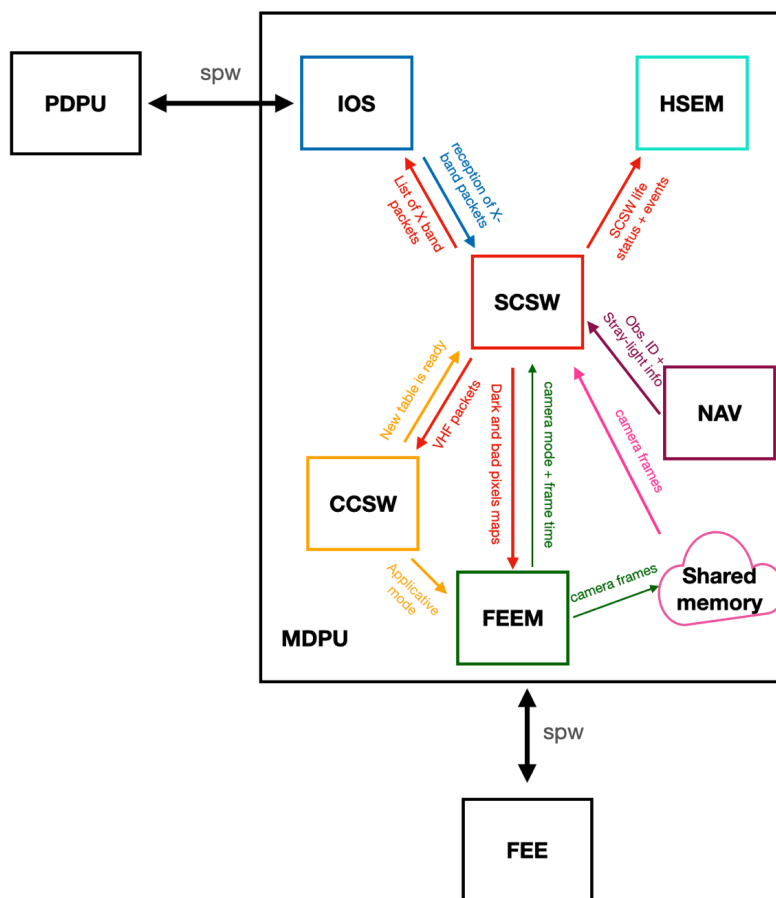


Figure 3.21: The interface of the scientific software partition with the other software partitions coded in the MDPU. The FEE and the PDPU are connected to the MDPU via a space-wire link (spw).

To manage the onboard algorithm, the SCSW partition receives and sends information from and to the other partitions in the MDPU. Moreover, it receives information organized in tables

from the ground. The tables that are received from the ground are the table of the PSF model as it is explained in Sec. 5.1.1, the energy gain table to compute the pixel energy onboard as explained in Sec. 4.2.1, and the configuration table that contains 58 parameters to tune the onboard analysis from the ground. The interface of the SCSW partition with the rest of the partitions is sketched in Fig. 3.21.

- The FEEM partition transmit the camera frames (images), the frame time, and the camera configuration (see Tab. 3.3) to the SCSW partition. On the other hand, the SCSW partition sends the noise offset O and threshold T maps to the FEEM partition
- The CCSW partition updates the SCSW partition if there is a new table uploaded from the ground, and it receives the VHF packets from the SCSW partition.
- The NAV partition sends to the SCSW partition the observation ID that indicates if there is a new observation.
- The IOS partition receives the X-band packet from the SCSW partition, and it informs the SCSW about the reception of the packets.
- The HSEM partition receives the life status of the SCSW partition.

3.4.2 . Development workflow

In this section, the implementation and the test of the science software partition is explained. The first step of the development of the onboard scientific algorithm is to prototype them on local computers. Simulated data by the SATANDLIGHT simulation tool (explained in Sec. 3.5) is used as an input for the prototype software. Once an algorithm is prototyped and tested, it is implemented in the onboard partition if it matches the requirements.

The onboard scientific algorithms are coded in the C language to have as optimized code as possible. The code is divided into modules, each of which is devoted to a specific algorithm. For example, the `dark` module performs the dark algorithm. During the development, we did not have the MDPU hardware. Therefore, to test the onboard code, the LEON3 emulator [180], provided by CNES, is used to emulate the MDPU. The sandbox [181] is used to simulate communication ports of other software seen in Fig. 3.21. The sandbox and science software partitions together simulate the partitions of the MDPU; they are compiled and integrated in real-time using the XtratuM hypervisor as explained in Sec. 3.3.3.

After implementing an algorithm, a "unit test" is performed. It calls the science functions individually. Only elementary functions are tested with the "unit test," and it does not need input data. Then a more complex test, called the "functional test," is performed. It is designed to test one or several requirements. In this test, the Sandbox plays the role of the FEEM partition and provides the input data to the science partition via a dedicated port, where simulated data is used as an input for this test. As mentioned in Sec. 3.4.2, a time slot is given for each algorithm. Thus, a "performance" test is developed to check if the algorithm fits in its defined time slot; if not, the code must be optimized. Moreover, testing the code quality

and standard check of the C coding rule is done with the SonarQube [182] quality management platform.

If the code passes all the tests mentioned above, it is validated at the level of IJCLab and a release of code is integrated and delivered to CNES. CNES integrates the code release with their test environment, the BVS, including the other partitions of the MDPU. The BVS is used for functional and system validation of the delivered software within the complete system where all partitions are simulated. The BVS is fed with input data simulated by the SATANDLIGHT tool and generates typical data products used for ground data processing validation as an output.

Once the camera is integrated, coupling tests were held at CEA, in which the MDPU is coupled to the camera. During these tests, the science partition receives real images directly from the camera. These tests verified part of the algorithm performance, like the X-band packet formatting and the noise characterization analysis. Nevertheless, not all of the algorithms are tested as no X-ray sources are used in the coupling test. Moreover, the optical module is not coupled to the camera. Figure 3.22 shows an image taken for the MDPU during one of the coupling tests at CEA.

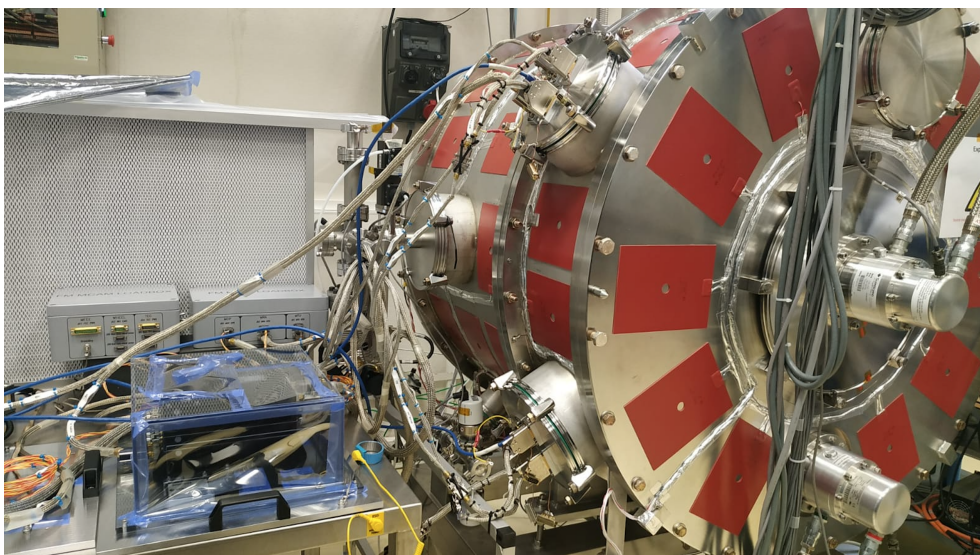


Figure 3.22: The MDPU (the black box to the left of the image) coupled to the camera that is placed inside a vacuum tank (the red tank), during one of the coupling test at CEA.

During the tests, the IJCLab team managed the data flow between the different working teams and ensured the right formatting of the data.

The main test was held in the PANTER [183] X-ray test facility of MPE located in Garching, Germany. It is the second-largest X-ray test facility in the world after the NASA one in the USA [184]. The Panter facility is used for the characterization of X-ray telescopes. It was built to test and characterize the ROSAT telescope [185]; after that, several space X-ray telescopes were tested in the facility, including BeppoSAX [48], XMM-Newton [186], Swift/XRT [59], Suzaku [187], eROSITA [188], and SVOM/MXT [138].

The facility is composed of a 130 m long vacuum tube, and the X-ray source is placed at one end of the tube to simulate a point-like source [189], as seen in Fig. 3.23. A wheel with 16 different targets is used to provide characteristic X-ray lines of the target element between 0.28 keV (corresponding to a C-K target) and up to 12 keV (corresponding to a Au-L target). Change of target can be performed within minutes. Two filter wheels are placed in front of the target wheel to suppress selected parts of the spectrum. The source flux is in the order of $1\text{-}10 \times 10^3 \text{ ph.cm}^{-2}.\text{s}^{-1}$. At the other end of the vacuum tube, there is the test chamber where the tested object is placed. The test chamber is 12 m long and has a diameter of 3.5 m [183].



Figure 3.23: The panter X-ray test facility of MPE in Germany. The photo shows the vacuum tube of 130 m long and a diameter of 1 m, with the X-ray source system at one end and the test chamber at the other end. Credit: MPE

For the MXT, three tests were held at PANTER, the qualification test, the performance test, and the flight model test with different hardware models. During the qualification and the performance tests, the SCSW partition was not completely implemented when these test took place. However, camera frames were saved to characterize the science partition later. During the flight model test, all of the MXT subsystems were coupled together, and the complete analysis chain of the SCSW partition was tested. Moreover, camera frames were saved for further investigation of the data and to perform complex characterization of the science partition. Figure 3.24 shows the flight model of the MXT in the test chamber of the PANTER facility.

A more detailed explanation of the flight model test at Panter and its results is given in Sec. 5.3.

3.5 . Simulation of the MXT telescope

The SATANDLIGHT simulation toolkit [190] has been developed to provide simulated data for the MXT. It is a set of C++ classes describing scientific telescopes mounted on a satellite. It is developed especially to characterize the MXT onboard science software. Single C++ classes are devoted to simulate the satellite, the astrophysical sources, the telescope subsystems, and the geometry. Taking advantage of the C++ class inheritance, a user-friendly program called `sn1-sequence` is developed to simulate end-to-end observation sequences with a space telescope by combining the different classes altogether.

The `sn1-sequence` program takes only one input which is an option file where all parameters needed to configure the satellite, the camera, the telescope, and the source are identified. Several sequences of camera frames can be generated. For example, a sequence with a closed wheel

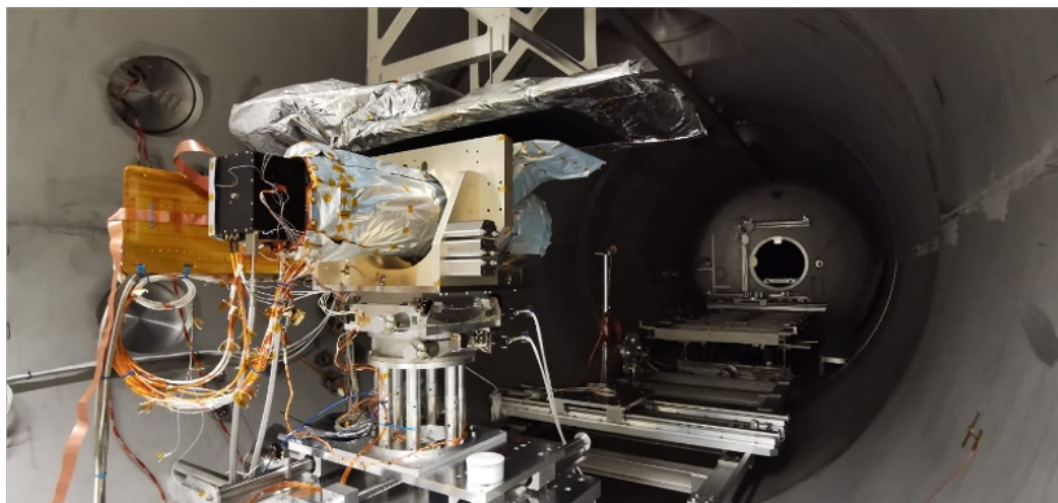


Figure 3.24: The MXT telescope placed in the test chamber of PANTER X-ray test facility during the flight model test. Credit: CNES.

position; with this sequence, only frames with intrinsic noise are saved. This sequence is used to characterize the dark algorithm as will be explained in Chap. 4. An observation sequence with an open-wheel position and with or without astrophysical sources in the field of view can also be simulated. This sequence is used to characterize the source localization as will be explained in Chap. 5. An example option file to generate an observation sequence is presented in Fig. 3.25.

The following sections describe the main sub-classes of the SATANDLIGHT tool.

3.5.1 . Satellite simulation

The `Satellite` class is the master class to simulate an entire sequence of frames. The user can configure more than one telescope combined with an internal timing onboard the satellite. Each telescope can be configured separately in terms of its geometry, detector, and optics. In addition, one or several astrophysical sources can be simulated and associated with each telescope. Moreover, the user can tune the satellite altitude as a function of time, which is parametrized by the Euler angles, see Sec. 3.2.

3.5.2 . Source simulation

Two types of sources are simulated with SATANDLIGHT, sources of photons, and sources of charged particles (cosmic rays). The source sky location is parametrized in spherical coordinates (θ_s, ϕ_s) as seen in Fig. 3.1. Moreover, each source is given a spherical cap parametrized by an opening angle ι_s to represents the spread of the particles out from the source. If $\iota_s = 0$, then the source is a point-like source. The charged particles are isotropic, thus $\iota_s = \pi$ and the source position (θ_s, ϕ_s) is irrelevant in the simulation.

The source is also characterized by its flux as a function of energy and time $\mathcal{F}(E, t) = \frac{d^4N}{dE dt dS}$, which is a measure of the particles crossing a unit surface per unit time per unit energy. If the source is not "on-axis," the flux must be corrected by the $\cos(\theta)$, the direction of the source

```

***** SATELLITE *****
// Satellite name
SATELLITE NAME SVOM

// Satellite timing [ms]: time start - duration - resolution
SATELLITE TIMING 0 400000 10000

// Satellite attitude file
SATELLITE ATTITUDE ./input/euler.root

// Sequence output directory
SATELLITE OUTDIR .

***** TELESCOPE *****
// Telescope names
TELESCOPE NAME MXT

// Telescope focal length [mm]
MXT FOCALLENGTH 1120

// Telescope PSF
MXT PSFFILE ./input/PSF_AI-K_P0_panter21.fits

// Telescope effective area
MXT EFFAREAPHOTON ./input/effarea_mxt.root effarea_mxt

// Telescope acceptance
MXT ACCPHOTON ./input/acc_photon.root photon_acc

***** CAMERA *****
// Camera size [mm] X/Y/Z
MXT_CAM SIZE 10 19.2 19.2

// Camera number of pixels Y/Z
MXT_CAM NPIXELS 256 256

// Camera integration time [ms]
MXT_CAM TIMING 100

// Noise parameters
MXT_CAM PIXELDARKNOISE 3000 100 150 10
MXT_CAM PIXELREADNOISE 5000 300 250 30

// Gain [ADU/eV]
MXT_CAM GAIN 0.00175

***** SOURCE *****
// Source names
SOURCE NAME GRB220930A

// Source type
GRB220930A TYPE PHOTON

// Source position: dec[rad]/ra[rad]/cone[rad] z y
GRB220930A POSITION 0.0 0.1 0.0

// SpecTime
GRB220930A SPECTIME ./input/spectime_GRB220930A.root

```

Figure 3.25: Example of an option file that is used as an input to generate an observation sequence. The parameters required to configure the satellite, the sources, the telescope, and its camera is must be specified in the file.

with respect to the telescope optical axis.

The source count rate which measures the number of particles crossing a detection surface with an effective area $\mathcal{S}(E)$ per unit time per unit energy $\mathcal{C}(E, t)$ is given by integrating the flux over the effective area $\mathcal{S}(E)$:

$$\mathcal{C}(E, t) = \frac{d^2 N}{dE dt} = \iint_{\mathcal{S}} \mathcal{F}(E, t) d\mathcal{S} = \mathcal{F}(E, t) \mathcal{S}(E). \quad (3.4)$$

To simulate the source light curve (explained in Sec. 1.2.3.2) as observed by a telescope in an energy range from E_1 to E_2 , the count rate is integrated over the energy:

$$\mathcal{L}(t) = \int_{E_1}^{E_2} \mathcal{C}(E, t) dE. \quad (3.5)$$

To simulate the source spectrum (explained in Sec. 1.2.3.1) as observed by an instrument between t_1 and t_2 , the count rate is integrated over the time:

$$N(E) = \frac{1}{t_2 - t_1} \int_{t_1}^{t_2} \mathcal{C}(E, t) dt. \quad (3.6)$$

The number of astroparticles N_p between E_1 and E_2 , that cross a surface with $\mathcal{S}(E)$ effective

area, during $\Delta t = t_2 - t_1$ is measured by integrating the source count rate over time and energy:

$$N_p = \int_{t_1}^{t_2} dt \int_{E_1}^{E_2} dE \mathcal{C}(E, t). \quad (3.7)$$

In SATANDLIGHT, the flux $\mathcal{F}(E, t)$ is simulated using a two-dimensional discrete function and represented by a two-dimensional matrix where the x -axis is binned in time with N_t bins, and the y -axis is binned in energy with N_E bins, the flux is computed at the center of each bin. The user must give the initial and final time t_1 and t_2 respectively, and the energy range $E_1 - E_2$. The flux outside the time and energy range is considered to be null. SATANDLIGHT offers several methods to model the flux distribution with energy and time; for example, the user can use a uniform, time exponentially decaying, energy decaying, or a realistic GRB flux as explained in Chap. 6. An Example of a simulated exponentially decaying flux is shown in Fig. 3.26.

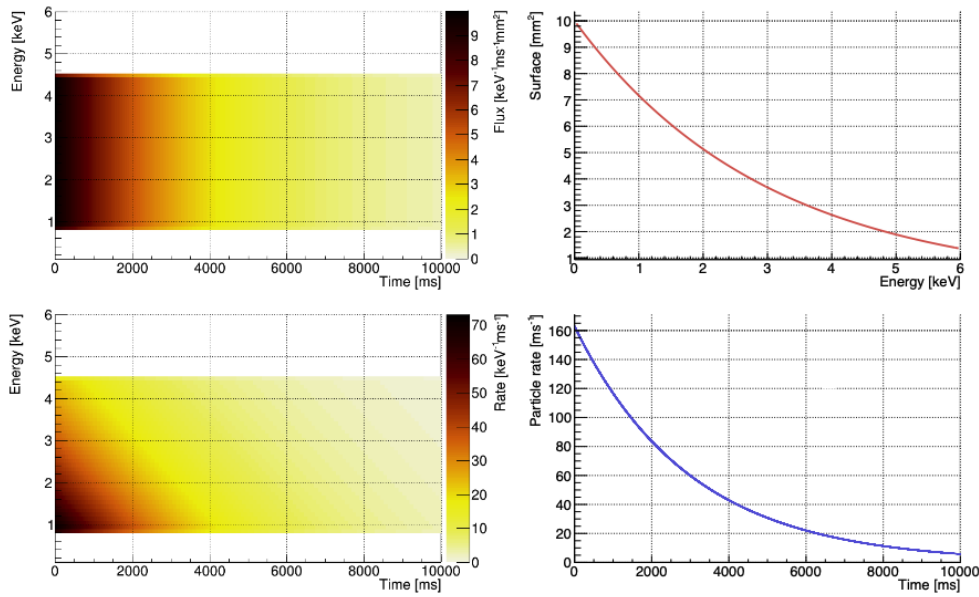


Figure 3.26: An example of a uniform source flux object between 0.8 keV and 4.5 keV and exponentially decays with time, simulated with the SATANDLIGHT (top-left). The rate plot (bottom-left) is obtained by multiplying the flux object with the effective area (top-right). The source light curve resulting from the integration of the rate over all energies (bottom-right).

The N_p astroparticles are generated one by one from the source. Each generated astroparticle is given energy E_p and t_p following the flux distribution in time and energy. Additionally, each particle is also given a random incoming direction (θ_p, ϕ_p) within the source opening angle ι . The interaction of the source astroparticles with the detector is explained in Sec. 3.5.3.

3.5.3 . Camera simulation

The **Camera** class is developed to describe CCD detectors in general, and it can also be tuned to simulate detectors with a similar working principle. The detector is simulated as a yz -plane divided in rectangle pixels distributed over $N_y \times N_z$ cell. The **Camera** class uses the two systems of coordinate explained in Sec. 3.2 to describe the detector geometry. The camera is also given a time t_{cam} and an integration time δt_{cam} , which is the time between two successive images. In SATANDLIGHT, each pixel is characterized by three parameters:

- Each pixel is given a value of intrinsic noise $I[i][j]$ in Analog to Digital Units (ADU), with two components, the read and the dark noise contributions, as explained in Sec. 3.3.2, $I[i][j] = D[i][j] + R[i][j]$. The $D[i][j]$ and $R[i][j]$ values are drawn separately from a Gaussian distribution with a per-pixel mean value and standard deviation.
- Each pixel is given a value of overall raw amplitude $A_r[i][j]$ in ADU. The $A_r[i][j]$ value is composed of the noise value $I[i][j]$ and the signal value $A[i][j]$, if any.
- Each pixel is given an energy gain value to convert amplitude from ADU to energy unit:

$$E[i][j] = G[i][j] \times A[i][j]. \quad (3.8)$$

In addition one can also include defects of the detector like dead pixels by setting $A_r[i][j] = 0$, or bright pixels by setting $A_r[i][j] = A^{max}$, where $A^{max} = 2^{14} - 1$ is the maximum coded amplitude value. An insensitive columns can be considered by simulating a columns of bright pixels. Figure 3.27 shows an example of a simulated camera picture showing the effect of the camera defects.

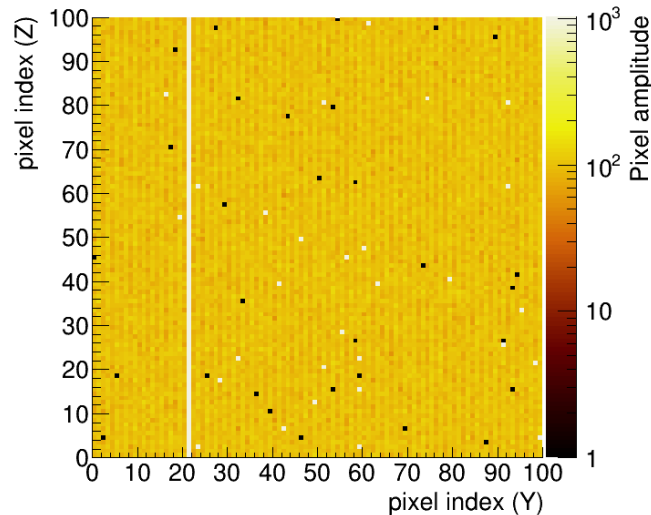


Figure 3.27: Example of a simulated camera image showing the effect of camera defects. Black points are dead pixels, white points are bright pixels, and the white column is a frozen column due to the saturation of readout electronics.

Moreover, the `Camera` class simulates the interaction of photons and cosmic rays with the detector. An incoming photon is defined by an energy E_p in [keV] and a hit position (y_p, z_p) in the detector plane given in camera intrinsic coordinates. A two-dimensional Gaussian distribution centered on (y_p, z_p) is used to distribute the photon energy over neighboring pixels. The width of the Gaussian is weighted with the photon energy and tuned to match the charge transfer in the MXT detector. The pixel energy is converted to a raw amplitude using the gain value $G[i][j]$ as in Eq. 3.8. Cosmic rays interact differently with the detector. They are very energetic; thus, they may travel across the entire detector plane. The interaction with the detector is simulated as a straight track determined by the direction of the particle (θ_p, ϕ_p) , the track is starting at the entry point (y_p, z_p) , and a fraction of energy is transferred for each hit pixel and distributed following a Gaussian function over neighboring pixels. If all the available energy has been transferred to the detector pixels, the track stops. Figure 3.28 shows the effect of a photon and a cosmic ray on the CCD detector as simulated by SATANDLIGHT.

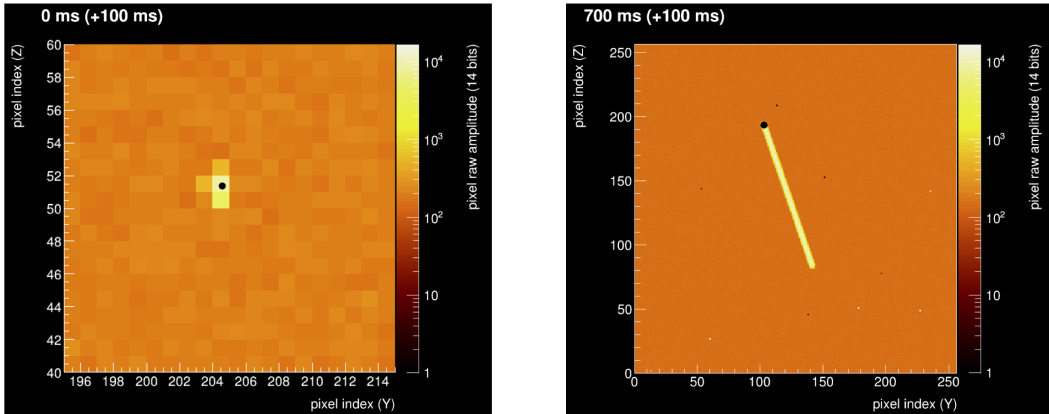


Figure 3.28: The effect of the interaction of astroparticles with a CCD detector as simulated by the SATANDLIGHT. Left: zoom on a camera image showing the effect of a photon where the energy is distributed over four pixels; the black circle represents the hit position of the photon. Right: a camera image shows the effect of a cosmic ray on the detector. The black point is the entry point of the cosmic ray.

3.5.4 . Telescope simulation

The `Telescope` class describes a telescope geometry and its optical design, which focuses photons on the focal plane. The optical axis is fixed to be the x -axis.

With the `Telescope` class, one can take pictures. To do so, the telescope position in the sky must be defined in the telescope reference frame \mathcal{R} . The telescope system of coordinates is identical to the satellite one. The transformation between the telescope reference frame and the Earth reference frame \mathcal{R}' is managed by the `Rotation` class from which the `Telescope` class inherits. The `Rotation` class simulates the three-dimensional rotation shown in Fig. 3.2.

The telescope CCD camera is added and configured as explained in Sec. 3.5.3. One or several sources can be simulated and configured as described in Sec. 3.5.2. If a source is

added, the corresponding on-axis effective area must also be included. In the simulation, the astroparticles generated from a source at (θ'_s, ϕ'_s) are given an energy E_p and a direction (θ'_p, ϕ'_p) in the Earth reference frame. Afterward, the particle incoming direction is computed in the telescope reference frame θ_p, ϕ_p by the `Rotation` class. The user must also define the telescope acceptance for a given source. The acceptance measures the probability for a particle with a given incoming direction to reach the camera depending on its angle. The horizontal axis is binned in $-1 < \cos \theta_p < 1$. The vertical axis is binned in $0 < \phi_p < 2\pi$.

The optical design parameterized by the PSF must be configured. The user gives a table of the PSF model or define the PSF discrete function $\mathcal{P}(y, z, E_{ph})$, with twice the size of the detector (see Sec. 3.9).

If the particle is a photon, the hit position in the detector plane is computed following Eq. 3.1, and is deflected by the optics to compute the final photon hit position (y_p, z_p) . The particle interaction with the camera is managed according to its type, as explained in Sec. 3.5.3.

4 - Camera images processing

Contents

3.1	The MXT features and scientific objectives	61
3.2	The MXT reference frames and system of coordinates	63
3.2.1	The reference frames	63
3.2.2	The system of coordinates	64
3.3	The MXT subsystem	66
3.3.1	The MXT optics	68
3.3.2	The MXT camera	72
3.3.3	The MXT data processing unit	78
3.4	The MXT onboard science software	79
3.4.1	The scientific algorithm	80
3.4.2	Development workflow	82
3.5	Simulation of the MXT telescope	84
3.5.1	Satellite simulation	85
3.5.2	Source simulation	85
3.5.3	Camera simulation	88
3.5.4	Telescope simulation	89

This chapter explains the image processing performed by the science partition in the operation/dark and operation/observation modes (see Tab. 3.3). The operation/dark mode is defined when the calibration wheel is set to the close position where no X-ray photons are hitting the detector and when the FEE is operated in the **FULL-FRAME** mode, as explained in Sec. 3.3.2. In the **FULL-FRAME** mode, the camera captures an image every 200 ms, and the FEEM partition transfers the image to the MDPU without any treatment. The science partition processes the images to characterize the detector noise. This analysis is presented in Sec. 4.1.

In the operation/observation mode, the calibration wheel is set to the open or filter position so that X-ray photons can reach the detector, and the FEE is operated in the **EVENT** mode, in which the image is integrated over 100 ms. Only pixels with amplitude above the noise level are transferred to the science partition, which processes the transferred pixel data to identify X-ray photons and localize the X-ray source. The image processing in the operation/observation mode to identify the X-ray photons is explained in Sec. 4.2.

4.1 . The MXT dark algorithm

The objective of this analysis is to characterize the pixel-by-pixel intrinsic noise (see Sec. 3.3.2) by computing the noise offset O and threshold T maps (the dark maps from now on) for the whole 256×256 pixels. $O[i][j]$ measures the average noise in pixel (i, j) , and $T[i][j]$ measures the noise fluctuations around the offset value.

The dark maps must be computed while no photons are hitting the detector and using the information of all pixels. Therefore, the calibration wheel is set to the closed position, and the FEE is operated in the FULL-FRAME mode. A sequence of frames taken with a closed wheel position and FULL-FRAME mode is called the dark sequence.

The closed wheel position prevents X-ray photons from interacting with the detector. However, charged particles like cosmic rays are energetic enough to reach the detector from all directions and deposit energy on top of the camera noise. Figure 4.1 shows a camera image captured during a coupling test at CEA with a closed wheel position, cosmic rays were still able to hit the detector, and their trajectory is seen in the image above the intrinsic noise. This cosmic ray issue must be addressed since they bias the estimation of the dark maps.

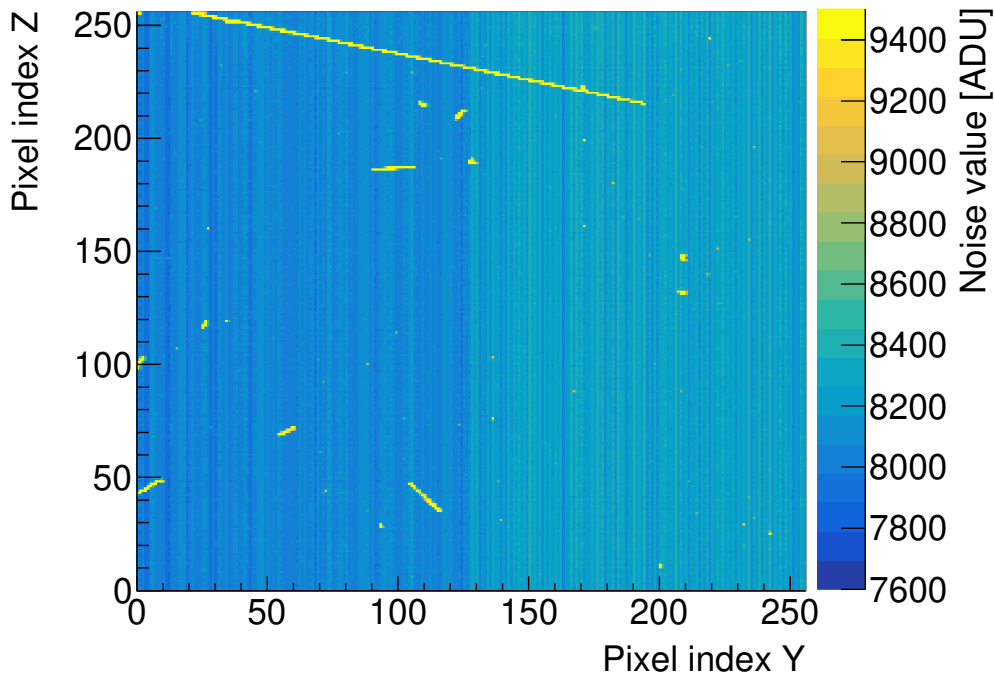


Figure 4.1: Example of a frame taken by the MXT detector during coupling test at CEA. The image was taken with a closed wheel position, so no X-ray photons interact with the detector. Meanwhile, the cosmic rays penetrated the wheel even with a closed position and added an energy above the noise.

As a reference, the algorithms implemented for the ground analysis are explained in Sec. 4.1.1.

The onboard dark algorithm is discussed in Sec. 4.1.2. The characterization and results of the onboard dark algorithm are presented in Sec. 4.1.3.

4.1.1 . Ground dark algorithm

We note for the offset and threshold maps computed with the ground analysis O^G and T^G respectively.

In the ground analysis [165], the offset map O^G is computed as the pixel-by-pixel median value across a sequence of dark frames $0 < k < N_d$:

$$O^G[i][j] = \left[A_r[k][i][j] \right]_{N_d}^{50\%}. \quad (4.1)$$

To compute $T^G[i][j]$, the frames must be smoothed by removing the offset and the common-mode noise $CM^G[k][c][j]$, which is a noise fluctuation affecting all the pixels in half a row due to the parallel read out process by the two CAMEX. We note c the CAMEX index: 0 for the left CAMEX, and 1 for the right CAMEX. The $CM^G[k][c][j]$ is computed as a median value for each half a row of the offset-subtracted frame:

$$CM^G[k][c][j] = \left[(A_r[k][i][j] - O^G[i][j]) \right]_{N/2}^{50\%}. \quad (4.2)$$

Finally, the flat frame value for each pixel $F[i][j]$ in frame k is defined as:

$$F^G[k][i][j] = A_r[k][i][j] - O^G[i][j] - CM^G[k][c][j]. \quad (4.3)$$

The threshold is given as n_t (=4) times the 84.13th percentile of the $F^G[i][j]$ across N_d frames, to select pixels at a $n_t\sigma$ level:

$$T^G[i][j] = n_t \times \left[F[i][j][k] \right]_{N_d}^{84.13\% - 50\%}. \quad (4.4)$$

The 84.13th percentile is equivalent to one standard deviation if the distribution is Gaussian. The dark maps computed with the ground analysis are shown in Fig. 4.2

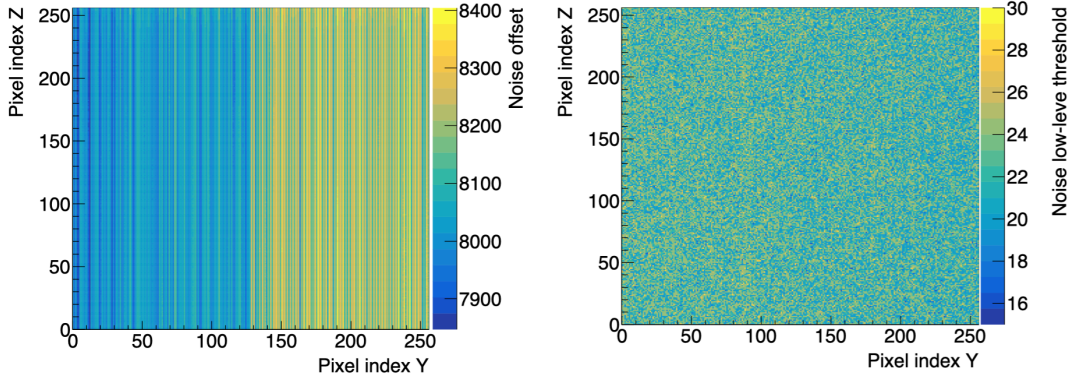


Figure 4.2: The dark maps computed with the ground analysis. The offset map (left), and the threshold map (right).

The advantage of using the median and the 84.13th percentile instead of a simple mean and standard deviation is the robustness in the presence of cosmic rays.

Finally, the O^G and T^G maps are used to select pixels above noise during an observation. The pixel (i, j) is selected by the FEE if:

$$A[i][j] = A_r[i][j] - O^G[i][j] > T^G[i][j] \quad (4.5)$$

The ground method (median and percentile) to compute dark maps requires keeping N_d frames in the memory which is not achievable onboard due to the lack of memory. Thus, the noise is characterized onboard with a different method than the ground analysis as it is explained in Sec. 4.1.2. Any method implemented onboard must produce dark maps comparable to the reference maps: O^G and T^G . The onboard dark algorithm are explained in the following section.

4.1.2 . Onboard dark algorithm

The intrinsic noise of the detector is temperature-dependent. Therefore, the noise characterization must be performed onboard in the same thermal environment as the observation and as often as possible since the temperature varies in the SVOM orbit.

The science partition computes $O[i][j]$ by taking the pixel-by-pixel mean value of the $A_r[i][j]$ distribution across a sequence of dark frames. Moreover, it includes a threshold to reject outliers like cosmic rays from the distribution to avoid biasing the mean value, as seen in Fig. 4.3.

To compute $T[i][j]$, the flat frame must be computed first as in Eq. 4.3, but using the onboard-computed offset map and common-mode noise. For pixel (i, j) , the $T[i][j]$ is given as the n_t ($=4$) times the standard deviation of the $F[k][i][j]$ across a sequence of dark frames.

Finally, the science partitions communicates the dark maps: O and T to the FEEM partition, so the FEE selects pixels above noise during the operation/observation mode as in Eq. 4.5.

The dark algorithm onboard can be divided into three steps: the outlier threshold calculation explained in Sec. 4.1.2.1, the offset map O analysis explained in Sec. 4.1.2.2, and the threshold

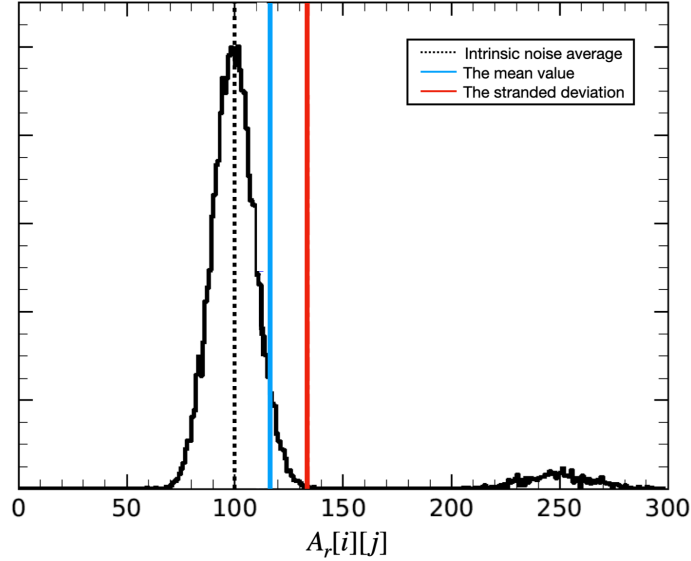


Figure 4.3: The $A_r[i][j]$ distribution of the (i, j) pixel. The distribution has two peaks, the first one corresponds to the intrinsic noise distribution with true value labelled with dashed black line. The second one corresponds to the cosmic ray distribution that is added on top of the intrinsic noise distribution. The presence of the cosmic rays biases the mean (the blue line) and the standard deviation (red line) of the distribution.

map T analysis explained in Sec. 4.1.2.3. A different set of camera frames is used for each analysis since the camera frames are not saved onboard. The monitoring and the configuration of the dark algorithm from the ground are explained in Sec. 4.1.2.4.

4.1.2.1 Outlier rejection

During this analysis step, the outlier threshold for each pixel is computed in order to avoid biasing the dark maps. The aim of computing the outlier threshold is to exclude outliers when the amplitude $A_r[i][j]$ deviates significantly from typical noise amplitudes. To achieve this, N_r camera frames in the dark sequence are first processed to compute the mean $\mu_r[i][j]$ and the variance $\sigma_r^2[i][j]$ of pixel raw amplitudes $A_r[i][j]$ as:

$$\begin{aligned}\mu_r[i][j] &= \frac{1}{N_r} \sum_{k=0}^{N_r-1} A_r[k][i][j], \\ \sigma_r^2[i][j] &= \frac{1}{N_r} \sum_{k=0}^{N_r-1} A_r^2[k][i][j] - \mu_r^2[i][j],\end{aligned}\quad (4.6)$$

where $A_r[k][i][j]$ is the raw amplitude of pixel (i, j) in the dark frame k . An example of the $A_r[k][i][j]$ distribution including cosmic rays is shown in Fig. 4.3. Outlier thresholds are applied

to the following analysis steps: the $O[i][j]$ and $T[i][j]$ computation. The pixel is rejected if:

$$(A_r[k \geq N_r][i][j] - \mu_r[i][j])^2 > n_r^2 \sigma_r^2[i][j], \quad (4.7)$$

where n_r is the number of standard deviation to reject outlier, the default value for n_r in the science partition is $n_r = 3$. As a consequence of the outlier rejection, the $A_r[i][j]$ distribution is truncated at $n_r \times \sigma_r$. Therefore the standard deviation of the truncated Gaussian must be corrected as it is explained in Sec. 4.1.2.3.

4.1.2.2 Offset map analysis

Once the outlier analysis is completed, the next N_o frames are processed to compute $O[i][j]$. For every pixel (i, j) in $N_r \leq k < N_r + N_o$ frame, the outlier threshold is applied: the pixel is rejected if it does not satisfy Eq. 4.7. Hence the number of frames passing the outlier threshold for pixel (i, j) can be less than the total analyzed frames: $N'_o(i, j) \leq N_o$. The offset value for pixel (i, j) is computed as:

$$O[i][j] = \frac{\sum_{k=N_r}^{N_r+N_o-1} A_r[k][i][j]}{N'_o(i, j)}, \quad (4.8)$$

where the sum is set to zero if $A_r[k][i][j]$ satisfies Eq. 4.7.

The science partition sets a minimum limit of dark frames N_o^{min} to be used effectively for each pixel in the offset analysis. If $N'_o(i_0, j_0) \leq N_o^{min}$ for the (i_0, j_0) pixel, a default offset is computed as the mean value of all pixels in the column i_0 and across all N_o frames including the outlier threshold. If all pixels in the column i_0 and across N_o frames are rejected by the outlier threshold, the default value is set to a maximum amplitude $O[i_0][j_0] = O_{def} = 2^{14} - 1$.

The final offset map O of size 256×256 is written and communicated to the FEEM partition for the pixel selection (see Eq. 4.5) during the observation mode. The offset map O is shown in Fig. 4.4.

4.1.2.3 Threshold map analysis

To compute the $T[i][j]$ map, the next N_t frames are processed. The outlier threshold in Eq. 4.7 is applied pixel by pixel across the N_t frames. Hence, the threshold analysis for pixel (i, j) is applied using $N'_t(i, j) < N_t$. A minimum number of dark frames N_t^{min} must be effectively used for $T[i][j]$ computation.

The $F[i][j]$ is computed as in Eq. 4.3. After subtracting $O[i][j]$ and the $CM[c][j]$, noise fluctuations remains in the $F[i][j]$ that should be measured by the T map.

$O[i][j]$ is computed in the previous section, and $CM[k][c][j]$ is computed for each half a row in every N_t frame. When $c=0$, this corresponds to the columns read by the left CAMEX: $0 < i < N/2 - 1$. When $c=1$, this corresponds to the columns read by the right CAMEX: $N/2 < i < N - 1$.

Onboard, the $CM[k][c][j]$ is computed as a mean value for each half a row of the offset-subtracted frame. The outlier threshold in Eq. 4.7 is applied while computing the $CM[k][c][j]$.

$$CM[k][c][j] = \frac{\sum_{i=cN/2}^{(c+1)N/2-1} (A_r[k][i][j] - O[i][j])}{N'_{CM}}, \quad (4.9)$$

where the sum is set to zero if $A_r[k][i][j]$ satisfies Eq. 4.7. N'_{CM} is the number of pixels in the j row and in the c CAMEX that pass the outlier threshold. If $N'_{CM} = 0$, the $CM[k][c][j]$ value is set to zero. Once $CM[k][c][j]$ is computed, the $F[k][i][j]$ is computed with Eq. 4.3 for each N_t frame. The $T[i][j]$ map is then given by the standard deviation of each pixel in $F[k][i][j]$ across the N_t frames:

$$T[i][j] = \kappa \times \sqrt{\frac{\sum_{k=N_r+N_o}^{N_r+N_o+N_t-1} F[k][i][j]^2}{N'_t[i][j]} - \left(\frac{\sum_{k=N_r+N_o}^{N_r+N_o+N_t-1} F[k][i][j]}{N'_t[i][j]} \right)^2}, \quad (4.10)$$

where the sum is set to zero if $A_r[k][i][j]$ satisfies Eq. 4.7. κ is a correction applied to the standard deviation of a truncated Gaussian distribution due to the outlier rejection (see Sec. 4.1.2.1).

If $N'_t[i_0][j_0] < N_t^{min}$ for pixel (i_0, j_0) , a default threshold value is given for this pixel. The default value is computed as the standard deviation of $F[i_0][j_0]$ evaluated over column i_0 and across all frames. If all pixels in the column i_0 and across N_t frames are rejected by the outlier threshold the default value is set to the maximum amplitude $T[i_0][j_0] = T_{def} = 2^{14} - 1$. Finally, the threshold is multiplied by the n_t factor to ensure selecting only pixels with photon hit during the observation.

$$T[i][j] = n_t \times T[i][j] \quad (4.11)$$

The final threshold $T[i][j]$ map of size 256×256 is written and communicated to the FEEM partition to be used for the pixel selection as in Eq. 4.5 during the observation mode.

The dark maps computed onboard are shown in Fig. 4.4

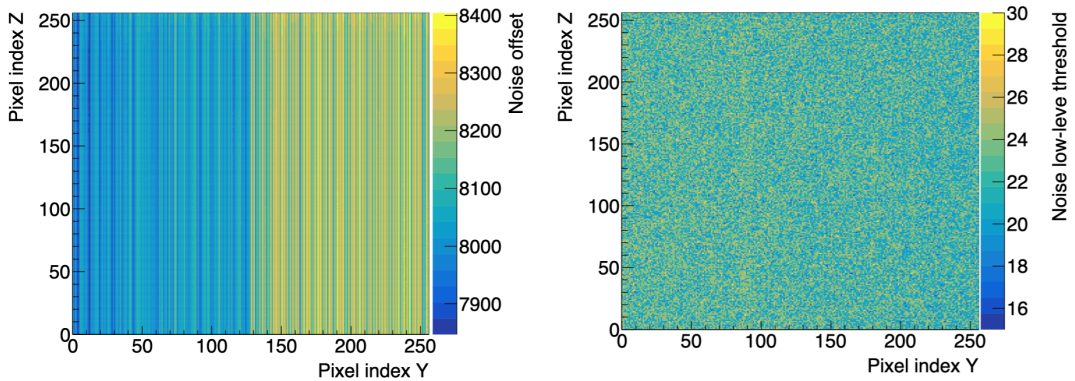


Figure 4.4: The dark maps computed with the onboard algorithm. The offset map (left), and the threshold map (right), both given in the [ADU] unit.

4.1.2.4 Monitoring and configuration of dark algorithm

The onboard dark algorithm is monitored from the ground using a table of intermediate results computed by the science partition and sent to the ground via a recurrent VHF packet. The science partition computes the mean and the standard deviation of the most recent $O[i][j]$ and $T[i][j]$ maps. In addition, the number of pixels with default offset O_{def} and default threshold T_{def} values is computed and sent to the ground.

The onboard dark algorithm needs to be configured from the ground by tuning different parameters that could not be performed onboard. The 9 parameters that are evaluated on the ground and uploaded with the configuration table to the science partition are listed in Tab. 4.1.

Table 4.1: List of parameters for the dark algorithm, that are tuned on the ground and uploaded with the configuration table to the science partition.

Notation	Description	Default value
N_r	Number of frames to compute the outlier threshold	50
n_r	Number of standard deviations to reject outliers	3
κ_r	Standard deviation correction for truncated Gaussian (noise analysis)	1.0022233
N_o	Number of frames to compute the pixel offset	80
N_o^{min}	Minimum number of frames to effectively compute the pixel offset	70
N_t	Number of frames to compute the pixel noise level	100
N_t^{min}	Minimum number of frames to effectively compute the pixel noise level	90
n_t	Number of standard deviations to define the pixel noise level	4

4.1.3 . Results and characterization

To ensure the compliance of the onboard algorithm with the MXT scientific requirements, the parameters in Tab. 4.1 must be tuned. In this section, the dark parameters and the dark maps are characterized. The input data used during the characterization are explained in Sec. 4.1.3.1. The robustness of the dark maps in the presence of cosmic rays is tested in Sec. 4.1.3.2. In addition, the N_r is characterized. Section 4.1.3.3 characterize the minimum number of frames needed to compute the dark maps: N_o and N_t . A study to compare the onboard dark maps with the reference maps (the ones computed with the ground analysis) is held in Sec. 4.1.3.4. Section 4.1.3.5 tests the effect of the onboard and ground dark maps on the spectral response of the detector.

4.1.3.1 Input data

In the characterization of the dark algorithms, two types of data are used as an input. The first input is dark sequence of frames saved during a coupling test at CEA (see Sec. 3.4.2), the real sequence from now on. The second input is simulated camera frames with SATANDLIGHT simulation tool (see Sec. 3.5), the simulated sequences from now on.

For the real sequence, 200 dark frames (for a total duration of 40 s) were provided by CEA, with an average value about 8150 ADU and standard deviation about 300 ADU for the 256×256

pixels. The dark maps (O^G and T^G) computed using these frames with the ground analysis are also provided as a reference. The ground dark maps are visualized in Fig. 4.2.

For the simulated sequences, two dark sequences are simulated with SATANDLIGHT. One sequence is simulated with no cosmic rays hitting the detector, and only intrinsic noise is simulated: $A_r[i][j] = I[i][j]$. In the second dark sequence, a high rate of cosmic rays (200/frame) is simulated on top of the intrinsic noise: $A_r[i][j] = I[i][j] + A_c[i][j]$. The same number of frames (200 frames) and the same noise distribution (mean value = 8000 ADU, standard deviation = 250 ADU) were simulated for both sequences. The mean energy of the simulated cosmic rays is 50 keV which saturates the pixel in the track of the cosmic ray.

4.1.3.2 Robustness against outlier

One of the onboard dark algorithm requirements is the robustness against the outlier. Thus the rejection of outliers with the onboard algorithm must be tested. For this purpose, we used the two simulated sequences with SATANDLIGHT: with and without cosmic rays as explained in Sec. 4.1.3.1.

The $O[i][j]$ and $T[i][j]$ maps are computed using Eqs. 4.8 and 4.11 respectively, for both sequences. We note for the dark maps computed for the sequence with cosmic ray as: O^c and T^c .

If the algorithms are robust against outliers, comparable dark maps from both sequences must be found. To verify that, the pixel offset and threshold ratios between the two sequences are computed per pixel as $r_o[i][j] = O^c[i][j]/O[i][j]$, $r_t[i][j] = T^c[i][j]/T[i][j]$, respectively. The distribution of $r_o[i][j]$ and $r_t[i][j]$ are drawn for 256×256 pixels, as shown in Fig. 4.5.

Figure 4.5 shows that the mean value of the (r_o) is one with a standard deviation of 1.69×10^{-4} , which means that the offset maps computed onboard from the two sequences are very similar: $O \equiv O^c$. Regarding the pixel threshold ratio r_t , the mean value is about one ($\mu = 1.006$), and the standard deviation of 0.107. More pixels deviate from the mean (μ) value in the threshold ratio due to including more sources of error in calculating the threshold map, such as the common-mode noise and the offset computation errors (see Eq. 4.3 and Eq. 4.10), the truncated Gaussian distribution correction. However, the threshold maps from both sequences are comparable: $T \equiv T^c$. In addition, the plot of $\Delta O_{ij} = O_{ij}^c - O_{ij}$ is plotted as seen in Fig. 4.6.

The onboard dark complies with the requirement of rejecting outliers, even in the case of a high rate of cosmic rays per frame.

In order to tune the N_r parameter, the O , O^c , T , and T^c maps are computed with an increasing number of N_r , starting with $N_r = 10$ frames. For each N_r , the r_o and r_t ratios are computed, the mean (μ) values of the ratio distributions is computed. Once μ value converges to 1 and stabilizes at N_r frame, this N_r is considered as the minimum number required to ensure not biasing the dark maps. N_r is found to be at least 30 frames. This is the default value of N_r , with a possibility to be changed with the configuration table.

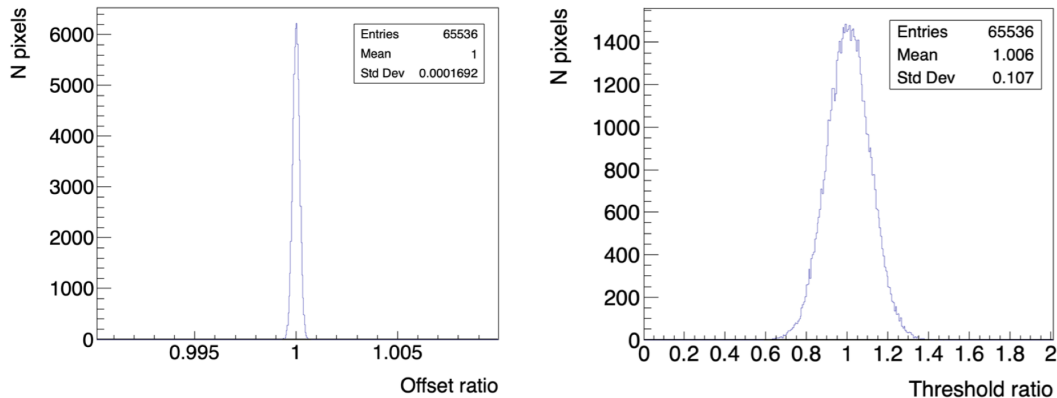


Figure 4.5: The ratio of the dark maps computed using a simulated dark sequence with no outliers and a dark sequence with the detector exposed to outliers. Left: the ratio of offset value ($r_o[i][j]$) for the 256×256 pixels. Right: the threshold ratio ($r_t[i][j]$) for the 256×256 pixels.

4.1.3.3 Tuning of N_o^{min} and N_t^{min} parameters

In order to get trustworthy dark maps, the algorithm must be executed with a minimum number of dark frames in one hand and ensuring a statistical significance in the other hand. This number differs from one analysis step to another. In this section, a statistical study is performed in order to determine the minimum number of frames that must be effectively used for the O and T analysis step: N_o^{min} and N_t^{min} .

For this purpose, the real sequence explained in Sec. 4.1.3.1 is used to run the onboard algorithm starting with an increasing number of frames starting from 10 dark frames. For each number of frames, three pixels are chosen as a reference based on their noise fluctuation: one with low noise fluctuation ($< 1\sigma$), one with medium noise fluctuation ($< 2\sigma$), and the last with high noise fluctuation ($> 2\sigma$). For each N dark frames the $O[i][j]$ and $T[i][j]$ values are computed for the three pixels, and are compared with the $O^G[i][j]$ and $T^G[i][j]$ values. Once the onboard offset values (resp. threshold) converge to the ground-computed values ± 3 ADU (which correspond to ~ 80 keV) and start to stabilize at N_o (resp. N_t) frames, this number of frames is considered as the N_o^{min} (resp. N_t^{min}).

Figure 4.7 shows the convergence of onboard offset (resp. threshold) values to the ground-computed values for three pixels with different noise fluctuations. It shows that the offset (resp. threshold) needs at least 70 dark frames (resp. 90 dark frames) to get a reliable result.

These values: $N_o^{min}=70$, and $N_t^{min}=90$ dark frames are set as the default values. The performance of the detector could degrade with time in the space and more frames maybe needed to compute the $O[i][j]$ and $T[i][j]$ maps. Thus, we must keep the possibility to tune

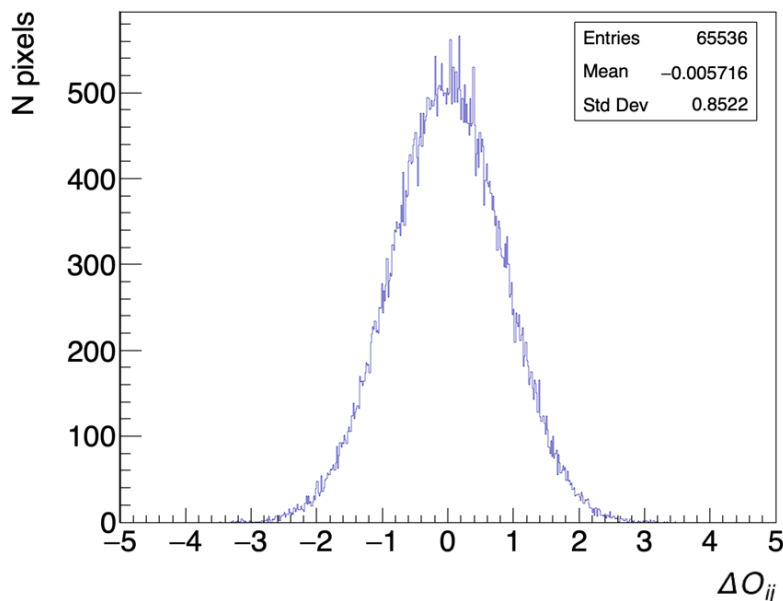


Figure 4.6: The difference of the offset map ΔO_{ij} for 256×256 pixels computed using a simulated dark sequence with no outliers and a dark sequence with the detector exposed to outliers.

N_o^{min} , and N_t^{min} from the ground as explained in Sec. 4.1.2.4

4.1.3.4 Onboard and ground analyses comparison

Any method implemented onboard must compute comparable O and T maps to the ones computed with the ground analysis $O^G[i][j]$ and $T^G[i][j]$. This section presents a comparison between the onboard and the ground algorithms. In this study we used the real sequence explained in Sec. 4.1.3.1. The real sequence is processed using the ground algorithm to compute the O^G and T^G maps. The same sequence is used to compute O and T maps, but only the first 190 frames are used: $N_r = 30$ frames, $N_o = 70$ frames, and $N_t = 90$ frames. The resulting dark maps from both algorithms are compared by computing the ratio of offset (r_o) and threshold (r_t) values for the 256×256 pixels: $r_o[i][j] = O[i][j]/O^G[i][j]$, $r_t[i][j] = T[i][j]/T^G[i][j]$.

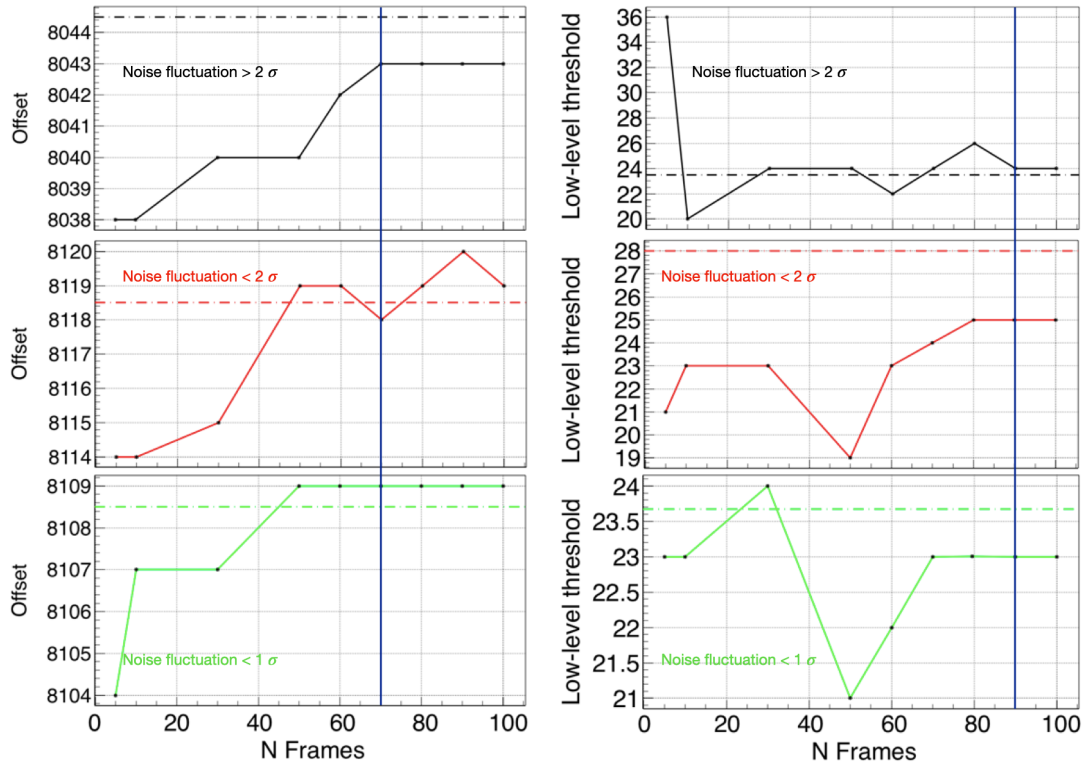


Figure 4.7: The convergence of the onboard offset (left column) and threshold (right column) values to the offline-computed values (dashed lines) as the number of dark frames processed onboard increases. The convergence is tested for three pixels with different noise fluctuations. Bottom: pixel with low noise fluctuation ($< 1\sigma$). Middle: pixel with medium noise fluctuation ($< 2\sigma$). Top: pixel with high noise fluctuation ($> 2\sigma$). It shows that the onboard offset (resp. threshold) converges to the offline-computed values after processing at least 70 frames (resp. 90 frames).

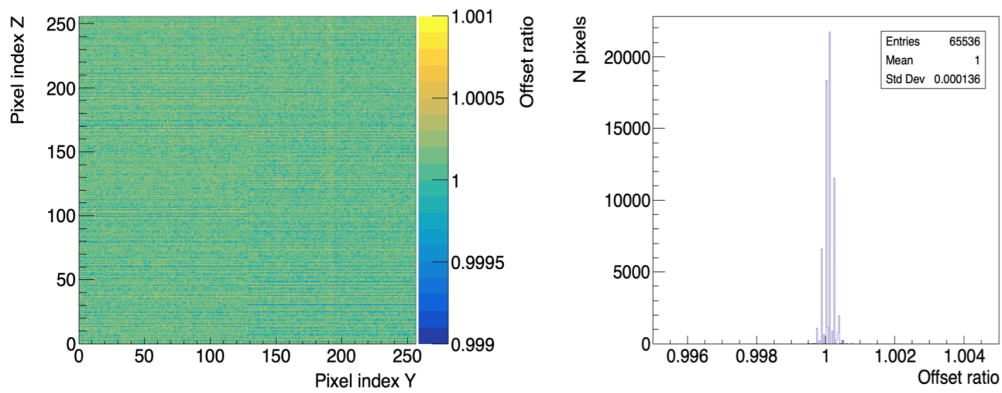


Figure 4.8: The offset map ratio. The ratio ($r_o = O[i][j]/O^G[i][j]$) between both offset maps for each pixel (left). The ratio (r_o) distribution for all pixels (right).

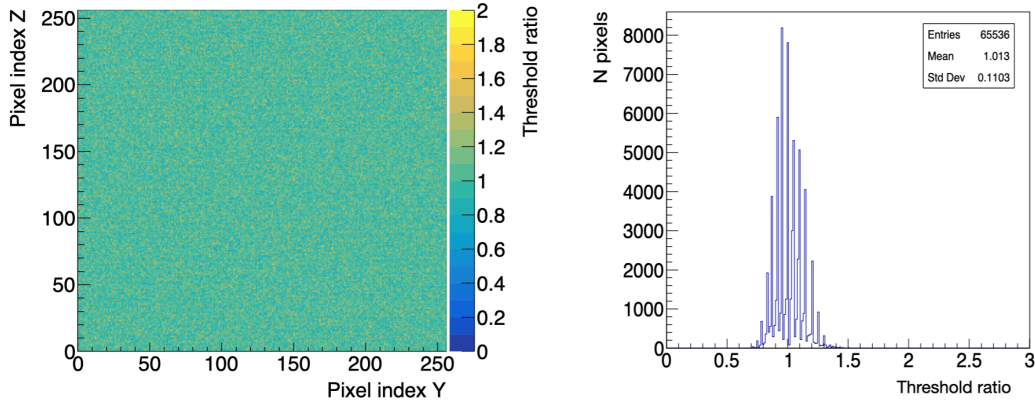


Figure 4.9: The threshold map ratio. The ratio ($r_t = T[i][j]/T^G[i][j]$) between both threshold maps for each pixel (left). The ratio (r_t) distribution for all pixels (right).

Figures 4.8 and 4.9 show the r_o and r_t ratio distributions. The dark maps computed onboard are comparable to the ones computed by the ground algorithm. This is demonstrated by the mean value μ of the ratio distributions, which is about one. For the r_o distribution, $\mu = 1$ with a standard deviation $\sigma = 1.35 \times 10^{-4}$. For the r_t distribution, $\mu = 1.013$ with a standard deviation $\sigma = 1.1 \times 10^{-1}$.

It is worth mentioning that the O^G and T^G are computed by analysing the same 200 frames per each. Meanwhile, the O map computation is performed using 70 frames, and the T map is performed using different 90 frames. Although, the onboard algorithm used less than half number of frames used for the ground analysis, it produced dark maps equivalent to the reference ones.

4.1.3.5 Test the detector spectral response

In this section, I report a work done completely by the camera team at CEA, but I presented for the completeness of the dark algorithm characterization. The dark maps have been used to characterize the spectral parameters of the detector at CEA. This analysis aims at characterizing the spectral resolution of the detector. Better noise characterization ensures the purification of the signal when selecting pixels above noise with Eq. 4.5. Therefore, it gives a better spectral resolution of the detector.

The dark maps O and T computed by the onboard algorithm are uploaded to the memory shared by the FEEM and the SCSW partitions. The detector is exposed to X-rays at a specific energy. The FEEM partition uses the uploaded dark maps to select pixels with amplitude above noise as in Eq. 4.5. The amplitude is converted to energy using the gain map (see Eq. 3.8), and the energy distribution of selected pixels is drawn and fitted. Then the fitted energy E_{ph}^f is compared to the actual injected energy E_{ph}^t . The same process is repeated with uploading the

O_G and T_G maps to select pixels. The test is performed with five X-ray energies (E_{ph}^t): 1.49 keV, 4.51 keV, 5.41 keV, 6.4 keV, and 8.04 keV.

For each E_{ph}^t energy, the spectral response of the detector is characterized by two parameters. The first parameter is the energy scale measured as the difference between the fitted and actual energies: $e_s = E_{ph}^t - E_{ph}^f$. The smallest the energy scale (e_s), the better the spectral response of the detector. The second parameter is the FWHM of the fitted distribution. The smaller FWHM, the better the spectral resolution of the detector.

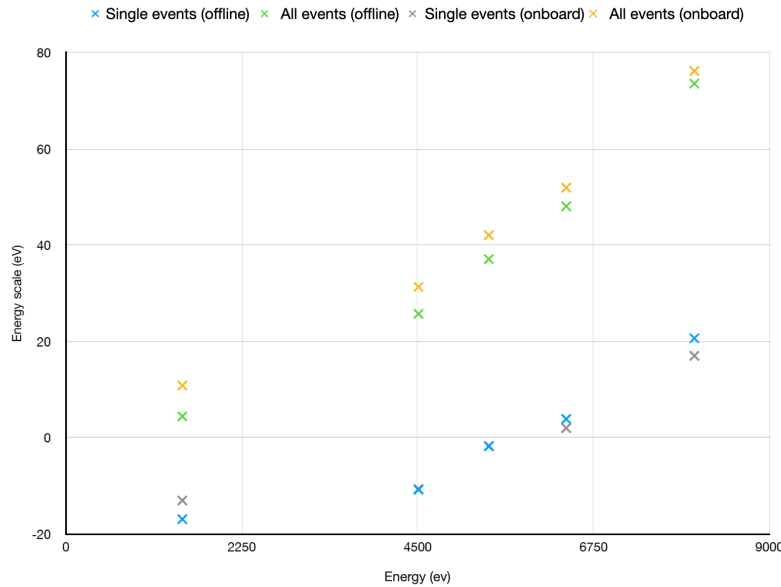


Figure 4.10: The measured energy scale calculated using both the onboard and the ground-computed dark maps as a function of the X-ray sources energy (E_{ph}^t). In each case, the energy scale (e_s) is calculated for single events (blue for the ground maps, gray for the onboard maps) and all events (green for the ground maps, yellow for the onboard maps). The plot shows that using the onboard maps improves the energy scale for single events. In the case of all events, using the dark maps computed with the ground algorithm gives a better energy scale. Credit: CEA.

Figure 4.10 (resp. 4.11) shows a comparison of pixels energy scale (resp. energy FWHM) by using the dark maps computed onboard and with the ground analysis for five different energies. Using the O and T maps improves the energy scale for singles events (photon transfers its energy to one pixel). For example, at 1.45 eV, the onboard algorithm gives an energy scale of 17 eV compared to 20.7 eV for the ground analysis. For all events (photon transfers its energy to one or more pixels), the dark maps computed with the ground analysis improve the energy scale slightly better than the onboard dark maps. However, using the onboard maps gives comparable results of energy scale for all events. Figure 4.10 shows that using the onboard O and T maps to select pixels above noise gives the detector a spectral resolution less than 80 eV at all energies, which complies with the MXT requirements (see Tab. 3.1).

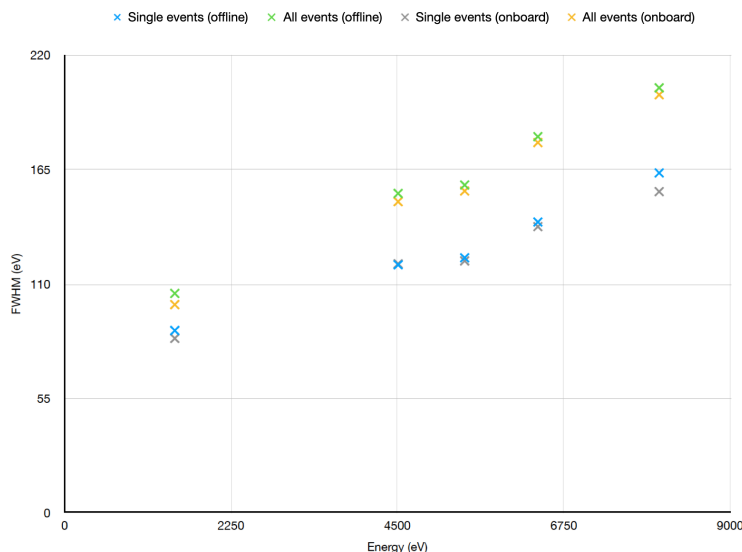


Figure 4.11: The measured energy FWHM as a function of the actual energy. The FWHM is measured after using both the onboard and the ground-computed dark maps. In each case, the FWHM is measured for single events (blue for the ground maps, gray for the onboard maps) and all events (green for the ground maps, yellow for the onboard maps). The plot shows that using the onboard maps improves slightly the energy FWHM. Credit: CEA.

Furthermore, the O and T maps improve the FWHM at all energies, both for single and all events, compared to the O^G and T^G maps. Hence, it improves the spectral response of the detector.

In conclusion, the onboard algorithm proves to be functional, robust against outliers, and compliant with the MXT scientific requirements to compute O and T maps that ensure having a spectral resolution < 80 eV.

Moreover, the O and T maps are comparable to the O^G and T^G , in spite of all the constraints on the science partition. In some cases, the onboard algorithm outperforms the ground algorithm. The main reason is that the ground algorithm computes the threshold using the 84th percentile, which corresponds to the standard deviation (one sigma) for a Gaussian distribution. However, the flat frame (see Eq. 4.3) distribution could be a not perfectly Gaussian. Consequently, the 84th percentile is not a good estimator of the standard deviation. The ground analysis shall be improved and taken into account this issue.

4.2 . Photon identification

The aim of this analysis is to identify the position and energy of X-ray photons in the MXT detector during an observation, where the MXT mode is set to operation/observation. The calibration wheel is set to the open position to allow the photons to interact with the detector. In an observation, we are only interested in pixels that have part of the X-ray photon signal.

Therefore, the FEE is operated in **EVENT** mode, in which the FEE selects pixels with amplitude above the noise level following Eq. 4.5. The transferred pixels amplitudes $A[i][j]$ in ADU must be converted to energy using the gain value $G[i]$, in order to identify the photon energy. The gain measurement is explained in Sec. 4.2.1. The clustering of the transferred pixels is explained in Sec. 4.2.2. Section 4.2.3 explains the reconstruction of the X-ray photons in the MXT detector. The camera images could suffer from defects like noisy pixels and frozen or insensitive columns which could be identified as photons. These deficiencies must be identified and vetoed out as explained in Sec. 4.2.4.

4.2.1 . Energy gain table

The CAMEX measures the detector pixel amplitudes $A_r[i][j]$ in ADU, and the gain G is used to convert the pixel amplitude after the selection $A[i][j]$ from ADU to a physical energy E as in Eq. 3.8. The gain values of all pixels in i column are the same, since the CAMEX reads the detector column by column. Thus, the amplitude of pixel (i, j) is converted to energy as the following

$$E[i][j] = G[i]A[i][j]. \quad (4.12)$$

The gain is estimated on the ground using calibration data collected with the ^{55}Fe radioactive source. Figure 4.12 shows the gain map of the final configuration of the detector measured with low-energy X-ray sources where the MXT has the largest detection effective area.

The calibration data is collected during operation/calibration or during Earth occultation modes, where the calibration wheel position is set to the ^{55}Fe source position. The data are downloaded to the ground to compute the gain, and a gain (G) table of 256 values (1/column) must be provided to the science partition to compute the photon energies onboard.

4.2.2 . Pixel clustering

In this section we use the coordinates and notations explained in Sec. 3.2.

Once the FEE selects pixels following Eq. 4.5 and the FEEM partition transfers them to the scientific partition, the later process all received pixels per images in order to identify X-ray photons. The first step in the image processing is to cluster pixels, i.e., to search for contiguous pixels and group them in a cluster as they probably originate from the same cosmic event. As the scientific partition scans an image, two pixels are clustered together if: $|i_1 - i_2| = 1$ and/or $|j_1 - j_2| = 1$. This condition is applied recursively to all pixels.

Each cluster is identified by three parameters. The first parameter is the number of pixels in the cluster m_c , which defines the cluster multiplicity. The second parameter is the cluster energy E_c . The energy of each pixel (i_k, j_k) in the cluster is obtained using the gain value of the i_k column $G[i_k]$ as in Eq. 4.12. The cluster energy is given by summing the energies of all pixels in the cluster:

$$E_c = \sum_{k=0}^{m_c} G[i_k] \times A[i_k][j_k]. \quad (4.13)$$

The last parameter is the cluster position (y_c, z_c) computed in the camera intrinsic coordinates. The cluster position is estimated using the energy-weighted average of pixel central positions

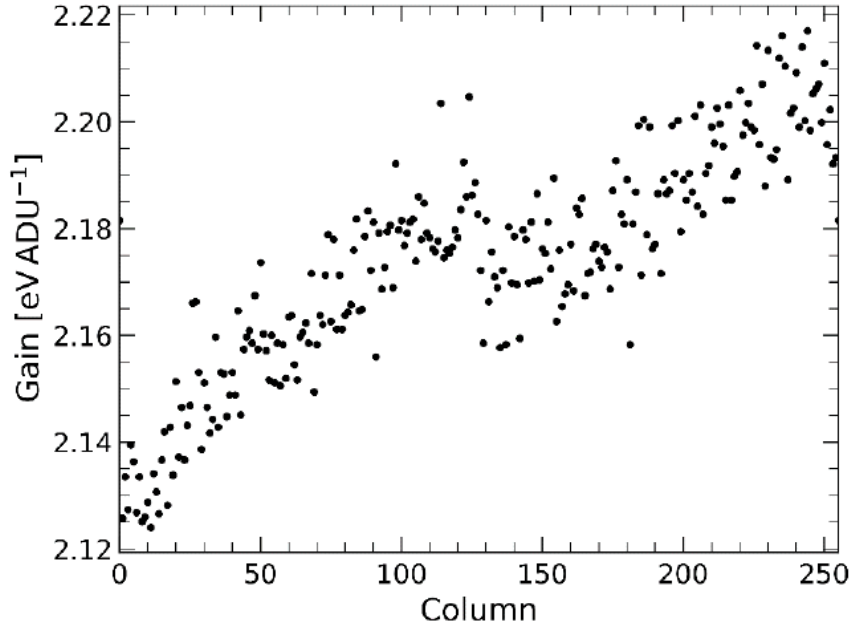


Figure 4.12: The energy gain values for the 256 columns of the MXT detector measured with six low-energy X-ray sources: C-K (0.277 keV), O-K (0.525 keV), Cu-L (0.93 keV), Mg-K (1.253 keV), Al-K (1.486 keV), and W-M (1.774 keV). Credit: CEA

within the cluster:

$$\begin{aligned}
 y_c &= \frac{\sum_{k=0}^{m_c} E[i_k][j_k] \times (i_k + 0.5)}{N \times E_c}, \\
 z_c &= \frac{\sum_{k=0}^{m_c} E[i_k][j_k] \times (j_k + 0.5)}{N \times E_c}.
 \end{aligned}
 \tag{4.14}$$

The maximum number of clusters per image is limited to 2000. The scientific partition rejects an image that contains more than 2000 clusters.

4.2.3 . Photon reconstruction

As X-ray photons interact with the MXT detector via the photoelectric effect, they deposit their energy to one or a few contiguous pixels forming a specific pattern. Figure 4.13 shows the most probable pixel patterns formed by X-ray photons with energy of (0.2 - 10 keV) after applying the noise threshold for each pixel. The number of pixels in each pattern defines the photon multiplicity.

A cluster identified in Sec. 4.2.2 is considered to be a photon if it matches one of the 13 patterns listed in Fig. 4.13, i.e., the cluster multiplicity must be less or equal to 4, the cluster size in the z- and y-directions must be less or equal to 2 without diagonal pixels. Otherwise, the cluster is considered noise and discarded.

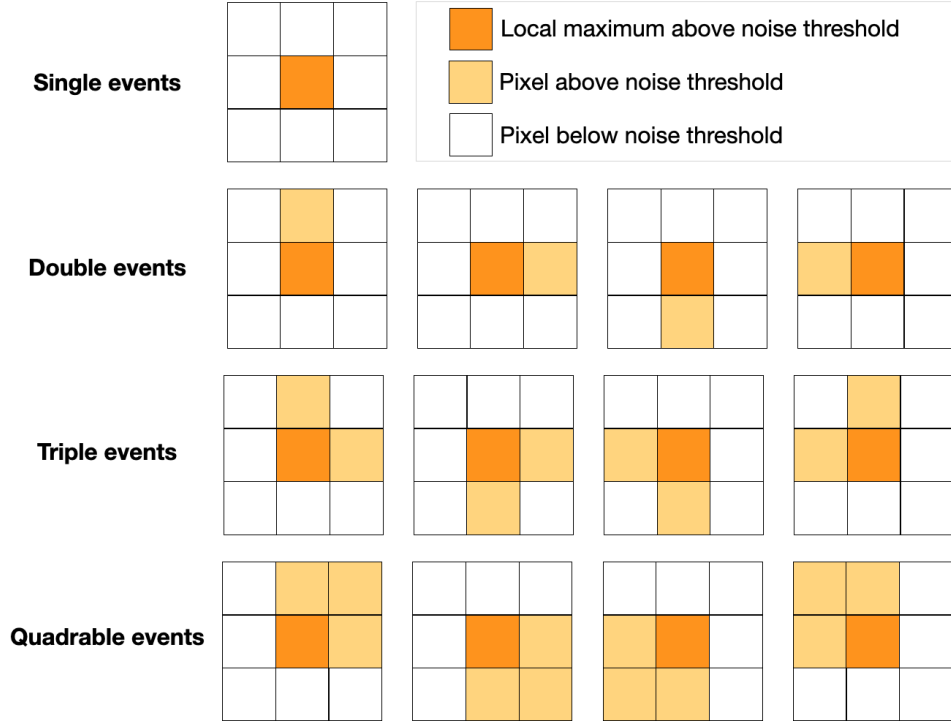


Figure 4.13: Most probable pixel patterns induced by a photon hitting a pnCCD detector. An incoming X-ray photon can transfer its energy to one or more pixels depending on its energy. The bright-orange pixel is the impacted pixel; the light-orange pixels have a fraction of the photon energy above the noise threshold. White pixels have an energy below the noise threshold.

Photons can be selected based on their energy E_{ph} by setting minimum and maximum energies to filter out photons outside this range: $E_{min} < E_{ph} < E_{max}$. E_{min} can take two values, the first one is the ultra violet minimum energy e_{uv} to filter out the straylight. As seen in Sec. 3.3.2, there was an UV filter to limit the straylight, but this filter was broken. Therefore, the science partition must limit the effect of straylight on the scientific process manually, by setting a minimum e_{uv} energy. The e_{uv} energy is selected when the straylight is detected. The second value of the minimum energy is the standard minimum energy (e_{std}) that is selected otherwise.

For some cases, using m_c selected events (for example, single-event) photons could give better results than all-event photons. Therefore, a selection based on the photon multiplicity can also be applied.

Finally, the identified photons are saved in VHF photon packets, that contains the photon energy E_p computed in Eq. 4.13, the photon pixel position (i_p, j_p) that is computed using Eq. 4.14: $i_p = \lfloor y_c \times N + 0.5 \rfloor$, and $j_p = \lfloor z_c \times N + 0.5 \rfloor$. VHF photon packets also contain the photon time t_p , which is the time of the camera image. The VHF photon packets are sent to

the ground for the *core* and *ToO* observations programs (see Sec. 2.3).

Furthermore, the identified photons are accumulated on a two-dimensional map called the photon map $D[i][j]$ that has a size of $\frac{N}{2} \times \frac{N}{2}$. Each (i, j) cell counts the number of photons accumulated inside the cell. Accumulating photons in a map with a resolution equal to 1/4 the resolution of the camera plan has a negligible effect on the scientific algorithm performance, as demonstrated in Sec. 5.2.2. Thus, a lower resolution (*128times128*) version of the photon map is used in the science partition as it is less memory demanding.

Fig. 4.14 shows an example of a photon map that the science partition could construct during an observation. Eight thousand photons are accumulated in this example. The photon distribution (spot and cross arms) is resulting from the MXT lobster-eye optical system (see Sec. 3.3.1).

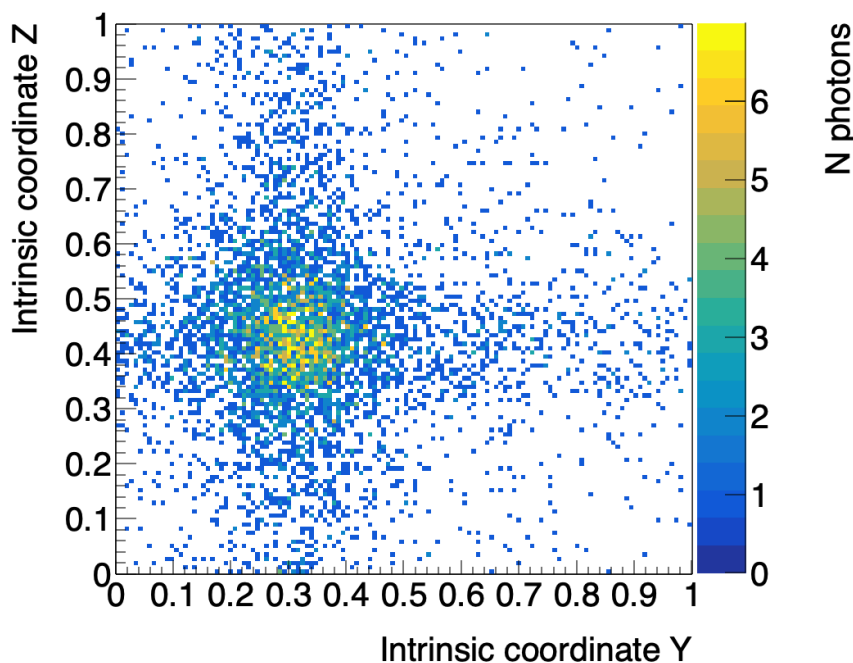


Figure 4.14: Example of a photon map constructed by the science partition with 8000 photons. The photon position in the map is given in intrinsic coordinates: $0 \leq z < 1$ and $0 \leq y < 1$.

The photon map is one of the inputs to perform the localization. However, some identified-photon clusters might not be of a cosmic origin. Instead, it is a noise resulting from noisy pixels or insensitive columns. The photon map must be cleaned from these events before executing the localization algorithm, as explained in the following section.

4.2.4 . Pixel veto and insensitive columns

The objective of this analysis is to identify noisy pixels in the photon map: dead or bright pixels, and veto them. For this purpose, the number of camera hits for each pixel $N_c[i][j]$ during an observation is tracked in a two-dimensional map called the pixel count map. This map is

used to detect noisy pixels before performing the localization algorithm. For each pixel in the count map, the hit rate $R[i][j]$ is computed as the following: $R[i][j] = N_c[i][j]/N_f$, where N_f is the number of frames used to construct the count map. The pixel (i, j) is considered as noisy if $R[i][j] > R_{min}$, and $N_f > N_f^{min}$. Where R_{min} is the minimum rate and N_f^{min} is the minimum number of frames needed to veto noisy pixels.

Once a pixel is identified as noisy, the content of the cells corresponding to this pixel in the photon map is set to zero. Since the photon map has 1/4 the camera pixels resolution, the content of 4 pixels is effectively set to zero.

A whole column (256 pixels) or a bunch of contiguous columns could be noisy or insensitive. These columns are identified on the ground and declared in the configuration table. Three groups of contiguous insensitive columns (bunches) can be declared. Each bunch is parametrized by the number of insensitive columns N_{bad} in the bunch and the index i_b of the first insensitive column in the bunch. The insensitive columns are set to zero in the photon map before performing the localization; as a result, two-pixel columns are effectively deactivated in the photon map. Insensitive columns have a consequence on the localization performance, and this effect must be evaluated and corrected. The insensitive columns effect is characterized in Sec. 5.2.4.

4.2.5 . Monitoring and configuration of photons identification

To verify that all the analyses explained in the previous sections are running as expected, the science partition computes monitoring data and send them to the ground via recurrent VHF packets. The science partition computes:

- Number of processed camera frames in the clustering analysis
- Number of rejected frames (>2000 clusters) in the clustering analysis
- Total number of clustered pixels
- Total number of clusters identified as photons
- Total number of photons with $E_p < E_{max}$
- Total number of photons with $E_p < E_{max}$ and $E_p > E_{min}$
- Total number of photons with $E_p < E_{max}$, $E_p > E_{min}$, and multiplicity (m_c) selection.
- Number of vetoed cells (=4 pixels) in the photon map.

The list of parameters that are provided to the science partition via the configuration table are given by Tab. 4.2

Table 4.2: List of parameters (12 parameters) needed for the photon identification analysis. The parameters are evaluated on the ground and uploaded with the configuration table to the science partition.

Notation	Description	Default value
e_{std}	Photon selection: standard minimum energy [eV]	160
e_{uv}	Photon selection: ultra-violet minimum energy [eV]	200
e_{max}	Photon selection: maximum energy [eV]	60000 (no selection)
m_{sel}	Photon selection: pixel multiplicity	30 (no selection)
R_{min}	Minimum counting rate to veto a noisy pixel (in percentage of frames)	95 (no veto)
N_f^{min}	Minimum number of frames to apply the pixel veto	0 (no veto)
$b_{bad}[0]$	Bin start index for the first bunch of bad columns	0 (no bad columns)
$N_{bad}[0]$	Number of bad bins for the first bunch of bad columns	0 (no bad columns)
$b_{bad}[1]$	Bin start index for the second bunch of bad columns	0 (no bad columns)
$N_{bad}[1]$	Number of bad bins for the second bunch of bad columns	0 (no bad columns)
$b_{bad}[2]$	Bin start index for the third bunch of bad columns	0 (no bad columns)
$N_{bad}[2]$	Number of bad bins for the second bunch of bad columns	0 (no bad columns)

5 - Source localization in real time with the MXT

Contents

4.1	The MXT dark algorithm	92
4.1.1	Ground dark algorithm	93
4.1.2	Onboard dark algorithm	94
4.1.3	Results and characterization	98
4.2	Photon identification	105
4.2.1	Energy gain table	106
4.2.2	Pixel clustering	106
4.2.3	Photon reconstruction	107
4.2.4	Pixel veto and insensitive columns	109
4.2.5	Monitoring and configuration of photons identification	110

In its *core* program, SVOM seeks to observe GRBs and determine their precise sky location in real-time. The MXT is responsible for the GRB localization precisely by detecting the afterglow in the soft X-ray range. Therefore, a dedicated algorithm must be implemented in the scientific partition to process the camera data in real-time and fulfill the MXT scientific requirement of localizing GRBs with accuracy down to $2'$ in a few minutes after the GRB trigger. The onboard localization algorithm highly depends on the geometry of the MXT, particularly the camera and the optics. In short, the photon map, introduced in Sec. 4.2.3, is cross-correlated with the PSF model to search for the source peak position.

This chapter describes the onboard localization algorithm and the challenges we faced during the implementation. The localization algorithm is discussed in Sec. 5.1. The characterization and results of the localization algorithm are explained in Sec. 5.2. Section 5.3 shows the Panter test of the final flight configuration of the MXT and the results of the test.

5.1 . Source localization method

With the MXT field of view of 58×58 arc min², and a sensitivity of 2×10^{-10} erg cm⁻² s⁻¹ in 10s and 4×10^{-12} erg cm⁻² s⁻¹ in 10⁴ s, we expect to have 3 X-ray sources at maximum in the MXT field of view. Thus, the localization algorithm delivers the source sky location in spherical coordinates (θ, ϕ) , for the three brightest X-ray sources in the field of view. In addition, the algorithm must compute the photon counts S , the signal-to-noise ratio ρ , and the position uncertainty r_{90} for each of the three sources. This information is packaged in VHF telemetry packets that are sent to the ground every 30 s to follow up the sources.

The onboard localization algorithm runs in the operation/observation mode periodically and continuously. The science partition checks if there is a running localization algorithm. If

not, the localization algorithm is scheduled, i.e., it is run as a background task whenever some time is spared. Therefore the duration of a localization analysis can vary depending on how much time is available. When the localization analysis is completed, a new analysis is scheduled if the conditions above remain valid.

The localization algorithm is based on the cross-correlation of the photon map presented in Sec. 4.2.3 with the PSF model. This method has been implemented onboard because it provides better localization accuracy for faint sources, in contrast to the simplistic barycenter (centroid) approach. Furthermore, one can take advantage of the specific MXT's optics geometry, for which the cross-arms pattern can guide the search for the source peak position.

In order to include the PSF model in the algorithm, it must be prepared first on the ground. The PSF model processing is described in Sec. 5.1.1. Section 5.1.2 lays out the implementation steps of the cross-correlation onboard and its mathematical formalism. In Sec. 5.1.3, the cross-correlation data is processed to search for local maxima and then compute the source position angles. Section 5.1.4 shows the signal-to-noise ratio computation for the localized sources. Finally, 5.1.5 shows how the localization algorithm is extended to localize multiple sources in the MXT field of view. In addition, during the localization, the science partition must be monitored and configured from the ground. The monitoring and configuration parameters are explained in Sec. 5.1.6

5.1.1 . The point spread function formatting

The dependency of the PSF on the incoming photon energy is very small. Thus, the PSF can be measured and modeled by a discrete two-dimensional function $P[i][j]$ measuring the hit position probability of an incoming photon and covering twice the camera plane size, $0 \leq i < 2N$ and $0 \leq j < 2N$ (see Sec. 3.3.1).

In order to use the PSF in the cross-correlation algorithm, it must be re-binned by a factor 2, to be double size of the photon map such that i and j run from 0 to $N - 1$. Moreover the PSF is normalized as the following:

$$\sum_{i=0}^{N-1} \sum_{j=0}^{N-1} P[i][j] = 1. \quad (5.1)$$

In addition, the PSF is Fourier-transformed, and one out of two Fourier coefficients is uploaded to the science partition as it is demonstrated in the following section. This treatment for the PSF is performed on the ground before uploading the PSF table to the science partition.

5.1.2 . Cross-correlation

The photon map D of size $N/2 \times N/2$ (see Sec. 4.2.3) is cross-correlated with the PSF function P of size $N \times N$ that is prepared on the ground and uploaded to the science partition (see Sec. 5.1.1). For simplicity and clarity of the mathematical notations, each function's size is added as a subscript in the following. For example, the photon map is noted as $D_{N/2}$, and the PSF as P_N .

The cross-correlation is computed by the following equation and is visualized in Fig. 5.1:

$$C_{N/2}[i][j] = \sum_{i'=0}^{N/2-1} \sum_{j'=0}^{N/2-1} D_{N/2}[i+i'][j+j'] \times P_N[i'][j']. \quad (5.2)$$

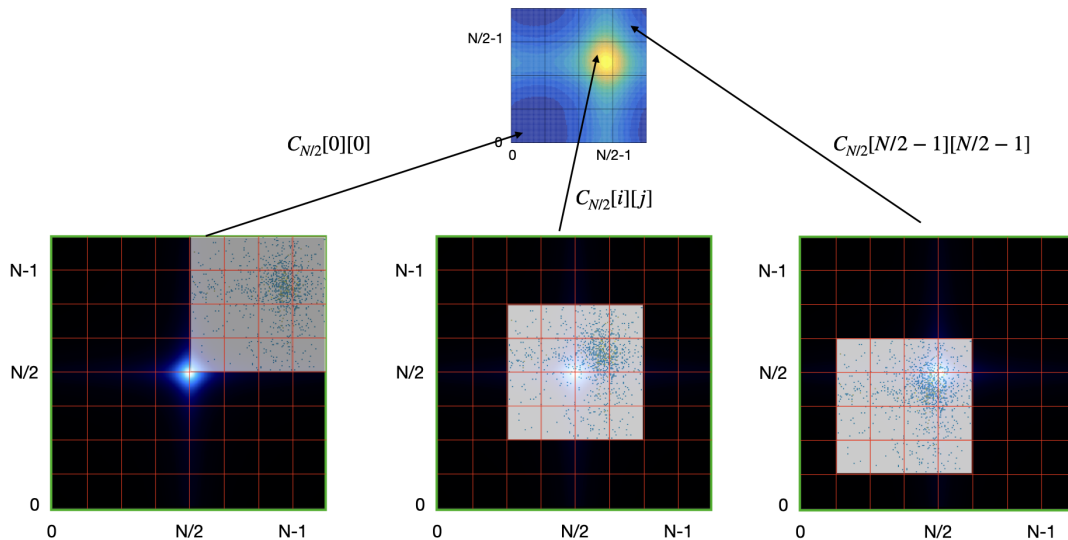


Figure 5.1: Example of the construction of the correlation matrix of a 4×4 photon map with a 8×8 PSF to produce a 4×4 correlation matrix.

In Fig. 5.1, the initial position of the photon map is set to be aligned with the cross-correlation map so that the peak of the photon map is found at the same location in the cross-correlation map. The photon map is slid over the PSF map, and, for each shift, the cross-correlation coefficients are obtained by summing N^2 elements in the green square in Fig. 5.1. In Eq. 5.2 the $D_{N/2}$ indices could be out-of-range. However, for finite discrete functions a circular periodicity is assumed such that: $(i+i') \pmod{N/2}$ and $(j+j') \pmod{N/2}$. As a consequence, $D_{N/2}$ in Eq. 5.2 is summed four times as it is half of the size of the PSF in both y- and z-directions. For simplicity, the out-of-range issues are not addressed in the notations in the following.

The cross-correlation function measures the degree of match between the two input maps for a given shift. Hence, the highest value in the cross-correlation map can then be used as a direct estimate of the source location, as discussed in Sec. 5.1.3.

The cross-correlation computed in Eq. 5.2 is computationally expensive, contrasting with the science partition constraint. Alternatively, one can compute the cross-correlation in the Fourier space. Therefore a discrete Fourier transform is implemented in the science partition using a radix-2 decimation-in-frequency algorithm [191]. The Fourier transform of the two-dimensional discrete function $X_{N/2}$ is defined by the following equation:

$$\tilde{X}_{N/2}[k][l] = \frac{4}{N^2} \sum_{i=0}^{(N/2-1)} \sum_{j=0}^{(N/2-1)} X_{N/2}[i][j] \times e^{-4\sqrt{-1}\pi(ik+jl)/N}. \quad (5.3)$$

Using Eq. 5.3, the Fourier transform of the cross-correlation in Eq. 5.2 is given by the following:

$$\tilde{C}_{N/2}[k][l] = \frac{4}{N^2} \sum_{i=0}^{(N/2-1)} \sum_{j=0}^{(N/2-1)} \sum_{i'=0}^{(N-1)} \sum_{j'=0}^{(N-1)} D_{N/2}[i+i'][j+j'] P_N[i'][j'] \times e^{-4\sqrt{-1}\pi(ik+jl)/N}. \quad (5.4)$$

By substituting m for $(i+i')$ and n for $(j+j')$, one can factorize the sum and the exponential as the following:

$$\tilde{C}[k][l] = \frac{4}{N^2} \sum_{i'=0}^{(N/2-1)} \sum_{j'=0}^{(N/2-1)} P_N[i'][j'] \times e^{+2\sqrt{-1}\pi(2i'k+2j'l)/N} \quad (5.5)$$

$$\sum_{m=i'}^{(N/2-1+i')} \sum_{n=j'}^{(N/2-1+j')} D_{N/2}[m][n] \times e^{-4\sqrt{-1}\pi(mk+nl)/N}. \quad (5.6)$$

The first double sum is the complex conjugate of the Fourier transform of P_N , where every other coefficient is selected. In the second sum, the exponential and $D_{N/2}$ are periodic functions of m and n , so applying an offset of i' and j' does not change the result, and Eq. 5.6 can be rewritten as the following:

$$\begin{aligned} \tilde{C}[k][l] &= N^2 \tilde{P}_N^*[2k][2l] \times \frac{4}{N^2} \sum_{m=0}^{(N/2-1)} \sum_{n=0}^{(N/2-1)} D_{N/2}[m][n] \times e^{-4\sqrt{-1}\pi(mk+nl)/N}. \\ &= N^2 \tilde{P}_N^*[2k][2l] \times \tilde{D}_{N/2}[k][l] \end{aligned} \quad (5.7)$$

The cross-correlation map is obtained by applying the inverse Fourier transform of Eq. 5.7:

$$C_{N/2}[i][j] = \sum_{k=0}^{N/2-1} \sum_{l=0}^{N/2-1} N^2 \tilde{P}_N^*[2k][2l] \times \tilde{D}_{N/2}[k][l] \times e^{+4\sqrt{-1}\pi(ik+jl)/N}. \quad (5.8)$$

Equation 5.8 is the result of the correlation theorem [192], demonstrating that the cross-correlation of two functions is equivalent to a complex conjugate multiplication of their Fourier transforms. The cross-correlation is calculated onboard using Eq. 5.8, where the PSF is Fourier-transformed on the ground. The implementation steps of the cross-correlation onboard is illustrated in Fig. 5.2.

In summary, the first step in the cross-correlation implementation is to Fourier-transform the processed PSF in Sec. 5.1.1 using Eq. 5.3. One Fourier coefficient over two is selected to be

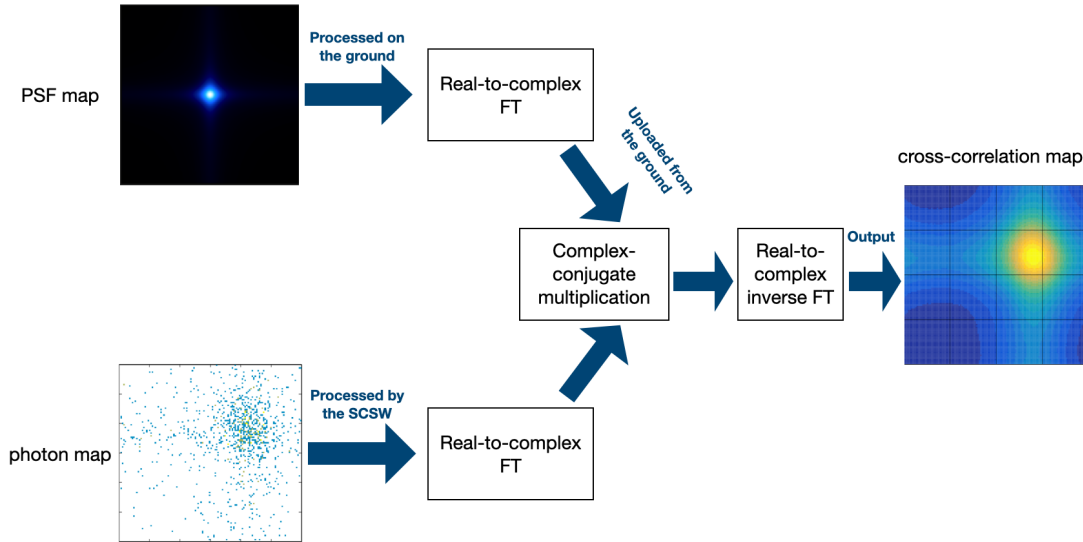


Figure 5.2: The implementation steps of the cross-correlation algorithm onboard.

uploaded to the science partition; as a result, a PSF table of size $N/2 \times N/2$ is uploaded. The photon map $D_{N/2}$ is Fourier-transformed onboard following Eq. 5.3. The Fourier coefficients of the photon map are multiplied with the complex conjugate of the PSF Fourier coefficients. The last step is to apply the inverse Fourier transform, as shown in Fig. 5.2, to get the cross-correlation map.

The advantage of computing the cross-correlation in the Fourier space is the reduction of the calculation complexity, and so reducing the memory and time needed to perform the calculation. The science partition takes ~ 2 s to perform the entire localization analysis. However, the cross-correlation computed onboard suffers from two systematic biases, which must be corrected. The first bias arises from the use of a PSF twice the size the photon map. Therefore, the photon map must be shifted by half of a sample ($2/N$) in both directions to be aligned with the PSF map, as seen in Fig. 5.1. As a result, the cross-correlation map is also shifted by half of a sample. This bias is removed by removing an offset of half of a sample in the y- and z-directions. The second bias is the result of an effect called spectral leakage due to the assumption of circular indices. This bias appears to be significant when the source is near the edge of the MXT field of view. Several simulations are performed to measure and correct this effect as discussed in Sec. 5.2.3.

5.1.3 . Source position angles

Once the cross-correlation map $C_{N/2}[i][j]$ is computed as explained in Sec. 5.1.2, the map is scanned to search for the peak associated with the X-ray source. The first step is to get the

(i_M, j_M) cell that contains the global maximum value $C[i_M][j_M]$ in the cross-correlation map. Afterward a square window is centered on this maximum, such that $i_M - N_w \leq i \leq i_M + N_w$ and $j_M - N_w \leq j \leq j_M + N_w$, where N_w is the half-size of the window. N_w must be chosen such that the central spot of the PSF is fully included inside the window. If the window overlaps the edges of the cross-correlation map, circular periodicity is used as explained in Sec. 5.1.2.

The peak position of the X-ray source (y_1, z_1) is finally computed as a two-dimensional barycenter inside the window:

$$y_1 = \frac{\sum_{i,j} C_{N/2}[i][j] \times (i + 0.5)}{(N/2) \times \sum_{i,j} C_{N/2}[i][j]}, \quad \text{and} \quad z_1 = \frac{\sum_{i,j} C_{N/2}[i][j] \times (j + 0.5)}{(N/2) \times \sum_{i,j} C_{N/2}[i][j]}. \quad (5.9)$$

The sums runs over indices (i, j) inside the window and where the cross-correlation coefficients take significant values: $C[i][j] > \alpha \times C[i_1][j_1]$. By default, $\alpha = 0.9$.

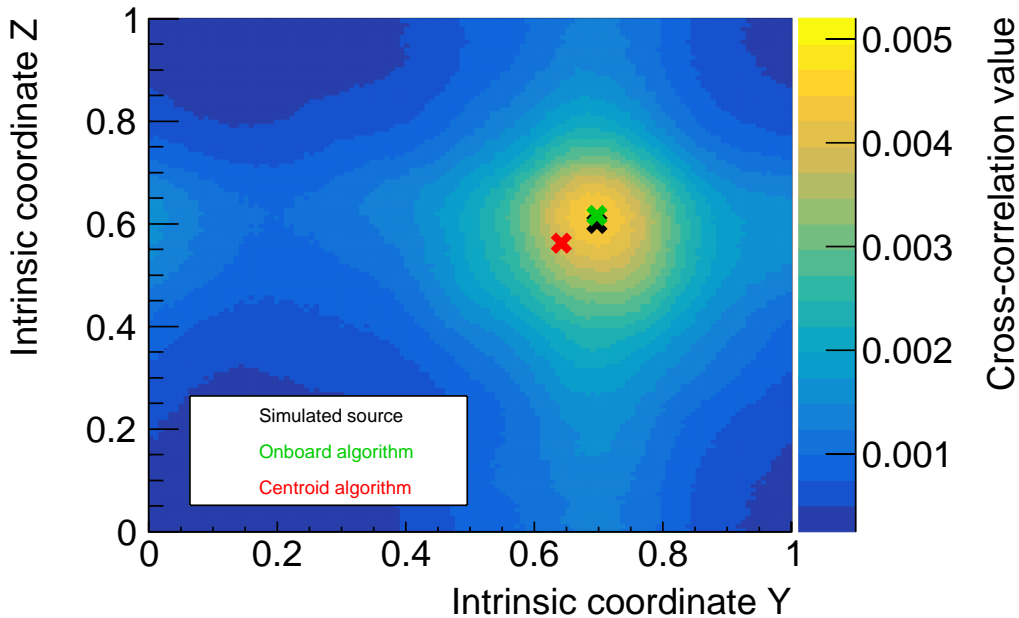


Figure 5.3: Example of a cross-correlation map between the PSF and a simulated photon map with 77 photons. The peak position is computed using the onboard algorithm (green cross) and a simple barycenter (red cross). The source true position is indicated by a black cross.

An example of a cross-correlation map computed with the onboard algorithm is shown in Fig. 5.3. The map is the result of correlating the PSF with a simulated photon map with a low number of photons (77 photons). The peak position labeled with the green cross is localized with the onboard algorithm and compared to the source true position indicated with a black cross. For comparison, the source is also localized with the centroid method over the entire photon map. The derived position is labeled with the red cross in the figure. The figure shows the advantage of the onboard algorithm over the centroid method for MXT. The source position offset ($\delta r = \sqrt{\delta y^2 + \delta z^2}$) obtained with the onboard algorithm is $\delta r = 38$ arcsec, while

$\delta r = 238$ arcsec as computed by the centroid method. Note that δr is computed in intrinsic coordinates, and then it is converted to arcsec as explained in Sec. 3.2.

As mentioned in Sec. 5.1.2, the cross-correlation map suffers from two biases. The first bias is the alignment asymmetry between the photon map and the PSF. This bias is corrected by applying a shift of half of a bin. The second bias is caused by the Fourier transform spectral leakage. To account for this effect, *ad hoc* corrections are applied: $\eta_1(y)$ and $\eta_2(z)$ are introduced to correct for the bias in both y - and z -directions. $\eta_1(y)$ and $\eta_2(z)$ are characterized and evaluated in Sec. 5.2.3. Hence, the source peak position (y_1, z_1) computed in Eq. 5.9 is corrected as the following:

$$y'_1 = y_1 - \eta_1(y_1) - \zeta(y_1) - \frac{1}{N}, \quad \text{and} \quad z'_1 = z_1 - \eta_2(z_1) - \frac{1}{N}, \quad (5.10)$$

where $\zeta(y_1)$ is a correction applied to remove the insensitive columns effect as it will be explained in Sec. 5.2.4.

Finally, the source position (y'_1, z'_1) is converted to spherical angles (θ, ϕ) using Eq. 3.1:

$$\begin{aligned} \theta &= \tan^{-1} \left(\frac{L}{F} \times \sqrt{(y'_1 - 0.5)^2 + (z'_1 - 0.5)^2} \right), \\ \phi &= \tan^{-1} \left(\frac{z'_1 - 0.5}{y'_1 - 0.5} \right). \end{aligned} \quad (5.11)$$

Figure 3.3 shows the system of coordinates for the MXT camera plane and the source in the field of view.

5.1.4 . Signal-to-noise ratio

The objective of this analysis step is to estimate the source signal S_1 and the background noise B_1 counts in the detector. Once S_1 and B_1 are estimated the signal-to-noise ratio ρ_1 is derived as: $\rho_1 = \frac{S_1}{\sqrt{B_1}}$. More than one method was tested for the onboard algorithm. In the following, the advantage and the limitation of each method are explained.

There are two main sources of the background noise in the detector: X-ray photons from the X-ray cosmic background, and the left over intrinsic noise after the pixel selection with Eq. 4.5. We assume that the background counts are distributed uniformly in the MXT detector.

5.1.4.1 Method 1: using the photon map

One can think about identifying an isolated region where the effect from the source is neglected to count the background counts and take a region around the source peak to estimate the signal + background component. However, this method is limited. For example, in the case of multiple-sources detection, it is challenging to find an isolated region to count the background and the signal of each source due to the PSF peculiar shape. Figure. 5.4 shows an example of a simulated photon map resulting from detecting three bright sources, demonstrating the difficulty in finding isolated regions. Furthermore, in the case of a faint source, this method would have a high statistical error due to the low statistics.

Due to the limitations mentioned above, this method was not selected.

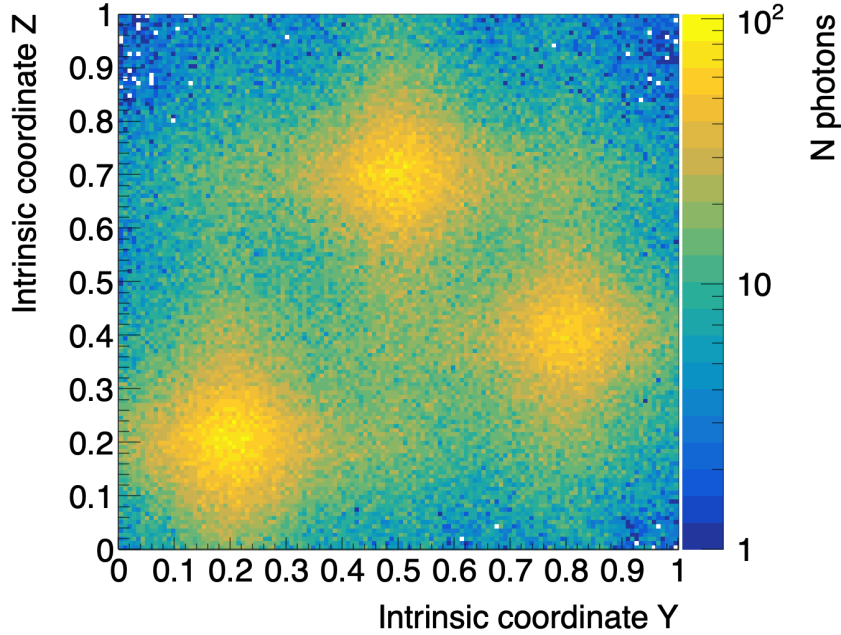


Figure 5.4: An example of a photon map constructed by simulating the detection of three bright sources. The plot shows that it is not trivial to identify regions with only a background or identify a region around a source without a contribution from another source.

5.1.4.2 Method 2: using the cross-correlation map

Instead of using the photon map to estimate S_1 and B_1 , one can use the cross-correlation map computed in Sec. 5.1.2. Each cross-correlation coefficient integrates the background and the signal counts over the entire detector plane.

The photon map $D[i][j]$ can be decomposed into a signal component s and a background component b , then Eq. 5.2 is written as:

$$\begin{aligned}
 C_{N/2}[i][j] &= \sum_{i'=0}^{N-1} \sum_{j'=0}^{N-1} (s[i+i'][j+j'] \times P_N[i'][j']) \\
 &+ \sum_{i'=0}^{N-1} \sum_{j'=0}^{N-1} (b[i+i'][j+j'] \times P_N[i'][j']). \quad (5.12)
 \end{aligned}$$

To solve this equation, for s , and b , two points are taken into account: the (i_m, j_m) cell that contains the minimum cross-correlation value. And the (i_1, j_1) cell that contains the cross-correlation peak value. At (i_m, j_m) cell, the signal contribution $s[i_m+i'][j_m+j']$ is maximum where the PSF $P[i'][j']$ is minimum, and *vice versa*. Thus, the signal contribution to the (i_m, j_m) cell is weak and is noted by ε_S . In addition, we assume that the noise in the detector

is distributed uniformly in the entire detector plane such that: $b[i][j] = b$. With these two hypotheses, Eq. 5.12 can be written at (i_m, j_m) as:

$$C_{N/2}[i_m][j_m] = \varepsilon_S + b \times \sum_{i'=0}^{N-1} \sum_{j'=0}^{N-1} P[i'][j'], \quad (5.13)$$

The double sum is equal to 1 (see Eq. 5.1), and assuming the source contribution is negligible $\varepsilon_S \approx 0$, Eq. 5.13 becomes:

$$C[i_m][j_m] = b. \quad (5.14)$$

The minimum cross-correlation value is a direct estimator of the noise level in each pixel. The cross-correlation value at (i_1, j_1) is given by:

$$C_{N/2}[i_1][j_1] = \sum_{i'=0}^{N-1} \sum_{j'=0}^{N-1} s[i_1 + i'][j_1 + j'] \times P[i'][j'] + b, \quad (5.15)$$

where Eq. 5.1 is used. The double sum in Eq. 5.15 is four times the expectation value for the source signal per cell in the whole detector $\sim 4 \times \langle s_1 \rangle$ since the signal is summed four times as explained in Sec. 5.1.2. Therefore, using Eqs. 5.14 and 5.15, the signal count is estimated as the following:

$$\hat{S}_1 = N^2 \times \frac{(C[i_1][j_1] - C[i_m][j_m])}{4}. \quad (5.16)$$

Using Eqs. 5.14 and 5.16, ρ then can be estimated as the following:

$$\rho = \frac{\hat{S}_1}{\sqrt{N^2 \times b}} \quad (5.17)$$

$$= \frac{N \times (C[i_1][j_1] - C[i_m][j_m])}{4 \times \sqrt{C[i_m][j_m]}}. \quad (5.18)$$

This method is fast and requires using only two cross-correlation values: the minimum and the peak values. However, the assumption of the $\varepsilon_S = 0$ is not absolutely true, and it can be applied in the case of a faint source. Nevertheless, in the case of brighter sources $\varepsilon_S \neq 0$, consequently, the background is over-estimated, and the source signal and the signal-to-noise ratio are under-estimated, as shown in Sec. 5.2.6. Moreover, the estimation accuracy degrades in the case of a multi-source detection since sources contribution to the minimum value increases and can not be neglected. This method was the first method implemented in the partition, but it has been replaced by an improved version, as it is explained in the following section.

5.1.4.3 Method 3: the cross-correlation and auto-correlation maps

As for method 2, this method relies on the cross-correlation map computed by Eq. 5.8. In addition, it uses the PSF auto-correlation that is explained in the following.

The PSF auto-correlation

The auto-correlation $W[i][j]$ of the PSF table is computed in the Fourier space using the cross-correlation definition in Eq. 5.7. As explained in Sec. 5.1.2, the PSF is Fourier transformed and decimated on the ground such that only one Fourier coefficient over two is retained. Consequently, part of the PSF information is missing onboard. If we inverse transform the decimated PSF that is uploaded to the science partition, we get:

$$P_{N/2} = P_N[i][j] + P_N[i][N/2 + j] + P_N[N/2 + i][j] + P_N[N/2 + i][N/2 + j], \quad (5.19)$$

where P_N is the original PSF. Equation 5.19 is given in the Fourier space by:

$$\tilde{P}_{N/2}[k][l] = 4 \times \tilde{P}_N[2k][2l]. \quad (5.20)$$

The decimated PSF computed by Eq. 5.19 combines the four-quarter regions of the total PSF P_N , and it is shown in the left plot of Fig. 5.5. The fact that we do not have the total PSF onboard does not impact the cross-correlation and the localization, as has been proved in Sec. 5.1.2. However, it has an impact on the auto-correlation of the PSF. In fact, we perform onboard the auto-correlation of the decimated PSF, not the original PSF. The auto-correlation is performed in the Fourier space by the following equation:

$$\tilde{W}_{N/2}[i][j] = 4N^2 \tilde{P}_N^*[2k][2l] \times \tilde{P}_N[2k][2l]. \quad (5.21)$$

Finally, the auto-correlation map is obtained with the inverse Fourier transform of Eq. 5.21:

$$W_{N/2}[i][j] = \sum_{k=0}^{N/2-1} \sum_{l=0}^{N/2-1} 4N^2 \tilde{P}_N^*[2k][2l] \times \tilde{P}_N[2k][2l] \times e^{+4\sqrt{-1}\pi(ik+jl)/N}. \quad (5.22)$$

Where $\tilde{P}_N[2k][2l]$ is the Fourier transform of the decimated PSF that is uploaded from the ground (see Sec. 5.1). The auto-correlation map computed by Eq. 5.22 is represented in the right plot of Fig. 5.5.

The auto-correlation $W_{N/2}$ is computed only once a new PSF table is uploaded to the science partition. It is used to measure the source signal S_1 , and the background counts B , as explained in the following section. Moreover, it is used to localize multiple sources, as we will discuss in Sec. 5.1.5.

Signal and background counts

As mentioned in Sec. 5.1.4.2, the background B is uniformly distributed in the detector plane. Thus, the background count at (i, j) in the photon map is given by:

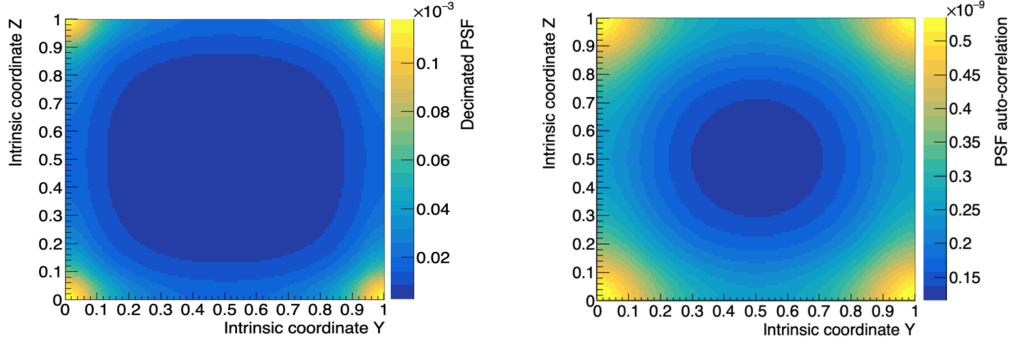


Figure 5.5: The inverse Fourier transform of the decimated PSF (left). An example of the PSF auto-correlation map, computed with the onboard algorithm using the Fourier-transformed and the decimated PSF on the ground (right).

$$b[i][j] = \frac{4B}{N^2}. \quad (5.23)$$

The source signal distribution s_1 in the photon map of size $N^2/4$ is driven by the PSF centred on the source peak position (i_1, j_1) :

$$s_1[i][j] = S_1 \times \frac{P_N[N/2 + i - i_1][N/2 + j - j_1]}{\sum_{i'=0}^{N/2-1} \sum_{j'=0}^{N/2-1} P_N[N/2 + i' - i_1][N/2 + j' - j_1]}. \quad (5.24)$$

Let us note β for the function in the denominator of Eq. 5.24:

$$\beta[i_1][j_1] = \sum_{i'=0}^{N/2-1} \sum_{j'=0}^{N/2-1} P_N[N/2 + i' - i_1][N/2 + j' - j_1]. \quad (5.25)$$

The s_1 distribution in Eq. 5.24 can be splitted into four parts centred on (i_1, j_1) as seen in Fig. 5.6. The decimated PSF in Eq. 5.19 is used to find the distribution in each part as the following:

$$s_1[i][j] = \frac{S_1}{\beta[i_1][j_1]} \begin{cases} P_{N/2}[i + N/2 - i_1][j + N/2 - j_1] - \varepsilon_1[i][j] & i < i' \text{ and } j < j', \\ P_{N/2}[i + N/2 - i_1][j - j_1] - \varepsilon_1[i][j] & i < i' \text{ and } j \geq j', \\ P_{N/2}[i - i_1][j + N/2 - j_1] - \varepsilon_1[i][j] & i \geq i' \text{ and } j < j', \\ P_{N/2}[i - i_1][j - j_1] - \varepsilon_1[i][j] & i \geq i' \text{ and } j \geq j'. \end{cases} \quad (5.26)$$

Since the $P_{N/2}$ function is $N/2$ -periodic, Eq. 5.26 can be rewritten as the following:

$$s_1[i][j] = \frac{S_1}{\beta[i_1][j_1]} \times (P_{N/2}[i - i_1][j - j_1] - \varepsilon_1[i][j]). \quad (5.27)$$

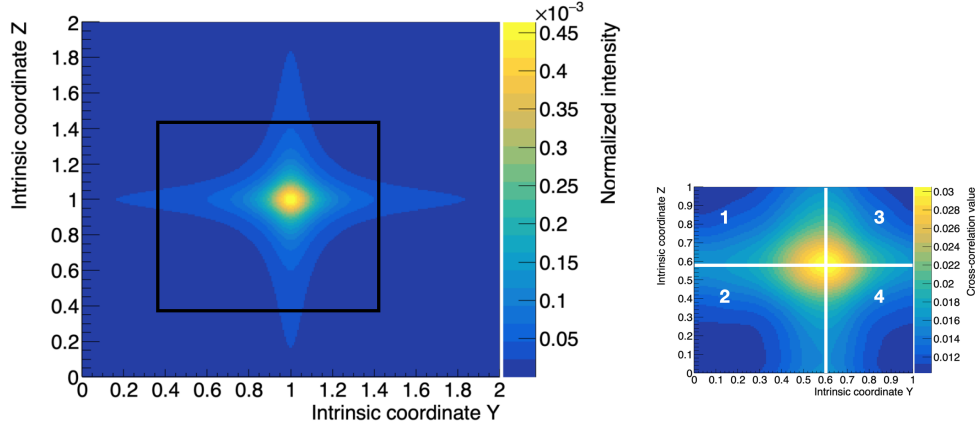


Figure 5.6: The PSF function (left), with a black square represent the camera. The cross-correlation map (right) divided into four quarters centred on (i_1, j_1) .

The ε_1 is a matrix which accounts for the parts of $P_{N/2}$ that are not included in the s_1 distribution. This matrix is seen in Fig. 5.6 outside the black square in the left-side plot. The source distribution s_1 is given in the Fourier space by:

$$\begin{aligned}\tilde{s}_1[k][l] &= \frac{S_1}{\beta[i_1][j_1]} \times (e^{-4\sqrt{-1}\pi(i_1k+j_1l)/N} \times \tilde{P}_{N/2}[k][l] - \tilde{\varepsilon}_1[k][l]) \\ &= \frac{S_1}{\beta[i_1][j_1]} \times (4 \times e^{-4\sqrt{-1}\pi(i_1k+j_1l)/N} \times \tilde{P}_N[2k][2l] - \tilde{\varepsilon}_1[k][l]),\end{aligned}\quad (5.28)$$

where Eq. 5.20 was used.

This method uses the cross-correlation map to estimate S_1 and B . If we consider the cross-correlation in Eq. 5.12, and apply a Fourier transform we get:

$$\tilde{C}_{N/2}[k][l] = N^2 \tilde{P}_N^*[2k][2l] \times (\tilde{s}_1[k][l] + \frac{4B}{N^2} \delta[k]\delta[l]),\quad (5.29)$$

where we used Eq. 5.23 to substitute for $b[i][j]$, δ is the Kronecker delta function. By substituting the source distribution computed in Eq. 5.28, and use the auto-correlation definition in Eq. 5.21, Eq. 5.29 becomes:

$$\begin{aligned}\tilde{C}_{N/2}[k][l] &= \frac{S_1}{\beta[i_1][j_1]} \times (\tilde{W}_{N/2}[k][l] \times e^{-4\sqrt{-1}\pi(i_1k+j_1l)/N} - N^2 \tilde{P}^*[2k][2l] \times \tilde{\varepsilon}_1[k][l]) \\ &\quad + \frac{4B}{N^2} \delta[k]\delta[l] \times N^2 \tilde{P}_N^*[2k][2l].\end{aligned}\quad (5.30)$$

Applying the inverse Fourier transform to Eq. 5.30 gives:

$$C_{N/2}[i][j] = \frac{S_1}{\beta[i_1][j_1]} \times (W_{N/1}[i - i_1][j - j_1] - C_{\varepsilon_1}[i][j]) + \frac{4B}{N^2},\quad (5.31)$$

where $C_{\varepsilon_1}[i][j]$ is the cross-correlation of ε_1 matrix with the PSF.

To solve for S_1 and B , two cross-correlation values are computed: the minimum $C_{N/2}[i_m][j_m]$ and the peak $C_{N/2}[i_1][j_1]$.

$$C_{N/2}[i_m][j_m] = \frac{S_1}{\beta[i_1][j_1]} \times (W_{N/2}[i_m - i_1][j_m - j_1] - C_{\varepsilon_1}[i_m][j_m]) + \frac{4B}{N^2}, \quad (5.32)$$

$$C_{N/2}[i_1][j_1] = \frac{S_1}{\beta[i_1][j_1]} \times (W_{N/2}[0][0] - C_{\varepsilon_1}[i_1][j_1]) + \frac{4B}{N^2}. \quad (5.33)$$

By combining Eqs. 5.32 and 5.33, the S_1 and B can be computed by:

$$S_1 = \beta[i_1][j_1] \times \frac{C_{N/2}[i_1][j_1] - C_{N/2}[i_m][j_m]}{W_{N/2}[0][0] - W_{N/2}[i_m - i_1][j_m - j_1] - C_{\varepsilon_1}[i_1][j_1] + C_{\varepsilon_1}[i_m][j_m]}, \quad (5.34)$$

and,

$$B = \frac{N^2}{4} \times \left(C_{N/2}[i_1][j_1] - \frac{S_1}{\beta[i_1][j_1]} \times (W_{N/2}[0][0] - C_{\varepsilon_1}[i_1][j_1]) \right) \quad (5.35)$$

The β function can not be computed onboard as the total PSF is not available. Thus, it is computed and fitted on the ground by the $\hat{\beta}(y, z)$ function:

$$\hat{\beta}(y, z) = b_0 - b_1(k(y) + k(z)), \quad (5.36)$$

with

$$k(x) = \begin{cases} \exp\left(-\frac{(x-0.5-b_2)^2}{2b_3^2}\right) & x > 0.5, \\ \exp\left(-\frac{(x-0.5+b_2)^2}{2b_3^2}\right) & \text{otherwise,} \end{cases} \quad (5.37)$$

where b_0, b_1, b_2 , and b_3 are the fit parameters that are uploaded to the science partition.

The C_{ε_1} function is purely geometrical and only depends on the PSF and the source peak position. C_{ε_1} can not be computed onboard, but it can be approximated when the source is at the center and with zero background in the detector. For the signal and the background estimation, only two values of C_{ε_1} are used: the maximum and the minimum values. For the background, the value $C_{\varepsilon_1}^B = \text{Max}(C_{\varepsilon_1}[i][j])$ is computed. And for the signal in Eq. 5.34, the $C_{\varepsilon_1}^s = \text{Max}(C_{\varepsilon_1}[i][j]) - \text{Min}(C_{\varepsilon_1}[i][j])$ is computed, both $C_{\varepsilon_1}^B$ and $C_{\varepsilon_1}^s$ are computed on the ground.

Finally the signal and background counts are estimated by:

$$\hat{S}_1 = \hat{\beta}(y_1, z_1) \times \frac{C_{N/2}[i_1][j_1] - C_{N/2}[i_m][j_m]}{W_{N/2}[0][0] - W_{N/2}[i_m - i_1][j_m - j_1] - C_{\varepsilon_1}^s}, \quad (5.38)$$

and,

$$\hat{B}_1 = \frac{N^2}{4} \times \left(C_{N/2}[i_1][j_1] - \frac{S_1}{\hat{\beta}(y_1, z_1)} \times (W_{N/2}[0][0] - C_{\varepsilon_1}^B) \right), \quad (5.39)$$

and the signal-to-noise ratio is estimated by:

$$\hat{\rho} = \frac{\hat{S}_1}{\sqrt{\hat{B}_1}}. \quad (5.40)$$

The source signal and background estimators are biased by the estimation of β and C_{ε_1} . The β function is approximated by a fit function in Eq. 5.36 that converges well to the β function so the bias can be neglected. However, C_{ε_1} is estimated by only two values, $C_{\varepsilon_1}^B$ and $C_{\varepsilon_1}^s$, when the source is at the center of the detector plane with zero background. This estimator is biased when the source moves away from the center. This geometrical bias is studied and characterized in Sec. 5.2.6.

This method is currently implemented in the science partition of MXT, and it is characterized in Sec. 5.2.6.

5.1.5 . Multi-source detection

The MXT must compute the position of the three brightest sources in its field of view. Sections 5.1.2 and 5.1.3 explain how the first source is localized. To localize the second source, the contribution of the first source to the cross-correlation map must be removed. Thus a method based on an iterative subtraction is implemented onboard.

The original cross-correlation map $C_{N/2}[i][j]$ is expressed as the following:

$$C_{N/2}[i][j] = \sum_{g=1}^3 C^g[i][j] + \frac{4B}{N^2}, \quad (5.41)$$

where C^g is the contribution of the g^{th} source to the cross-correlation map, with $1 \leq g \leq 3$.

The contribution from the first source is estimated using Eq. 5.31:

$$\hat{C}^1[i][j] = \frac{\hat{S}_1}{\hat{\beta}(y_1, z_1)} \times (W_{N/2}[i - i_1][j - j_1] - C_{\varepsilon}^B), \quad (5.42)$$

where \hat{S}_1 , $\hat{\beta}$, and C_{ε}^B are introduced in Sec. 5.1.4.3.

The \hat{C}^1 map is subtracted from the original cross-correlation map:

$$C'_{N/2} = C_{N/2}^0 - \hat{C}_{N/2}^1, \quad (5.43)$$

where $C'_{N/2}$ is the cross-correlation after subtracting the first source contribution, and it is processed to localize the second source peak by computing the barycenter inside a window around the maximum cross-correlation coefficient in the subtracted map, as explained in Sec. 5.1.3. The second source peak is found at (y_2, z_2) in the intrinsic coordinates that is converted to spherical coordinates (θ_2, ϕ_2) .

An example of the subtraction is presented in Fig. 5.7, where two sources are simulated in the MXT field of view. The first source is localized and subtracted, as explained above, in order to localize the secondary sources. The right-side plot shows that the first source is subtracted completely, where the cross-correlation values are about zero around the first source peak.

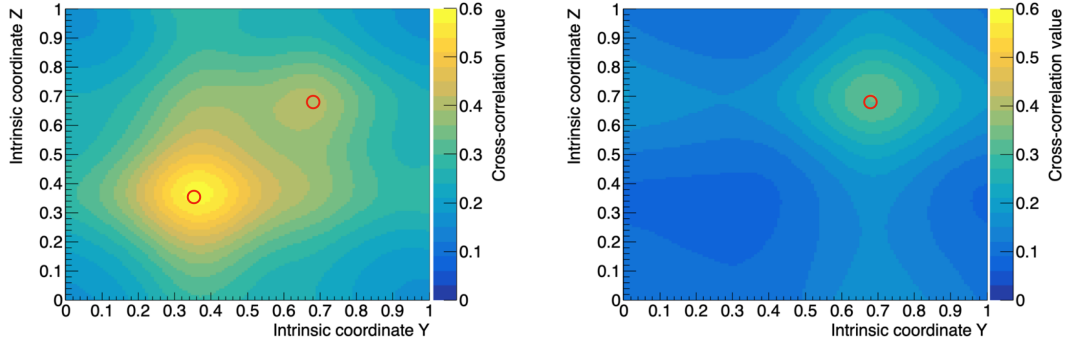


Figure 5.7: Two sources in the MXT field of view (left), the first source is localized with the cross-correlation and barycenter method. The first source is subtracted (right) in order to localize the second source, and the latter is then localized with the same method as the first source. The true positions of the two sources are labeled with red circles.

The second source signal and the associated background in the detector are computed with Eq. 5.38 and 5.39:

$$\hat{S}_2 = \hat{\beta}(y_2, z_2) \times \frac{C'_{N/2}[i_2][j_2] - C'_{N/2}[i_m][j_m]}{W_{N/2}[0][0] - W_{N/2}[i_m - i_2][j_m - j_2] - C_{\varepsilon_1}^s}, \quad (5.44)$$

and,

$$\hat{B}_2 = \frac{N^2}{4} \times \left(C'_{N/2}[i_2][j_2] - \frac{S_2}{\hat{\beta}(y_2, z_2)} \times (W_{N/2}[0][0] - C_{\varepsilon_1}^B) \right), \quad (5.45)$$

where (i_2, j_2) is the cell containing the source second peak (y_2, z_2) , and (i_m, j_m) is the minimum of $C'_{N/2}$.

The same steps are repeated for the third source that is localized at (i_3, j_3) , (y_3, z_3) , and (θ_3, ϕ_3) . The source signal and associated background are noted \hat{S}_3 , and \hat{B}_3 , respectively. The multiple source localization is characterized in Sec. 5.2.5.

Once the $\hat{\rho}_i = \hat{S}_i / \sqrt{\hat{B}_i}$ is computed for i source, it is then converted to a r_{90} value by Eq. 5.46. The r_{90} value is a measure of the localization uncertainty that is characterized in Sec. 5.2:

$$r_{90} = R_0 + R_1 \times \hat{\rho}^{R_2}, \quad (5.46)$$

where R_0 , R_1 , and R_2 are parameters fitted to simulation results as explained in Sec. 5.2.6. Three threshold values are used for r_{90} : (r_1, r_2, r_3) . One threshold is used for the signal-to-noise ratio (ρ_q), and a threshold value of minimum number of photons (S_q) is set. These thresholds are used to assign a quality factor q_f for the localization of the first source based on its accuracy. The quality factor takes values from 0 -4, where $q_f = 4$ is the best localization:

- $q_f = 4$ if $\hat{\rho} \geq \rho_q$ and $r_{90} \leq r_3$.

- $q_f = 3$ if $\hat{\rho} \geq \rho_q$ and $r_{90} \leq r_2$.
- $q_f = 2$ if $\hat{\rho} \geq \rho_q$ and $r_{90} \leq r_1$.
- $q_f = 1$ if $\hat{\rho} \geq \rho_q$ and $r_{90} > r_1$.
- $q_f = 0$ if $\hat{\rho} < \rho_q$ or $\hat{S} < S_q$.

The information about the three sources is sent to the ground via the VHF position packets, and it is updated every 30 s (see Fig. 2.17). The information sent to the ground is listed in Tab. 5.1.

Table 5.1: Quantities computed onboard for the three brightest sources in the MXT field of view, this information is sent to the ground with the VHF position packets every 30 s.

1 st source	2 nd source	3 rd source
θ_1	θ_2	θ_3
ϕ_1	ϕ_2	ϕ_3
$\hat{\rho}_1$	$\hat{\rho}_2$	$\hat{\rho}_3$
r_{90}^1	r_{90}^2	r_{90}^3
\hat{S}^1	\hat{S}^2	\hat{S}^3

5.1.6 . Configuration of localization algorithm

To control the onboard localization algorithm, a large number of parameters (24) are used to tune the algorithm. These parameters are evaluated in the ground and uploaded to the science partition via the configuration table. The list of the localization parameters tuned and uploaded with the configuration table is given in Tab. 5.2.

Table 5.2: List of localization parameters (24), that are evaluated on the ground and uploaded with the configuration table to the science partition.

Notation	Description	Default value
N_w	Window size to compute the source peak barycenter	50
α_{loc}	Peak fraction to compute the source peak barycenter given as a percentage	90
$g_y[0]$	Fit parameter [0] to correct for spectral leakage in the Y direction	1.02472×10^{-3}
$g_y[1]$	Fit parameter [1] to correct for spectral leakage in the Y direction	2.92406×10^1
$g_y[2]$	Fit parameter [2] to correct for spectral leakage in the Y direction	-5.17523×10^{-1}
$g_y[3]$	Fit parameter [3] to correct for spectral leakage in the Y direction	-3.11185×10^1
$g_z[0]$	Fit parameter [0] to correct for spectral leakage in the Z direction	2.62201×10^{-3}
$g_z[1]$	Fit parameter [1] to correct for spectral leakage in the Z direction	2.81842×10^1
$g_z[2]$	Fit parameter [2] to correct for spectral leakage in the Z direction	-4.51601×10^{-1}
$g_z[3]$	Fit parameter [3] to correct for spectral leakage in the Z direction	-2.96345×10^1
R_0	Fit parameter [0] to derive r_{90} from the signal-to-noise ratio	794.404
R_1	parameter [1] to derive r_{90} from the signal-to-noise ratio	-0.834816
R_2	parameter [2] to derive r_{90} from the signal-to-noise ratio	10.5734
S_q	Quality factor definition: minimum number of photons	100
ρ_q	Quality factor definition: minimum signal-to-noise ratio	4
r_3	Quality factor definition: r_{90} threshold 4 (best accuracy) [arcsecond]	30
r_2	Quality factor definition: r_{90} threshold 3 (medium accuracy) [arcsecond]	60
r_1	Quality factor definition: r_{90} threshold 2 (low accuracy) [arcsecond]	120
b_0	parameter for signal/background reconstruction	0.681879
b_1	parameter for signal/background reconstruction	42.3743
b_2	parameter for signal/background reconstruction	1.82772
b_3	parameter for signal/background reconstruction	0.411599
$C_{\varepsilon_1}^B$	parameter for signal/background reconstruction	2.71749×10^{-5}
$C_{\varepsilon_1}^S$	parameter for signal/background reconstruction	1.17001×10^{-5}

5.2 . Results and characterization

The localization algorithm performance is characterized and tested with several scenarios to verify the compliance of the localization algorithm described in Sec. 5.1 with the MXT scientific requirement. The results of the characterization are presented in the following sections.

The main measure of the localization uncertainty is the r_{90} value that is computed as the following: for a given scenario, about 1000 simulations of sources are generated at different positions within the field of view of the telescope. For each of the 1000 simulations, the source position is measured with the onboard localization algorithm r_m . The offset of the measured position with respect to the true position r_t is computed: $\delta r = \sqrt{\delta y^2 + \delta z^2}$. The distribution of δr is built, and the r_{90} is given by the 90th percentile of δr distribution. As a requirement for MXT, the localization accuracy parameterized by r_{90} must be < 2 arcmin within 5-10 minutes after the beginning of observation.

For some scenarios, the r_{90} value can not be computed, and the localization performance is characterized by δr .

5.2.1 . The source intensity

In this section, the localization accuracy is characterized as a function of the source intensity. This characterization study aims at identifying the minimum number of photons detected with MXT to reach the targeted accuracy of $r_{90} < 2$ arcmin after 5 and 10 minutes of observation. As the observation time increases, the number of detected X-ray photons also increases. However, the X-ray background noise also increases. The expected count rate of X-ray background must be estimated in order to simulate the number of background counts in the MXT detector after 5 and 10 minutes of observation. The main contribution to the X-ray background on the detector comes from the Cosmic X-ray Background (CXB). The Leicester team estimated this contribution by convolving the CXB model measured by Swift [193] with the response expected by the optics and the detector of the MXT. A uniform background noise of 1.5×10^{-5} counts. s^{-1} . $pixel^{-1}$ is obtained on the detector, which corresponds to 0.98 counts. s^{-1} over the entire detector of 256×256 pixels.

After 5 minutes (resp. 10 minutes) of observation, the number of background counts in the detector is ~ 300 counts (resp. ~ 600 counts). For each observation time (5 and 10 minutes), sources with intensities between 10 and 10^4 photons are simulated; by intensity here, we mean the number of photons detected by the MXT. For each intensity scenario, the r_{90} is computed as explained above, but the sources are simulated within ± 50 pixels around the center to avoid the accuracy degradation due to the spectral leakage explained in Sec. 5.1. In this study, the photons are accumulated in a photon map of size 256×256 , the same as the detector pixel matrix resolution.

Figure 5.8 shows the r_{90} value for each source intensity, after 5 and 10 minutes of observation. This characterization study shows that the MXT must detect more than 164 ± 5 (resp. 197 ± 6) photons during 5 minutes (resp. 10 minutes) of observation time to match the MXT requirement of localization accuracy of < 2 arcmin. The errors in the plot correspond to the statistical errors.

From the Swift/XRT database, the typical number of photons received during the first

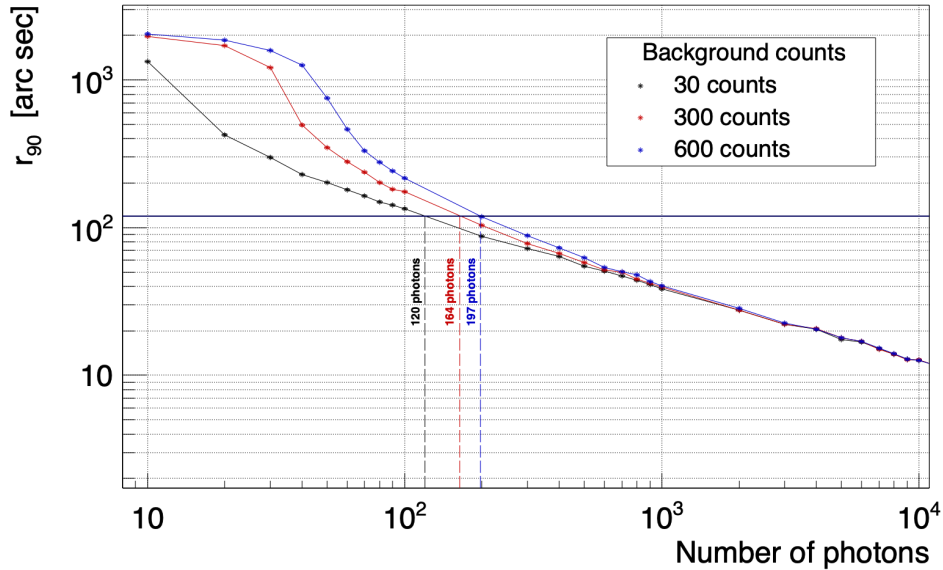


Figure 5.8: The onboard localization uncertainty of the MXT measured as a function of the source intensity. The measurement is done after 30 s (in black), 5 minutes (in red), and 10 minutes (in blue) of simulated observations. For each observation duration, source intensities from 10 to 10^4 photons are simulated. The source intensity is parametrized by the number of photons hitting the MXT detector. This plot shows that MXT must detect at least 120 ± 3 , 164 ± 5 , and 197 ± 6 photons after 30 s, 5 minutes, and 10 minutes of observation, respectively, in order to reach the MXT required accuracy of 2 arcmin.

10 minutes is between a few hundred and a few thousand photons. However, the number of detected photons depends on the telescope properties like the sensitivity and the effective area. In Chap. 6, a simulated observation using real observation by similar telescopes like Swift/XRT is performed to estimate the number of photons that the MXT detects after a given observation time. For 80% of GRBs, the MXT will detect more than 200 photons after 10 min of observation. Hence, MXT is expected to detect 80% of GRBs with accuracy better than 2 arcmin.

A simulation of localization after 30 s of observation is also performed, and the result is shown in Fig. 5.8. This simulation is performed because the VHF position packet is sent to the ground every 30 s. The figure shows that the first localization would have an accuracy of < 2 arcmin if more than 120 ± 3 photons were detected.

5.2.2 . The photon map resolution

The identified photons are accumulated in a two-dimensional map called the photon map, one of the localization algorithm inputs (see Sec. 4.2.3). The resolution of the photon map must be kept at a minimum to limit the computing cost associated with the Fourier transform

used to cross-correlate the photon map with the point spread function (see Sec. 5.1). However, it should be chosen high enough to maximize the localization performance. The impact of the photon map resolution on the localization performance is measured by repeating the same test in Sec. 5.2.1, but using a different resolution of the photon map. The localization uncertainty is measured using three-photon maps with different resolutions: (256×256) , (128×128) , and (64×64) , and the result is presented in Fig. 5.9

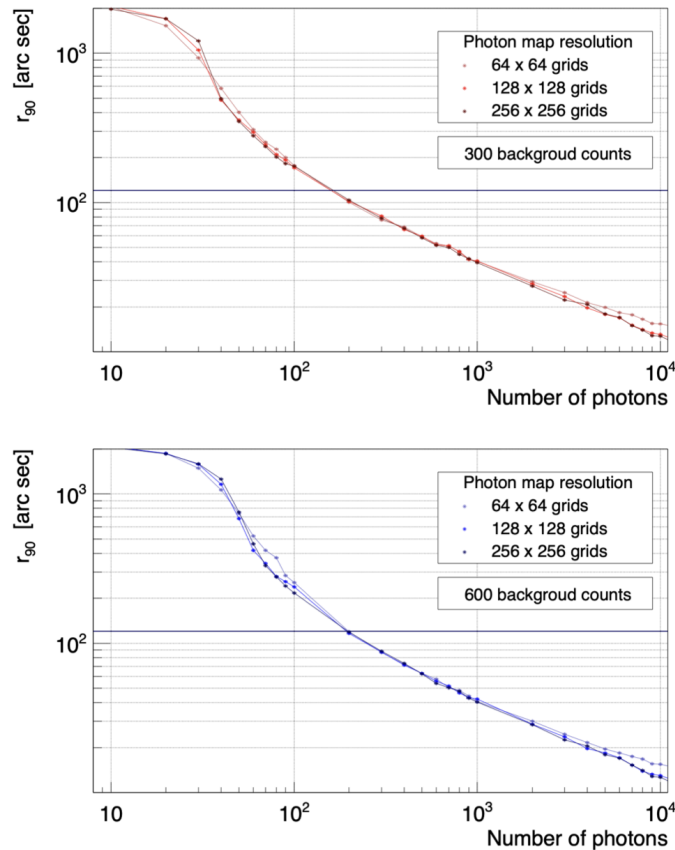


Figure 5.9: The localization uncertainty as a function of the number of photons, measured for photon maps with resolutions: 64×64 , 128×128 , and 256×256 , after 5 minutes (top) and 10 minutes (bottom) of observation.

Reducing the photon map size from the original resolution of 256×256 to 128×128 has no significant impact, as demonstrated by Fig. 5.9. The accuracy degradation is $< 3\%$ if more than 100 photons are detected, and it reaches $< 6\%$ otherwise. Meanwhile, reducing the resolution further could degrade the resolution by more than 30%. Consequently, photons are accumulated in a photon map of size 128×128 .

5.2.3 . Edge bias

As a consequence of the localization method implemented onboard (see Sec. 5.1), the computed position is biased due to the spectral leakage. When the discrete Fourier transform is applied to the photon map, it is assumed to be periodic. This assumption is valid if the source peak is at the center of the detector plane. However, this assumption is invalid when the source gets closer to the detector edges, and the detector does not observe part of the source peak. As the source is closer to the detector edge, the spectral-leakage effects become larger, and they bias the peak position in the cross-correlation map. This effect is seen in Fig. 5.10 where the source position is moved over the entire detector from $(y = 0, z = 0)$ to $(y = 1, z = 1)$. The source position is measured with the onboard method for each point and compared to the true position to compute the position offset δr . The bias seen in the plot is significant and can not be neglected when the source is more than 70 pixels away from the center. δr could degrade from a few arcseconds to a few hundred arcseconds when the source is near the detector edges.

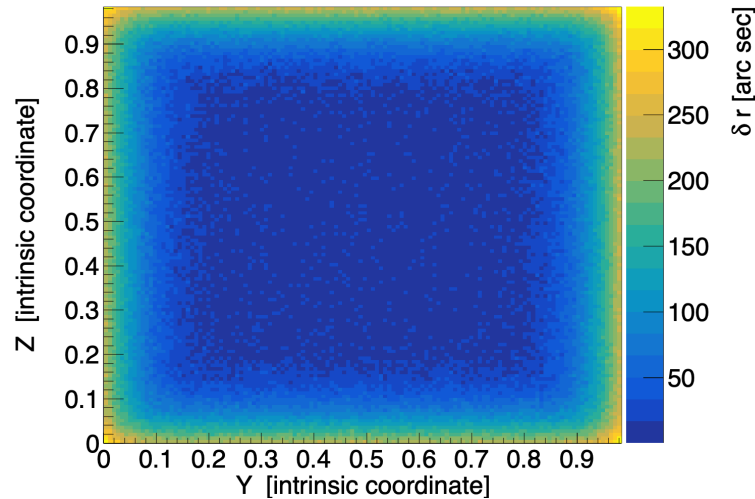


Figure 5.10: The position bias measured while the simulated source is moved in all directions in the detector. As the source gets closer to the edge of the detector, the localization degrades significantly due to the spectral-leakage effect.

As mentioned in Sec. 2.3.2, the MXT observation is triggered by ECLAIRs, and the satellite slews so that MXT points toward the source and its field of view is centered on the source coordinates computed by ECLAIRs. The ECLAIRs uncertainty could reach 12 arcmin, which means that the source could be ± 12 arcmin (± 51 pixels) away from the center of the MXT detector, and secondary sources could be detected anywhere in the MXT field of view. Therefore, the localization degradation due to spectral leakage at the detector edges must be removed or reduced.

The usual way to deal with the spectral leakage effect is to use the padding method, but this method increases the data size, which leads to longer Fourier transform calculations which we want to avoid onboard. Instead, the bias along each axis is measured separately, as seen in Fig. 5.11. Once the bias is measured and evaluated, it can be fitted with a given function that

should be implemented onboard to correct the bias.

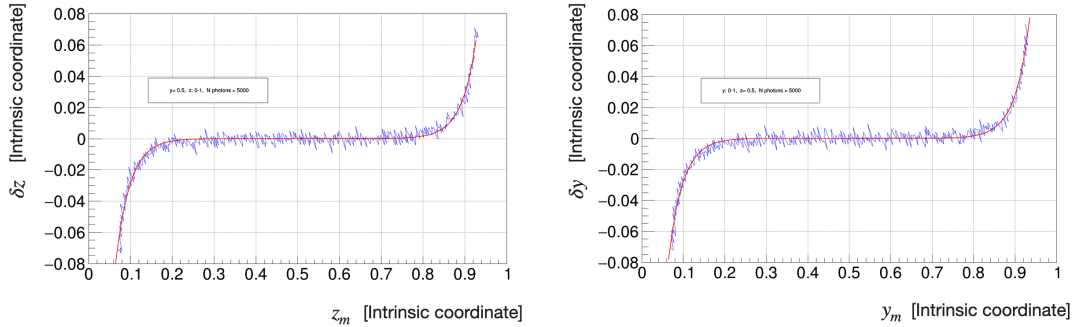


Figure 5.11: The edge bias measured in each direction separately. Left: the bias in the z -direction measured as the source is moved vertically from $z=0$ to $z=1$, where $y=0.5$. The source position offset is measured at each point in the intrinsic coordinate (in blue curve). The points are fitted (in red curve) to correct the edge bias. Right: the edge bias in the y -direction measured the same way as the z -direction, but the source is moved horizontally from $y=0$ to $y=1$ and $z=0.5$. In both plots, a source with a high intensity is simulated without background.

The bias in the x direction is then can be fitted by the following function:

$$\eta(x_m) = \begin{cases} g_0 \times e^{g_1 \times x_m} & \text{if } x_m > 0.5 \\ g_2 \times e^{g_3 \times x_m} & \text{otherwise,} \end{cases} \quad (5.47)$$

where g_0 , g_1 , g_2 , and g_3 are the fit parameters measured separately for y and z directions. Applying this *ad hoc* corrections to the measured position (y_m, z_m) reduces the edge bias effectively as seen in Fig. 5.12. Two scenarios are simulated with a different number of photons to prove that this effect is independent of the source intensity. In each scenario, the source position offset δr is measured before and after the correction as the source is moved toward the detector edge. The deviation is plotted vs. the source distance from the detector center given in pixels. The vertical dashed line indicates when the source peak starts to be outside the detector. Therefore, the degradation starts at this point. The plot shows that the edge bias is effectively reduced (red circles) by applying the *ad hoc* correction. As explained in Sec. 5.1, the edge bias is characterized and fitted in the ground, and the fit parameters are uploaded to the science partition with the configuration table (see Tab. 5.2).

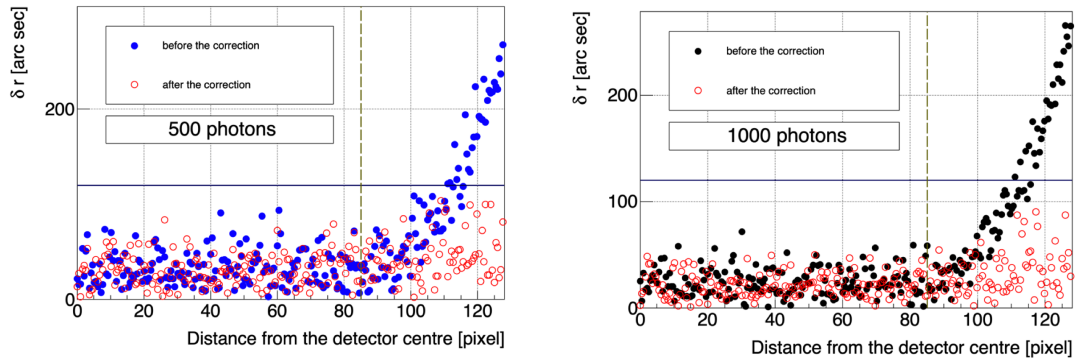


Figure 5.12: The source position offset δr as a function of the source distance (in pixel) from the detector centre. The dots show the bias before correction, while the open circles show the bias after applying $\eta(y)$ and $\eta(z)$ corrections. Two source intensities are simulated: 500 photons (left) and 1000 photons (right).

5.2.4 . Insensitive columns

Insensitive columns are set to zero in the photon map before performing the localization algorithm, as seen in Fig. 5.13.

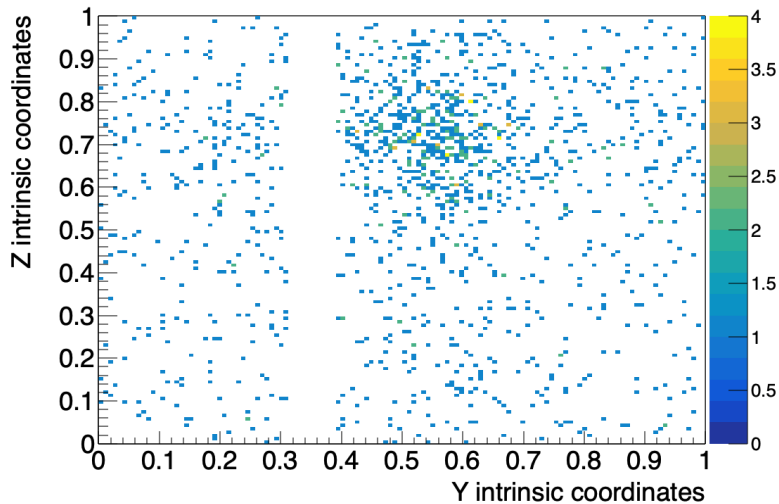


Figure 5.13: Example of a photon map constructed while the detector has 7 insensitive columns. The cells in the photon map corresponding to the insensitive columns are set to zero, as a consequence 8 columns in the photon map are deactivated.

The insensitive columns could affect the localization accuracy depending on their number and location in the detector. One of the tests performed by CNES for the MXT flight model shows that two columns could be insensitive at the nominal operating temperature of MXT

(- 65° C) and even more than two columns at a lower temperature (-75 ° C). During the Panter test of the MXT flight model in 2021, none of the columns appeared insensitive at the nominal operating temperature, and the detectors worked normally, as explained in Sec. 5.3. However, one can expect some insensitive columns could appear as the detector is aging in space. Therefore, we have to characterize the effect of the insensitive columns on the telescope scientific performance and find a method to reduce this effect. To compensate for the missing data due to the deactivation of the insensitive columns, one can think about interpolating the missing data using the data from neighboring columns.

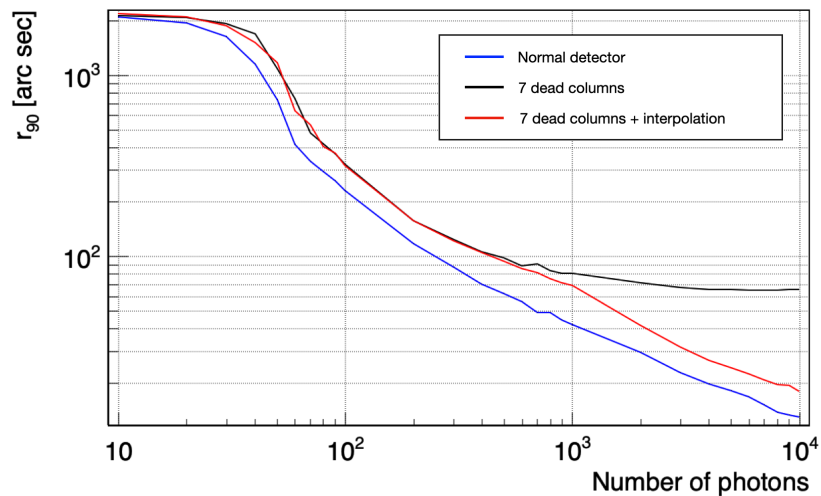


Figure 5.14: r_{90} as a function of the source intensity computed with the normal detector (blue curve), and with 7 insensitive columns in the detector (black curve). The interpolation method is used to reduce the effect of the insensitive columns (red curve).

The interpolation could be efficient in the case of high statistics, i.e., very bright sources, but it is not the case for the faint sources, as demonstrated in Fig 5.14. The plot shows that the presence of 7 insensitive columns degrades the localization accuracy (r_{90}) more than 80% at some intensities. The interpolation method reduces the localization performance degradation once the number of detected photons is more than ~ 700 , which is not sufficient. The correction must be intensity independent. Thus, we correct the effect of the insensitive columns analytically, as we did for the edge bias. First, we identify the parameters that control the effect of the insensitive columns. For this purpose, N_{bad} insensitive columns are simulated. For each N_{bad} value, the source is moved horizontally along the detector from $y_t = 0$ to $y_t = 1$, and the source position offset is measured at each point, the results are presented in Fig. 5.15 for $N_{bad} = 1, 3, 5, 7, 9$, and 11.

The plot shows that the effect of the insensitive columns starts to appear as the source peak starts to be located on these columns (~ 45 pixels away from the center of the insensitive columns), and the effect is greater (the δy increases) as N_{bad} is larger. This effect can be

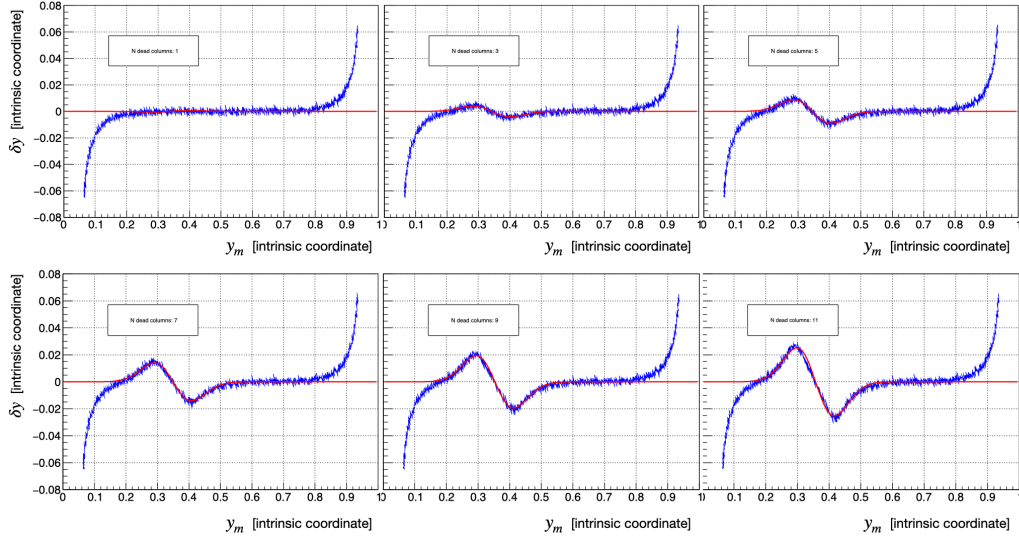


Figure 5.15: The y bias (in blue) measured as the source is moved horizontally from $y=0$ to $y=1$. $N_{bad} = 1, 3, 5, 7, 9,$ and 11 insensitive columns are simulated to evaluate the insensitive columns effect in the localization performance. The best fit is also drawn (in red).

fitted with a Sine-Gaussian function with only two free parameters: N_{bad} , and the center of the insensitive columns b :

$$\zeta(y) = \sum_{i=0}^2 \times N_{bad}[i] \times \left[\exp\left(-\frac{(y - b[i])^2}{0.007}\right) - \exp\left(-\frac{y - b[i] - 2/N}{0.007}\right) \right], \quad (5.48)$$

where $0 < i < 3$ is the index of the insensitive column bunch. The science partition corrects up to three bunches of insensitive columns. The correction is applied to the source measured y position as in Eq. 5.10.

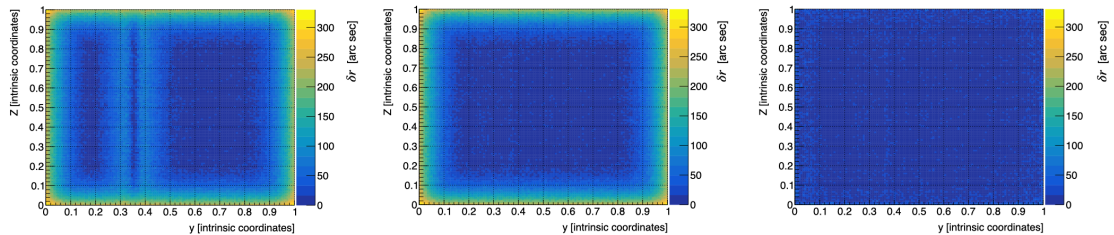


Figure 5.16: δr measured as the source is moved along the entire detector with 7 insensitive columns. Left: the effect of the insensitive columns appears in the y -direction with no effect on the z -direction. In addition, the edge bias is seen near the detector edges. Center: the effect of the insensitive columns is reduced by the analytical correction. Right: the effect of the insensitive columns and the edge bias are reduced by the analytical corrections.

Note that the insensitive columns do not affect the source measured position in the z -direction, which can be seen in Fig. 5.16 where the source is moved over the entire detector that has 7 insensitive columns, the source position bias is measured at each point. The bias due to the insensitive columns appears only in the y -direction. The figure also shows that applying the analytical correction explained above and the edge bias correction explained in Sec. 5.2.3 gives a uniform localization performance over the entire detector.

We measure r_{90} as a function of the source intensity, where 7 insensitive columns are simulated in the detector. r_{90} is measured with and without applying the analytical correction of the insensitive columns effect in Eq. 5.48, and both are compared to r_{90} measured with a normal detector. The results are plotted in Fig. 5.17

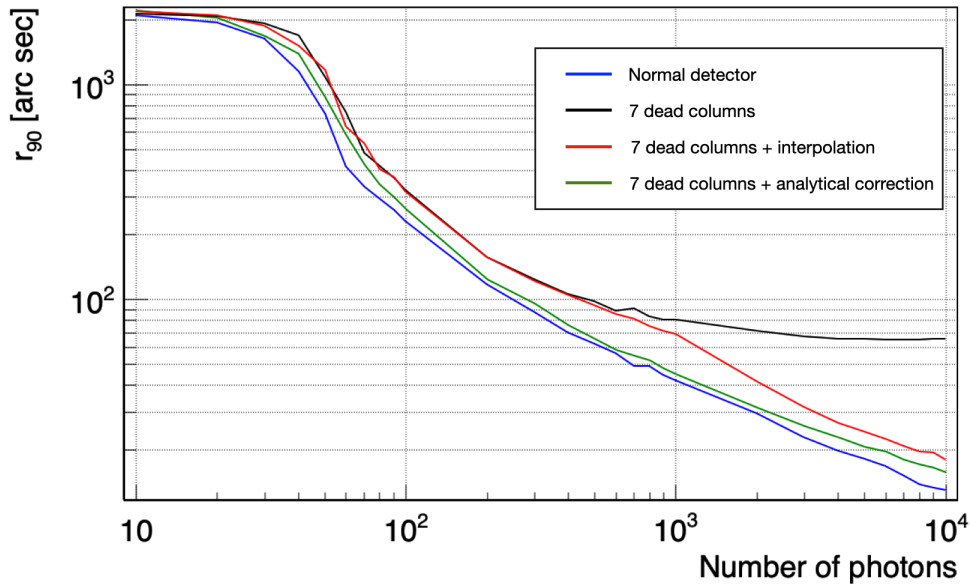


Figure 5.17: The r_{90} as a function of the source intensity computed with the normal detector (blue curve), and with 7 insensitive columns in the detector (black curve). The analytical correction method is applied to reduce the effect of the insensitive columns (green curve), and it is compared to the interpolation method (red curve).

This method proves to be efficient in reducing the effect of the insensitive columns, and hence, it is applied onboard. The insensitive columns are identified on the ground by processing the downloaded data, and the fit parameters (number of insensitive columns bunches and the center of each bunch) to correct for the insensitive columns effect are uploaded to the science partition with the configuration table (see Tab. 5.2).

5.2.5 . Multiple sources

Having more than one X-ray source in the MXT field of view could affect the localization algorithm accuracy. The computed coordinates of the first source could be biased by the existence of the second source, particularly if the two sources are close to each other and have comparable intensities. Therefore, the localization algorithm must be characterized in terms of the distance between the sources and their relative intensities.

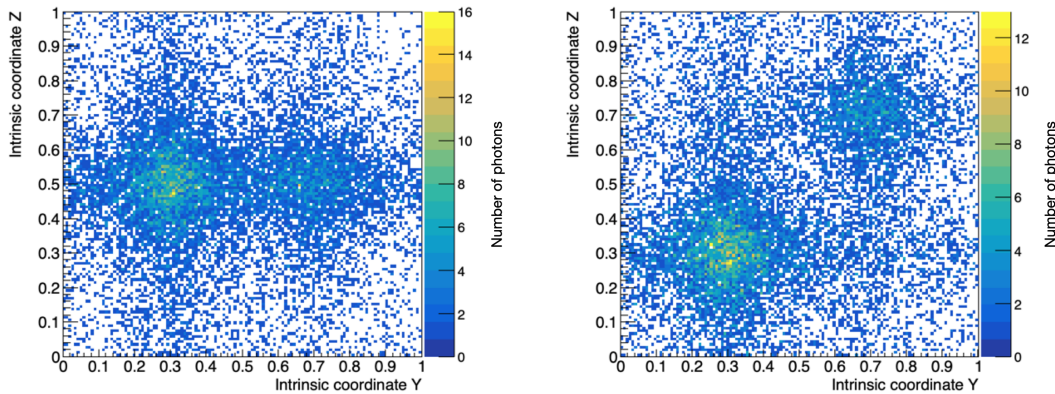


Figure 5.18: A photon map showing a detection of two sources in the MXT field of view. Left: the two sources are aligned in the y direction. Right: the two sources are located in the diagonal of the detector.

Figure 5.18 shows two scenarios of a multi-source detection. In the first scenario, the two sources are aligned in the y -direction, i.e., the arm of each source overlaps the peak of the other source. In the second scenario, the two sources are diagonal.

In both scenarios, one source is fixed, and the other is moving away from the stationary source. As the second source is moving, the two sources are localized with the onboard algorithm, and the bias in the measured sources positions (δr_i) is computed for the first and second sources respectively. For each scenario (the y -aligned and the diagonal sources), two relative intensities are simulated: the fixed source is two times brighter, or four times brighter than the moving source. The bias in the measured position as a function of the distance between the two sources is shown in Fig. 5.19.

The bias in the two sources measured position is clearer when the two sources are along the diagonal because the sources bias each other in both directions while computing the cross-correlation, and hence, the sources are not subtracted correctly. Meanwhile, when the two sources are aligned, they bias each other only in the alignment direction.

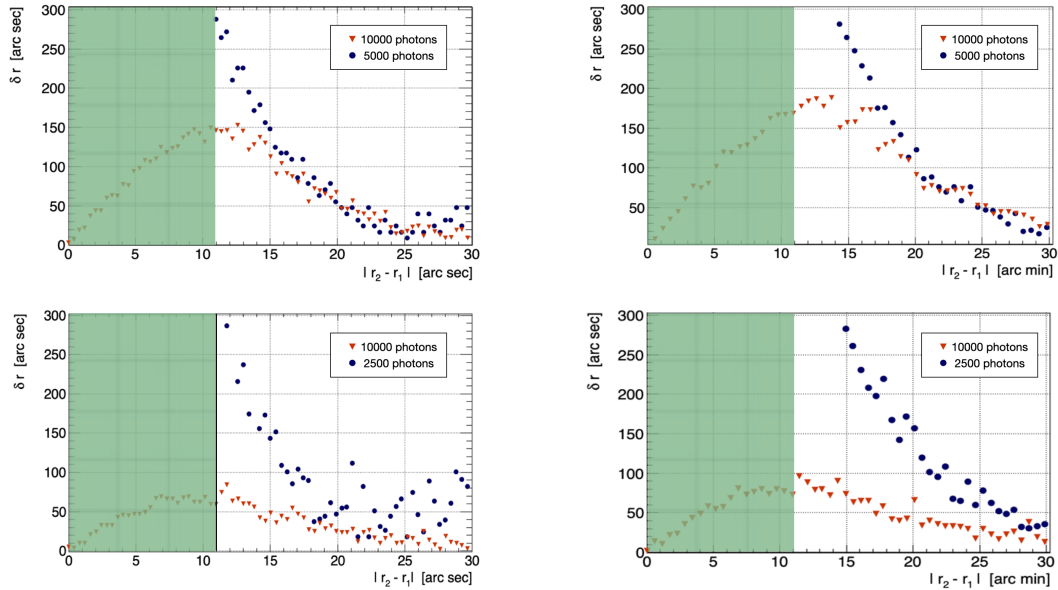


Figure 5.19: the bias of two source positions (δr) as a function of the distance between them. In the left column, the two sources are aligned in the y -direction, one source is fixed (orange triangle), and the second is moved away from the first one (blue points), where the fixed source is double brighter (top) and four times brighter (bottom) than the moving source. In the right column, the two sources are simulated in the detector diagonal, where the fixed source is double brighter (top) and four times brighter (bottom) than the moving source. The green shaded region corresponds to the distance below the MXT angular resolution (11 arcmin).

When the two sources have comparable intensities, the localization performance degrades more and requires the two sources to be far enough from each other to reduce their reciprocal effect.

The two sources must be away from each other by at least 11 arcmin, which is the angular resolution of the MXT, in order to be distinguished from each other. As the secondary source is further away from the first source, the localization performs better and starts to stabilize as the distance between the two sources is two times the angular resolution (22 arcmin), where the two peaks are totally decoupled.

5.2.6 . Signal-to-noise ratio

In this section, the performance of the signal-to-noise ratio estimation is evaluated. The r_{90} value is computed onboard using the measured signal-to-noise ratio as in Eq. 5.46. For this purpose, an observation is simulated with a certain number of photons and background counts, and the observation is repeated 1000 times, ± 10 pixels around the detector center. For each observation, the signal-to-noise ratio is measured. The final signal-to-noise ratio value ρ_m is given by the mean value of the 1000 measurements. r_{90} is computed as explained at

the beginning of Sec. 5.2. The r_{90} is plotted as a function of ρ_m , the plot is fitted in order to identify the relation between the r_{90} and the ρ_m values.

Figure 5.20 shows the r_{90} Vs ρ_m plot and the fit function. From this plot one can extract the values of the R_0 , R_1 , and R_2 parameters. The r_{90} is given by:

$$r_{90} = 462 \times \rho^{-0.635} + 4 \quad (5.49)$$

The current r_{90} thresholds (r_2, r_3, r_4) are labeled in blue in the plot.

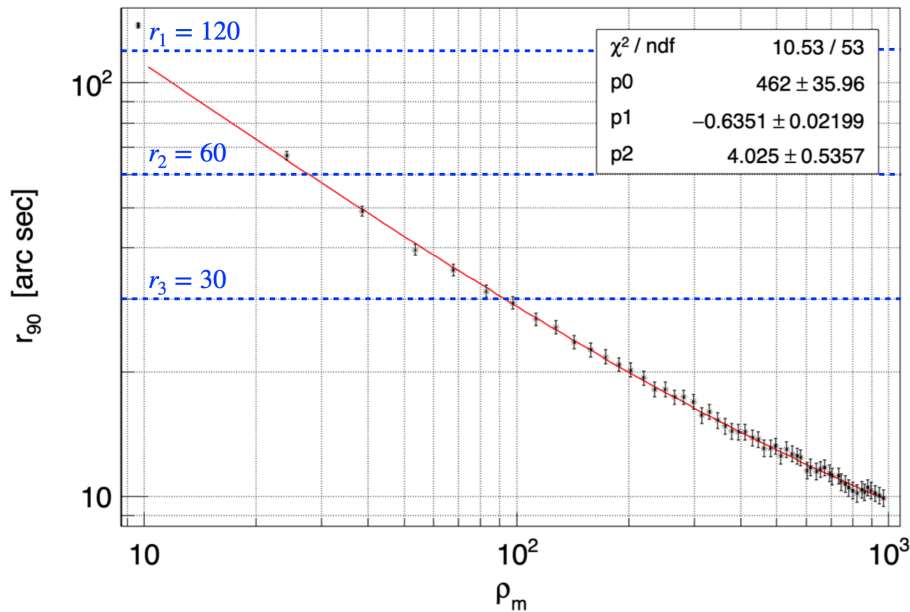


Figure 5.20: r_{90} as a function of the signal-to-noise ratio (black points) and the best fit is plotted in red. The dashed blue lines are the r_{90} thresholds that define the detection quality.

As discussed in Sec. 5.1.4.2, the estimation of the signal-to-noise ratio is under-estimated as the source is brighter (ε_S bias can not be neglected). This issue is solved in the method described in Sec. 5.1.4.3. To compare the two methods (method 2 that uses the cross-correlation map and method 3 that uses the cross-correlation and the auto-correlation maps), we simulated different observation scenarios fixing the number of source photons and the background counts. For each simulation, the source is localized, and the signal-to-noise ratio is computed with the two methods in Sec. 5.1.4.2 and Sec. 5.1.4.3.

Figure 5.21 shows the measured signal-to-noise ratio compared to the true value. For a given signal-to-noise ratio, more than 500 observations are simulated where the source is placed ± 10 pixels around the center. For each observation, the signal-to-noise ratio is measured, the final signal-to-noise ratio value is computed as the mean value of the 500 observations, and the standard error is computed. The two methods give a comparable estimator at low signal-to-noise ratio ($\rho < 15$), but at higher signal-to-noise ratio, method 2 underestimates the

signal-to-noise ratio. However, method 3 has no dependence on the source intensity, and the bias is a systematic bias caused by the imperfect estimation of C_ϵ as discussed in Sec. 5.1.4.3. This bias is minimal and can be neglected. Therefore method 3 is applied onboard to estimate the source signal-to-noise ratio.

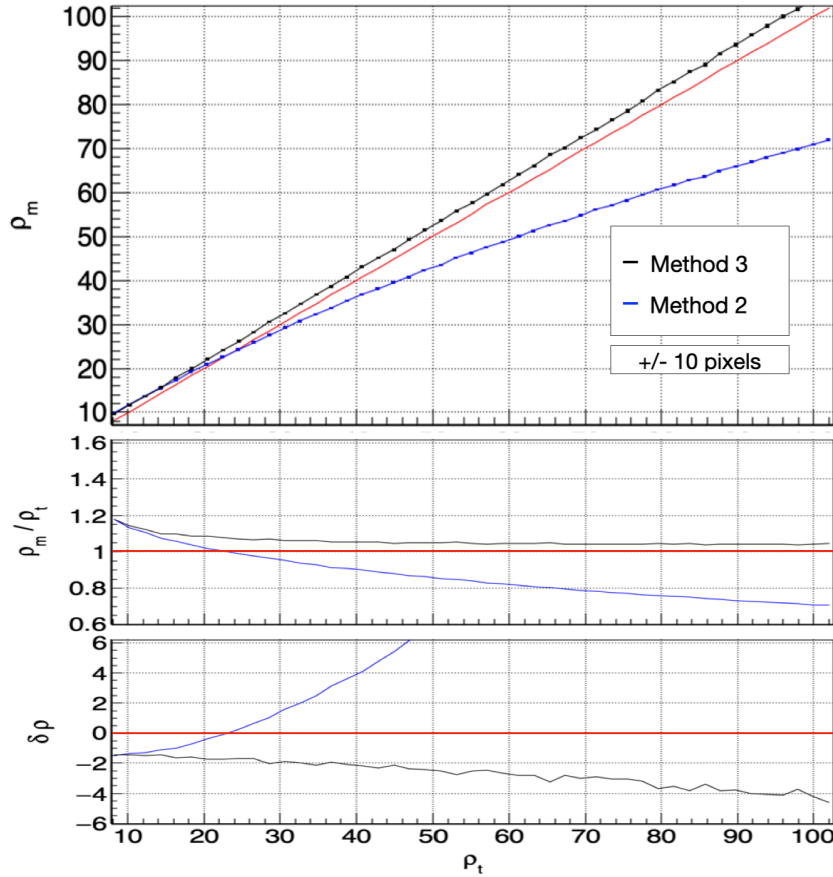


Figure 5.21: A comparison between the true signal-to-noise ratio (red line) and the measured signal-to-noise ratio with method 2 (blue line) and with method 3 (black line) (top), each point is measured as the mean value of ~ 500 observations are simulated ± 10 pixels around the center. The ratio between the measured and the true signal-to-noise ratio for method 2 and method 3 (middle). The deviation of the measured signal-to-noise ratio from the true signal-to-noise ratio for method 2 and method 3 (bottom).

The offset in background, signal, and signal-to-noise ratio are characterized as a function of the source location in the MXT field of view. The study is repeated with three source intensities: 300, 1000, and 3000 photons, where the number of background counts is fixed to

600. The results of this characterization are presented in Fig. 5.22, which shows that the signal, background, and signal-to-noise ratio estimations are intensity independent and depend on the source location in the detector. As the source is away from the detector center, the background and the signal are under-estimated, and the signal-to-noise ratio is overestimated. The bias appears to be more visible in the background estimation than in the signal estimation because the estimation of the background depends on the signal estimation, as seen in Eq. 5.39. Thus, the background computation includes more sources of error.

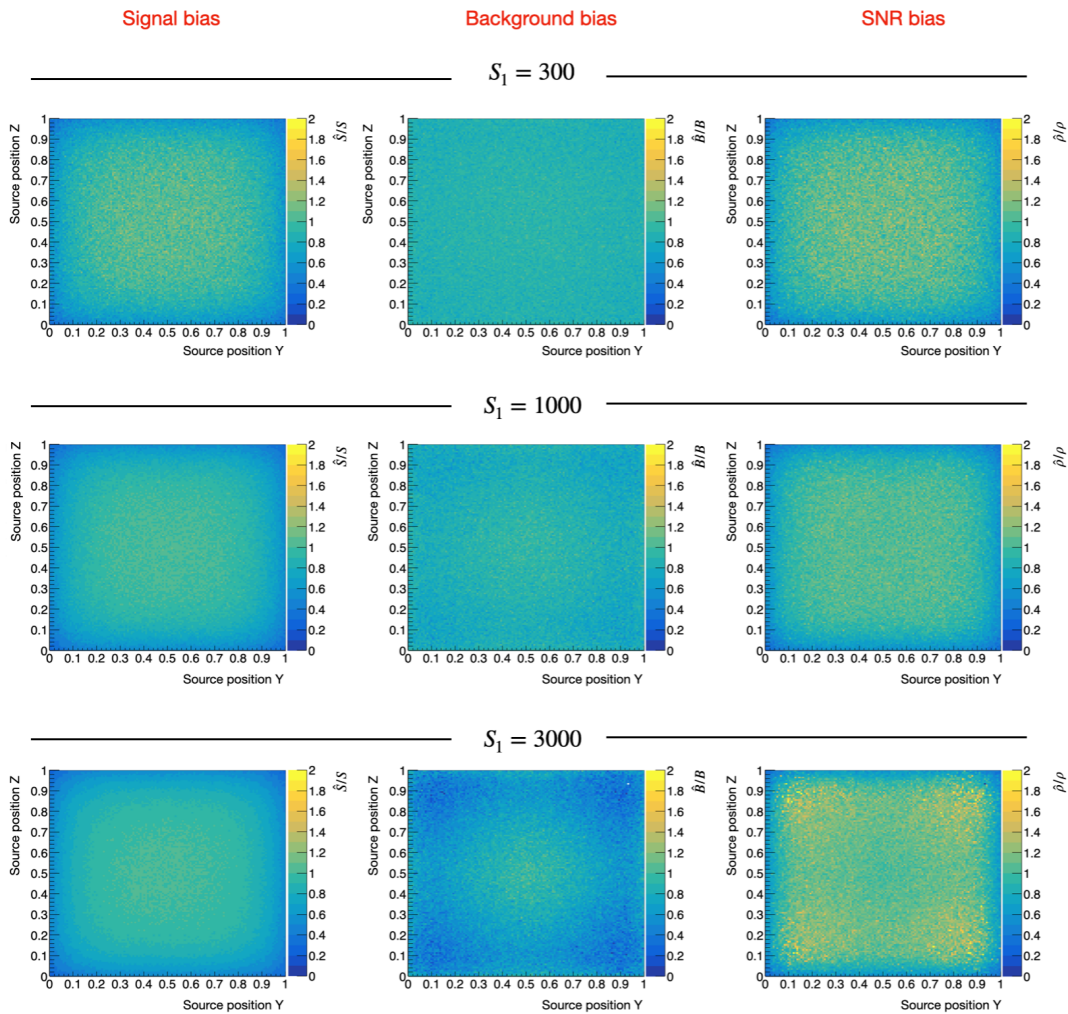


Figure 5.22: The signal bias \hat{S}/S (left column), background bias \hat{B}/B (central column) and the signal-to-noise ratio bias $\hat{\rho}/\rho$ (right column) for different source positions in the camera plane and different source intensities: $S_1 = 300$ (top), $S_1 = 1000$ (middle), and $S_1 = 3000$ (bottom).

The MXT must detect the three brightest sources in its field of view and estimate their

signal-to-noise ratio. Figure 5.21 shows that the signal-to-noise ratio computation algorithm performs efficiently if only one source exists in the field of view.

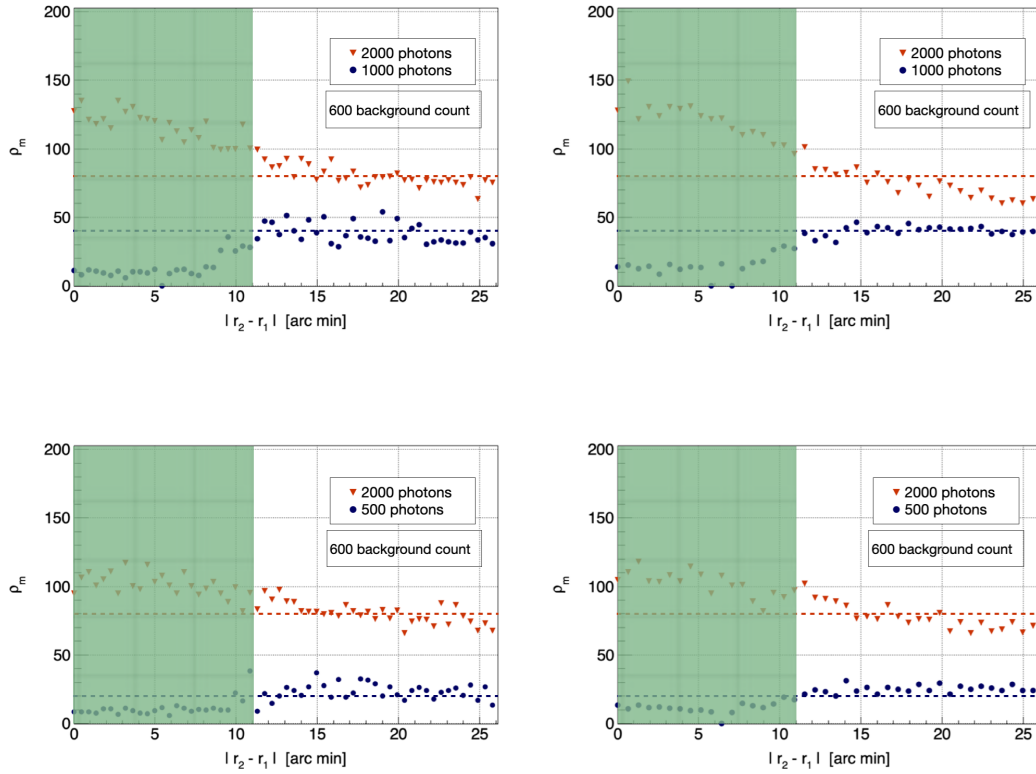


Figure 5.23: the measured signal-to-noise ratio of two sources in the MXT field of view as a function of the distance between them. In the left column, the two sources are aligned in the y -direction, one source is fixed (orange triangle), and the second is moved away from the first one (blue points), where the fixed source is two times brighter (top) and four times brighter (bottom) than the moved source. In the right column, the two sources are simulated in the detector diagonal, where the fixed source is two times brighter (top) and four times brighter (bottom) than the moved source. The green shaded region corresponds to the distance below the MXT angular resolution and the dashed lines correspond to the sources true signal-to-noise ratio values

The performance must be characterized in the case of a multi-source detection. The same simulated scenarios explained in Sec. 5.2.5 are used: the two aligned and the diagonal sources are used to test the signal-to-noise ratio estimation in case of a multi-source detection. For each scenario, two relative intensities are simulated: the first source (the fixed one) is two times and four times brighter than the secondary source (the moving one). As the second source moves away from the fixed source, the signal-to-noise ratio of the two sources is computed. The

signal-to-noise ratio as a function of the distance between two sources is shown in Fig. 5.23. The plot shows that the signal-to-noise ratio of the two sources is not affected either by the distance between them or their relative intensities. However, when the two sources are diagonal, there is more fluctuation in the measured signal-to-noise ratio of the brightest source. This is caused by the bias in the source localization (i_1, j_1) , where the signal and background estimation depend on the cross-correlation value of the source peak position.

5.3 . The MXT flight model test at Panter

The previous section explained how the scientific algorithm onboard the MXT is characterized using simulated data. However, the simulated data is not enough to test the scientific performance, as some unexpected effects could appear in reality. In order to trust the MXT science software, it must be extensively tested while the MDPU is coupled to the rest of the hardware: the structure, the camera, and the optics, and while the telescope is exposed to real X-ray emission. For this purpose, a test campaign was held at the Panter test facility (see Sec. 3.4.2) for the MXT flight model. The main objectives of the Panter test campaign can be summarized in the following:

- Measure the telescope PSF as a function of energy and position in the MXT field of view.
- Measure the telescope effective area.
- Measure the detector spectral response.
- Measure the impact of stray light using lasers in order to evaluate the impact of the filter absence.
- Evaluate the telescope performance at different temperatures.
- Test the onboard scientific algorithm, particularly the real-time localization.

5.3.1 . Test overview

The flight model test lasted one month: from October to November 2021. Three hundred thirty-nine test runs were performed to evaluate the MXT scientific performance. During the test runs, the MXT is exposed to 14 different X-ray energy from 0.277 keV up to ~ 8.9 keV. Table 5.3 gives the list of energies explored during the test.

The data collected with the X-ray sources listed in Tab. 5.3 are used to calibrate the detector and compute the energy gain of each column of the detector.

Table 5.3: List of X-ray sources and their energies used to characterize the MXT performance during the Panter test campaign.

Source	Energy [keV]
C-k	0.277
O-K	0.525
Cu-L	0.93
Mg-K	1.253
Al-K	1.486
W-M	1.774
Ag-L	2.98
Ti-K _α	4.508
Ti-K _β	4.93
Cr-K _α	5.405
Fe-K _α	6.398
Fe-K _β	7.053
Cu-K _α	8.047
Cu-K _β	8.901

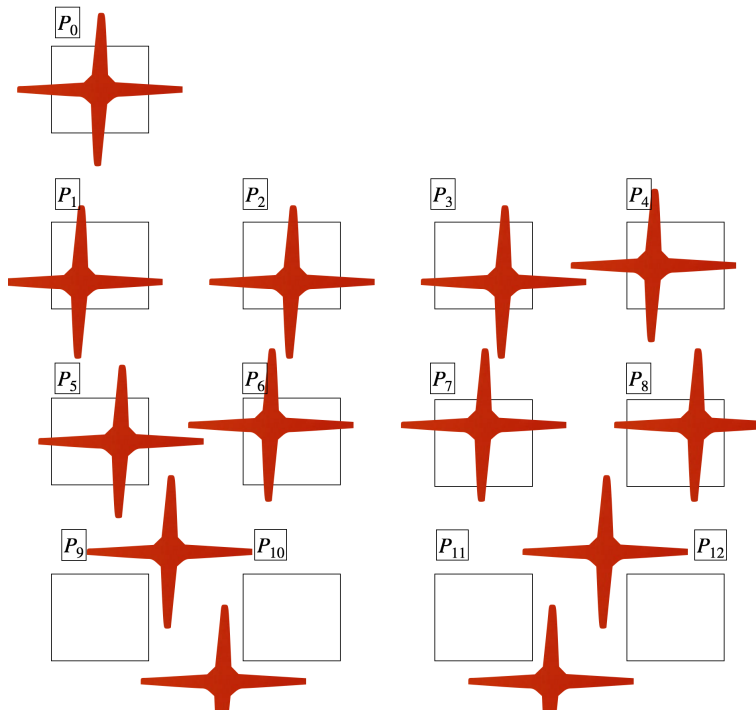


Figure 5.24: The different positions of the X-ray test beam during the Panter test. Nine positions with the source peak is in the MXT field of view , and four positions while the source peak is outside the field of view are performed.

Furthermore, the X-ray beam is placed in 13 positions in the MXT field of view. The different beam positions are visualized in Fig. 5.24. By definition, the P_0 position is used as a reference (0, 0) and is considered to be at the center of the camera plane: $y = 0.5$ and $z = 0.5$ in detector intrinsic coordinates. The list of beam positions and their offset in [arcmin] from the reference P_0 position are given in Tab. 5.4. For nine positions, the source peak is within the MXT field of view, and it is outside the field of view for four positions. These four positions are used to complete the study of the detector spectral response and energy calibration.

Table 5.4: List of X-ray beam positions in the MXT field of view during the Panter test campaign. The P_0 position is used as a reference (0, 0).

Position name	(y, z) offset [arc min]	source peak index [pixel]
P_0	(0, 0)	(127, 127)
P_1	(-15, -15)	(64, 64)
P_2	(0, -15)	(127, 64)
P_3	(15, -15)	(191, 64)
P_4	(-15, 0)	(64, 127)
P_5	(15, 0)	(191, 127)
P_6	(-15, 15)	(64, 191)
P_7	(0, 15)	(127, 191)
P_8	(15, 15)	(191, 191)
P_9	(50, 50)	NA
P_{10}	(-50, -50)	NA
P_{11}	(50, -50)	NA
P_{12}	(-50, 50)	NA

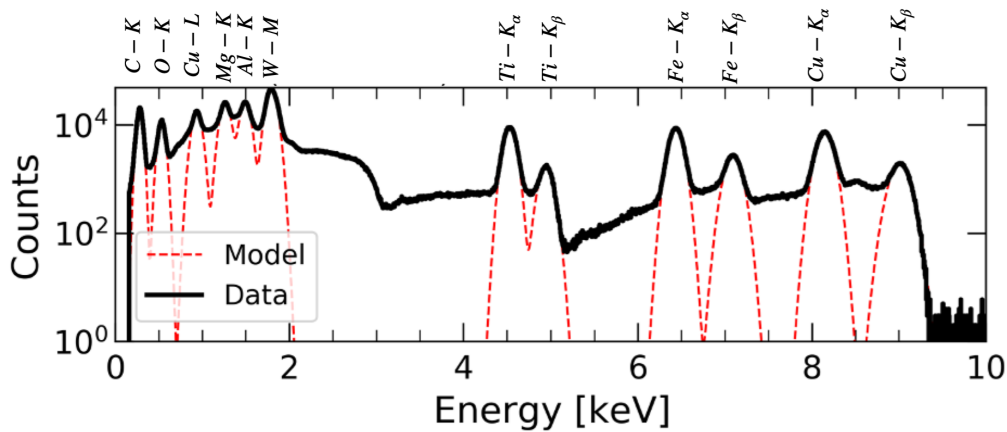


Figure 5.25: The energy spectrum obtained by the MXT at Panter by combining data from all test beam positions and all X-ray sources used during the test. Credit: the camera team/CEA.

The spectral study shows that MXT can detect the X-ray in the energy range of (0.2 - 10 keV), matching the requirements. Moreover, MXT can measure events down to 0.06 keV. The combined X-ray spectrum as seen by MXT is shown in Fig. 5.25.

Moreover the performance was tested at temperatures different from the nominal operating temperature of -65° C: -67° C, -69° C, -70° C, -71° C, and -75° C. The performance of the onboard localization algorithm is tested in all beam positions, energies, and temperatures mentioned above. The result of the localization performance is presented in the following sections.

The dark algorithm was stable during the test, and the dark maps computed onboard proved to be sufficient to reject dark noise, and this is seen in the energy spectrum in Fig. 5.25, where there is no dark noise background.

5.3.2 . Localization performance

The PSF is modeled as a function of energy using data from all test positions and energies mentioned in Sec. 5.3.1. Then the PSF at each energy is used to perform the localization algorithm in order to estimate the minimum number of photons needed to reach the targeted localization accuracy of $r_{90} = 120$ arcsec at each energy. Table 5.5 lists the minimum number of photons needed to achieve $r_{90} < 120$ arcsec with 5 minutes and 10 minutes.

Table 5.5: Minimum number of photons to achieve a localization accuracy of $r_{90} < 120$ arcsec after 5 and 10 minutes of observations. These values for r_{90} is given for the different source energies used at PANTER.

Energy	Number of photons (5 minutes)	Number of photons (10 minutes)
0.277	203 ± 6	237 ± 9
0.525	177 ± 6	222 ± 7
0.93	192 ± 6	255 ± 8
1.253	211 ± 7	264 ± 8
1.486	180 ± 6	216 ± 7
2.98	239 ± 7	336 ± 10
4.508	317 ± 10	445 ± 14
5.405	444 ± 14	524 ± 16
6.398	575 ± 18	622 ± 19
8.047	588 ± 18	710 ± 22

For the different energies and source positions, the source coordinates are computed and compared to the source true position. The onboard algorithm shows a good performance where it achieves a sub-pixel resolution for low energies. Figure 5.26 shows the offset in arcsec and in number of pixels of the source measured position with respect to the true beam position $\delta r = \sqrt{\delta y^2 + \delta z^2}$. It shows the position offset for six different source energies. For each energy, the offset is computed when the source position moves from P_0 to P_8 , for which the source peak is within the MXT field of view. First, the plot shows that the localization is the same along the y and z directions, and it is uniform over the entire detector.

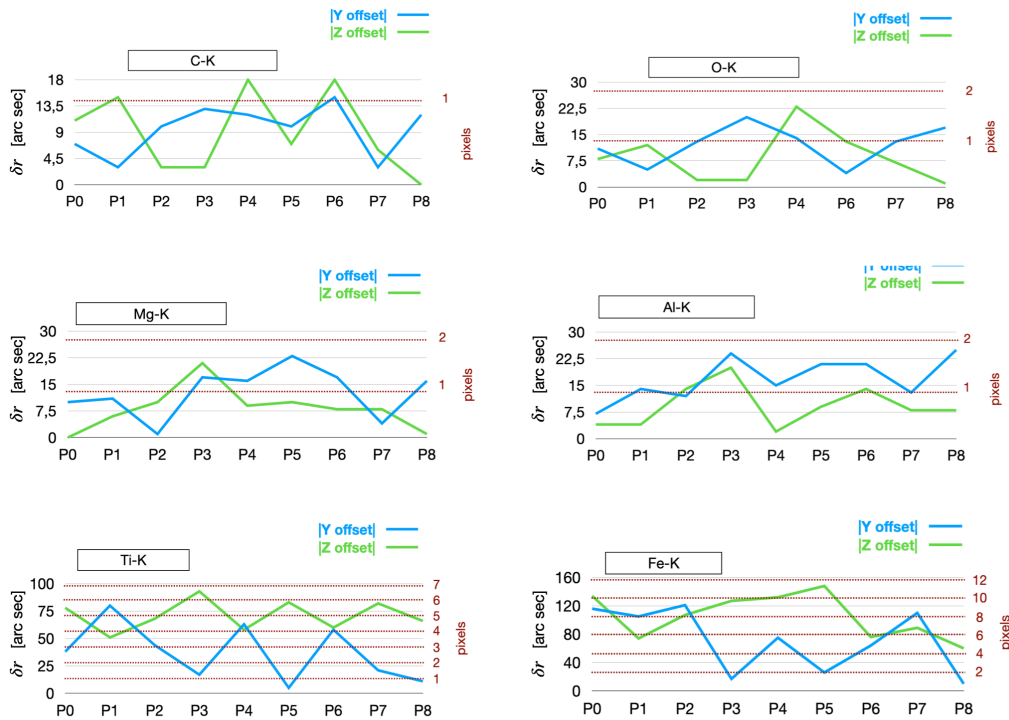


Figure 5.26: Localization performance for six photon energies: C-k (0.30 keV), O-k (0.53 keV), Mg-k (1.2 keV), Al-K (1.4 keV), Ti-K (5.20 keV), and Fe-K (6.40 keV). The offset between the measured position and the true position is evaluated in the y -direction (blue) and in the z -direction (green), and it is given in arcsec and pixels.

However, the localization algorithm shows better resolution at low energies because more photons are focused on the peak rather than the cross arms.

The Panter test was not ideal for evaluating the signal-to-noise ratio measurement since there is no X-ray background, and the number of photon counts is high. Hence the signal-to-noise ratio is always high during the test runs.

5.3.3 . Edge bias characterization

As mentioned in Sec. 5.1, the cross-correlation method is biased when the source is located near the detector edges due to spectral leakage. This bias is characterized during the Panter test campaign, where 13 near-the-edge positions were tested with an Al-K source. The measured position offset is computed for the 13 positions, and the results are shown in Fig. 5.27. Positions labeled with a b correspond to a 22 arcmin shift from the center and c correspond to a 25 arcmin shift from the center.

For some beam positions, the localization accuracy is degraded up to 50% as seen in Fig. 5.27 compared to the nominal case in Fig. 5.26. After applying the bias correction explained in Sec. 5.2.3, the localization accuracy is almost back to nominal values shown in Fig. 5.26 for

the Al-K source. Figure 5.28 shows an example of a photon map constructed while the source

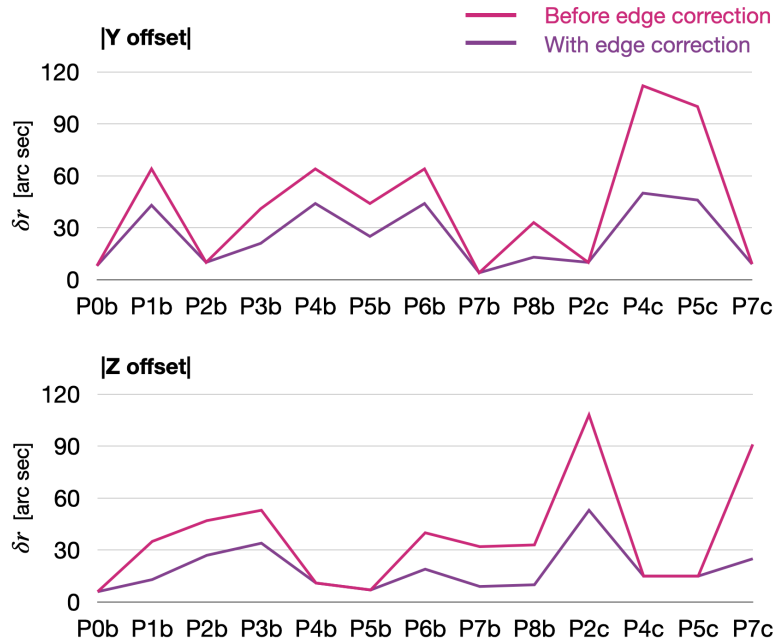


Figure 5.27: Localization performance tested for 13 near-the-edge positions performed with an Al-K (1.4 keV) source. The measured position offset is evaluated in the y direction (top) and in the z direction (bottom) with (purple curve) and without (pink curve) the edge-bias correction.

beam is placed at (25, 0) arcmin away from the detector center.

5.3.4 . Insensitive columns

The scientific performance during the Panter test campaign was tested with the nominal temperature (-65°C) and lower temperatures. The test shows that pixel columns in the detector can be insensitive when working outside the nominal temperature range. All the columns work normally at -65°C , -67°C , -69°C , one insensitive column appears at -70°C and two columns at -71°C and -75°C .

The onboard scientific algorithm can correct analytically the bias caused by insensitive columns as explained in Sec. 5.2.4. To characterize the insensitive columns effect and the correction performance with real data, some columns were deactivated at Panter while using the Al-K source. First, one bunch of 2, 5, 7, and 10 columns were deactivated. Then, two bunches: 5 in the left CAMEX and 3 in the right one. Then it is repeated with 5 columns in each CAMEX (see Fig. 5.29). Figure 5.30 shows the effect of the correction for different numbers of insensitive columns. After the correction, the localization performance is similar to the nominal case (in Fig. 5.26) where all columns are active.

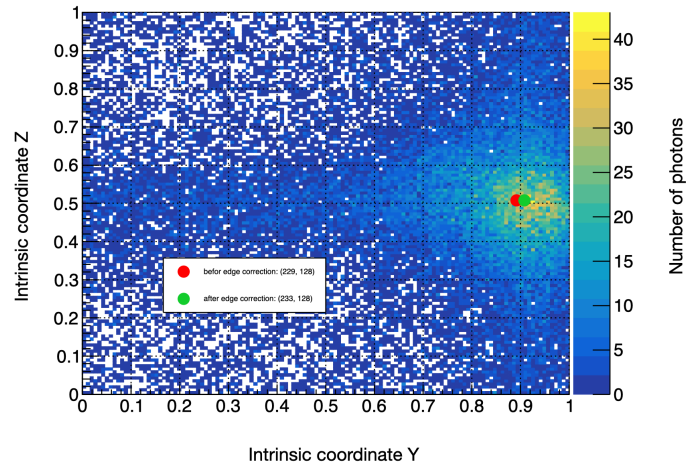


Figure 5.28: Example of photon map constructed during Panter test while the source beam is placed near the edge of the MXT filed of view. The source position before (red point) and after (green point) the bias correction is labeled on top of the photon map

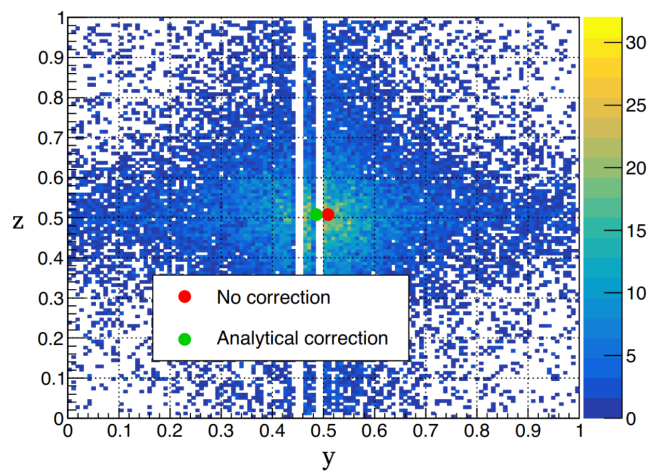


Figure 5.29: Example of a photon map constructed by the MXT science partition during the Panter test, while deactivating 10 pixels columns.

The Panter test campaign allowed us to fully characterize the MXT instrument, and it shows that the scientific partition can be operated reliably and in a long run. Using the model of the PSF, the localization algorithm presents a performance that complies with scientific requirements: a source detected with a few hundred photons can be localized with an accuracy better than 120 arcsec. The scientific partition also includes features to compensate for hardware effects discovered during the development process, like the presence of insensitive columns of

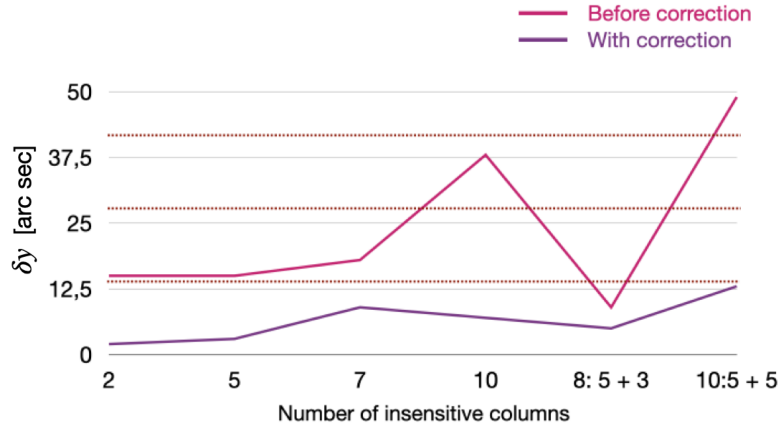


Figure 5.30: Localization performance tested with insensitive columns, for an Al-K (1.4 keV) source, and with a P_0 beam position. The measured position offset is evaluated before (pink curve) and after (purple curve) applying the correction function of the insensitive columns. The offset is given in arcsec and pixel units.

pixels in the detector when working outside nominal conditions. The scientific partition is able to recover the loss of localization accuracy almost completely. The Panter test has proven that the main goal of MXT of rapid localization of GRB afterglows in an autonomous way can be reached. The next step is to further characterize the MXT onboard scientific algorithm with astrophysical scenarios with various spectral and temporal properties. This is explained in the following chapter.

6 - Observation of GRBs with the MXT

Contents

5.1	Source localization method	113
5.1.1	The point spread function formatting	114
5.1.2	Cross-correlation	114
5.1.3	Source position angles	117
5.1.4	Signal-to-noise ratio	119
5.1.5	Multi-source detection	126
5.1.6	Configuration of localization algorithm	128
5.2	Results and characterization	130
5.2.1	The source intensity	130
5.2.2	The photon map resolution	131
5.2.3	Edge bias	133
5.2.4	Insensitive columns	135
5.2.5	Multiple sources	139
5.2.6	Signal-to-noise ratio	140
5.3	The MXT flight model test at Panter	145
5.3.1	Test overview	145
5.3.2	Localization performance	148
5.3.3	Edge bias characterization	149
5.3.4	Insensitive columns	150

The Panter flight model test has validated the onboard scientific software in terms of its functionality, compliance with the requirements, and its ability to run for a long observation. However, the MXT scientific software must be tested and characterized with real GRB scenarios.

As discussed in Sec. 3.1, the sensitivity and the high energy resolution of the MXT allow to study the spectral properties of GRB X-ray afterglows like the spectral index and the distribution of energetic particles. In addition, the MXT is able to study the temporal properties and evolution of the X-ray afterglows. Analyzing the spectral and temporal properties of the X-ray afterglows with the MXT must be tested by running the algorithm with a simulation of a realistic scenario of GRB X-ray afterglows.

For this purpose, a simulation is developed to simulate an X-ray afterglow observation with the MXT based on GRBs observed by the Swift mission. The simulation of GRB observation with the MXT is explained in Sec. 6.1. In Sec. 6.2, the observation of short-duration GRBs is studied. Section 6.3 presents some prospects and perspectives studies for the MXT.

6.1 . Simulation of realistic GRB scenarios

As a part of the SATANDLIGHT simulation tool (see 3.5), a program is developed to simulate realistic observation of X-ray afterglows by the MXT. This section describes the features and the validation of the simulation. Examples of simulated observations are also presented. Furthermore, the localization algorithm explained in Sec. 5.1 is applied to a simulated sample of realistic observations.

6.1.1 . Simulation features and validation

This section explains the simulation of the MXT count $\mathcal{C}(E, t) = d^2N/dEdt$. The count rate can be factorized: $\mathcal{C}(E, t) = f_1(t)f_2(E)$. The spectrum $N(E)$ (resp. the light curve $\mathcal{L}(t)$) is computed by integrating $\mathcal{C}(E, t)$ over time (resp. over energy) as in the Eqs. 3.5 and 3.6. In order to simulate $\mathcal{C}(E, t)$, the $f_1(t)$ and $f_2(E)$ functions are computed with real data or with a physical model.

The f_2 function can be modeled by a simple power law, including the X-ray absorption in the host galaxy and the intergalactic medium as in Eq. 1.8, but with a different normalization A :

$$f_2(E) = A \times E^\lambda \times \exp(-N_H^{int} \sigma(E)) \times \exp(-N_H^{Gal} \sigma(\frac{E}{(1+z)})), \quad (6.1)$$

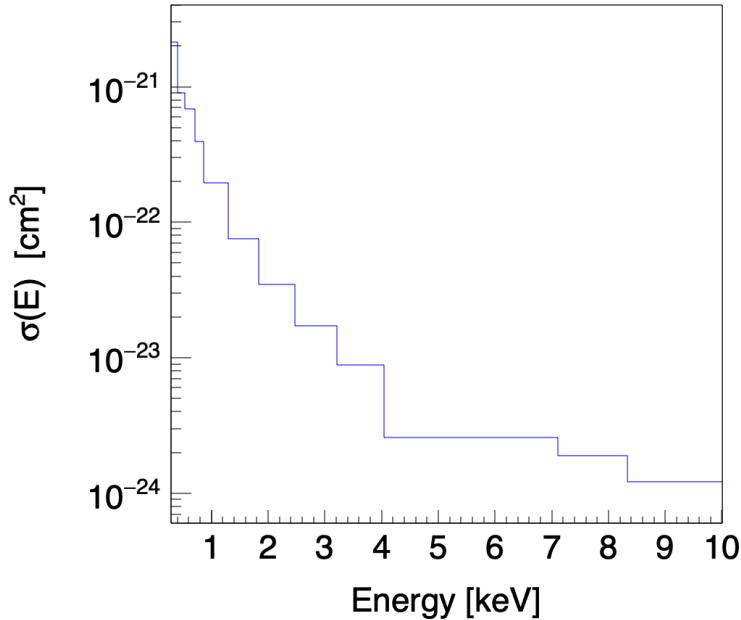


Figure 6.1: The cross section in [cm^2] of the photoelectric effect at a given energy within the range of (0.2 - 10 keV) based on elements abundances in the solar system [194]

where $\sigma(E)$ is the cross section of the photoelectric effect, N_H^{int} is the intrinsic column density, N_H^{Gal} is the galactic column density (see Sec. 1.2.3.1). We can rewrite Eq. 3.5 as:

$$\begin{aligned}\mathcal{L}(t) &= \int_{E_1}^{E_2} \mathcal{C}(E, t) dE, \\ &= f_1(t) \int_{E_1}^{E_2} f_2(E) dE.\end{aligned}\tag{6.2}$$

The $f_1(t)$ is then given by:

$$f_1(t) = \frac{\mathcal{L}(t)}{A \int_{E_1}^{E_2} E^\lambda \times \exp(-N_H^{int} \sigma(E)) \times \exp(-N_H^{Gal} \sigma(E/(1+z))) dE},\tag{6.3}$$

where we substitute f_2 by Eq. 6.1. Finally, the count rate is given by:

$$\mathcal{C}(E, t) = \frac{\mathcal{L}(t) \times E^\lambda \times \exp(-N_H^{int} \sigma(E)) \times \exp(-N_H^{Gal} \sigma(E/(1+z)))}{\int_{E_1}^{E_2} E^\lambda \times \exp(-N_H^{int} \sigma(E)) \times \exp(-N_H^{Gal} \sigma(E/(1+z))) dE},\tag{6.4}$$

To compute the count rate, the $f_2(E)$ model parameters: λ , N_H^{int} , N_H^{Gal} , z , and $\sigma(E)$ are required. In addition, the data for the light curve is needed.

The cross-section $\sigma(E)$ of the photoelectric effect at a given energy is extracted from paper [194], and plotted in Fig. 6.1.

The light curve data, λ , N_H^{int} , N_H^{Gal} , and z values, can be obtained from catalogs of GRBs. In this study, we choose to use the Swift database, where 1550 GRBs were detected among which 1253 X-ray afterglows were observed by the Swift/XRT between 2005 and today (26th July 2022). the Swift/XRT database offers the most extensive homogeneous set of GRBs afterglow observed up to today.

From the XRT spectra repository one can get the model parameters for a given GRB as seen in Fig. 6.2. The light curve $\mathcal{L}(t)$ can be obtained from the XRT light curves repository. Note that the unabsorbed light curves must be considered because the absorption is included in the spectrum model.

N_H (Galactic)	$4.74 \times 10^{21} \text{ cm}^{-2}$
N_H (intrinsic)	$0 (+8.20 \times 10^{20}, -0) \text{ cm}^{-2}$
z of absorber	0
Photon index	$2.32 (+0.26, -0.21)$
Flux (0.3-10 keV) (Observed)	$9.9 (+1.9, -1.4) \times 10^{-13} \text{ erg cm}^{-2} \text{ s}^{-1}$
Flux (0.3-10 keV) (Unabsorbed)	$2.0 (+0.4, -0.7) \times 10^{-12} \text{ erg cm}^{-2} \text{ s}^{-1}$
Counts to flux (obs)	$3.38 \times 10^{-11} \text{ erg cm}^{-2} \text{ ct}^{-1}$
Counts to flux (unabs)	$6.66 \times 10^{-11} \text{ erg cm}^{-2} \text{ ct}^{-1}$
W-stat (dof) <small>What's this?</small>	118.04 (126)
Spectrum exposure	11.4 ks

Figure 6.2: An example of the parameters of the spectrum power-law model, obtained from the Swift/XRT database [122]

Using the data from Swift/XRT to get $\mathcal{C}(E, t)$ in Eq. 6.4, gives the number of counts detected by XRT $\mathcal{C}_{xrt}(E, t)$. In order to get the count rate detected by the MXT $\mathcal{C}_{mxt}(E, t)$, $\mathcal{C}_{xrt}(E, t)$ must be deconvolved with the XRT effective area and convolved with the MXT effective area as:

$$\mathcal{C}_{mxt}(E, t) = \mathcal{C}_{xrt}(E, t) \times \frac{\mathcal{S}(E)_{mxt}}{\mathcal{S}(E)_{xrt}}, \quad (6.5)$$

$\mathcal{C}_{mxt}(E, t)$ is then used to simulate MXT observations. The MXT and XRT effective areas are shown in Fig. 6.3.

One could use the opposite of what we used in our simulation, i.e., use a model for $f_1(t)$ and get the spectrum data for $f_2(E)$ from the Swift/XRT database. However, modeling the light curve is more complex than modeling the spectrum because the X-ray light curve can not be given by a single model. Instead, it is given by one or several broken power laws as discussed in Sec. 1.2.3.2. Hence, modeling the spectrum and using the light curve data gives a more reliable simulation.

The simulation of $\mathcal{C}(E, t)$ must be tested and validated before using it in further studies. Therefore, a GRB with a bright X-ray afterglow, GRB091020 [195] is selected. The light curve of GRB091020 goes through four out of the five phases explained in Sec. 1.2.3.2. It has a steep decay phase, a normal decay phase, a fast decay phase, and an X-ray flare, as seen in Fig. 6.4.

The unabsorbed light curve and the $f_2(E)$ parameters values are downloaded from the XRT database. $\mathcal{C}(E, t)$ for XRT is computed in the simulation with those input data following Eq. 6.5. The simulated XRT $\mathcal{C}_{xrt}(E, t)$ is shown in Fig. 6.5.

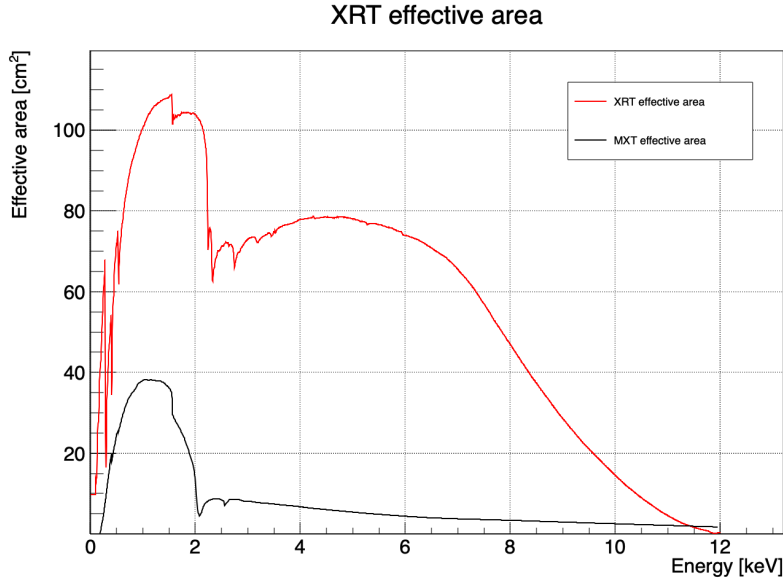


Figure 6.3: The MXT effective area (in black) compared to XRT effective area (in red)

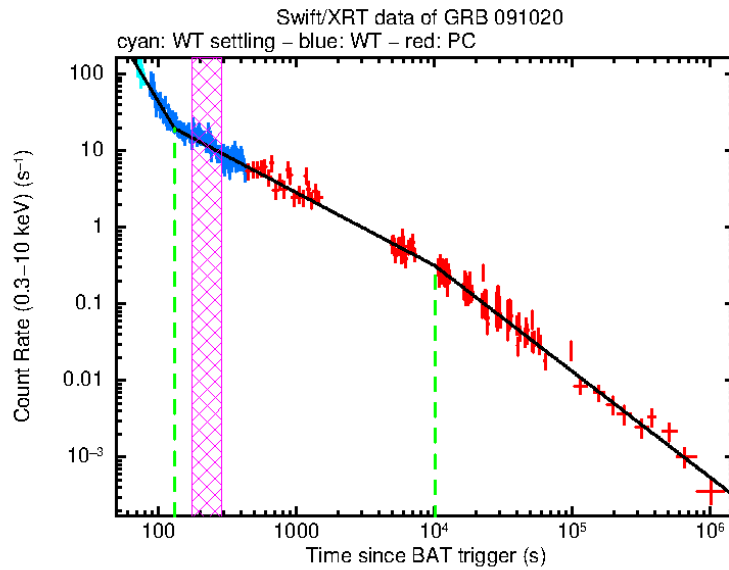


Figure 6.4: The light curve of GRB091020 observed by Swift/XRT. The light curve is fitted with multiple broken laws, and it has four different phases. The flare is labelled with the hashed pink region Credit [122]

From the count rate in Fig. 6.5, the light curve and the spectrum are computed using Eqs. 3.5 and 3.6. The method is validated if these simulated light curve and spectrum are the same as the input data. Figure 6.6 shows that the simulated light curve as observed by XRT compared to the real data points extracted from the XRT database. It shows that the

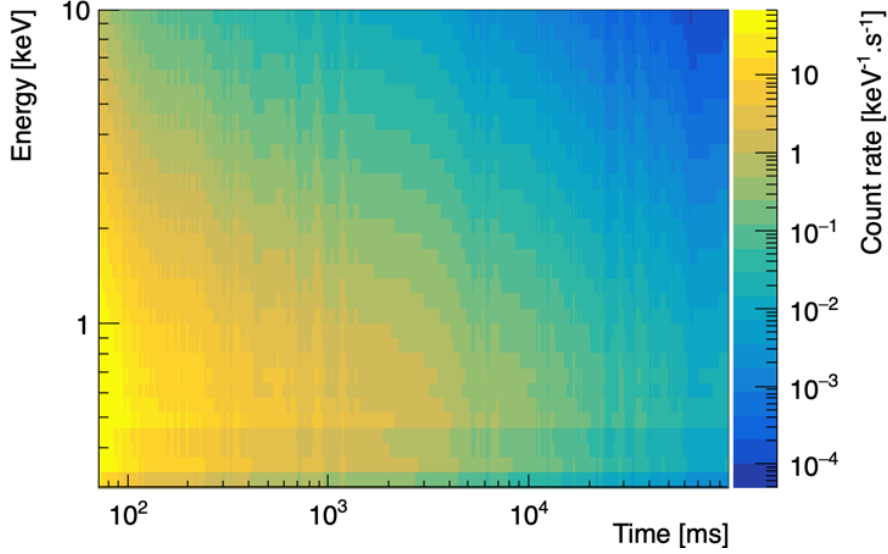


Figure 6.5: The simulated count rate of GRB091020 as observed by XRT.

simulated light curve is equivalent to the real one. In the simulation, we add the option of using a logarithmic interpolation to fill the gaps between the XRT real data points due to instrument limitations.

Concerning the spectrum, the spectrum observed with the PC¹ mode from T_0 (which is the Swift/BAT trigger time) up to 10^4 s is considered. The spectrum parameters for this observation are given in Tab. 6.1.

Table 6.1: Spectrum parameter of GRB091020 for the PC mode after 10^4 s of observation.

N_H^{Gal}	$1.45 \times 10^{20} \text{ cm}^{-2}$
N_H^{Int}	$8.4 \times 10^{21} \text{ cm}^{-2}$
z	1.71
λ	2.01
flux (0.3-10 keV) (observed)	$4.3 \times 10^{-11} \text{ erg. cm}^{-2} \cdot \text{s}^{-1}$
Counts to flux (observed)	$3.29 \times 10^{-11} \text{ erg. cm}^{-2} \cdot \text{count}^{-1}$
Counts to flux (unabsorbed)	$4.04 \times 10^{-11} \text{ erg. cm}^{-2} \cdot \text{count}^{-1}$

The simulated and real spectrum are shown in Fig. 6.7, but with a different energy binning, so it is difficult to compare the two spectra by eye. In the Swift/XRT database, the access to the spectrum data is not straightforward. However, to compare the simulated spectrum to the true one, we computed the average counts per second from both spectra. For the simulated spectrum, the count/s is computed by integrating the spectrum. For the real data, the count/s is given by dividing the "flux (observed)" over the "counts to flux (observed)" in the Tab. 6.1.

¹The Photon Counting (PC) mode is one of the four observation modes of XRT [196]

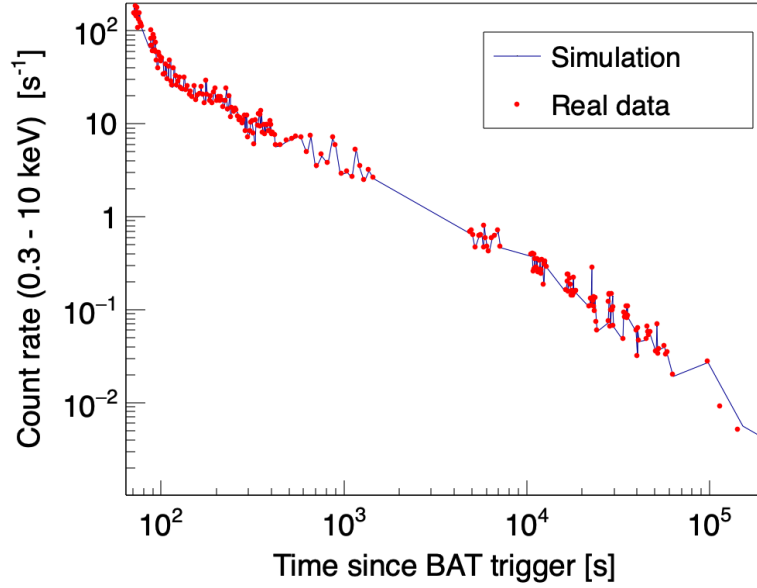


Figure 6.6: The simulated light curve of GRB091020 as observed by XRT (blue line), compared to real XRT data (red points).

From the real data, we have ~ 1.31 count/s after 10^4 s in the energy range of (0.3 - 10 keV). At the same energy range and duration, we get 1.301 count/s from the simulated spectrum, which is ~ 0.6 % less than the real data, i.e., it is equivalent to the real observed spectrum. The resulting light curve and spectrum from the simulation validate the simulation, they proved that it is able to simulate the temporal and spectral features of GRBs based on ones observed by similar missions. The next step is to use $\mathcal{C}(E, t)$ to simulate observations with MXT.

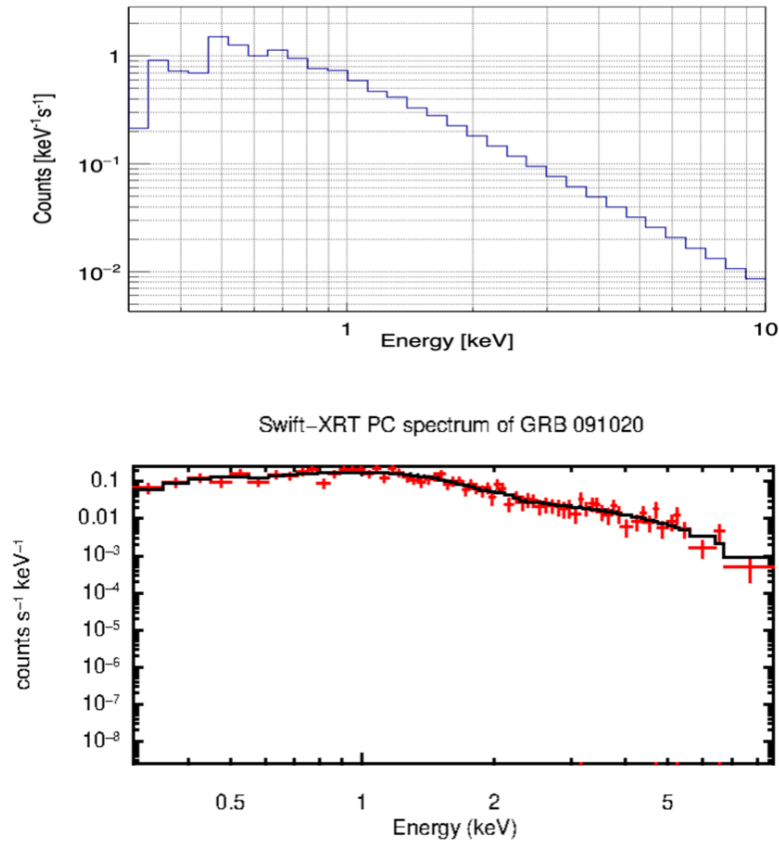


Figure 6.7: The XRT simulated spectrum of GRB091020 after 10^4 s of observation (top). The spectrum observed by the XRT for the same GRB with the same duration (bottom).

6.1.2 . Simulation of MXT observations

In this section, the `sn1-sequence` program that is explained in Sec. 3.5 is used to generate observation sequences based on the count rate derived in Sec. 6.1.1. To have a realistic observation, the intrinsic detector noise is simulated first.

To simulate noise in the MXT detector, a sequence of 400 camera images captured at Panter with observation/dark mode is used. From this sequence, the mean $\mu_I[i][j]$ and standard deviation $\sigma_I[i][j]$ is computed per pixel. Afterward, along simulated sequence of camera frames, the noise value for pixel (i, j) is generated randomly by SATANDLIGHT from a Gaussian distribution with mean value = $\mu_I[i][j]$ and standard deviation = $\sigma_I[i][j]$.

Using the same sequence of frames, the offset O and threshold T maps are computed using Eq. 4.8 and Eq. 4.11, respectively. O and T maps are used to select pixels above the noise level during the observation as in Eq. 4.5.

An observation of GRB091020 is simulated from 0 to 6×10^4 s after the trigger:

- First, $\mathcal{C}_{xrt}(E, t)$ (in Fig. 6.5) must be deconvolved with the XRT effective area $\mathcal{S}_{xrt}(E)$ to get the flux $\mathcal{F}(E, t) = \mathcal{C}_{xrt}(E, t)/\mathcal{S}_{xrt}(E)$ in [count. keV⁻¹. s⁻¹. cm⁻²].
- Then, the source with flux $\mathcal{F}(E, t)$ is simulated to be on axis at the center of the MXT field of view: $\theta_s = 0$, and ϕ_s is irrelevant.
- $\mathcal{F}(E, t)$ is convolved with the MXT effective area $\mathcal{S}_{mxt}(E)$ (in Fig. 3.13) to get $\mathcal{C}_{mxt}(E, t) = \mathcal{F}(E, t) \times \mathcal{S}_{mxt}(E)$.
- The total number of photons to be generated is computed by Eq. 3.7. Each photon is given a random energy and time following the count rate distribution $\mathcal{C}_{mxt}(E, t)$.
- The photon position (y_p, z_p) at the MXT detector plane is given by Eq. 3.1, and the PSF model (in the left plot of Fig. 3.11) is included to distribute the photons following the MXT optical design configuration and get their final position in the detector.
- Each photon transfers its energy to the camera pixels following a Gaussian distribution centered on the final position and weighted with the photon energy. The photon energy is added on top of the detector intrinsic noise
- A source of cosmic ray and X-ray background can be added. In this observation study, a cosmic ray source is added, but no X-ray background is included in order to compare only photons from the GRB091020 with XRT.
- Finally, camera images are integrated and saved each 100 ms. An example of a camera image that is simulated during the observation is shown in Fig. 6.8, where photons and a cosmic ray are hitting the detector and add their energy on top of noise

The next analysis step is to process the camera images to identify X-ray photons and build the light curve and the spectrum. The image processing is done as explained in Chap. 4. In summary: the O and T maps are used to select pixels above the noise level that could be associated to X-ray photons. The selected pixels are clustered as they could be associated with the same astroparticle. The cluster is considered to be a photon if it satisfies one of the patterns in Fig. 4.13. The identified photons are used to build the light curve following their arrival time at the MXT detector, which corresponds to the camera frame time. The spectrum of the photons is constructed as well. Moreover, the photons are accumulated in a photon map in order to test the localization of the source with time as well. In this simulation, no bad pixels (dead or bright) or insensitive columns (see Sec. 4.2.4) are included. No selection in the photons energy or multiplicity (see Sec. 4.2.3) is applied.

Figure. 6.9 shows the resulting light curve of GRB091020 as observed by the MXT (in black) compared to the one observed by the XRT (in red). Each time bin in the plot is 1 s. The plot shows that the MXT detects fewer photons than the XRT. For example, after 10 minutes of observation, the XRT detects about 3600 counts. If we include the interpolation, XRT detects

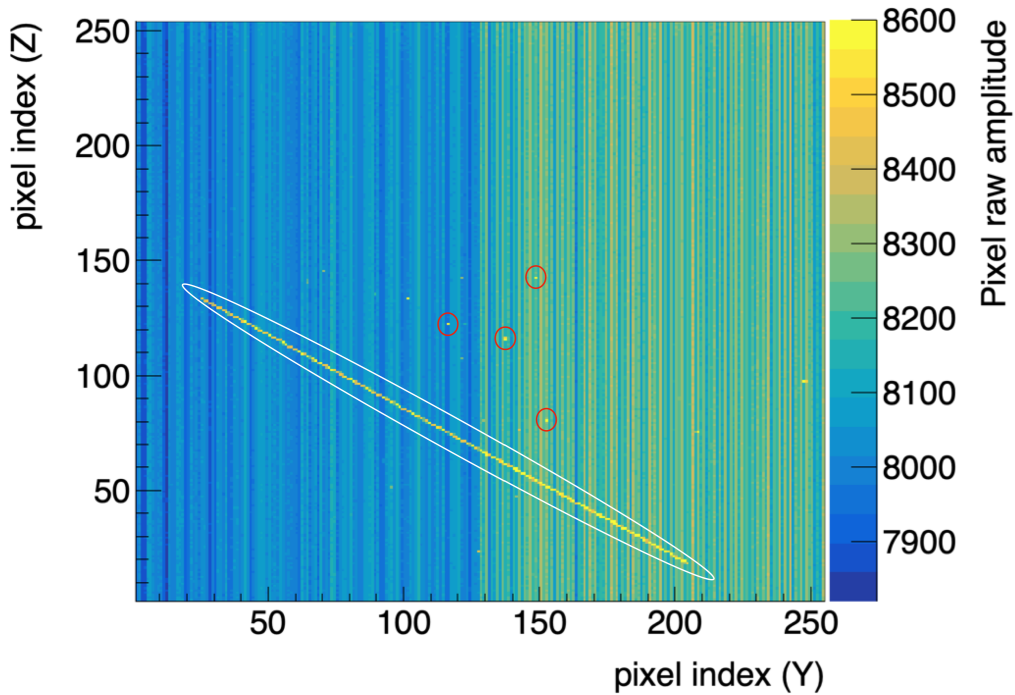


Figure 6.8: A camera image saved from a simulation of GRB091020 observed with the MXT. The image is captured 74 s after the trigger. One cosmic ray (in yellow) and a few photons (red circles) deposit their energies on top of noise in the detector. The simulation is performed using the SATANDLIGHT toolkit.

about 7100 counts. Meanwhile, the MXT detects about 28% of what XRT detects; it detects 1030 counts and 2030 counts if we include the interpolation. This is expected since the MXT has a smaller effective area than the XRT, as shown in Fig. 6.3.

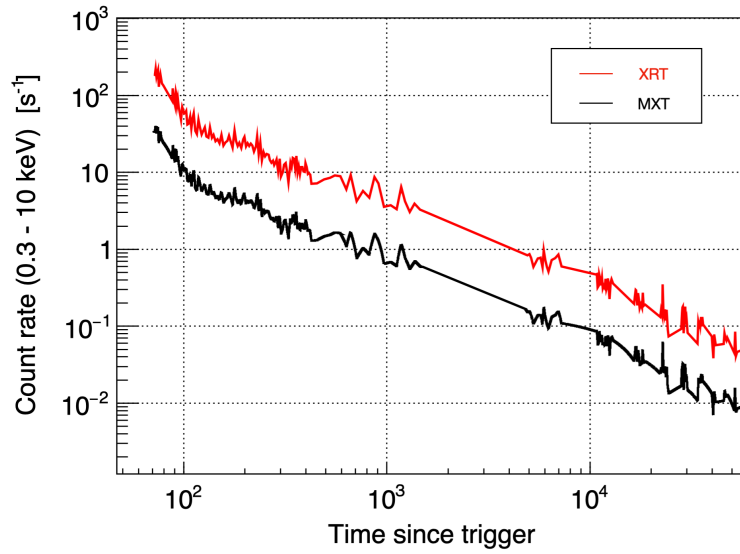


Figure 6.9: The simulated light curve of GRB091020 as observed by the MXT (in black) and as observed by the XRT (in red), the logarithmic interpolation is included in both.

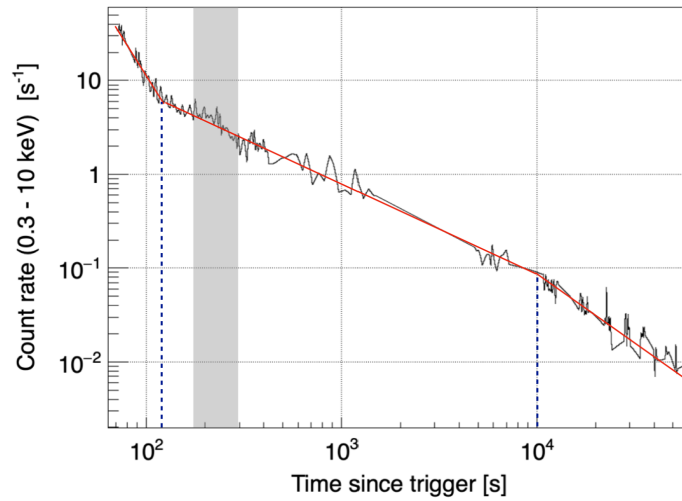


Figure 6.10: The simulated light curve of GRB091020 as observed by the MXT (in black). The light curve has three decaying phases and by an X-ray flare phase that is shaded with gray rectangular. The best fit of the different decaying phases is shown in red. The X-ray flare is excluded from the fit.

Although the MXT detects fewer counts than XRT, it is able to detect and hence, charac-

terize the temporal evolution of the afterglow as seen in Fig. 6.10, where three phases of decays can be fitted. In addition, the X-ray flare is observed starting around 190 s and up to 300 s. The number of the observed count at the beginning 30 s of the flare is about 40 counts, which is 50% more than the counts observed in the previous 30 s.

The spectrum of GRB091020 as observed by the MXT is shown in Fig. 6.11, and it is compared to the GRB091020 spectrum as observed by the XRT. The absorption at low X-ray energies is seen in the MXT spectrum, which allows to study and characterize the N_H parameter. At about 2.2 keV energy, we notice a small peak, which follows the shape of the MXT effective area (see Fig. 6.3).

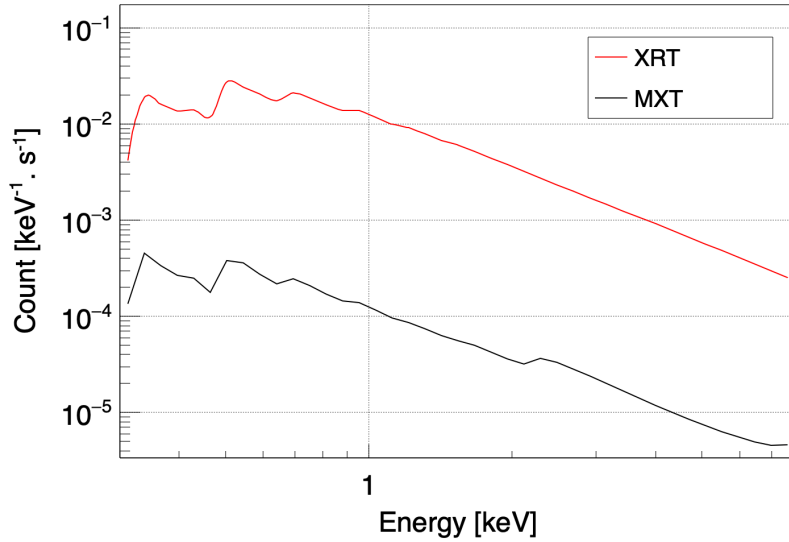


Figure 6.11: The simulated spectrum of GRB091020 as observed by the MXT (in black) and as observed by the XRT (in red).

As the photons are accumulated in the photon map, the total cumulative number of photons is computed over time. Moreover, the localization uncertainty given by the r_{90} is computed following Eq. 5.49. In this simulation, we did not inject background photons. To have realistic results, in the calculation of r_{90} , we added a background with a rate of 1 counts/s. The cumulative number of photons and the r_{90} as a function of the observation time are seen in Fig. 6.12.

At the first ~ 100 s of observation, the number of cumulative photons is increasing dramatically, while the cumulative number of the background photons is relatively still low, as seen in Fig. 6.12. Hence, the r_{90} improves. As the observation time increases, the number of GRB cumulative photons starts to stabilize. Meanwhile, the background has a constant rate. Thus the total cumulative number of backgrounds is increasing. As the cumulative number of backgrounds increases to reach the number of cumulative photons, the r_{90} starts to degrade.

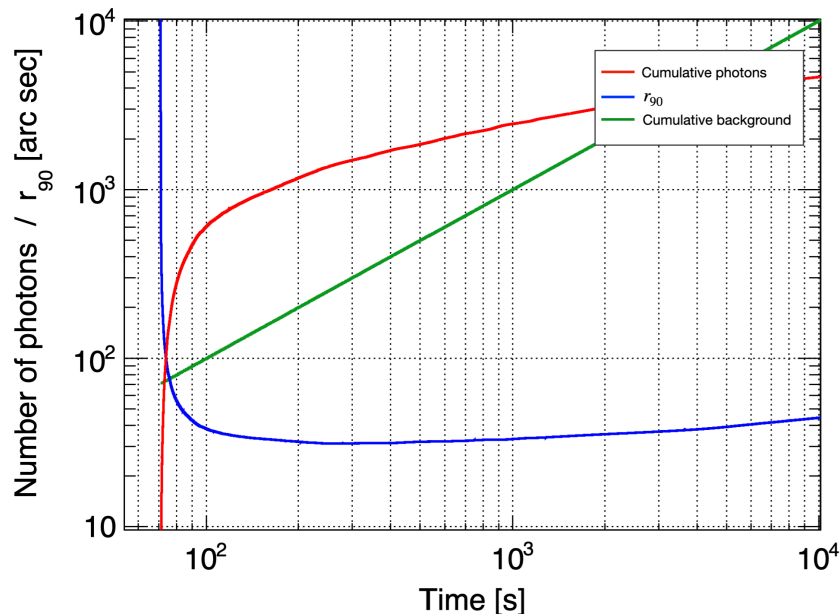


Figure 6.12: The cumulative number of photons from GRB091020 (in red), the cumulative number of background photons (in green), and the localization uncertainty, r_{90} (in blue). The higher the signal-to-noise ratio, the lower the localization uncertainty.

In the following section, the simulation is applied to all GRBs observed by the XRT GRBs in order to test the MXT localization.

6.1.3 . Localization of real GRBs sample with the MXT

This section tests the percentage of GRBs that would be localized with the MXT with an accuracy below two arcmin after 10 min of observation. To do so, we take advantage of the high statistics of GRBs observed by the XRT. In this study, we consider all GRBs (= 1550 GRBs) observed by Swift up to today (26th July 2022). If a GRB is observed by the XRT (1254 GRBs), the X-ray light curve $\mathcal{L}(t)$ is downloaded. These light curves are used as input to simulate observations with the MXT, as explained in Sec. 6.1.2. An observation of 10 min is considered. The total number of counts observed by the MXT after 10 min is computed. A background with a rate of 1 count/s is added. From the total number of counts observed by the MXT and the total number of simulated background counts, the signal-to-noise ratio is computed after 10 min. Finally, the r_{90} is computed using Eq. 5.46.

Since the MXT is triggered by the ECLAIRS (see Sec. 2.3), the probability of a GRB detection by ECLAIRS must be included. First, we assume that ECLAIRS observes all GRBs observed by Swift/BAT that triggers the XRT. Figure. 6.14 shows that the MXT localizes up to 54% of GRBs below two arcmin after 10 min. Among them, 70% of GRBs are localized to better than one arcmin, and 36% are localized to better than 30 arcsec, if we did not consider any detection constraints by ECLAIRS.

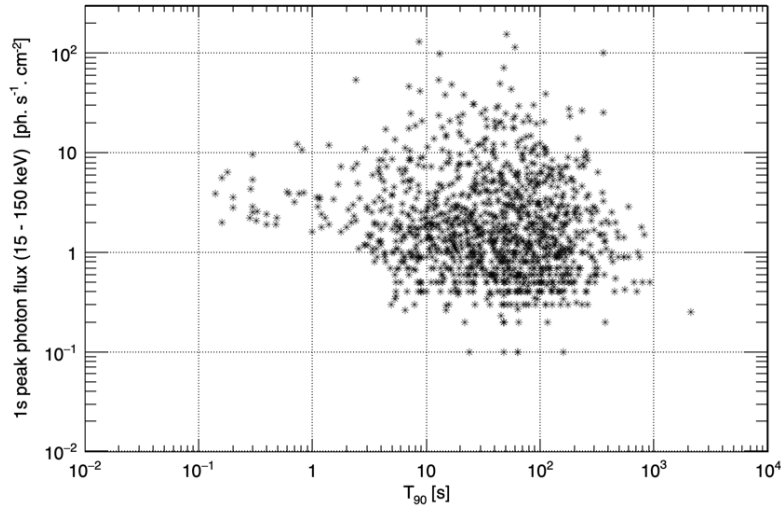


Figure 6.13: The peak photon flux after 1 s in the energy range 15 - 150 keV as a function of T_{90} for the Swift GRBs.

However, ECLAIRS is less sensitive than BAT. Hence, some GRBs observed by BAT would have a lower probability of being observed by ECLAIRS [136]. The GRBs that have $\geq 50\%$ and $\geq 90\%$ probability of detection by ECLAIRS with a signal-to-noise ratio > 8 are selected to perform the analysis to test the MXT localization. The probability of detection depends on two parameters: the duration parametrized by T_{90} and the photon flux. The ECLAIRS would have a probability of detection of 50% if $T_{90} > 0.1$ s and if the flux is more than $0.07 \text{ ph.s}^{-1}.\text{cm}^{-2}$. ECLAIRS would have a probability of detection of 90% if $T_{90} > 0.7$ s and if the flux is more than $0.3 \text{ ph.s}^{-1}.\text{cm}^{-2}$ [136]. The peak flux after 1 s distribution of the Swift GRBs vs T_{90} is shown in Fig. 6.13. Among 1550 GRBs detected by Swift, ECLAIRS observes 1283 GRBs ($\sim 83\%$) with a probability of 50%, where the X-ray afterglow is detected for $\sim 80\%$ of them.

Figure 6.14. shows the percentage of XRT GRBs that would be localized by the MXT with a given uncertainty (r_{90}). It shows that the MXT localizes 65% of XRT GRBs with uncertainty less than two arcmin after 10 min of observation for the GRB with detection probability $> 50\%$.

If we select GRBs that would have a $\geq 90\%$ detection probability by ECLAIRS, we end up with 696 GRBs ($\sim 45\%$). From the 696 GRBs, XRT observes the X-ray afterglow of $\sim 82\%$ of them, 572 GRBs. The MXT localizes $\sim 80\%$ of the 572 GRBs to better than two arcmin after 10 min of observation, as seen in Fig. 6.14. Table. 6.2 summarizes the result of the MXT localization of the XRT GRBs.

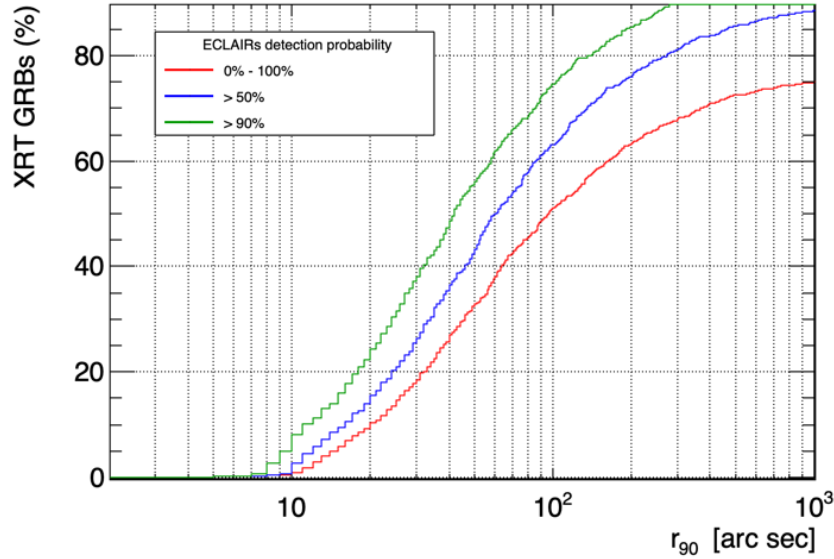


Figure 6.14: Cumulative curve of the XRT GRBs (represented in a percentage) as observed and localized with the MXT after 10 min of the observation. GRBs that have $>90\%$ (green), $>50\%$ (blue), and $(0\% - 100\%)$ (red) probability of being detected by ECLAIRs are selected.

Table 6.2: The percentage of the XRT GRBs that are detected by the MXT with a given uncertainty and for a given detection probability by ECLAIRs.

ECLAIRs detection probability	< 120 arcsec	< 60 arcsec	< 30 arcsec
$\geq 90\%$	78%	64%	37%
$\geq 50\%$	67%	53%	25%
0% – 100%	54%	38%	19%

The list of Swift GRBs that have a 90% and 50% detection probability with ECLAIRs are given in the Appx. A.

In the following section, short-duration Swift GRBs are studied.

6.2 . Short GRBs study

The short-duration GRBs are selected to be studied in this section since their progenitors, the merger of two binaries including at least one neutron star (see Sec. 1.2.1.3), have a higher probability of being observed in gravitational waves than the progenitors of the long-duration GRBs which are the supernovae.

Observation of gravitational-wave and the electromagnetic radiations from the same GRB events is required to understand the GRB from the early moments up to the fading of the afterglow. So far, only one GRB event was observed in the gravitational wave and the elec-

tromagnetic radiations simultaneously, which is the short-duration GRB170817A discussed in Sec. 1.3.3.

In this section, we aim at studying all the short GRBs using a selected sample of short GRBs from the Swift database with favorable observing conditions for the redshift determination. Measuring the redshift of GRBs allows us to study them in the source reference frame and build their luminosity light curves. First, the sample was built with GRBs observed from 2004 until June 2013 [197]. It includes 16 short GRBs, where the redshift is measured for $\sim 69\%$ (11 short GRBs). During my PhD, I worked on building an extended sample of short GRBs to include the observed ones up to the end of 2021 to increase our statistics. This work has been done with the XRT team in the Astronomical Observatory of Brera-INAF in Italy. The selection criteria of the sample are explained in the following section.

6.2.1 . Selection criteria

As mentioned in Sec. 1.1.1.2, the main separation between the long and short GRBs is the duration of their prompt emission parametrized by the T_{90} value. Among a sample of 1513 GRBs, all GRBs with $T_{90} \leq 2s$ are selected, so we end up with a sample of 132 short GRBs. Some GRBs have a T_{90} greater than 2 s, but they have a short GRB-like spectrum, these GRBs are called short GRBs with extended emission. In the Swift database, seven GRBs have an extended emission, and they are added to the sample to have 139 short GRBs. Afterward, a selection is applied based on the XRT re-pointing time. All short GRB events observed immediately (< 200 s) after the trigger are selected. This selection ensures that the early time emission is observed, which is necessary for the rapid follow-up from the ground and the determination of the event redshift. After this selection, the sample consists of 95 short GRBs.

A second selection is applied based on the galactic extinction A_ν , which is the absorption and scattering of electromagnetic radiation by the medium between an emitting astrophysical object and the observer. A_ν is computed using the extinction calculator tool of the NASA/IPAC extragalactic database [198]. A short GRB is selected if it has $A_\nu < 0.5$, which increases the probability of the ground-based optical follow-up. With this selection, the sample contains 71 short GRBs, where the redshift is measured almost for half of them (36 short GRBs). The *total* sample consist of all GRBs after this selection.

Finally, to increase the percentage of the redshift completeness we restrict ourselves to the short GRBs that are bright enough with a peak photon flux $> 3.5 \text{ ph.s}^{-1}.\text{cm}^{-2}$ in the energy range of 15-150 keV. This selection is applied by Michela Maria Dinatolo, a former student of the XRT team. 41 short GRBs are left after the selection on the flux as shown in Tab. 6.3, we name this sample the *complete* sample.

Table 6.3: The complete sample of the short GRBs (41 GRBs) after applying selection on the XRT pointing time T_0 , the galactic extinction, and on the photon flux after 64 ms.

GRB	T_{90} [s]	Ph-flux [$\text{ph. s}^{-1}.\text{cm}^{-2}$]	XRT T_0 [s]	XRT r_{90} [arc sec]	z
051221A	1.4	40.7	88	1.4	0.547
060313	0.74	30.9	78.69	1.4	-

GRB	T_{90} [s]	Ph-flux [ph. s ⁻¹ . cm ⁻²]	XRT T_0 [s]	XRT r_{90} [arc sec]	z
061201	0.76	8.0	81.32	1.4	0.11
070714B	64	8.1	61.37	1.4	0.92
080123	115	6.1	101.81	1.7	-
080503	170	4	74.90	1.6	-
080905A	1.0	3.7	130.38	1.6	0.122
090426	1.2	4.7	84.62	1.4	2.609
090510	0.3	20.1	94.10	1.4	0.903
090515	0.036	5.2	63.85	2.9	-
100117A	0.3	4.4	80.1	2.4	0.915
100625A	0.33	9.3	48.26	1.8	0.452
101219A	0.6	8.9	221.92	1.7	0.718
111117A	0.47	5.8	-	-	1.3
130515A	0.29	8.4	75.2	2.4	-
130603B	0.18	54.2	59.05	1.4	0.356
140622A	0.13	4.1	93.40	2.4	0.959
140903A	0.30	10.03	59	1.4	0.351
140930B	0.84	5.94	196.93	1.6	-
141212A	0.30	7.6	69.11	2.6	0.596
150423A	0.22	4.4	70.12	1.6	1.394
150424A	91	37.42	87.87	1.4	0.3
150831A	1.15	3.7	83.44	1.6	-
151229A	1.78	9.5	86.91	1.4	-
160410A	8.2	6.1	82.89	2.3	1.717
160601A	0.12	6.1	73.97	3.1	-
160821B	0.48	7.1	65.97	2.2	0.16
161001A	2.6	7.1	65.05	1.4	0.891
161104A	0.1	4.1	58.28	3.0	0.793
170127B	0.51	4.8	74.68	2	-
170428A	0.20	14.4	84.63	2.3	0.454
180204A	1.16	9.1	87.17	1.4	-
180618A	47.4	5.8	77.62	1.4	-
181123B	0.26	4.7	80.25	1.5	-
191031D	0.29	19	88.83	1.7	-
200411A	0.22	5.5	50.74	1.4	-
201221D	0.16	36.6	87.42	4.3	1.046
210323A	1.12	9.5	85.2	2.2	-
210919A	0.16	6.3	97.02	4.0	0.27
211211A	51.37	196.1	79.15	1.9	0.076
211227A	83.79	6.1	73.46	2.4	0.228

The selection summary and the number of GRBs after each selection is given in Tab. 6.4.

Table 6.4: The selection criteria of the short-duration GRBs sample and the number of GRBs after each selection.

Selection	number of GRBs
$T_{90} < 2$ s	132
+ extended emission	139
XRT pointing time < 200s	95
$A_\nu < 0.5$	71
peak photon flux > 3.5 ph.s ⁻¹ .cm ⁻²	41

Among the *complete* sample, 25 short GRBs (61% of short GRBs) observed by the Swift with a reliable redshift. To get the redshift for the GRBs, some of them are given in the Swift database. For the others, we investigated the GCN circulars [161] and the literature for each GRB in the complete sample to check the redshift. Then we investigated if this redshift is reliable or not by looking at the method of measuring it.

In astrophysics, the redshift of a given event is measured in three ways: First, one can use optical spectroscopy if the optical afterglow is detected with clear absorption lines in their spectrum [199]. In this case, the redshift is measured as in Eq. 1.1. The spectroscopic redshift is the most reliable.

The second method is the host galaxy spectroscopy [200], which is divided into two parts. The first part is when the optical afterglow is detected but with no absorption line in its spectrum. In this case, the host galaxy is identified, and the GRB event has the same redshift as the host galaxy. This measured redshift is reliable. In the complete sample, nine short GRBs have a redshift computed with this method. The second part is when no optical afterglow is observed, so the host galaxy is not identified easily. In this case, a galaxy catalog is used to look for the galaxies within the XRT error radius r_{90} . In this study, we used the Vizier database [201] to search for the galaxies. If there is only one galaxy in the XRT error radius, this galaxy is considered the host galaxy of the GRB event, which has the same redshift as the host. If there is more than one galaxy in the error radius, the chance of the probability is computed by assuming a uniform distribution of the galaxies following a Poisson distribution [202].

The chance of the probability computes the probability of a random or false coincidence to find a galaxy within a given radius, and it is given by:

$$P_{i, \text{chance}} = 1 - \exp(-\eta_i), \quad (6.6)$$

where i is the galaxy index, and

$$\eta_i = \pi r^2 \sigma(\leq m_i), \quad (6.7)$$

is the expected number of galaxies within a circle of radius r_i , and

$$\sigma(\leq m_i) = \frac{1}{3600^2 \times 0.334 \log_e 10} 10^{0.334(m_i - 22.963) + 4.32}, \quad (6.8)$$

is the mean surface density of galaxies brighter than the red band magnitude of m_i of the i galaxy. The galaxy with the lowest chance of probability is considered. In the complete sample, GRB061201, GRB161001A, and GRB161104A have a redshift measured by the host galaxy spectroscopy with no optical afterglow. The three GRBs have a chance probability of < 0.05 . The third way to compute the redshift is the photometry [203] [204]. The photometric redshift is the least reliable redshift among the three methods. In the complete sample, only GRB210919A has a photometric redshift.

In the complete sample, 5 short GRBs have an extended emission: GRB070714B [205], GRB150424A [206], GRB160410A [207], GRB211211A [208], and GRB211227A [209]. The GRB211211A is a special event associated with the merger of binary neutron stars because of the detection of the Kilonova emission from the same event. However, no gravitational-wave signal was observed from this event.

GRB090426 has the highest redshift in the complete sample: $z = 2.609$. However, the classification of this GRB is still debated. Even if it has a $T_{90} < 2s$, it has been shown in [197] that this GRB follows the properties of long GRBs.

In the complete sample, six short GRBs have the plateau phase in their light curves, whereas three short GRBs have an X-ray flare in their light curves.

In the next section, the luminosities of the X-ray afterglow of the short GRB complete sample are studied in the source rest frame.

6.2.2 . The luminosity in the rest frame

The X-ray afterglow luminosity can be obtained from the flux light curve. For each short GRB in the complete sample, the flux light curve is downloaded from the Swift Burst Analyser repository [210]. Then, the fluxes in the rest frame (\mathcal{F}_{rf}) energy (2 - 10 keV) is computed as [197]:

$$\mathcal{F}_{rf} (2 - 10 \text{ keV}) = \mathcal{F} (0.3 - 10 \text{ keV}) \frac{\left(\frac{10}{1+z}\right)^{2-\Gamma} - \left(\frac{2}{1+z}\right)^{2-\Gamma}}{10^{2-\Gamma} - 0.3^{2-\Gamma}}. \quad (6.9)$$

The energy range of (2 - 10 keV) is chosen to have a common minimum energy for the complete sample in the rest frame.

The X-ray afterglow luminosity in the rest frame is given by:

$$L_x = \mathcal{F}_{rf} \times 4\pi D_L^2, \quad (6.10)$$

where D_L is the luminosity distance, and it is given by:

$$D_L = (1+z) \frac{c}{H_0} \int_0^z \frac{dz'}{\sqrt{\Omega_m(1+z')^3 + \Omega_\lambda}}, \quad (6.11)$$

where $H_0 = 73.8 \text{ km.s}^{-1}.\text{Mpc}^{-1}$ is the Hubble parameter today, Ω_m is the normalized value of the present matter density, and Ω_λ is the normalized value of the present dark energy density. We consider a standard cosmology, where $\Omega_m = 0.3$ and $\Omega_\lambda = 0.7$.

The emitted time t_{emit} is also computed as:

$$t_{emit} = \frac{t_{obs}}{(1+z)}. \quad (6.12)$$

From Eq 6.10 and Eq. 6.12, we estimate the luminosity light curve at the source rest frame for the X-ray afterglow of the complete sample. Figure. 6.15 shows the luminosity light curve of the complete sample.

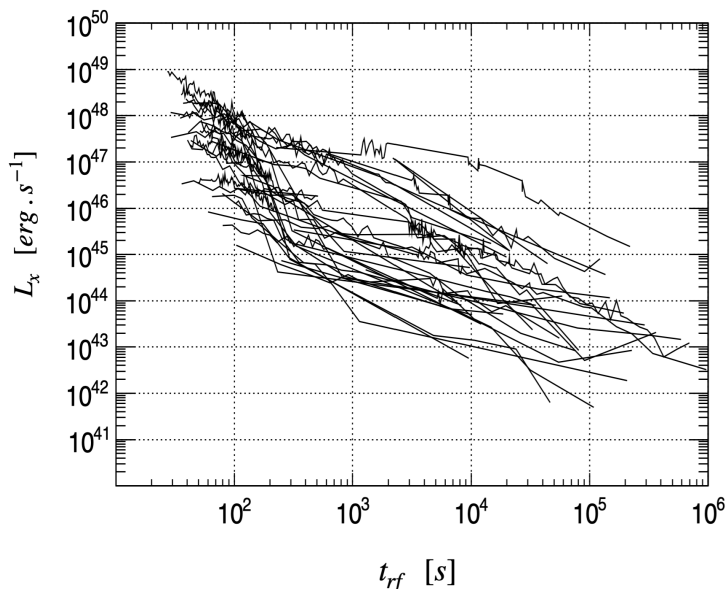


Figure 6.15: The luminosity light curves of the X-ray afterglow of the complete sample, estimated in the rest frame energy range (2 - 10 keV).

The luminosity light curves are distributed over a wide range, covering 5 order of magnitudes. Two parameters play the main role in the brightness of the GRB, the isotropic energy of the central engine E_{iso} and the density of the surrounding medium (n). Almost all short GRBs have the same environment properties with low medium density. Therefore, if the luminosity light curves are normalized to the E_{iso} , they should be homogeneous and have a typical model.

E_{iso} is computed as:

$$E_{iso} = \frac{4\pi D_L^2}{1+z} F_{bol}, \quad (6.13)$$

where,

$$F_{bol} = A \int_1^{10^4} EN(E) dE, \quad (6.14)$$

is the bolometric fluence, which is the total fluence of a GRB between 1 - 10^4 keV. Instruments could observe part of this fluence. $N(E)$ is the photon number spectrum of the prompt emission (see Sec. 1.2.2.1), and A is a normalization factor.

To determine the value of A , the measured fluence and spectrum are used:

$$F_{(E_1-E_2)} = A \int_{E_1}^{E_2} EN(E) dE. \quad (6.15)$$

$(E_1 - E_2)$ is the energy band for the instrument. Finally, the bolometric fluence is computed as:

$$F_{bol} = \frac{F_{(E_1-E_2)}}{\int_{E_1}^{E_2} N(E) dE} \int_1^{10^4} EN(E) dE. \quad (6.16)$$

To compute F_{bol} in Eq. 6.16, $N(E)$ shall be fitted by one of the three models explained in Sec. 1.2.3.1, based on the GRB brightness and the instrument energy band. The GRB prompt emission spectrum is typically fitted with the Band function or a power law with an exponential cutoff function. The Swift/BAT instrument is operated in the energy band of (15 - 150 keV). Therefore, the observed spectrum is fitted by a power law. If we extrapolate the spectrum observed by the Swift/BAT and compute E_{iso} , the E_{iso} will be overestimated, as seen in Fig. 6.16, where the $N(E)$ is integrated under the dashed orange line. Thus, E_{iso} should not be computed using the Swift/BAT observation.

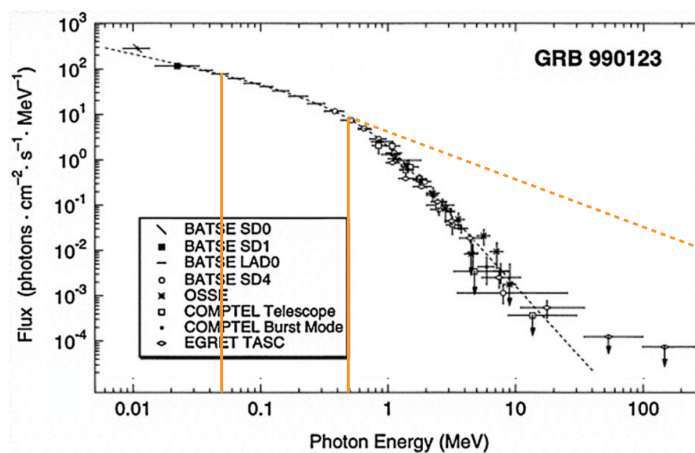


Figure 6.16: The band model spectrum of the prompt emission, where the energy band of the Swift/BAT is indicated by the orange lines.

To compute E_{iso} , we look in the GCN circulars for a detection of the same GRB with high-energy band instruments: Fermi [211] or Konus [212]. If the detection is performed by one of these instruments, we get the best fit from the GCN circulars or the Fermi catalog [213]. If there is no detection by these instruments, we fit the spectrum with the exponential cutoff power law in Eq. 1.6, with the typical value for $\alpha = -0.5$ and $E_p = 730\text{keV}$. The E_{iso} values of the complete sample are given in Tab. 6.5.

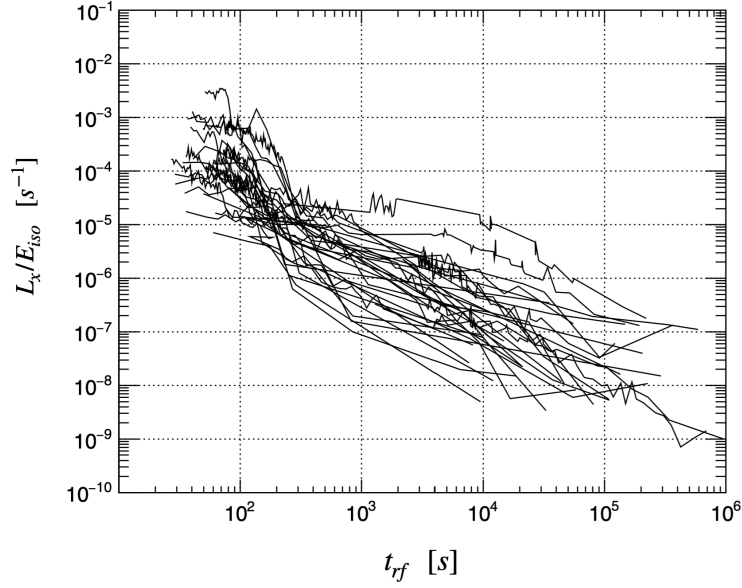


Figure 6.17: The normalized luminosity light curves of the X-ray afterglow of the complete sample, estimated in the rest frame energy range (2 - 10 keV).

The luminosity light curves in Fig. 6.15 are normalized to the corresponding E_{iso} value in Tab. 6.5. The normalized light curves are shown in Fig. 6.17. The plot shows that we have a homogeneous set of X-ray normalized luminosity light curves that covers 3 order of magnitudes. Indeed, short GRBs seem to have similar environment properties.

Table 6.5: The isotropic energy of the prompt emission of the GRBs that have ≥ 3 detection points in the complete sample. In addition, the X-ray luminosities in the 2–10 keV rest-frame energy band are computed at two rest-frame times (1 h and 24 h).

GRB	z	E_{iso}	$L_{x,1h} [erg \cdot s^{-1}]$	$L_{x,24h} [erg \cdot s^{-1}]$
051221A	0.547	2.60×10^{51}	1.86×10^{45}	6.48×10^{43}
061201	0.11	9.06×10^{49}	1.26×10^{45}	2.35×10^{44}
070714B	0.92	1.53×10^{52}	1.53×10^{46}	1.05×10^{43}
080905A	0.122	4.67×10^{49}	2.79×10^{43}	5.45×10^{38}
090426	2.609	2.29×10^{52}	2.86×10^{46}	1.19×10^{45}
090510	0.903	6.98×10^{52}	5.46×10^{45}	7.28×10^{42}
100117A	0.915	1.69×10^{51}	1.17×10^{44}	1.90×10^{41}
100625A	0.452	1.51×10^{51}	3.37×10^{43}	2.24×10^{41}
101219A	0.718	5.96×10^{51}	3.69×10^{43}	3.04×10^{40}
130603B	0.356	1.92×10^{51}	2.06×10^{45}	1.25×10^{43}
140903A	0.351	4.15×10^{50}	1.36×10^{43}	1.08×10^{42}

GRB	z	E_{iso}	$L_{x,1h} [erg.s^{-1}]$	$L_{x,24h} [erg.s^{-1}]$
150423A	1.394	2.99×10^{51}	5.25×10^{44}	3.45×10^{42}
150424A	0.3	3.21×10^{51}	4.06×10^{45}	1.70×10^{44}
160410A	1.717	5.38×10^{52}	4.27×10^{46}	1.78×10^{45}
160821B	0.16	5.83×10^{49}	6.79×10^{44}	2.83×10^{43}
161001A	0.891	1.34×10^{52}	1.49×10^{46}	6.24×10^{44}
211211A	0.076	2.5×10^{51}	5.71×10^{45}	2.38×10^{44}
211227A	0.228	4.9×10^{51}	2.70×10^{45}	1.13×10^{44}

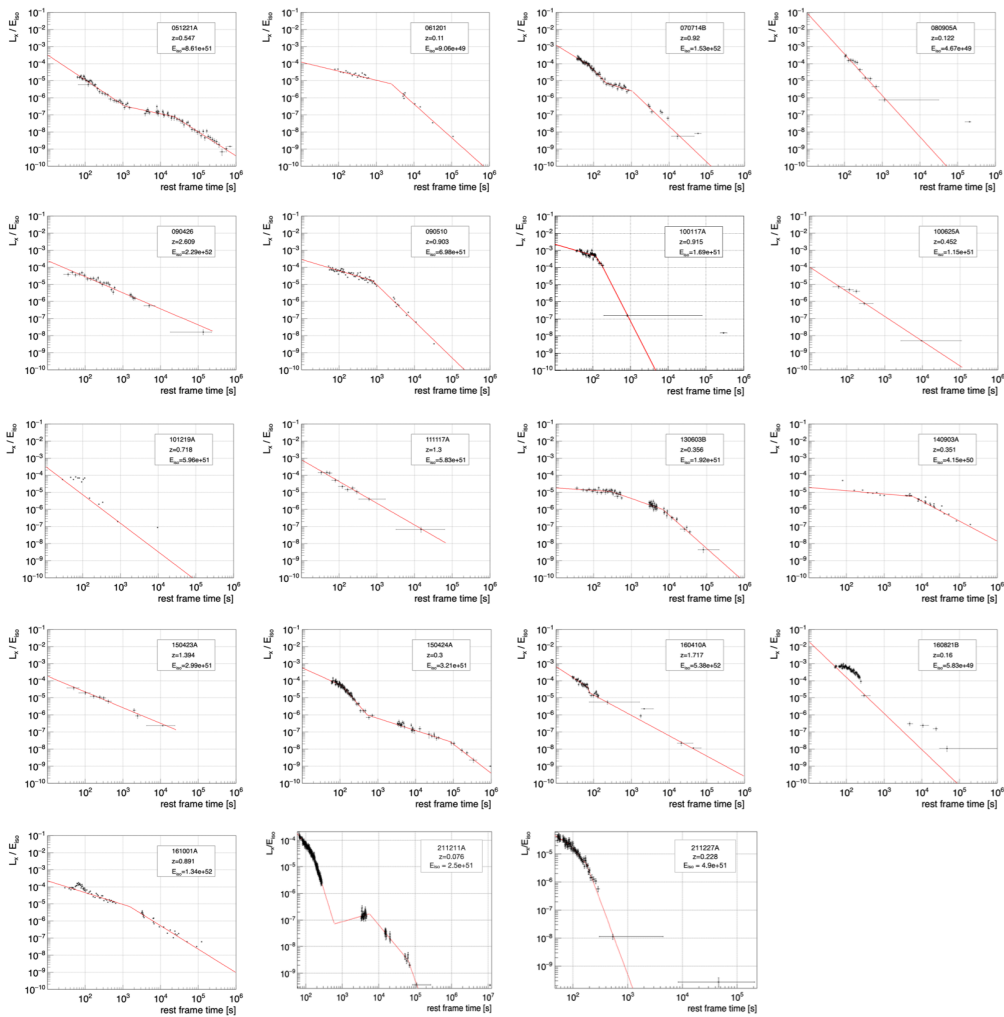


Figure 6.18: The normalized luminosity light curves of the X-ray afterglow of the short GRBs with ≥ 3 observations in the complete sample. The light curves are fitted with single or multiple broken power laws.

Moreover, if the luminosity light curve has ≥ 3 detection points, it is fitted with a single or multiple broken power law as seen in Fig. 6.18. From the best fit, the luminosity of each short GRB in the complete sample is estimated at the early time (1 h) and at the late time (24 h). The luminosities of the complete sample after a given time are given in Tab. 6.5.

Figure 6.19 shows the correlation between the E_{iso} and the X-ray luminosity at the early time (after 1 hour) and at the late time (after 24 hours). This shows the correlation between the prompt emission properties and the X-ray afterglow properties. The luminosity is drawn vs E_{iso} , fitted with a linear function, and the dispersion of the points from the best fit is computed. The dispersion (standard deviation) at the early time is about 0.32, and it is about 0.5 at the late time. This shows that L_x at early times correlates with the E_{iso} better than at the late time, which is consistent with the theory. In theory, the first steep decay and the plateau phases (see Sec. 1.2.3.2) of the X-ray afterglow light curves are believed to be connected with the prompt emission. The later phase, the normal decay phase, is purely associated with external forward shock afterglow emission; this is why at the late time, the X-ray afterglow luminosity is less correlated with E_{iso} .

In the next section, we will discuss how to use the complete sample to study the MXT observation performance, particularly the observation of the electromagnetic counterparts.

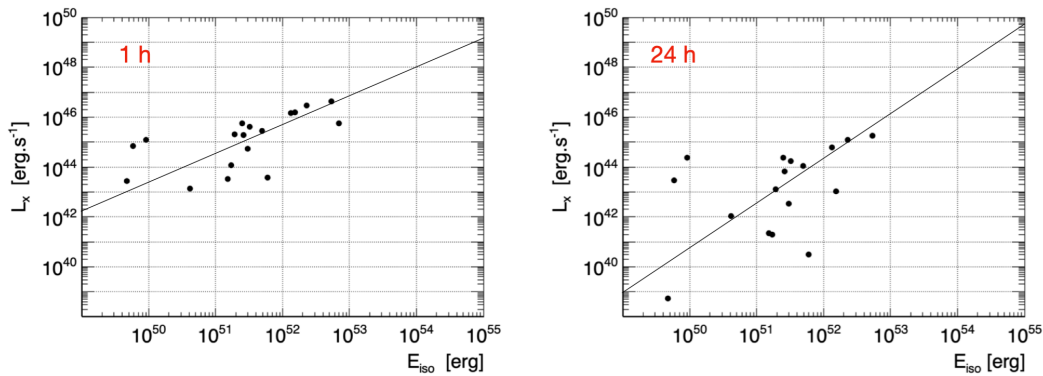


Figure 6.19: The $L_x - E_{iso}$ correlation studied for the complete sample at different rest-frame times. Left: at the early time (after 1 hour), right: at the late time (after 24 hours). The solid lines represent the best fit.

6.3 . Multi-messenger astronomy with the MXT

This section discusses the perspectives of the MXT contribution in the observation of electromagnetic counterparts of a gravitational-wave trigger originating from the coalescence of a binary system, including at least one neutron star. The electromagnetic counterpart of a supernova (the progenitor of long GRBs) is not studied because with the current sensitivity of gravitational-wave detectors, the probability of detection of a gravitational-wave signal from the supernova is low.

The observed electromagnetic emissions from merger of a binary systems are different depending on the observer angle θ_{obs} , as seen in Fig. 6.20.

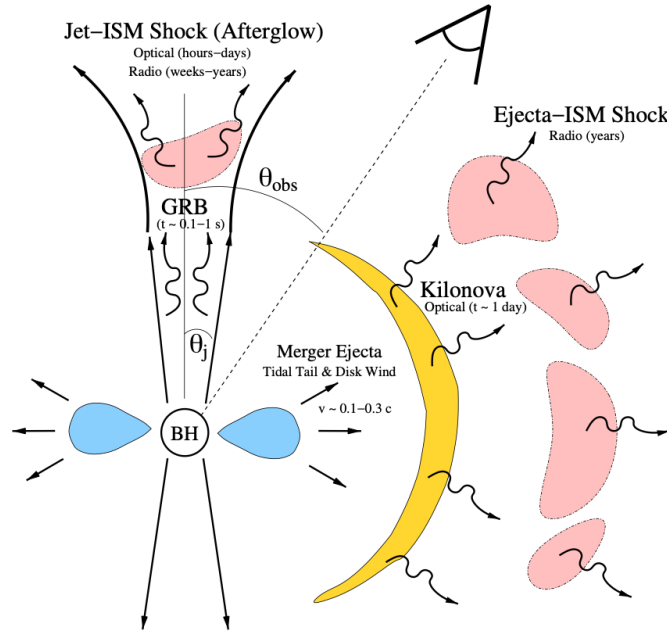


Figure 6.20: The expected electromagnetic counterparts to the merger of the binary system as a function of the observer angle θ_{obs} . The rapid accretion powers a collimated relativistic jet, which produces a short GRB with a half-opening angle θ_j . An afterglow emission results from the interaction of the jet with the surrounding medium (pink). Radio afterglow emission is observable isotropic on a timescale of weeks–months, and years. Short-lived isotropic optical emission lasting a few days (kilonova; yellow) can also accompany the merger, powered by the decay of radioactive heavy elements. Credit: [214].

If $\theta_{obs} \leq \theta_j$ (the half-opening angle of the jet), the short GRB: gamma ray, X-ray, optical, near-infrared, and radio emissions are observed. If $\theta_j < \theta_{obs} \leq 2\theta_j$ orphan afterglows (X-ray, optical, near-infrared, radio) are observed. The kilonova emission (optical and near-infrared) and the late-time radio remnant are observed from all directions.

In the ToO-MM program (see Sec. 2.2.3), the MXT receives alerts from the gravitational waves detector in order to search for the X-ray emission. In this section, only a simple case of on-axis short GRBs emissions is studied since the model of the emission differs according to the θ_{obs} angle. Further studies must include the MXT observation of the different electromagnetic emissions based on the observer angle θ_{obs} .

The gravitational-wave localization error box is relatively large compared to the localization error box of the electromagnetic waves detectors. Figure 6.21 shows that for the binary neutron stars, 50% have a localization error of about 25° , whereas, for the neutron star and black hole system, 50% of them have a localization error of about 35° , during the next observing run, which is O4 [130].

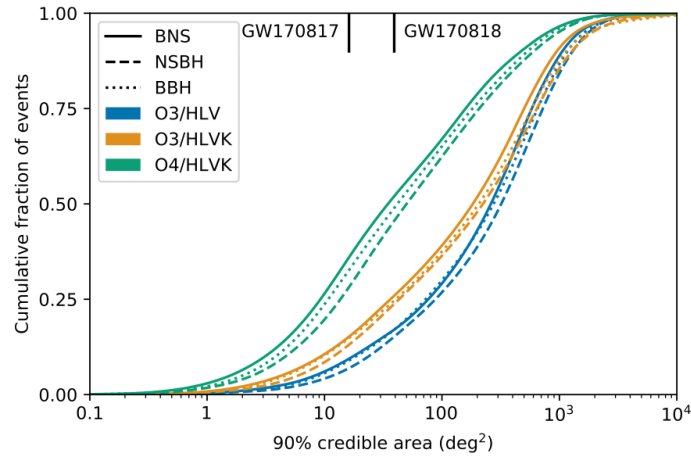


Figure 6.21: The gravitational waves sky localization error box for binary neutron stars BNS (solid line), a neutron star and a black hole (dashed line), and two black holes (dotted line) signals during the third *O3* and fourth *O4* runs. Credit: [130].

However, in the fifth observing run, one more detector is expected to join the gravitational-wave detector network, which is the LIGO-India. The inclusion of the fifth site improves the localization of the binary systems to reach about 20° , as seen in Fig. 6.22.

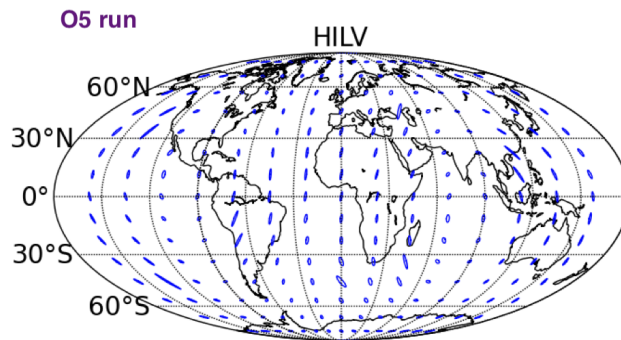


Figure 6.22: The expected localization accuracy for binary neutron star systems with advanced-detector networks during the *O5* run. The ellipses show 90% confidence localization areas by the four-detector network (HILV) LIGO Hanford (H)–LIGO India (I)–LIGO Livingston (L)–Virgo (V). The joining of the fifth site in India improves the localization over the whole sky. Credit: [215].

The MXT field of view is about 1° . Therefore the MXT must perform several observations (tiles) in order to cover the localization error box of gravitational-waves detectors and search for the X-ray counterpart. The MXT can observe five tiles per orbit, and each tile needs 500 s. Hence, the MXT needs typically four orbits (see Sec. 2.3.1 for the MXT orbit time) to

cover the error box of the gravitational-wave detectors. The total time expected to cover the gravitational-wave error box is ~ 6 hours, including the observation time and the satellite slew time [216]. The MXT could find the X-ray counterpart in the first tile or in the last tile. Thus, the observation of the X-ray counterpart by the MXT after a given time must be characterized. First, the limits and constraints of the gravitational-wave detectors must be considered.

Table 6.6 summarizes the expected horizon for the detection of binary systems during the O4, and O5 runs with LIGO/Virgo/KAGRA network. The O4 run is expected to start at the beginning of 2023 and will last one year so that SVOM could overlap the end of the O4 run. The O5 run is expected to start in 2026 [130].

Table 6.6: projected detector sensitivities for a $1.4 M_{\odot} + 1.4 M_{\odot}$ binary neutron star system (BNS), and a $1.4 M_{\odot} + 10 M_{\odot}$ neutron star and black hole system (NSBH) during the O4 and O5 runs.

			LIGO	Virgo	KAGRA
O4	BNS	Range [Mpc]	160-190	90-120	25-130
		Redshift	0.037 - 0.044	0.021 - 0.028	0.006 - 0.03
	NSBH	Range [Mpc]	300-330	170-220	45-290
		Redshift	0.07-0.077	0.04-0.051	0.01 - 0.067
O5	BNS	Range [Mpc]	330	150-260	130+
		Redshift	0.077	0.035- 0.06	0.03+
	NSBH	Range [Mpc]	590	270-480	290+
		Redshift	0.137	0.063-0.112	0.067+

During the O4 run, it is expected to observe binary systems with a redshift up to $z=0.077$; for O5 it will be $z = 0.137$. In order to test the MXT observation of the counterpart, the short GRB must be simulated at a redshift ≤ 0.077 (resp. ≤ 0.137) for the O4 (resp. O5) run. The typical X-ray afterglow light curve of short GRBs must be modeled in the rest frame. This is achieved by averaging the light curves of the complete sample in the rest frame or simply by isolating the light curve of one short GRB of the complete sample since they are almost homogeneous in the rest frame. Afterward, this light curve model is simulated at the desired redshift.

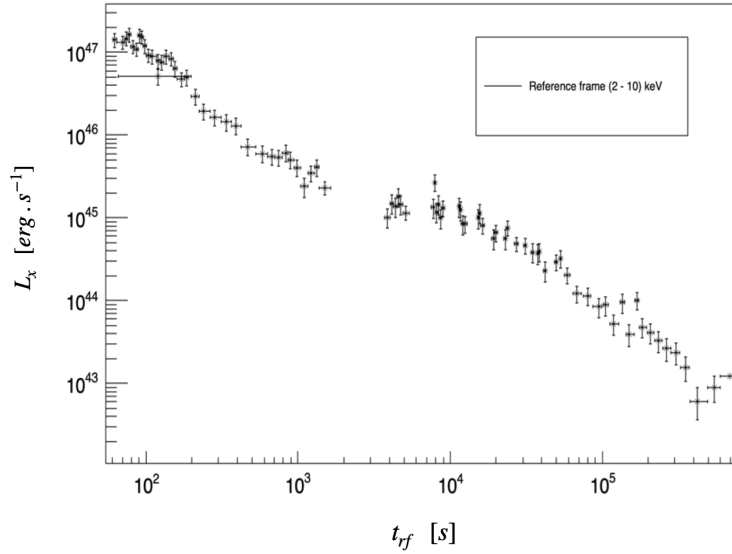


Figure 6.23: The luminosity light curve of the GRB051221A X-ray afterglow at the source rest frame (2 - 10 keV).

A simulation of an MXT observation of this light curve is simulated as described in Sec. 6.1 at different times after the gravitational-wave alert and for 500 s, which is the observation time for each tile. The number of counts observed in a tile after a pointing time of 1, 4, 8, and 12 hours is computed, then the localization uncertainty is computed using Eq. 5.49. We choose to simulate the GRB051221A, which was observed at $z = 0.547$. The X-ray luminosity light curve of GRB051221A at the rest frame is shown in Fig. 6.23.

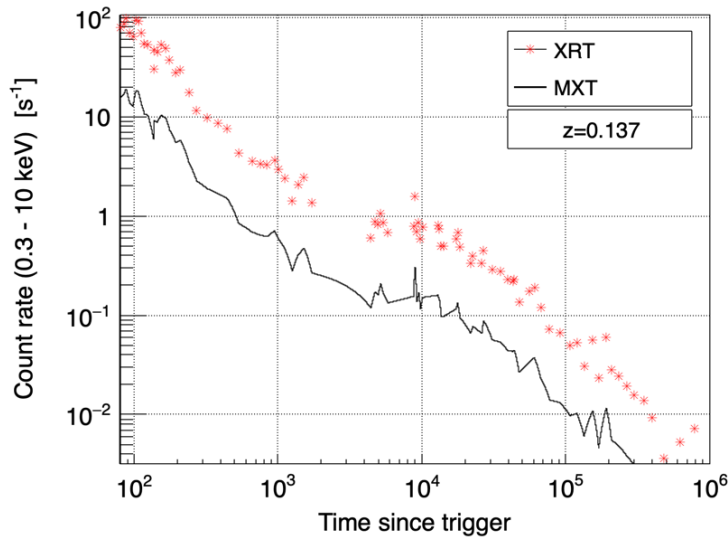


Figure 6.24: The light curve for GRB051221A, simulated at $z=0.137$. Observations with the XRT (red stars) and the MXT (black line) are simulated.

The flux at $z = 0.137$ and at $z = 0.077$ is obtained using Eq. 6.10, then it is converted to a flux in the XRT observer frame using Eq. 6.9. The flux and the number of counts in the MXT frame are simulated as described in Sec. 6.1.

Figure. 6.24 shows the X-ray afterglow light curve for GRB051221A simulated at $z = 0.137$ as observed by the XRT and the MXT. The number of counts observed by the MXT after a certain time and for 500 s is given in Tab. 6.7. Note that for the MXT observation, we include the interpolation of the data. The signal-to-noise ratio is computed assuming 500 background counts, and then r_{90} is computed as in Eq. 5.49. The MXT localizes the counterpart at $z = 0.077$ to better than two arcmin if they are found in less than ~ 4 hour. After that, the precise localization of the counterpart becomes more difficult as the number of counts becomes less. For far distant GRBs $z = 0.137$, the best accuracy achieved is 222 arcsec, if the GRB is found after 1 hour, as seen in Tab. 6.7.

Table 6.7: The maximum number of photons that would be detected in a tile after different observation times (1h, 4h, 8h, and 12h). The table gives the associated localization uncertainty r_{90} for each tile after a certain time from the alert time.

		1h	4h	8h	12h
$z=0.137$	number of photons	73	50	35	22
	r_{90} [arc sec]	222	281	352	471
$z=0.077$	number of photons	223	175	96	58
	r_{90} [arc sec]	111	129	187	256

Conclusion

The MXT is one of the four instruments onboard the SVOM satellite. SVOM has three observational programs: the core, the general, and the ToO programs. In the core program of the SVOM mission, the MXT observes and localizes GRB X-ray afterglow in the energy range of (0.2 - 10 keV) and rapidly communicates the source information to the ground to follow up the source. In the general program, the MXT observes X-rays from other types of astrophysical objects based on proposals. In the ToO program, the MXT observes the X-ray counterparts of multi-messenger sources, particularly the merger of binary systems, including at least one neutron star that emits gravitational waves in addition to the GRB.

This thesis studies the core program observations with the MXT. The MXT plays a vital role in localizing the GRB events precisely. The accurate and rapid localization allows to follow up the source at lower energies (the ultraviolet, optical, infrared, and radio). The rapid follow-up increases the probability of measuring the event redshift, which is the key to study the event in its rest frame, and to study its surrounding medium.

The MXT consists mainly of three parts, the optics, the camera, and the data processing unit. The MXT optics are micro-channel optics based on the lobster eyes geometry resulting in a peculiar PSF of a central spot and two cross arms. This optical system is attached to the camera based on a low-noise pnCCD detector. The MXT is equipped with a data processing unit (MDPU) to analyze images captured by the camera and perform scientific processing.

The scientific processing managed by the MDPU is divided into 4 categories: the noise characterization, the photon reconstruction and source localization, the management of the telemetry packet to be sent to the ground, and data monitoring by producing intermediate results of the previous three processing. The first two categories are developed and characterized during this thesis.

The first category is the noise characterization, in which the intrinsic noise level in the detector is measured. The intrinsic noise is temperature-dependent. Thus, the noise must be characterized frequently onboard to match observation conditions. The noise is characterized by computing noise offset and threshold maps (the dark maps) for all pixels. We developed a method to compute the offset map as the pixel-by-pixel mean value across N frames and the threshold map as the n_t standard deviation of the noise fluctuation around the offset. To ensure not biasing the dark maps, an outlier threshold is included to reject outlier pixels from the analysis. The dark maps (offset and threshold) proved to be robust in the presence of outliers and equivalent to the reference maps computed with the ground analysis. Using the onboard dark maps to select pixels above noise proved to give the detector an equivalent or even better spectral response than using the reference maps.

During observations, the dark maps are used to select pixels above noise. The MDPU

processes the selected pixels to reconstruct the X-ray photons and accumulate them in the photon map. The photon map is used to localize the source and compute its sky coordinate precisely and rapidly, which is the main scientific requirement of the MXT. The MXT must localize the sources onboard with accuracy better than 2 arcmin after 10 min of observation.

During my thesis, I designed and tested the MXT localization algorithm. The algorithm takes advantage of the shape of the MXT's PSF (central spot and cross arms) to guide the search for the source peak. The photon map (the detected signal) is cross-correlated with the PSF (the shape of the expected signal). The source peak position in the MXT detector is given by the 2D barycenter around the maximum cross-correlation value. This method proved to perform better than the simple barycenter over the photon map, particularly in the case of a low photon flux. The cross-correlation method is computed in the Fourier space onboard as it is faster than computing it in the spatial domain. To match the requirements of localization accuracy < 2 arcmin after 10 min, the MXT must detect at least 200 photons. The typical number of photons received during the first seconds of the X-ray afterglow ranges between a few hundred and a few thousand, which means that MXT will match the requirements in most observations.

We studied the impact of several effects on the performance of the localization. We tested the effect of reducing the photon map resolution, which proves to have no effect if it is reduced to half the original size. In addition, we characterized the bias caused by observing sources in the field of view of the MXT, and we corrected for this bias. Furthermore, we characterized and corrected the effect of the hardware limitation, like the presence of insensitive columns.

The localization algorithm onboard the MXT must be able to detect up to three sources in the field of view. The MXT derives the sky coordinate, the number of photons, and the signal-to-noise ratio for each source. In order to compute the signal-to-noise ratio onboard, a method is developed using the cross-correlation data. The method is based on selecting two cross-correlation values to compute the number of photons and the background count in the detector and hence compute the signal-to-noise ratio for each of the three sources. The onboard method to compute the signal-to-noise ratio proved to be functional and fast.

The flight model of the MXT, including the onboard scientific algorithms, was thoroughly tested at the Panter X-ray test facility in Germany from October to November 2021. The test proves that the MXT onboard science algorithms can be operated reliably and in a long run. The onboard dark maps proved to characterize the detector intrinsic noise and select pixels with signal above noise during the observation. With the onboard maps, photons with energy down to 0.08 keV can be identified above the noise level. The localization algorithms proved to give a precise location of the injected source beam, even when it is placed at the edge of the field of view of the MXT. The localization algorithm showed robustness in the presence of insensitive columns.

The MXT performance is tested using realistic scenarios of GRBs based on the Swift/XRT

observation. The SATANDLIGHT toolkit has been developed to simulate such scenarios. SATANDLIGHT simulates MXT optics, camera, geometry, sources in the field of view, and the MXT observation. Moreover, a realistic GRB with a physical spectrum and light curve model can be simulated based on previous observations by similar missions like Swift. During my thesis, I participated in developing and characterizing this simulation for the MXT.

The MXT has shown that it is able to study and characterize the temporal evolution of the X-ray afterglow. In addition, the MXT is able to characterize the spectrum of X-ray afterglows, in particular, the absorption of X-ray photons at low energies (<1 keV). The localization performance is tested using the GRB population of the XRT. The GRBs observed by the XRT are converted to the MXT observations, and they are localized by the onboard localization algorithm. The MXT localizes $\sim 80\%$ of XRT GRBs to better than 2 arcmin after 10 min of observation.

We perform a selection of short GRBs sample with computed redshift. We perform a study of the rest frame properties of the sample. Among the studied properties is the X-ray luminosities. Finally, the sample was used to test the MXT observation during the ToO program, where the MXT searches for X-ray counterpart of a multi-messenger source. The detection of the counterpart with the MXT depends on how fast the telescope points toward the source and whether the MXT found the source from the first observations. The MXT must point to the source in less than 4 hours to localize a multi-messenger source with an accuracy of < 2 arcmin. For the far distant sources $z \approx 0.1$, the MXT is not able to localize them with such accuracy, but, it will be able to observe and localize these sources with less precision.

A - Swift GRBs detected by ECLAIRs

The Swift GRBs that would have a certain probability to be detected by ECLAIRs are listed in this appendix, tab. A.1 shows the list with 50% detection probability and tab. A.2 shows the list with 90% detection probability

Table A.1: The Swift GRBs that have 50% detection probability with SVOM/ECLAIRs.

GRB name	BAT T_{90} [sec]	BAT 1-sec peak photon flux (15-150 keV)
220806A	4.78	1.1
220715B	40.40	1.3
220714B	50.10	3.8
220711B	88.64	2.0
220708A	4.4	0.8
220706A	86.9	0.9
220701A	5.77	0.7
220623A	57.11	4.5
220618A	96.00	0.8
220521A	13.55	4.7
220518A	12.29	1.8
220501A	202.24	1.2
220430A	43.10	29.6
220427A	57.2	3.0
220412A	41.66	0.5
220408A	17.25	4.9
220404A	2.54	1.1
220403B	27.0	2.7
220325A	3.50	2.0
220319A	6.44	1.5
220306B	12.34	2.3
220305A	21.12	2.1
220118A	10.61	3.3
220117B	24.37	0.5
220117A	49.81	1.9
220101A	173.36	7.3

GRB name	BAT T_{90} [sec]	BAT 1-sec peak photon flux (15-150 keV)
211227A	83.79	5.1
211225B	121.54	6.1
211223C	15.00	3.1
211221A	671.67	0.5
211211A	51.37	155.0
211207A	3.73	0.9
211129A	113.01	1.5
211025A	103.5	0.5
211024B	603.5	0.9
211023B	1.30	2.2
210930A	11.81	0.7
210912A	28.35	1.7
210901A	46.77	2.4
210824A	37.55	1.3
210822A	180.8	27.7
210820A	196.8	0.8
210818A	73.56	11.2
210807C	89.97	4.0
210807A	156.30	1.8
210731A	22.51	1.6
210730A	3.86	7.1
210725B	48.00	0.6
210725A	53.54	1.0
210724A	50.57	2.5
210723A	48.54	3.1
210722A	50.20	2.2
210712A	136.41	2.3
210619B	60.90	115.0
210610B	69.38	13.5
210610A	13.62	2.4
210527A	63.21	0.4
210517A	3.06	1.5
210515C	55.7	0.6
210514A	70.21	8.7
210509A	8.22	1.2
210504A	135.06	0.9
210430A	11.53	1.9
210422A	39.00	1.3
210421A	79.52	2.0
210420B	158.8	0.5
210419C	73.00	0.8
210419A	64.43	0.6
210411C	12.80	4.8
210410A	52.88	4.0

GRB name	BAT T_{90} [sec]	BAT 1-sec peak photon flux (15-150 keV)
210403A	168.3	1.1
210402A	238.7	1.6
210323A	1.12	2.9
210321A	8.21	1.7
210318B	14.95	14.5
210318A	48.00	0.3
210308A	5.3	13.6
210307A	262	1.0
210306B	24.32	2.4
210306A	9.12	20.9
210305A	68.6	3.4
210226A	20.80	2.8
210222B	12.82	1.4
210218A	240	1.0
210217A	4.22	5.1
210212A	80.0	0.5
210211A	6.1	1.0
210210A	6.60	7.0
210209A	139.4	0.6
210207B	95.69	3.1
210205A	22.70	1.6
210112A	107.60	20.5
210104B	19.94	1.9
210104A	32.06	12.1
210102C	87.25	4.4
201229A	53.3	1.7
201223A	29.0	1.5
201221D	0.16	5.6
201221A	44.5	1.0
201216C	48.0	18.0
201209A	48.0	12.2
201203A	12.18	0.5
201128A	5.41	0.4
201105A	33.82	13.9
201104B	8.66	4.1
201029A	120.55	0.6
201027A	546.73	1.4
201026A	135.38	2.2
201024A	5.00	3.7
201021C	24.38	1.0
201020A	14.17	2.1
201017A	22.08	1.8
201015A	9.78	1.8
201014A	36.2	0.3

GRB name	BAT T_{90} [sec]	BAT 1-sec peak photon flux (15-150 keV)
201013A	7.36	24.6
201029A	120.55	0.6
201027A	546.73	1.4
201026A	135.38	2.2
201024A	5.00	3.7
201021C	24.38	1.0
201020A	14.17	2.1
201017A	22.08	1.8
201015A	9.78	1.8
201014A	36.2	0.3
201013A	7.36	24.6
201006A	0.49	2.2
201001A	15.2	1.0
200925B	18.25	3.0
200922A	10.30	11.4
200919A	76.0	1.2
200917A	19.4	0.6
200909B	16.9	1.3
200906A	70.90	2.5
200903A	24.15	3.8
200901B	705.94	0.4
200901A	20.37	7.7
200829A	13.04	98.7
200819A	23.62	0.6
200806A	38.8	12.1
200729A	122.0	0.7
200716C	86	10.7
200713A	48.98	0.8
200711A	29.39	7.7
200701A	38.9	0.7
200630A	14.83	1.4
200612A	171.48	0.7
200608A	119.2	0.7
200529A	79.57	1.8
200528A	58.7	17.5
200519A	71.88	20.6
200512A	74.0	0.4
200509A	828.2	1.5
200425A	81.0	0.7
200416A	5.04	3.8
200410A	108.8	1.8
200409A	17.91	1.2
200306C	53.5	1.3
200306A	32.87	7.0

GRB name	BAT T_{90} [sec]	BAT 1-sec peak photon flux (15-150 keV)
200303A	94.2	5.0
200228B	7.37	1.0
200227A	32.8	5.7
200224A	45.0	0.4
200219A	288.0	2.4
200216B	81.3	1.5
200215A	11.7	2.7
200205B	458.0	2.0
200131A	32.74	26.9
200127A	216.9	0.7
200125A	350.83	4.0
200122A	174.96	9.1
200115A	158.4	3.6
200109A	112.0	0.7
200107B	86.68	1.9
191228A	166.9	0.6
191227A	58.5	21.8
191221B	48.00	4.8
191220A	175.55	1.1
191218A	44.67	6.3
191130A	17.6	1.1
191123A	275.1	1.2
191122A	153.3	3.1
191106A	3.42	1.1
191101A	137.95	1.3
191031D	0.29	4.3
191031C	93.2	4.6
191031A	19.1	1.0
191029A	39.5	1.1
191024A	7.08	1.6
191019A	64.35	5.7
191017B	5.95	1.9
191016A	219.70	1.5
191011A	7.37	1.8
191004B	37.7	5.0
191004A	2.44	7.8
191001B	108.9	1.8
190926A	368.9	0.6
190829A	58.2	18.0
190828B	66.6	2.3
190824A	169.4	5.0
190821A	57.1	2.8
190816A	375.0	1.3
190727B	40.14	20.9

GRB name	BAT T_{90} [sec]	BAT 1-sec peak photon flux (15-150 keV)
190719C	185.7	5.5
190718A	720.0	1.0
190706B	25.16	1.4
190701A	52.4	1.2
190630C	38.4	2.0
190630B	5.6	1.1
190613B	160.84	5.7
190613A	17.6	1.5
190611A	41.8	0.9
190610A	0.62	3.9
190604B	220.2	7.3
190519A	45.58	20.6
190515B	46.4	1.1
190512A	40.1	1.0
190511A	27.7	6.2
190424A	10.6	2.0
190331A	4.3	2.8
190324A	28.4	11.9
190320A	64.0	1.3
190311A	17.0	1.8
190220A	10.0	2.6
190219A	167.8	1.9
190211A	12.48	1.9
190204A	26.4	30.5
190203A	96	3.1
190202A	19.4	7.8
190123A	24.4	1.0
190114C	361.5	101.0
190114B	26.5	0.5
190114A	66.6	0.5
190110A	9.3	9.0
190109B	5.92	1.7
190109A	115.0	1.9
190106A	76.8	5.5
190103B	19.5	16.3
181228A	257.3	9.5
181224A	12.5	1.0
181213A	15.31	2.1
181203A	15.30	1.1
181202A	6.56	0.9
181126A	2.09	2.7
181125A	10.5	1.5
181110A	138.4	3.7
181103A	8.38	0.8

GRB name	BAT T_{90} [sec]	BAT 1-sec peak photon flux (15-150 keV)
181030A	304.7	0.8
181027A	81.16	1.2
181023A	58.0	1.0
181022A	6.74	0.4
181020A	238.0	7.7
181016A	111.6	0.7
181013A	104.1	0.5
181010A	16.4	1.4
181003A	21.5	0.6
181002A	63.4	0.6
180925A	81.70	3.1
180924A	95.1	0.6
180905A	165.3	1.0
180904A	5.40	0.5
180828A	14.0	17.8
180823A	80.3	2.3
180818B	134.4	1.2
180818A	13.7	0.6
180812A	16.51	1.9
180809B	233.2	26.3
180805B	122.5	1.7
180728A	8.68	132.0
180727A	1.1	3.6
180721A	47.6	0.9
180720C	124.2	1.1
180709A	215.1	0.6
180706A	42.7	3.2
180705A	123.2	0.7
180704A	19.7	9.6
180630A	18.85	6.6
180626A	30.07	4.1
180624A	486.4	1.4
180623A	114.9	5.6
180620B	198.8	3.6
180620A	23.16	7.7
180618A	47.4	2.2
180614A	7.04	0.7
180602A	45.4	0.9
180514A	46.9	0.7
180512A	24.0	0.6
180510B	134.3	1.2
180510A	40.4	8.9
180504A	88.3	0.8
180425A	11.2	2.2

GRB name	BAT T_{90} [sec]	BAT 1-sec peak photon flux (15-150 keV)
180418A	2.29	3.0
180411A	77.5	6.1
180410A	100.7	0.7
180407A	95.9	0.9
180404B	111.5	5.2
180404A	35.2	1.3
180331B	147.0	2.8
180331A	48.0	0.5
180329B	210.0	1.4
180329A	9.1	0.5
180325A	94.1	9.4
180324A	7.2	4.4
180316A	87.0	3.3
180314B	73.0	1.1
180314A	51.2	7.9
180311A	23.0	0.6
180224A	10.9	1.4
180222A	64.0	0.4
180205A	15.5	3.4
180204A	1.16	3.6
180115A	40.9	0.6
180113A	64	2.5
180111A	50.6	4.9
180102A	10.8	1.0
171222A	174.8	0.7
171216A	30.0	0.8
171212A	320	0.7
171211A	2.32	2.3
171209A	161.7	1.6
171205A	189.4	1.0
171123A	58.5	0.8
171120A	64	11.4
171115A	38.2	0.6
171103A	3.90	3.6
171102B	17.8	1.2
171027A	96.6	3.0
171020A	41.9	0.7
171011A	2.27	7.0
171007A	105	0.4
171004A	107.1	0.9
171001A	22.8	0.9
170921A	28.9	0.8
170912B	19.6	5.7
170912A	21.9	2.0

GRB name	BAT T_{90} [sec]	BAT 1-sec peak photon flux (15-150 keV)
170906C	48.4	7.2
170906A	88.1	10.9
170903A	29.2	3.9
170827A	94.0	0.4
170823A	69.4	3.7
170822A	64	4.2
170813A	75.5	0.8
170810A	152.4	1.2
170807A	48.5	1.4
170804A	43.4	0.9
170803A	3.82	6.5
170728B	47.7	1.21
170724A	98.0	0.5
170711A	31.3	4.8
170710B	54.4	1.2
170710A	32.6	1.0
170705A	217.3	13.9
170629A	34.4	4.1
170626A	12.94	23.6
170604A	26.70	4.2
170531B	164.13	0.8
170526A	7.9	0.3
170524B	46.4	0.3
170519A	216.4	0.7
170516A	36.78	1.3
170428A	0.20	2.8
170419B	77.2	2.4
170419A	8.18	1.5
170331A	17.57	1.2
170330A	144.73	4.5
170318B	160.0	0.1
170318A	133.7	1.2
170317A	11.94	3.5
170311A	6.32	0.8
170307A	56.92	1.4
170306A	17.8	1.3
170208B	128.07	8.4
170208A	7.45	5.4
170206B	13.36	0.4
170205A	26.1	4.3
170203A	45.2	0.8
170202A	46.2	4.7
170127A	62.26	0.3
170126A	9.5	7.3

GRB name	BAT T_{90} [sec]	BAT 1-sec peak photon flux (15-150 keV)
170115A	48.0	0.2
170113A	20.66	1.1
170111A	29.9	0.9
170101A	2.43	54.4
161224A	47.04	0.8
161220A	6	0.5
161219B	6.94	5.3
161218A	7.1	17.6
161217A	18.2	0.4
161214B	24.8	2.2
161129A	35.53	3.4
161117B	152.51	6.0
161117A	125.7	6.8
161113A	42.60	1.4
161108A	105.1	0.6
161105A	177.3	1.4
161022A	7.3	1.6
161017A	216.3	2.8
161014A	18.3	2.9
161011A	4.3	0.9
161007A	201.7	0.4
161004B	15.9	10.1
161001A	2.6	3.5
160927A	0.48	1.9
160917A	16	2.2
160905A	64	6.3
160827A	13.3	0.7
160826A	52.6	0.4
160824A	99.3	1.3
160815A	8.6	4.7
160804A	144.2	2.9
160801A	2.85	1.2
160726A	0.7	3.2
160716A	6.39	0.8
160709A	4.8	2.7
160705B	54.4	0.5
160703A	44.4	5.8
160630A	29.50	1.2
160625A	53.9	3.0
160611A	34.1	2.0
160607A	33.4	21.8
160519A	35.57	2.4
160506A	254.5	0.4
160504A	53.9	0.7

GRB name	BAT T_{90} [sec]	BAT 1-sec peak photon flux (15-150 keV)
160501A	118	0.5
160425A	304.58	2.8
160424A	6.3	5.1
160419A	8.8	8.9
160417A	15	1.0
160412A	31.6	1.6
160410A	8.2	3.5
160408A	0.32	2.1
160327A	28	1.8
160325A	64.9	5.2
160321A	33.6	0.5
160314A	8.73	0.9
160313A	42.6	0.4
160303A	5.0	1.0
160228A	98.36	1.2
160227A	316.5	0.6
160225A	157	1.0
160223A	127	3.1
160220B	31.4	6.6
160220A	8.3	1.0
160216A	11.0	7.3
160203A	20.2	1.3
160131A	325	6.4
160127A	6.16	1.4
160123A	3.95	1.3
160121A	12.0	1.2
160119A	116	2.9
160117A	118.58	1.4
160104A	16.2	1.0
151229A	1.78	7.2
151228B	48.0	1.0
151215A	17.8	1.6
151210A	94.9	0.8
151205A	62.8	0.6
151118A	23.4	1.2
151114A	4.86	2.9
151112A	19.32	1.9
151111A	76.93	1.0
151031A	5.00	1.7
151029A	8.95	1.8
151027A	129.69	6.8
151023A	10.66	1.1
151022A	116.7	0.8
151021A	110.2	9.7

GRB name	BAT T_{90} [sec]	BAT 1-sec peak photon flux (15-150 keV)
151006A	203.9	2.6
151004A	128.40	0.4
151001B	109	0.5
151001A	8.94	1.3
150925A	121	0.6
150915A	164.7	0.5
150911A	7.2	5.2
150910A	112.2	1.1
150907B	62.0	1.0
150831B	6.2	6.1
150831A	1.15	3.4
150819A	52.1	0.3
150818A	123.3	2.4
150817A	38.8	9.6
150811A	34.00	0.5
150801B	426	2.5
150727A	88	1.0
150724A	280	0.9
150722A	67	0.4
150720A	151	0.3
150716A	44	0.8
150711A	64.2	3.8
150710B	15	8.3
150626B	48.0	0.6
150626A	144	0.4
150616A	599.5	2.9
150615A	27.6	0.6
150607A	26.3	4.9
150530A	6.62	4.1
150527A	112	0.3
150513A	162	2.9
150430A	107.1	5.0
150428B	130.9	1.4
150428A	53.2	3.0
150424A	91	12.0
150413A	263.6	1.6
150403A	40.90	17.6
150323C	159.4	1.1
150323A	149.6	5.4
150318A	83.88	1.1
150317A	23.29	1.2
150314A	14.79	38.5
150309A	242	9.0
150302A	23.74	0.4

GRB name	BAT T_{90} [sec]	BAT 1-sec peak photon flux (15-150 keV)
150301B	12.44	3.0
150222A	15.90	4.7
150213B	181	1.1
150212A	11.4	1.9
150206A	83.2	10.1
150204A	12	1.85
150203A	25.8	0.9
150202A	25.7	1.0
150120B	24.30	1.2
150120A	1.20	1.8
150110B	10.6	1.4
150103A	49.1	0.5
141229A	7	1.2
141225A	40.24	1.3
141221A	36.9	3.1
141220A	7.21	8.9
141212B	10.5	3.9
141130A	62.9	1.2
141121A	549.9	0.9
141109B	54.2	0.4
141109A	200	2.5
141031B	16.0	0.3
141031A	920	0.5
141026A	146	0.4
141022A	8.72	0.9
141020A	15.55	0.7
141017A	55.7	6.7
141015A	11.0	0.5
141005A	4.34	4.2
141004A	3.92	6.1
140930B	0.84	4.0
140927A	6.26	0.9
140919A	151.3	2.0
140916A	80.1	1.3
140907A	79.2	2.5
140903A	0.30	2.5
140828A	18.8	2.2
140824A	3.09	1.2
140818B	18.1	1.1
140817A	244	7.2
140730A	41.3	0.5
140719B	53.0	0.7
140719A	48	0.2
140716A	104	5.2

GRB name	BAT T_{90} [sec]	BAT 1-sec peak photon flux (15-150 keV)
140713A	5.30	1.9
140710A	3.52	1.9
140709B	155.0	0.9
140709A	98.6	3.1
140706A	48.3	1.8
140703A	67.1	2.8
140629A	42.0	4.2
140628A	10.5	2.8
140626A	16.4	0.7
140619A	233.9	4.6
140614B	49.8	0.5
140607A	109.9	0.9
140529A	4.5	11.5
140521A	9.88	1.9
140518A	60.5	1.0
140515A	23.4	0.9
140512A	154.8	6.8
140509A	23.20	1.6
140506A	111.1	10.9
140502A	16.9	0.9
140430A	173.6	2.5
140428A	17.42	0.6
140423A	134	2.1
140419A	94.7	4.9
140413A	139.6	2.3
140412A	39.6	1.1
140408A	4.00	1.2
140331A	209	0.31
140323A	104.9	6.2
140318A	8.43	0.5
140311A	71.4	1.3
140305A	13.7	1.0
140304A	15.6	1.7
140302A	87.5	1.7
140301A	31.0	0.7
140215A	84.2	7.9
140213A	60.0	23.5
140211A	89.4	0.7
140209A	21.3	38.1
140206A	93.6	19.4
140118A	84.15	1.9
140114A	139.7	0.9
140108A	94	6.1
140103A	17.3	2.1

GRB name	BAT T_{90} [sec]	BAT 1-sec peak photon flux (15-150 keV)
140102A	65	29.8
131229A	13.86	10.7
131227A	18.0	1.1
131226A	7.20	10.4
131205A	37.5	0.6
131202A	30.4	0.7
131128A	3.00	2.7
131127A	92.1	1.3
131120A	131	0.5
131117A	11.00	0.7
131105A	112.3	3.5
131103A	17.3	1.5
131030A	41.1	28.1
131024B	64.00	0.1
131024A	112.00	0.3
131018A	73.22	0.5
131004A	1.54	3.4
131002B	39.10	0.6
131002A	55.59	1.3
131001A	4.9	2.57
130929A	11.10	1.7
130919A	97.3	0.5
130912A	0.28	2.2
130907A	360	25.6
130831B	37.8	2.4
130831A	32.5	13.6
130829A	42.56	0.6
130816B	10.00	0.9
130816A	29.97	1.5
130812A	7.6	2.8
130806A	6.1	1.3
130803A	44	5.1
130727A	13.57	7.0
130725B	10.0	2.2
130725A	101.8	0.6
130719A	177.7	0.6
130701A	4.38	17.1
130627B	28.6	0.8
130627A	30.8	1.8
130625A	38.1	1.2
130623A	15	1.4
130615A	304	0.7
130612A	4.0	1.7
130610A	46.4	1.7

GRB name	BAT T_{90} [sec]	BAT 1-sec peak photon flux (15-150 keV)
130609B	210.6	8.5
130609A	7.0	1.8
130608A	151.38	0.6
130606A	276.58	2.6
130605A	12.6	4.1
130604A	37.7	0.8
130603B	0.18	6.4
130603A	76	0.8
130529A	128	0.5
130528A	59.4	3.0
130527A	44	20.1
130521A	11.0	1.9
130514A	204	2.8
130511A	5.43	1.3
130508A	42	0.7
130505A	88	30.0
130504A	50	0.9
130502A	3.0	2.9
130427B	27.0	3.0
130427A	162.83	331.0
130420B	10.2	1.4
130420A	123.5	3.4
130419A	75.7	0.3
130418A	300	0.6
130408A	28	4.9
130327A	9.0	0.9
130315A	233.4	1.0
130216B	3.7	7.4
130216A	6.5	6.5
130215A	65.7	2.5
130211A	25.1	0.7
130206A	128.0	0.3
130131B	4.30	1.0
130131A	51.6	0.7
130122A	64	0.4
130102A	77.5	0.4
121226A	1.00	1.6
121217A	778	1.8
121212A	6.8	0.7
121211A	182	1.0
121209A	42.7	3.4
121202A	20.1	1.2
121201A	85	0.8
121128A	23.3	12.9

GRB name	BAT T_{90} [sec]	BAT 1-sec peak photon flux (15-150 keV)
121125A	52.2	2.9
121123A	317	2.6
121117A	30	1.1
121108A	89	1.6
121102A	24.7	2.3
121031A	226	2.4
121028A	3.8	1.9
121027A	62.6	1.3
121024A	69	1.3
121017A	4.2	3.3
121014A	80.0	0.3
121011A	75.6	1.2
121001A	147	0.5
120927A	43	1.6
120923A	27.2	0.6
120922A	173	2.0
120918A	25.1	4.5
120913B	126	3.2
120913A	30.1	2.3
120911A	17.8	2.7
120907A	16.9	2.9
120819A	71	0.8
120817A	28.2	0.8
120816A	7.6	2.1
120815A	9.7	2.2
120811C	26.8	4.1
120811A	166	1.0
120807A	20.0	0.9
120805A	48.00	0.37
120804A	0.81	10.8
120803B	37.5	1.5
120803A	10.0	0.4
120802A	50	3.0
120729A	71.5	2.9
120728A	22.06	2.4
120724A	72.8	0.6
120722A	42.4	1.0
120714B	159	0.4
120714A	16.2	1.5
120712A	14.7	2.4
120711B	60	0.4
120703A	25.2	10.5
120701A	13.8	1.6
120624B	192	5.5

GRB name	BAT T_{90} [sec]	BAT 1-sec peak photon flux (15-150 keV)
120612A	90	0.5
120521C	26.7	1.9
120521B	31.4	0.9
120514A	164.4	1.9
120422A	5.35	0.6
120404A	38.7	1.2
120403B	7.3	0.9
120328A	24.2	0.7
120327A	62.9	3.9
120326A	69.6	4.6
120324A	118	5.9
120320A	25.74	0.5
120312A	14.2	1.3
120311B	28.2	1.5
120311A	3.5	3.2
120308A	60.6	06
120224A	8.13	0.9
120219A	90.5	0.3
120218A	27.5	9.1
120215A	26.5	0.6
120213A	48.9	1.7
120212A	5.52	2.1
120211A	61.7	0.5
120121A	26.1	0.7
120119A	253.8	10.3
120118B	23.26	2.2
120116A	41.0	4.1
120106A	61.6	1.5
120102A	38.7	10.3
111229A	25.4	1.0
111228A	101.20	12.4
111225A	106.8	0.7
111215A	796	0.5
111204A	48.0	0.3
111129A	7.6	0.9
111123A	290.0	0.9
111121A	119	7.1
111109A	13.0	0.5
111107A	26.6	1.2
111103B	167	7.2
111103A	11.6	3.1
111029A	7.6	1.5
111026A	3.62	1.1
111022B	79.1	0.4

GRB name	BAT T_{90} [sec]	BAT 1-sec peak photon flux (15-150 keV)
111022A	24.7	2.5
111018A	36	0.4
111016A	550	0.9
111008A	63.46	6.4
111005A	26	1.1
110928A	26.7	0.9
110921A	48.00	0.2
110915A	78.76	3.3
110827A	8.5	0.4
110820A	256	0.4
110818A	103	1.6
110808A	48	0.4
110801A	385	1.1
110731A	38.8	11.0
110726A	5.2	1.0
110719A	41.0	1.3
110715A	13.0	53.9
110709B	55.6	3.4
110709A	44.7	6.2
110625A	44.5	49.5
110610A	46.4	4.2
110530A	19.6	0.4
110521A	13.8	0.5
110520A	15.7	1.1
110519A	27.2	4.6
110503A	10.0	1.35
110422A	25.9	30.7
110420A	11.8	14.0
110414A	152.0	1.1
110412A	23.4	2.0
110411A	80.3	1.3
110407A	145	1.73
110402A	60.9	4.1
110319B	14.5	1.25
110319A	19.3	2.2
110318B	4.8	0.7
110318A	16.0	8.0
110315A	77	1.7
110312A	28.7	1.2
110305A	12.0	1.2
110223B	54.0	0.6
110223A	7.0	0.6
110213A	48.0	1.6
110212A	3.3	1.5

GRB name	BAT T_{90} [sec]	BAT 1-sec peak photon flux (15-150 keV)
110210A	233	0.3
110208A	37.4	0.6
110207A	80.3	1.1
110205A	257	3.6
110201A	13.0	1.1
110128A	30.7	0.8
110119A	208	2.2
110106B	24.8	2.1
110106A	4.3	1.9
110102A	264	8.4
101219B	34	0.6
101219A	0.6	4.1
101213A	135	2.2
101117B	5.2	4.5
101114A	10	1.8
101030A	92.0	0.9
101024A	18.7	5.5
101020A	175.0	0.5
101017A	70.0	9.4
101011A	71.5	1.3
101008A	104	1.6
100928A	3.3	2.5
100924A	96.0	1.5
100917A	66	0.6
100915A	200	0.5
100906A	114.4	10.1
100904A	31.3	1.6
100902A	428.8	1.0
100901A	439	0.8
100823A	16.9	1.0
100816A	2.9	10.9
100814A	174.5	2.5
100807A	7.9	1.8
100805A	15.0	0.7
100802A	487	0.9
100728B	12.1	3.5
100728A	198.5	5.1
100727A	84	1.2
100725B	200	2.4
100725A	141	0.7
100724A	1.4	1.9
100719A	36.0	0.6
100704A	197.5	4.3
100702A	0.16	2.0

GRB name	BAT T_{90} [sec]	BAT 1-sec peak photon flux (15-150 keV)
100625A	0.33	2.6
100621A	63.6	12.8
100619A	97.5	4.8
100615A	39	5.4
100614A	225	0.7
100606A	480	1.6
100526B	64.0	0.1
100526A	102	0.7
100522A	35.3	7.1
100513A	84	0.6
100508A	52	0.4
100504A	97.3	1.7
100425A	37.0	1.4
100424A	104	0.4
100418A	7.0	1.0
100413A	191	0.7
100324A	6	0.3
100316C	9.3	0.4
100316B	3.8	1.3
100316A	7.0	2.3
100305A	69.7	0.9
100302A	17.9	0.5
100219A	18.8	0.4
100213B	48.0	0.5
100213A	2.4	2.1
100212A	136	2.2
100205A	26.0	0.4
100119A	23.8	7.7
100117A	0.3	2.9
100111A	12.9	1.9
091221	68.5	3.0
091208B	14.9	15.2
091208A	29.1	1.8
091130B	112.5	1.1
091127	7.1	46.5
091112	17	1.9
091109B	0.3	5.4
091109A	48	1.3
091104	99.3	0.4
091102	6.6	1.4
091029	39.2	1.8
091026	41.6	2.2
091024	109.8	2.0
091020	34.6	4.2

GRB name	BAT T_{90} [sec]	BAT 1-sec peak photon flux (15-150 keV)
091018	4.4	10.3
090929B	360	3.3
090927	2.2	2.0
090926B	109.7	3.2
090916	63.4	1.9
090915	8	0.8
090912	144.0	1.0
090904B	47.0	5.3
090904A	122	1.9
090814A	80	0.6
090813	7.1	8.5
090812	66.7	3.6
090809	5.4	1.1
090807	140.8	0.7
090728	59	1.0
090727	302	0.5
090726	67.0	0.7
090715B	266	3.8
090715A	63	3.9
090712	145	0.9
090709B	27.2	2.1
090709A	89	7.8
090708	15.0	1.3
090628	20.1	1.5
090621B	0.14	3.9
090618	113.2	38.9
090531B	80	1.25
090531A	32	1.3
090530	48	2.5
090529	100	0.4
090519	64	0.6
090518	6.9	2.4
090516A	210	1.6
090510	0.3	9.7
090509	335	1.5
090429B	5.5	1.6
090429A	188	0.6
090426	1.2	2.4
090424	48	71.0
090423	10.3	1.7
090422	8.5	1.7
090419	450	0.4
090418A	56	1.9
090417B	260	0.3

GRB name	BAT T_{90} [sec]	BAT 1-sec peak photon flux (15-150 keV)
090410	165	1.9
090407	310	0.6
090404	84	1.9
090401B	183	23.1
090401A	112	10.9
090313	79	0.8
090308A	48	0.1
090307A	22	0.2
090306B	20.4	2.5
090305A	0.4	1.9
090301A	41.0	18.7
090205	8.8	0.5
090201	83	14.7
090129	17.5	3.7
090123	131	1.7
090113	9.1	2.5
090111	24.8	0.9
090107A	12.2	1.1
090102	27.0	5.5
081230	60.7	0.7
081226A	0.4	2.4
081222	24	7.7
081221	34	18.2
081211A	3.5	0.8
081210	146	2.5
081203A	294	2.9
081128	100	1.3
081127	37	0.6
081126	54	3.7
081121	14	4.4
081118	67	0.6
081109A	190	1.1
081104	59.1	1.0
081102	63	1.4
081101	0.20	3.6
081029	270	0.5
081028A	260	0.5
081025	23	1.3
081022	160	0.6
081012	29	1.0
081011	9	0.4
081008	185.5	1.3
081007	10.0	2.6
080928	280	2.1

GRB name	BAT T_{90} [sec]	BAT 1-sec peak photon flux (15-150 keV)
080916B	32	0.6
080916A	60	2.7
080915B	3.9	8.5
080915A	14	0.5
080913	8	1.4
080906	147	1.0
080905B	128	0.5
080903	66	0.8
080810	106	2.0
080805	78	1.1
080804	34	3.1
080802	176	0.3
080727C	79.7	2.3
080727B	8.6	7.6
080727A	4.9	0.3
080725	120	2.3
080723A	17.3	0.9
080721	16.2	20.9
080714	33	4.2
080710	120	1.0
080707	27.1	1.0
080703	3.4	1.0
080702B	20	0.5
080701	18	2.2
080623	15.2	2.0
080613B	105	2.7
080607	79	23.1
080605	20	19.9
080604	82	0.4
080603B	60	3.5
080602	74	2.9
080524	9	0.4
080523	102	0.5
080517	64.6	0.6
080516	5.8	1.8
080515	21	3.9
080506	150	0.4
080503	170	0.9
080430	16.2	2.6
080426	1.7	4.8
080413B	8.0	18.7
080413A	46	5.6
080411	56	43.2
080409	20.2	3.7

GRB name	BAT T_{90} [sec]	BAT 1-sec peak photon flux (15-150 keV)
080330	61	0.9
080328	90.6	5.5
080325	128.4	1.4
080320	14	0.6
080319D	24	0.1
080319C	34	5.2
080319B	50	24.8
080319A	64	1.2
080310	365	1.3
080307	125.9	0.4
080303	67	1.4
080229A	64	5.7
080218B	6.2	3.1
080218A	27.6	1.4
080212	123	1.2
080210	45	1.6
080207	340	1.0
080205	106.5	1.4
080130	65	0.2
080129	48	0.2
080123	115	1.8
071227	1.8	1.6
071129	420	0.9
071122	68.7	0.4
071118	71	0.3
071117	6.6	11.3
071112C	15	8
071101	9.0	0.4
071031	180	0.5
071028B	55	1.4
071028A	27.0	0.3
071025	109	1.6
071021	225	0.7
071020	4.2	8.4
071018	376.0	0.2
071013	26	0.4
071011	61	1.7
071010B	35.7	7.7
071010A	6	0.8
071008	18	0.5
071006	50	13
071003	150	6.3
071001	58.5	0.9
070920B	20.2	0.8

GRB name	BAT T_{90} [sec]	BAT 1-sec peak photon flux (15-150 keV)
070920A	56	0.3
070917	7.3	8.5
070913	3.2	1.4
070911	162	3.9
070810A	11.0	1.9
070808	32	2.0
070805	31.0	0.7
070802	16.4	0.4
070731	2.9	1.2
070721B	340	1.5
070714B	64	2.7
070714A	2.0	1.8
070704	380	2.1
070628	39.1	5.1
070621	33.3	2.5
070616	402.400	1.93
070612B	13.500	2.47
070612A	368.800	1.51
070611	12.200	0.82
070531	44.500	1.00
070529	109.200	1.43
070521	37.900	6.53
070520B	65.800	0.43
070520A	18.100	0.44
070518	5.500	0.68
070517	7.600	0.95
070509	7.700	0.68
070508	20.900	24.10
070506	4.300	0.96
070429A	163.300	0.41
070427	11.100	1.34
070420	76.500	7.12
070419B	236.400	1.38
070419A	115.600	0.20
070412	33.800	0.66
070411	121.500	0.91
070330	9.000	0.88
070328	75.300	4.22
070318	74.600	1.76
070306	209.500	4.07
070227	7	4.62
070224	34.500	0.34
070223	88.500 ²¹²	0.69
070220	129.000	5.88

GRB name	BAT T_{90} [sec]	BAT 1-sec peak photon flux (15-150 keV)
070219	16.600	0.67
070208	47.700	0.90
070129	460.600	0.55
070110	88.400	0.60
070107	347.300	1.97
070103	18.600	1.04
061222B	40.000	1.59
061222A	71.400	8.53
061218	6.500	0.26
061210	85.300	5.31
061202	91.200	2.51
061201	0.760	3.86
061126	70.800	9.76
061121	81.300	21.10
061110B	134.000	0.45
061110A	40.700	0.53
061102	45.600	0.23
061028	106.200	0.65
061021	46.200	6.11
061019	183.800	2.12
061007	75.300	14.60
061006	129.900	5.24
061004	6.200	2.54
061002	17.600	0.81
060929	554.000	0.42
060927	22.500	2.70
060926	8.000	1.09
060923C	75.800	0.96
060923B	8.600	1.52
060923A	51.700	1.32
060919	9.100	2.12
060912A	5.000	8.58
060908	19.300	3.03
060906	43.500	1.97
060904B	171.500	2.44
060904A	80.100	4.87
060825	8.000	2.66
060814	145.300	7.27
060813	16.100	8.84
060807	54.000	0.83
060805A	5.300	0.34
060804	17.800	1.13
060729	115.300 213	1.17
060719	66.900	2.16

GRB name	BAT T_{90} [sec]	BAT 1-sec peak photon flux (15-150 keV)
060714	115.000	1.28
060712	26.300	1.64
060708	10.200	1.94
060707	66.200	1.01
060614	108.700	11.50
060607B	31.100	1.46
060607A	102.200	1.40
060605	79.100	0.46
060604	95.000	0.34
060602A	75.000	0.56
060526	298.200	1.67
060522	71.100	0.55
060516	161.600	0.34
060515	52.000	0.82
060512	8.500	0.88
060510B	275.200	0.57
060510A	20.400	14.70
060507	183.300	1.27
060505	4	2.65
060502A	28.400	1.69
060501	21.900	1.98
060428B	57.900	0.66
060428A	39.500	2.28
060427	64.000	0.27
060424	37.500	1.61
060421	12.200	2.94
060418	103.100	6.52
060413	147.700	0.93
060403	30.100	0.95
060323	25.400	0.78
060322	221.500	2.08
060319	10.600	1.09
060313	0.740	12.10
060312	50.600	1.53
060306	61.200	5.97
060223B	10.300	2.87
060223A	11.300	1.35
060219	62.100	0.56
060218	2100	0.25
060211B	27.700	0.73
060211A	126.300	0.42
060210	255.000	2.72
060206	7.600	2.79
060204B	139.400	1.35

GRB name	BAT T_{90} [sec]	BAT 1-sec peak photon flux (15-150 keV)
060203	68.200	0.60
060202	198.900	0.51
060124	750	0.89
060117	16.900	48.30
060116	105.900	1.11
060115	139.600	0.87
060111B	58.800	1.40
060111A	13.200	1.71
060110	26.000	1.89
060109	115.400	0.47
060108	14.300	0.77
060105	54.400	7.44
060102	19.000	0.38
051227	114.600	0.95
051221B	39.900	0.54
051221A	1.400	12.00
051213	71.100	0.48
051117B	9.000	0.49
051117A	136.300	0.95
051113	93.300	2.25
051111	46.100	2.66
051109B	14.300	0.55
051109A	37.200	3.94
051021B	46.500	0.80
051016B	4.000	1.30
051016A	23.000	1.39
051012	13	0.53
051008	32	5.44
051006	34.800	1.62
051001	189.100	0.49
050922C	4.500	7.26
050922B	150.900	1.01
050916	49.500	0.65
050915B	40.900	2.31
050915A	52.000	0.77
050911	16.200	1.33
050908	19.400	0.70
050904	174.200	0.62
050827	50.000	1.84
050826	35.500	0.38
050824	22.600	0.50
050822	103.400	2.24
050820B	12.000	3.95
050820A	26	2.45

GRB name	BAT T_{90} [sec]	BAT 1-sec peak photon flux (15-150 keV)
050819	37.700	0.38
050814	150.900	0.71
050803	87.900	0.96
050802	19.000	2.75
050801	19.400	1.46
050730	156.500	0.55
050726	49.900	1.38
050724	96.000	3.26
050721	98.400	2.24
050717	85.000	6.23
050716	69.100	2.18
050715	51.600	1.05
050714B	46.700	0.52
050713B	54.200	1.60
050713A	124.700	4.67
050712	51.600	0.55
050701	21.800	2.74
050607	26.400	0.95
050603	12.400	21.50
050528	11.300	1.18
050525A	8.800	41.70
050509A	11.400	0.90
050507	15	0.29
050505	58.900	1.85
050502B	17.700	1.42
050422	59.300	0.57
050421	15.000	0.26
050418	82.300	3.68
050416B	3.400	5.93
050416A	2.500	4.88
050412	26.500	0.48
050410	42.500	1.80
050406	5.400	0.36
050401	33.300	10.70
050326	29.300	12.20
050319	152.500	1.52
050318	32	3.16
050315	95.600	1.93
050306	158.300	3.58
050223	22.500	0.69
050219B	30.700	24.80
050219A	23.700	3.53
050215B	8.100	0.67
050215A	87.300	0.49

GRB name	BAT T_{90} [sec]	BAT 1-sec peak photon flux (15-150 keV)
050128	19.200	7.42
050126	24.800	0.71
050124	4.000	5.46
050117	166.600	2.35
041228	55.400	1.61
041226	89.700	0.35
041224	177.200	2.94
041223	109.100	7.35
041220	5.600	1.81
041219C	4.800	2.45
041217	5.800	6.86

Table A.2: The Swift GRBs that have 90% detection probability with SVOM/ECLAIRs.

GRB name	BAT T_{90} [sec]	BAT 1-sec peak photon flux (15-150 keV)
220714B	50.10	3.8
220711B	88.64	2.0
220623A	57.11	4.5
220521A	13.55	4.7
220501A	202.24	1.2
220430A	43.10	29.6
220427A	57.2	3.0
220408A	17.25	4.9
220403B	27.0	2.7
220325A	3.50	2.0
220306B	12.34	2.3
220305A	21.12	2.1
220118A	10.61	3.3
220117A	49.81	1.9
220101A	173.36	7.3

GRB name	BAT T_{90} [sec]	BAT 1-sec peak photon flux (15-150 keV)
211227A	83.79	5.1
211225B	121.54	6.1
211223C	15.00	3.1
211211A	51.37	155.0
211129A	113.01	1.5
211023B	1.30	2.2
210901A	46.77	2.4
210822A	180.8	27.7
210820A	196.8	0.8
210818A	73.56	11.2
210807C	89.97	4.0
210807A	156.30	1.8
210730A	3.86	7.1
210724A	50.57	2.5
210723A	48.54	3.1
210722A	50.20	2.2
210712A	136.41	2.3
210619B	60.90	115.0
210610B	69.38	13.5
210610A	13.62	2.4
210514A	70.21	8.7
210504A	135.06	0.9
210430A	11.53	1.9
210421A	79.52	2.0
210411C	12.80	4.8
210410A	52.88	4.0
210403A	168.3	1.1
210402A	238.7	1.6
210323A	1.12	2.9
210318B	14.95	14.5
210308A	5.3	13.6
210307A	262	1.0
210306B	24.32	2.4
210306A	9.12	20.9
210305A	68.6	3.4
210226A	20.80	2.8
210218A	240	1.0
210217A	4.22	5.1
210210A	6.60	7.0
210207B	95.69	3.1
210112A	107.60	20.5
210104B	19.94	1.9
210104A	32.06	12.1
210102C	87.25	4.4

GRB name	BAT T_{90} [sec]	BAT 1-sec peak photon flux (15-150 keV)
201229A	53.3	1.7
201216C	48.0	18.0
201209A	48.0	12.2
201105A	33.82	13.9
201104B	8.66	4.1
201027A	546.73	1.4
201026A	135.38	2.2
201024A	5.00	3.7
201020A	14.17	2.1
201017A	22.08	1.8
201013A	7.36	24.6
200925B	18.25	3.0
200922A	10.30	11.4
200906A	70.90	2.5
200903A	24.15	3.8
200901A	20.37	7.7
200829A	13.04	98.7
200806A	38.8	12.1
200716C	86	10.7
200711A	29.39	7.7
200612A	171.48	0.7
200529A	79.57	1.8
200528A	58.7	17.5
200519A	71.88	20.6
200416A	5.04	3.8
200410A	108.8	1.8
200306A	32.87	7.0
200303A	94.2	5.0
200227A	32.8	5.7
200219A	288.0	2.4
200216B	81.3	1.5
200215A	11.7	2.7
200205B	458.0	2.0
200131A	32.74	26.9
200127A	216.9	0.7
200125A	350.83	4.0
200122A	174.96	9.1
200115A	158.4	3.6
200107B	86.68	1.9
191227A	58.5	21.8
191221B	48.00	4.8
191220A	175.55	1.1
191218A	44.67	6.3

GRB name	BAT T_{90} [sec]	BAT 1-sec peak photon flux (15-150 keV)
191123A	275.1	1.2
191122A	153.3	3.1
191101A	137.95	1.3
191031C	93.2	4.6
191019A	64.35	5.7
191016A	219.70	1.5
191004B	37.7	5.0
191004A	2.44	7.8
191001B	108.9	1.8
190926A	368.9	0.6
190829A	58.2	18.0
190828B	66.6	2.3
190824A	169.4	5.0
190821A	57.1	2.8
190816A	375.0	1.3
190727B	40.14	20.9
190719C	185.7	5.5
190630C	38.4	2.0
190613B	160.84	5.7
190604B	220.2	7.3
190519A	45.58	20.6
190511A	27.7	6.2
190424A	10.6	2.0
190331A	4.3	2.8
190324A	28.4	11.9
190220A	10.0	2.6
190219A	167.8	1.9
190211A	12.48	1.9
190204A	26.4	30.5
190203A	96	3.1
190202A	19.4	7.8
190114C	361.5	101.0
190110A	9.3	9.0
190109A	115.0	1.9
190106A	76.8	5.5
190103B	19.5	16.3
181228A	257.3	9.5
181213A	15.31	2.1
181126A	2.09	2.7
181110A	138.4	3.7
181030A	304.7	0.8
181020A	238.0	7.7
180925A	81.70	3.1
180905A	165.3	1.0

GRB name	BAT T_{90} [sec]	BAT 1-sec peak photon flux (15-150 keV)
180828A	14.0	17.8
180823A	80.3	2.3
180818B	134.4	1.2
180812A	16.51	1.9
180809B	233.2	26.3
180805B	122.5	1.7
180728A	8.68	132.0
180727A	1.1	3.6
180720C	124.2	1.1
180709A	215.1	0.6
180706A	42.7	3.2
180704A	19.7	9.6
180630A	18.85	6.6
180626A	30.07	4.1
180624A	486.4	1.4
180623A	114.9	5.6
180620B	198.8	3.6
180620A	23.16	7.7
180618A	47.4	2.2
180510B	134.3	1.2
180510A	40.4	8.9
180425A	11.2	2.2
180418A	2.29	3.0
180411A	77.5	6.1
180404B	111.5	5.2
180331B	147.0	2.8
180329B	210.0	1.4
180325A	94.1	9.4
180324A	7.2	4.4
180316A	87.0	3.3
180314A	51.2	7.9
180205A	15.5	3.4
180204A	1.16	3.6
180113A	64	2.5
180111A	50.6	4.9
171222A	174.8	0.7
171212A	320	0.7
171211A	2.32	2.3
171209A	161.7	1.6
171205A	189.4	1.0
171120A	64	11.4
171103A	3.90	3.6
171027A	96.6	3.0
171011A	2.27	7.0

GRB name	BAT T_{90} [sec]	BAT 1-sec peak photon flux (15-150 keV)
170912B	19.6	5.7
170912A	21.9	2.0
170906C	48.4	7.2
170906A	88.1	10.9
170903A	29.2	3.9
170823A	69.4	3.7
170822A	64	4.2
170810A	152.4	1.2
170803A	3.82	6.5
170711A	31.3	4.8
170705A	217.3	13.9
170629A	34.4	4.1
170626A	12.94	23.6
170604A	26.70	4.2
170531B	164.13	0.8
170519A	216.4	0.7
170419B	77.2	2.4
170330A	144.73	4.5
170318A	133.7	1.2
170317A	11.94	3.5
170208B	128.07	8.4
170208A	7.45	5.4
170205A	26.1	4.3
170202A	46.2	4.7
170126A	9.5	7.3
170101A	2.43	54.4
161219B	6.94	5.3
161218A	7.1	17.6
161214B	24.8	2.2
161129A	35.53	3.4
161117B	152.51	6.0
161117A	125.7	6.8
161105A	177.3	1.4
161017A	216.3	2.8
161014A	18.3	2.9
161007A	201.7	0.4
161004B	15.9	10.1
161001A	2.6	3.5
160917A	16	2.2
160905A	64	6.3
160824A	99.3	1.3
160815A	8.6	4.7
160804A	144.2	2.9
160709A	4.8	2.7

GRB name	BAT T_{90} [sec]	BAT 1-sec peak photon flux (15-150 keV)
160703A	44.4	5.8
160625A	53.9	3.0
160611A	34.1	2.0
160607A	33.4	21.8
160519A	35.57	2.4
160506A	254.5	0.4
160425A	304.58	2.8
160424A	6.3	5.1
160419A	8.8	8.9
160410A	8.2	3.5
160327A	28	1.8
160325A	64.9	5.2
160228A	98.36	1.2
160227A	316.5	0.6
160225A	157	1.0
160223A	127	3.1
160220B	31.4	6.6
160216A	11.0	7.3
160131A	325	6.4
160119A	116	2.9
160117A	118.58	1.4
151229A	1.78	7.2
151114A	4.86	2.9
151112A	19.32	1.9
151027A	129.69	6.8
151021A	110.2	9.7
151006A	203.9	2.6
150911A	7.2	5.2
150910A	112.2	1.1
150831B	6.2	6.1
150831A	1.15	3.4
150818A	123.3	2.4
150817A	38.8	9.6
150801B	426	2.5
150724A	280	0.9
150711A	64.2	3.8
150710B	15	8.3
150616A	599.5	2.9
150607A	26.3	4.9
150530A	6.62	4.1
150513A	162	2.9
150430A	107.1	5.0
150428B	130.9	1.4
150428A	53.2	3.0

GRB name	BAT T_{90} [sec]	BAT 1-sec peak photon flux (15-150 keV)
150424A	91	12.0
150413A	263.6	1.6
150403A	40.90	17.6
150323C	159.4	1.1
150323A	149.6	5.4
150314A	14.79	38.5
150309A	242	9.0
150301B	12.44	3.0
150222A	15.90	4.7
150213B	181	1.1
150212A	11.4	1.9
150206A	83.2	10.1
141221A	36.9	3.1
141220A	7.21	8.9
141212B	10.5	3.9
141121A	549.9	0.9
141109A	200	2.5
141017A	55.7	6.7
141005A	4.34	4.2
141004A	3.92	6.1
140930B	0.84	4.0
140919A	151.3	2.0
140907A	79.2	2.5
140828A	18.8	2.2
140817A	244	7.2
140716A	104	5.2
140709B	155.0	0.9
140709A	98.6	3.1
140706A	48.3	1.8
140703A	67.1	2.8
140629A	42.0	4.2
140628A	10.5	2.8
140619A	233.9	4.6
140529A	4.5	11.5
140521A	9.88	1.9
140512A	154.8	6.8
140506A	111.1	10.9
140430A	173.6	2.5
140423A	134	2.1
140419A	94.7	4.9
140413A	139.6	2.3
140331A	209	0.31
140323A	104.9	6.2
140302A	87.5	1.7

GRB name	BAT T_{90} [sec]	BAT 1-sec peak photon flux (15-150 keV)
140215A	84.2	7.9
140213A	60.0	23.5
140209A	21.3	38.1
140206A	93.6	19.4
140118A	84.15	1.9
140114A	139.7	0.9
140108A	94	6.1
140103A	17.3	2.1
140102A	65	29.8
131229A	13.86	10.7
131226A	7.20	10.4
131128A	3.00	2.7
131127A	92.1	1.3
131105A	112.3	3.5
131030A	41.1	28.1
131004A	1.54	3.4
131001A	4.9	2.57
130907A	360	25.6
130831B	37.8	2.4
130831A	32.5	13.6
130812A	7.6	2.8
130803A	44	5.1
130727A	13.57	7.0
130725B	10.0	2.2
130719A	177.7	0.6
130701A	4.38	17.1
130627A	30.8	1.8
130615A	304	0.7
130610A	46.4	1.7
130609B	210.6	8.5
130606A	276.58	2.6
130605A	12.6	4.1
130528A	59.4	3.0
130527A	44	20.1
130521A	11.0	1.9
130514A	204	2.8
130505A	88	30.0
130502A	3.0	2.9
130427B	27.0	3.0
130427A	162.83	331.0
130420A	123.5	3.4
130418A	300	0.6
130408A	28	4.9
130315A	233.4	1.0

GRB name	BAT T_{90} [sec]	BAT 1-sec peak photon flux (15-150 keV)
130216B	3.7	7.4
130216A	6.5	6.5
130215A	65.7	2.5
121211A	182	1.0
121209A	42.7	3.4
121128A	23.3	12.9
121125A	52.2	2.9
121123A	317	2.6
121108A	89	1.6
121102A	24.7	2.3
121031A	226	2.4
121017A	4.2	3.3
120922A	173	2.0
120918A	25.1	4.5
120913B	126	3.2
120913A	30.1	2.3
120911A	17.8	2.7
120907A	16.9	2.9
120816A	7.6	2.1
120815A	9.7	2.2
120811C	26.8	4.1
120811A	166	1.0
120804A	0.81	10.8
120802A	50	3.0
120729A	71.5	2.9
120728A	22.06	2.4
120712A	14.7	2.4
120703A	25.2	10.5
120624B	192	5.5
120521C	26.7	1.9
120514A	164.4	1.9
120327A	62.9	3.9
120326A	69.6	4.6
120324A	118	5.9
120311A	3.5	3.2
120308A	60.6	06
120218A	27.5	9.1
120213A	48.9	1.7
120212A	5.52	2.1
120119A	253.8	10.3
120118B	23.26	2.2
120116A	41.0	4.1
120106A	61.6	1.5
120102A	38.7	10.3

GRB name	BAT T_{90} [sec]	BAT 1-sec peak photon flux (15-150 keV)
111228A	101.20	12.4
111123A	290.0	0.9
111121A	119	7.1
111103B	167	7.2
111103A	11.6	3.1
111022A	24.7	2.5
111016A	550	0.9
111008A	63.46	6.4
110915A	78.76	3.3
110820A	256	0.4
110818A	103	1.6
110801A	385	1.1
110731A	38.8	11.0
110715A	13.0	53.9
110709B	55.6	3.4
110709A	44.7	6.2
110625A	44.5	49.5
110610A	46.4	4.2
110519A	27.2	4.6
110422A	25.9	30.7
110420A	11.8	14.0
110414A	152.0	1.1
110412A	23.4	2.0
110407A	145	1.73
110402A	60.9	4.1
110319A	19.3	2.2
110318A	16.0	8.0
110315A	77	1.7
110213A	48.0	1.6
110205A	257	3.6
110119A	208	2.2
110106B	24.8	2.1
110102A	264	8.4
101213A	135	2.2
101117B	5.2	4.5
101024A	18.7	5.5
101017A	70.0	9.4
101008A	104	1.6
100928A	3.3	2.5
100924A	96.0	1.5
100915A	200	0.5
100906A	114.4	10.1
100902A	428.8	1.0
100901A	439	0.8

GRB name	BAT T_{90} [sec]	BAT 1-sec peak photon flux (15-150 keV)
100816A	2.9	10.9
100814A	174.5	2.5
100802A	487	0.9
100728B	12.1	3.5
100728A	198.5	5.1
100725B	200	2.4
100704A	197.5	4.3
100621A	63.6	12.8
100619A	97.5	4.8
100615A	39	5.4
100614A	225	0.7
100606A	480	1.6
100522A	35.3	7.1
100504A	97.3	1.7
100413A	191	0.7
100316A	7.0	2.3
100213A	2.4	2.1
100212A	136	2.2
100119A	23.8	7.7
100111A	12.9	1.9
091221	68.5	3.0
091208B	14.9	15.2
091208A	29.1	1.8
091130B	112.5	1.1
091127	7.1	46.5
091112	17	1.9
091029	39.2	1.8
091026	41.6	2.2
091024	109.8	2.0
091020	34.6	4.2
091018	4.4	10.3
090929B	360	3.3
090927	2.2	2.0
090926B	109.7	3.2
090916	63.4	1.9
090912	144.0	1.0
090904B	47.0	5.3
090904A	122	1.9
090813	7.1	8.5
090812	66.7	3.6
090727	302	0.5
090715B	266	3.8
090715A	63	3.9
090712	145	0.9

GRB name	BAT T_{90} [sec]	BAT 1-sec peak photon flux (15-150 keV)
090709B	27.2	2.1
090709A	89	7.8
090618	113.2	38.9
090530	48	2.5
090518	6.9	2.4
090516A	210	1.6
090509	335	1.5
090429A	188	0.6
090426	1.2	2.4
090424	48	71.0
090419	450	0.4
090418A	56	1.9
090410	165	1.9
090407	310	0.6
090404	84	1.9
090401B	183	23.1
090401A	112	10.9
090306B	20.4	2.5
090301A	41.0	18.7
090201	83	14.7
090129	17.5	3.7
090123	131	1.7
090113	9.1	2.5
090102	27.0	5.5
081222	24	7.7
081221	34	18.2
081210	146	2.5
081203A	294	2.9
081128	100	1.3
081126	54	3.7
081121	14	4.4
081109A	190	1.1
081029	270	0.5
081028A	260	0.5
081008	185.5	1.3
081007	10.0	2.6
080928	280	2.1
080916A	60	2.7
080915B	3.9	8.5
080906	147	1.0
080810	106	2.0
080804	34	3.1
080727C	79.7	2.3
080727B	8.6	7.6

GRB name	BAT T_{90} [sec]	BAT 1-sec peak photon flux (15-150 keV)
080725	120	2.3
080721	16.2	20.9
080714	33	4.2
080710	120	1.0
080701	18	2.2
080623	15.2	2.0
080613B	105	2.7
080607	79	23.1
080605	20	19.9
080603B	60	3.5
080602	74	2.9
080515	21	3.9
080503	170	0.9
080430	16.2	2.6
080426	1.7	4.8
080413B	8.0	18.7
080413A	46	5.6
080411	56	43.2
080409	20.2	3.7
080328	90.6	5.5
080325	128.4	1.4
080319C	34	5.2
080319B	50	24.8
080310	365	1.3
080229A	64	5.7
080218B	6.2	3.1
080212	123	1.2
080210	45	1.6
080207	340	1.0
080205	106.5	1.4
080123	115	1.8
071129	420	0.9
071117	6.6	11.3
071112C	15	8
071025	109	1.6
071021	225	0.7
071020	4.2	8.4
071011	61	1.7
071010B	35.7	7.7
071006	50	13
071003	150	6.3
070917	7.3	8.5
070911	162	3.9
070810A	11.0	1.9

GRB name	BAT T_{90} [sec]	BAT 1-sec peak photon flux (15-150 keV)
070808	32	2.0
070721B	340	1.5
070714B	64	2.7
070704	380	2.1
070628	39.1	5.1
070621	33.3	2.5
070616	402.400	1.93
070612B	13.500	2.47
070612A	368.800	1.51
070529	109.200	1.43
070521	37.900	6.53
070508	20.900	24.10
070420	76.500	7.12
070419B	236.400	1.38
070328	75.300	4.22
070318	74.600	1.76
070306	209.500	4.07
070227	7	4.62
070220	129.000	5.88
070129	460.600	0.55
070107	347.300	1.97
061222A	71.400	8.53
061210	85.300	5.31
061202	91.200	2.51
061201	0.760	3.86
061126	70.800	9.76
061121	81.300	21.10
061021	46.200	6.11
061019	183.800	2.12
061007	75.300	14.60
061006	129.900	5.24
061004	6.200	2.54
060929	554.000	0.42
060927	22.500	2.70
060919	9.100	2.12
060912A	5.000	8.58
060908	19.300	3.03
060906	43.500	1.97
060904B	171.500	2.44
060904A	80.100	4.87
060825	8.000	2.66
060814	145.300	7.27
060813	16.100	8.84
060729	115.300	1.17

GRB name	BAT T_{90} [sec]	BAT 1-sec peak photon flux (15-150 keV)
060719	66.900	2.16
060714	115.000	1.28
060708	10.200	1.94
060614	108.700	11.50
060607A	102.200	1.40
060526	298.200	1.67
060510B	275.200	0.57
060510A	20.400	14.70
060507	183.300	1.27
060505	4	2.65
060501	21.900	1.98
060428A	39.500	2.28
060421	12.200	2.94
060418	103.100	6.52
060413	147.700	0.93
060322	221.500	2.08
060313	0.740	12.10
060306	61.200	5.97
060223B	10.300	2.87
060210	255.000	2.72
060206	7.600	2.79
060204B	139.400	1.35
060202	198.900	0.51
060117	16.900	48.30
060116	105.900	1.11
060115	139.600	0.87
060110	26.000	1.89
060105	54.400	7.44
051221A	1.400	12.00
051117A	136.300	0.95
051113	93.300	2.25
051111	46.100	2.66
051109A	37.200	3.94
051008	32	5.44
051001	189.100	0.49
050922C	4.500	7.26
050922B	150.900	1.01
050915B	40.900	2.31
050904	174.200	0.62
050827	50.000	1.84
050822	103.400	2.24
050820B	12.000	3.95
050820A	26	2.45
050802	19.000	2.75

GRB name	BAT T_{90} [sec]	BAT 1-sec peak photon flux (15-150 keV)
050724	96.000	3.26
050721	98.400	2.24
050717	85.000	6.23
050716	69.100	2.18
050713B	54.200	1.60
050713A	124.700	4.67
050701	21.800	2.74
050603	12.400	21.50
050525A	8.800	41.70
050505	58.900	1.85
050418	82.300	3.68
050416B	3.400	5.93
050416A	2.500	4.88
050410	42.500	1.80
050401	33.300	10.70
050326	29.300	12.20
050319	152.500	1.52
050318	32	3.16
050315	95.600	1.93
050306	158.300	3.58
050219B	30.700	24.80
050219A	23.700	3.53
050128	19.200	7.42
050124	4.000	5.46
050117	166.600	2.35
041228	55.400	1.61
041224	177.200	2.94
041223	109.100	7.35
041219C	4.800	2.45
041217	5.800	6.86

B - publications

- S. Hussein, F. Robinet, M. Boutelier, D. Götz, A. Gros, B. Schneider. Analysis methods to localize and characterize X-ray sources with the Micro-channel X-ray Telescope on board the SVOM satellite, <https://doi.org/10.48550/arXiv.2209.13330>.
- D. Götz, [..] S. Hussein et al. The Scientific Performance of the Microchannel X-ray Telescope on board the SVOM Mission, <https://doi.org/10.21203/rs.3.rs-2064925/v1>.

List of Figures

1.1	Light curve of the first GRB detected by Vela showing the intensity of the photons as a function of time, about 1500 photons were detected in the first second. The GRB's duration is less than 10 s. Credit: NASA	18
1.2	Structure of the CGRO satellite with its instruments: OSSE, COMPTEL, EGRET, BATSE. the BATSE 8 detectors are placed at each corner of CGRO structure .	19
1.3	The angular distribution of 2704 GRBs recorded with BATSE. The projection is given in galactic coordinates. The GRBs locations are color-coded based on the fluence. This figure shows an isotropic distribution of GRBs that reveals an extra-galactic origin. Credit: [41].	20
1.4	Distribution of GRB T_{90} and r_h , taken from the BATSE first catalog [41]. The plot shows a bimodal distribution for the T_{90} and r_h (HR in the plot), indicating two different classes of GRBs with different progenitors. Credit [43].	21
1.5	X-ray light curve of the first detected GRB afterglow. The light curve was constructed from data collected by several instruments onboard the BeppoSAX satellite. Credit: [51].	22
1.6	The spectrum of GRB 970508 optical afterglow as it is detected by LRIS (left). The Fe and Mg spectral lines are identified and constrained the GRB redshift to $z=0.835\pm 0.001$ (right). Credit: [53].	23
1.7	Spectral evolution of the GRB 030329 optical afterglow flux. The spectrum five days after the burst (April 3.10) shows a typical power-law spectrum. The supernova-like features appear 12 days after the burst (on April 10.04) and continue to develop in the weeks after. (May 1.02), SN2003dh dominates the spectrum with a spectrum similar to SN1998bw (dashed line) after 33 days. Credit [55].	24
1.8	The distribution of GRB redshift z measured by Swift (in dark purple) and before swift (in orange). The Swift mission increased the number of GRBs with measured redshift and observed a far-distant GRB with redshift $z=8.3$. GRB 090429B has a photometric redshift $z=9.06$ with large error bars with a lower limit of $z > 7$ [63]. No spectral lines have been identified in the afterglow spectrum of GRB 090429B, so GRB 090423 is the most distant GRB with confirmed redshift. Credit: [64].	25
1.9	The simultaneous detection of GRB 170817A and GW170817 from an NS-NS merger. Top: GRB light curve observed by Fermi/GBM, middle: GRB light curve observed by INTEGRAL. Bottom: gravitational-wave signal as observed by LIGO interferometers. The three signals are co-aligned in time, the black line indicates the time of the merger, and the gray line indicates the beginning of the GRB emission with a delay of about 2 seconds after the merger. Credit: [70]. . .	26
1.10	The five-telescope H.E.S.S. array located in Namibia. Credit: HESS collaboration.	27

1.11	The fireball model showing how the energy from a GRB progenitor is turned into radiation. Credit NASA.	30
1.12	The scenario of a neutron star merger as a function of time. The expected gravitational wave and electromagnetic signatures from minutes before until years after the merger are illustrated on top. A merger of two neutron stars could produce a black hole (BH) and a Kilonova. The merger forms a more massive neutron star with a strong magnetic field if the two neutron stars are not massive enough. Credit: [110].	32
1.13	The spectrum of GRB 990123, taken from CGRO detectors and well fitted by the Band function given in Eq. 1.4. Top: the photon number spectrum $N(E)$. Bottom: the energy spectrum $E^2N(E)$ with peak energy $\sim 1470 \pm 110\text{keV}$. Credit: [119].	34
1.14	Sample of 12 GRBs light curves from the BATSE database showing their irregular shape. Credit: NASA	35
1.15	GRB 220305A X-ray afterglow spectrum, taken from the Swift/XRT database. The effect of galactic and extra-galactic absorption is visible for energies $<1\text{ keV}$. Credit: [122]	36
1.16	A canonical model for the X-ray afterglow light curve, showing all possible phases that can be seen in the light curve based on the Swift/XRT observation. Credit: [123]	38
1.17	GRB 210905A light curve as observed by the Swift/XRT telescope. Four phases have occurred in this light curve, with the slope noted on top of each phase segment, and the index of each decay step is noted bottom of the light curve line. Credit: [122]	39
1.18	Timeline of the GW170817, GRB 170817A, and AT2017gfo signals. Top: LIGO/Virgo spectrogram of GW170817 (left), the Fermi and INTEGRAL observed light curves of GRB 170817A (center), and the Chandra observation of the X-ray counterpart (right). Middle: The observations sequence of the multi messengers. Two types of information are shown for each band/messenger. The shaded dashes represent the times when information was reported for each wavelength. The names of the relevant instruments are indicated at the beginning of the row. Solid circles represent observations in each band, circles areas scaled by brightness. The solid lines indicate when the source was detectable by at least one telescope. Bottom: the optical afterglow observations by different 6 telescopes (left), the Kilonova spectrum (center), and the radio afterglow observation by VLA (right). Credit. [70]	41
1.19	The observational panorama in the SVOM era. The simultaneous observations with SVOM and these facilities will be important to understand many transient phenomena like GRBs. Credit: [19].	42
2.1	Graphical picture showing the SVOM components with its space- and ground-based instruments. The flag for each country contributing to the development of the instruments is indicated. Credit: SVOM collaboration.	44

2.2	The flight model of the ECLAIRs coded mask (left). A schematic of the ECLAIRs telescope, showing its subsystem (right). Credits: SVOM collaboration.	45
2.3	ECLAIRs total effective area for on-axis sources (black line), and the GRM effective area for 30 ° off-axis source (blue line). The Fermi/GBM effective area corresponds to four NaI and one BGO detectors (red dashed lines). Credit [135]	45
2.4	Example of the ECLAIRs shadow-gram image showing the number of counts recorded by the detection plane through the coded mask (left). A sky image reconstructed using the deconvolution algorithm, showing the source in the center of the ECLAIRs field of view (right). Credit: SVOM collaboration.	46
2.5	A graphical image of a single GRD detector composing the GRM instrument showing the subsystems of the detector (left). A graphical photo showing the arrangement of the three GRD detectors onboard the SVOM satellite (center). The combined field of view of the three GRD detectors (the red, blue, and green circles), superimposed with ECLAIRs field of view. The figure shows that the GRM covers the field of view of ECLAIRs completely (right). Credit: SVOM collaboration.	47
2.6	A graphical photo showing the MXT with its subsystems. Credit: SVOM collaboration.	48
2.7	A graphical photo showing the different subsystems of the VT telescope (left). The qualification model of the VT telescope during the performance test at NAOC Beijing (right). Credit: SVOM collaboration	49
2.8	The optical path through the VT showing both the red and blue channels. Credit: SVOM collaboration	49
2.9	Panorama for the GWAC system prototype installed at Xinglong Observatory in China. Credit: SVOM collaboration.	50
2.10	The two Ground Follow-up Telescopes. Left: the French telescope. Right: the Chinese telescope at Jilin observatory. Credit: The SVOM collaboration.	51
2.11	distribution of the VHF antennas between -30° and +30° around the equator. . .	52
2.12	The observation time percentage planned for the different scientific programs of SVOM during the nominal mission (left), and the extended mission (right) after 3 years.	53
2.13	Simulation of the expected distribution for GRBs detected by ECLAIRs during the SVOM nominal mission (3 years), plotted as a function of their redshift. Credit: [19].	55
2.14	An AGN with an accretion disk and a relativistic jet [84]. The different classes based in the viewing angle are shown. Credit:UCSP	56
2.15	The orbit of SVOM over several revolutions (green lines) where the SVOM inclination is about +/-30° with respect to the equator. Credit:CNES.	57
2.16	An illustrate of the B1 law orbit followed by SVOM (left), where the satellite points toward the anti solar direction. A simulation for ECLAIRs exposure in galactic coordinates (right), where most ECLAIRs observation time is spent near the galactic poles avoiding the galactic plane. Credit: SVOM collaboration . . .	57

2.17	SVOM observation scenario during the core program. The observation starts when ECLAIRs detects a new GRB within its field of view at T_0 . ECLAIRs sends an alert with the GRB coordinates to the ground, and the GRB follow-up at lower energy starts at $T_0 + 1$ min by the GFTs and GWAC system. If the GRB is bright enough (in term of the signal-to-noise-ratio), the satellite auto slew and the observation with the narrow field of view telescopes start at $T_0 + 5$ min. The MXT and the VT refine the GRB position and transmit it to the French science center (FSC) that communicates it to the Chinese science center (CSC) and the ground segment.	58
2.18	A scenario of one year of observation for the three scientific programs showing the sky map in galactic coordinates with 65 simulated GRBs and one ToO per day. Red points are the GRB observation (<i>Core</i> program), green points are the <i>general</i> program observation, orange points are the <i>ToO-Nom</i> observations, and purple points are the <i>ToO-Exp</i> and <i>ToO-MM</i> observations. Credit: SVOM collaboration.	60
3.1	The Earth reference frame \mathcal{R}' and its celestial coordinates (x', y', z') , where the rotation axis is the z' -axis (left). The MXT reference frame \mathcal{R} and its associated coordinates, where the telescope pointing direction is toward the x -axis, by convention (right). The spherical coordinates are used to describe an astrophysical object in the sky (in red), where all quantities in the Earth reference frames are primed.	63
3.2	The rotation to change the system of coordinates between \mathcal{R} and \mathcal{R}' , performed using the Euler angles is represented in green. N is the line of nodes which is a common perpendicular line to the z and z' axes.	64
3.3	System of coordinates used to describe the MXT camera plane and the astrophysical source direction.	65
3.4	The right-ascension (RA) and declination (DEC) of a star derived from the Earth celestial coordinates.	66
3.5	An astrophysical object as seen from the Earth reference frame. The object central position is given (θ'_s, ϕ'_s) . The source has an opening angle ι'_s	67
3.6	The MXT flight model at CNES integration room, covered with protection layers. The subsystems are labeled in red. Credit:CNES	67
3.7	Cross-section of a typical Wolter type space telescope showing the light path in grazing incidence optics before it is focused on a detection plane. Credit: [169].	68
3.8	The eye of a lobster as viewed by the microscope. Left: the square channels arranged on a spherical plane. Right: closer view for the square channels of the lobster eye. Credit: NASA.	69
3.9	Flight model assembly of the MXT optics, showing the 25 plates. Credit: University of Leicester.	69

3.10	The spherical plane and the focal length of the optics (left). The reflection of photons by the optics (right), photons labeled by (a) undergoing two reflections are focused on the central spot, whereas those reflected only once are focused on the cross-arms (b and c), and photons (d) passing straight through without any reflection form the diffused background. Credit: [175].	70
3.11	The PSF model of the final configuration of the optics. It is composed of a central spot and cross arms, where the intensity of photons on the central spot changes with energy. Left: at Al-K energy (1.49 keV). Right: at Fe-K energy (6.4 keV).	71
3.12	The one dimensional projection of the PSF model. Top: the y projection of the PSF model at Al-K energy with a FWHM of 11 arcmin (left). The z projection of the PSF model at Al-K energy with the same FWHM as the y projection one: 11 arcmin (right). Bottom: the y projection of the PSF model at Fe-K energy with FWHM of 12.8 arcmin (left). Bottom: the z projection of the PSF model at Fe-K energy with the same FWHM as the y projection one: 12.8 arcmin (right).	71
3.13	The effective area of the MXT telescope corresponds to the case in which only the central spot is considered. The black line is the designed effective area based on simulation. The green and red points are the measured effective area of the flight model telescope. It perfectly matches the predicted one. Credit: the University of Leicester.	72
3.14	The flight model of the camera (left). A schematic of the camera showing the different components, the calibration wheel, the detector and the FEE (right). Credit: CEA.	73
3.15	Cross sectional view of the MXT pnCCD detector. Left: is the flight model of the detector. Right: Schematic of the detector showing the image area composed of 256×256 pixels, each of size $75 \mu\text{m} \times 75 \mu\text{m}$; a frame store area is at the bottom of the image area with shielding against X-ray photons. The detector readout system (the two CAMEX) is attached to the frame store area. Credit: CEA. . .	73
3.16	Schematic views of a CCD detector based on a pn-junction. Credit [177].	75
3.17	Example of a frame taken by the MXT detector with intrinsic noise only. The effect of the read-out process is clearly seen where the structure of the columns appears with a distinction between the two CAMEX.	76
3.18	The MXT calibration wheel shows the four positions and the motor that turns the wheel. Credit: [178].	77
3.19	The MDPU architecture consists of two cores, one of which (core 2) is reserved for the science partition. Partitions are scheduled by the XtratuM hypervisor in a periodically repeated MAF. The MAF is divided into time slots used by a given partition to perform scheduled or background tasks.	79

- 3.20 Onboard data processing flowchart. The purple box represents the FEEM partition, the green box represents the SCSW partition, and the red one is shared memory between the two partitions. The analysis during the **FULL-FRAME** and **EVENT** modes are shadowed in yellow and blue, respectively. Four analyses are performed, the noise characterization that is performed with the **FULL-FRAME** mode, the source localization that is performed during the **EVENT** mode, the telemetry packets formatting, and the data monitoring in both modes. 80
- 3.21 The interface of the scientific software partition with the other software partitions coded in the MDPU. The FEE and the PDPU are connected to the MDPU via a space-wire link (spw). 81
- 3.22 The MDPU (the black box to the left of the image) coupled to the camera that is placed inside a vacuum tank (the red tank), during one of the coupling test at CEA. 83
- 3.23 The panter X-ray test facility of MPE in Germany. The photo shows the vacuum tube of 130 m long and a diameter of 1 m, with the X-ray source system at one end and the test chamber at the other end. Credit: MPE 84
- 3.24 The MXT telescope placed in the test chamber of PANTER X-ray test facility during the flight model test. Credit: CNES. 85
- 3.25 Example of an option file that is used as an input to generate an observation sequence. The parameters required to configure the satellite, the sources, the telescope, and its camera is must be specified in the file. 86
- 3.26 An example of a uniform source flux object between 0.8 keV and 4.5 keV and exponentially decays with time, simulated with the SATANDLIGHT (top-left). The rate plot (bottom-left) is obtained by multiplying the flux object with the effective area (top-right). The source light curve resulting from the integration of the rate over all energies (bottom-right). 87
- 3.27 Example of a simulated camera image showing the effect of camera defects. Black points are dead pixels, white points are bright pixels, and the white column is a frozen column due to the saturation of readout electronics. 88
- 3.28 The effect of the interaction of astroparticles with a CCD detector as simulated by the SATANDLIGHT. Left: zoom on a camera image showing the effect of a photon where the energy is distributed over four pixels; the black circle represents the hit position of the photon. Right: a camera image shows the effect of a cosmic ray on the detector. The black point is the entry point of the cosmic ray. 89
- 4.1 Example of a frame taken by the MXT detector during coupling test at CEA. The image was taken with a closed wheel position, so no X-ray photons interact with the detector. Meanwhile, the cosmic rays penetrated the wheel even with a closed position and added an energy above the noise. 92
- 4.2 The dark maps computed with the ground analysis. The offset map (left), and the threshold map (right). 94

4.3	The $A_r[i][j]$ distribution of the (i, j) pixel. The distribution has two peaks, the first one corresponds to the intrinsic noise distribution with true value labelled with dashed black line. The second one corresponds to the cosmic ray distribution that is added on top of the intrinsic noise distribution. The presence of the cosmic rays biases the mean (the blue line) and the standard deviation (red line) of the distribution.	95
4.4	The dark maps computed with the onboard algorithm. The offset map (left), and the threshold map (right), both given in the [ADU] unit.	97
4.5	The ratio of the dark maps computed using a simulated dark sequence with no outliers and a dark sequence with the detector exposed to outliers. Left: the ratio of offset value ($r_o[i][j]$) for the 256×256 pixels. Right: the threshold ratio ($r_t[i][j]$) for the 256×256 pixels.	100
4.6	The difference of the offset map ΔO_{ij} for 256×256 pixels computed using a simulated dark sequence with no outliers and a dark sequence with the detector exposed to outliers.	101
4.7	The convergence of the onboard offset (left column) and threshold (right column) values to the offline-computed values (dashed lines) as the number of dark frames processed onboard increases. The convergence is tested for three pixels with different noise fluctuations. Bottom: pixel with low noise fluctuation ($< 1\sigma$). Middle: pixel with medium noise fluctuation ($< 2\sigma$). Top: pixel with high noise fluctuation ($> 2\sigma$). It shows that the onboard offset (resp. threshold) converges to the offline-computed values after processing at least 70 frames (resp. 90 frames).	102
4.8	The offset map ratio. The ratio ($r_o = O[i][j]/O^G[i][j]$) between both offset maps for each pixel (left). The ratio (r_o) distribution for all pixels (right).	102
4.9	The threshold map ratio. The ratio ($r_t = T[i][j]/T^G[i][j]$) between both threshold maps for each pixel (left). The ratio (r_t) distribution for all pixels (right).	103
4.10	The measured energy scale calculated using both the onboard and the ground-computed dark maps as a function of the X-ray sources energy (E_{ph}^t). In each case, the energy scale (e_s) is calculated for single events (blue for the ground maps, gray for the onboard maps) and all events (green for the ground maps, yellow for the onboard maps). The plot shows that using the onboard maps improves the energy scale for single events. In the case of all events, using the dark maps computed with the ground algorithm gives a better energy scale. Credit: CEA.	104
4.11	The measured energy FWHM as a function of the actual energy. The FWHM is measured after using both the onboard and the ground-computed dark maps. In each case, the FWHM is measured for single events (blue for the ground maps, gray for the onboard maps) and all events (green for the ground maps, yellow for the onboard maps). The plot shows that using the onboard maps improves slightly the energy FWHM. Credit: CEA.	105

4.12	The energy gain values for the 256 columns of the MXT detector measured with six low-energy X-ray sources: C-K (0.277 keV), O-K (0.525 keV), Cu-L (0.93 keV), Mg-K (1.253 keV), Al-K (1.486 keV), and W-M (1.774 keV). Credit: CEA	107
4.13	Most probable pixel patterns induced by a photon hitting a pnCCD detector. An incoming X-ray photon can transfer its energy to one or more pixels depending on its energy. The bright-orange pixel is the impacted pixel; the light-orange pixels have a fraction of the photon energy above the noise threshold. White pixels have an energy below the noise threshold.	108
4.14	Example of a photon map constructed by the science partition with 8000 photons. The photon position in the map is given in intrinsic coordinates: $0 \leq z < 1$ and $0 \leq y < 1$	109
5.1	Example of the construction of the correlation matrix of a 4×4 photon map with a 8×8 PSF to produce a 4×4 correlation matrix.	115
5.2	The implementation steps of the cross-correlation algorithm onboard.	117
5.3	Example of a cross-correlation map between the PSF and a simulated photon map with 77 photons. The peak position is computed using the onboard algorithm (green cross) and a simple barycenter (red cross). The source true position is indicated by a black cross.	118
5.4	An example of a photon map constructed by simulating the detection of three bright sources. The plot shows that it is not trivial to identify regions with only a background or identify a region around a source without a contribution from another source.	120
5.5	The inverse Fourier transform of the decimated PSF (left). An example of the PSF auto-correlation map, computed with the onboard algorithm using the Fourier-transformed and the decimated PSF on the ground (right).	123
5.6	The PSF function (left), with a black square represent the camera. The cross-correlation map (right) divided into four quarters centred on (i_1, j_1)	124
5.7	Two sources in the MXT field of view (left), the first source is localized with the cross-correlation and barycenter method. The first source is subtracted (right) in order to localize the second source, and the latter is then localized with the same method as the first source. The true positions of the two sources are labeled with red circles.	127
5.8	The onboard localization uncertainty of the MXT measured as a function of the source intensity. The measurement is done after 30 s (in black), 5 minutes (in red), and 10 minutes (in blue) of simulated observations. For each observation duration, source intensities from 10 to 10^4 photons are simulated. The source intensity is parametrized by the number of photons hitting the MXT detector. This plot shows that MXT must detect at least 120 ± 3 , 164 ± 5 , and 197 ± 6 photons after 30 s, 5 minutes, and 10 minutes of observation, respectively, in order to reach the MXT required accuracy of 2 arcmin.	131

- 5.9 The localization uncertainty as a function of the number of photons, measured for photon maps with resolutions: 64×64 , 128×128 , and 256×256 , after 5 minutes (top) and 10 minutes (bottom) of observation. 132
- 5.10 The position bias measured while the simulated source is moved in all directions in the detector. As the source gets closer to the edge of the detector, the localization degrades significantly due to the spectral-leakage effect. 133
- 5.11 The edge bias measured in each direction separately. Left: the bias in the z -direction measured as the source is moved vertically from $z=0$ to $z=1$, where $y=0.5$. The source position offset is measured at each point in the intrinsic coordinate (in blue curve). The points are fitted (in red curve) to correct the edge bias. Right: the edge bias in the y -direction measured the same way as the z -direction, but the source is moved horizontally from $y=0$ to $y=1$ and $z=0.5$. In both plots, a source with a high intensity is simulated without background. . . 134
- 5.12 The source position offset δr as a function of the source distance (in pixel) from the detector centre. The dots show the bias before correction, while the open circles show the bias after applying $\eta(y)$ and $\eta(z)$ corrections. Two source intensities are simulated: 500 photons (left) and 1000 photons (right). 135
- 5.13 Example of a photon map constructed while the detector has 7 insensitive columns. The cells in the photon map corresponding to the insensitive columns are set to zero, as a consequence 8 columns in the photon map are deactivated. 135
- 5.14 r_{90} as a function of the source intensity computed with the normal detector (blue curve), and with 7 insensitive columns in the detector (black curve). The interpolation method is used to reduce the effect of the insensitive columns (red curve). 136
- 5.15 The y bias (in blue) measured as the source is moved horizontally from $y=0$ to $y=1$. $N_{bad} = 1, 3, 5, 7, 9$, and 11 insensitive columns are simulated to evaluate the insensitive columns effect in the localization performance. The best fit is also drawn (in red). 137
- 5.16 δr measured as the source is moved along the entire detector with 7 insensitive columns. Left: the effect of the insensitive columns appears in the y -direction with no effect on the z -direction. In addition, the edge bias is seen near the detector edges. Center: the effect of the insensitive columns is reduced by the analytical correction. Right: the effect of the insensitive columns and the edge bias are reduced by the analytical corrections. 137
- 5.17 The r_{90} as a function of the source intensity computed with the normal detector (blue curve), and with 7 insensitive columns in the detector (black curve). The analytical correction method is applied to reduce the effect of the insensitive columns (green curve), and it is compared to the interpolation method (red curve). 138
- 5.18 A photon map showing a detection of two sources in the MXT field of view. Left: the two sources are aligned in the y direction. Right: the two sources are located in the diagonal of the detector. 139

5.19 the bias of two source positions (δr) as a function of the distance between them. In the left column, the two sources are aligned in the y -direction, one source is fixed (orange triangle), and the second is moved away from the first one (blue points), where the fixed source is double brighter (top) and four times brighter (bottom) than the moving source. In the right column, the two sources are simulated in the detector diagonal, where the fixed source is double brighter (top) and four times brighter (bottom) than the moving source. The green shaded region corresponds to the distance below the MXT angular resolution (11 arcmin). 140

5.20 r_{90} as a function of the signal-to-noise ratio (black points) and the best fit is plotted in red. The dashed blue lines are the r_{90} thresholds that define the detection quality. 141

5.21 A comparison between the true signal-to-noise ratio (red line) and the measured signal-to-noise ratio with method 2 (blue line) and with method 3 (black line) (top), each point is measured as the mean value of ~ 500 observations are simulated ± 10 pixels around the center. The ratio between the measured and the true signal-to-noise ratio for method 2 and method 3 (middle). The deviation of the measured signal-to-noise ratio from the true signal-to-noise ratio for method 2 and method 3 (bottom). 142

5.22 The signal bias \hat{S}/S (left column), background bias \hat{B}/B (central column) and the signal-to-noise ratio bias $\hat{\rho}/\rho$ (right column) for different source positions in the camera plane and different source intensities: $S_1 = 300$ (top), $S_1 = 1000$ (middle), and $S_1 = 3000$ (bottom). 143

5.23 the measured signal-to-noise ratio of two sources in the MXT field of view as a function of the distance between them. In the left column, the two sources are aligned in the y -direction, one source is fixed (orange triangle), and the second is moved away from the first one (blue points), where the fixed source is two times brighter (top) and four times brighter (bottom) than the moved source. In the left column, the two sources are simulated in the detector diagonal, where the fixed source is two times brighter (top) and four times brighter (bottom) than the moved source. The green shaded region corresponds to the distance below the MXT angular resolution and the dashed lines correspond to the sources true signal-to-noise ratio values 144

5.24 The different positions of the X-ray test beam during the Panter test. Nine positions with the source peak is in the MXT field of view , and four positions while the source peak is outside the field of view are performed. 146

5.25 The energy spectrum obtained by the MXT at Panter by combining data from all test beam positions and all X-ray sources used during the test. Credit: the camera team/CEA. 147

5.26	Localization performance for six photon energies: C-k (0.30 keV), O-k (0.53 keV), Mg-k (1.2 keV), Al-K (1.4 keV), Ti-K (5.20 keV), and Fe-K (6.40 keV). The offset between the measured position and the true position is evaluated in the y -direction (blue) and in the z -direction (green), and it is given in arcsec and pixels.	149
5.27	Localization performance tested for 13 near-the-edge positions performed with an Al-K (1.4 keV) source. The measured position offset is evaluated in the y direction (top) and in the z direction (bottom) with (purple curve) and without (pink curve) the edge-bias correction.	150
5.28	Example of photon map constructed during Panter test while the source beam is placed near the edge of the MXT field of view. The source position before (red point) and after (green point) the bias correction is labeled on top of the photon map	151
5.29	Example of a photon map constructed by the MXT science partition during the Panter test, while deactivating 10 pixels columns.	151
5.30	Localization performance tested with insensitive columns, for an Al-K (1.4 keV) source, and with a P_0 beam position. The measured position offset is evaluated before (pink curve) and after (purple curve) applying the correction function of the insensitive columns. The offset is given in arcsec and pixel units.	152
6.1	The cross section in [cm^2] of the photoelectric effect at a given energy within the range of (0.2 - 10 keV) based on elements abundances in the solar system [194] .	154
6.2	An example of the parameters of the spectrum power-law model, obtained from the Swift/XRT database [122]	156
6.3	The MXT effective area (in black) compared to XRT effective area (in red) . . .	157
6.4	The light curve of GRB091020 observed by Swift/XRT. The light curve is fitted with multiple broken laws, and it has four different phases. The flare is labelled with the hashed pink region Credit [122]	157
6.5	The simulated count rate of GRB091020 as observed by XRT.	158
6.6	The simulated light curve of GRB091020 as observed by XRT (blue line), compared to real XRT data (red points).	159
6.7	The XRT simulated spectrum of GRB091020 after 10^4 s of observation (top). The spectrum observed by the XRT for the same GRB with the same duration (bottom).	160
6.8	A camera image saved from a simulation of GRB091020 observed with the MXT. The image is captured 74 s after the trigger. One cosmic ray (in yellow) and a few photons (red circles) deposit their energies on top of noise in the detector. The simulation is performed using the SATANDLIGHT toolkit.	162
6.9	The simulated light curve of GRB091020 as observed by the MXT (in black) and as observed by the XRT (in red), the logarithmic interpolation is included in both.	163

6.10	The simulated light curve of GRB091020 as observed by the MXT (in black). The light curve has three decaying phases and by an X-ray flare phase that is shaded with gray rectangular. The best fit of the different decaying phases is shown in red. The X-ray flare is excluded from the fit.	163
6.11	The simulated spectrum of GRB091020 as observed by the MXT (in black) and as observed by the XRT (in red).	164
6.12	The cumulative number of photons from GRB091020 (in red), the cumulative number of background photons (in green), and the localization uncertainty, r_{90} (in blue). The higher the signal-to-noise ratio, the lower the localization uncertainty.	165
6.13	The peak photon flux after 1 s in the energy range 15 - 150 keV as a function of T_{90} for the Swift GRBs.	166
6.14	Cumulative curve of the XRT GRBs (represented in a percentage) as observed and localized with the MXT after 10 min of the observation. GRBs that have >90% (green), >50% (blue), and (0% - 100%) (red) probability of being detected by ECLAIRs are selected.	167
6.15	The luminosity light curves of the X-ray afterglow of the complete sample, estimated in the rest frame energy range (2 - 10 keV).	172
6.16	The band model spectrum of the prompt emission, where the energy band of the Swift/BAT is indicated by the orange lines.	173
6.17	The normalized luminosity light curves of the X-ray afterglow of the complete sample, estimated in the rest frame energy range (2 - 10 keV).	174
6.18	The normalized luminosity light curves of the X-ray afterglow of the short GRBs with ≥ 3 observations in the complete sample. The light curves are fitted with single or multiple broken power laws.	175
6.19	The $L_x - E_{iso}$ correlation studied for the complete sample at different rest-frame times. Left: at the early time (after 1 hour), right: at the late time (after 24 hours). The solid lines represent the best fit.	176
6.20	The expected electromagnetic counterparts to the merger of the binary system as a function of the observer angle θ_{obs} . The rapid accretion powers a collimated relativistic jet, which produces a short GRB with a half-opening angle θ_j . An afterglow emission results from the interaction of the jet with the surrounding medium (pink). Radio afterglow emission is observable isotropic on a timescale of weeks-months, and years. Short-lived isotropic optical emission lasting a few days (kilonova; yellow) can also accompany the merger, powered by the decay of radioactive heavy elements. Credit: [214].	177
6.21	The gravitational waves sky localization error box for binary neutron stars BNS (solid line), a neutron star and a black hole (dashed line), and two black holes (dotted line) signals during the third O3 and fourth O4 runs. Credit: [130].	178

6.22	The expected localization accuracy for binary neutron star systems with advanced-detector networks during the O5 run. The ellipses show 90% confidence localization areas by the four-detector network (HILV) LIGO Hanford (H)–LIGO India (I)–LIGO Livingston (L)–Virgo (V). The joining of the fifth site in India improves the localization over the whole sky. Credit: [215].	178
6.23	The luminosity light curve of the GRB051221A X-ray afterglow at the source rest frame (2 - 10 keV).	180
6.24	The light curve for GRB051221A, simulated at $z=0.137$. Observations with the XRT (red stars) and the MXT (black line) are simulated.	180

List of Tables

2.1	Scientific and technical characteristics of the SVOM space payload and ground segment.	52
3.1	Scientific and technical characteristics of the MXT compared to the requirements.	62
3.2	Compression between the three operating modes of the FEE.	77
3.3	List of global modes of the MXT that are a combination of the wheel position and the FEE mode.	78
4.1	List of parameters for the dark algorithm, that are tuned on the ground and uploaded with the configuration table to the science partition.	98
4.2	List of parameters (12 parameters) needed for the photon identification analysis. The parameters are evaluated on the ground and uploaded with the configuration table to the science partition.	111
5.1	Quantities computed onboard for the three brightest sources in the MXT field of view, this information is sent to the ground with the VHF position packets every 30 s.	128
5.2	List of localization parameters (24), that are evaluated on the ground and uploaded with the configuration table to the science partition.	129
5.3	List of X-ray sources and their energies used to characterize the MXT performance during the Panter test campaign.	146
5.4	List of X-ray beam positions in the MXT field of view during the Panter test campaign. The P0 position is used as a reference (0, 0).	147
5.5	Minimum number of photons to achieve a localization accuracy of $r_{90} < 120$ arcsec after 5 and 10 minutes of observations. These values for r_{90} is given for the different source energies used at PANTER.	148
6.1	Spectrum parameter of GRB091020 for the PC mode after 10^4 s of observation.	158
6.2	The percentage of the XRT GRBs that are detected by the MXT with a given uncertainty and for a given detection probability by ECLAIRs.	167
6.3	The complete sample of the short GRBs (41 GRBs) after applying selection on the XRT pointing time T_0 , the galactic extinction, and on the photon flux after 64 ms.	168
6.4	The selection criteria of the short-duration GRBs sample and the number of GRBs after each selection.	170
6.5	The isotropic energy of the prompt emission of the GRBs that have ≥ 3 detection points in the complete sample. In addition, the X-ray luminosities in the 2–10 keV rest-frame energy band are computed at two rest-frame times (1 h and 24 h).	174

6.6	projected detector sensitivities for a $1.4 M_{\odot} + 1.4 M_{\odot}$ binary neutron star system (BNS), and a $1.4 M_{\odot} + 10 M_{\odot}$ neutron star and black hole system (NSBH) during the O4 and O5 runs.	179
6.7	The maximum number of photons that would be detected in a tile after different observation times (1h, 4h, 8h, and 12h). The table gives the associated localization uncertainty r_{90} for each tile after a certain time from the alert time.	181
A.1	The Swift GRBs that have 50% detection probability with SVOM/ECLAIRS.	187
A.2	The Swift GRBs that have 90% detection probability with SVOM/ECLAIRS.	217

Bibliography

- [1] Peter Meszaros. Gamma-ray bursts. *Reports on Progress in Physics*, 69(8):2259, 2006.
- [2] Neil Gehrels and Péter Mészáros. Gamma-ray bursts. *Science*, 337(6097):932–936, 2012.
- [3] Asaf Pe’Er. Physics of gamma-ray bursts prompt emission. *Advances in Astronomy*, 2015, 2015.
- [4] Chryssa Kouveliotou, Charles A Meegan, Gerald J Fishman, Narayana P Bhat, Michael S Briggs, Thomas M Koshut, William S Paciesas, and Geoffrey N Pendleton. Identification of two classes of gamma-ray bursts. *The Astrophysical Journal*, 413:L101–L104, 1993.
- [5] EPJ Van den Heuvel and S-C Yoon. Long gamma-ray burst progenitors: boundary conditions and binary models. *Astrophysics and Space Science*, 311(1):177–183, 2007.
- [6] DA Kann, P Schady, S Klose, A Rossi, DA Perley, T Krühler, J Greiner, A Nicuesa Guelbenzu, J Elliott, F Knust, et al. Highly luminous supernovae associated with gamma-ray bursts-i. grb 111209a/sn 2011kl in the context of stripped-envelope and superluminous supernovae. *Astronomy & Astrophysics*, 624:A143, 2019.
- [7] Paul C Joss and Saul A Rappaport. Neutron stars in interacting binary systems. *Annual review of astronomy and astrophysics*, 22(1):537–592, 1984.
- [8] Krzysztof Belczynski, Rosalba Perna, Tomasz Bulik, Vassiliki Kalogera, Natalia Ivanova, and Donald Q Lamb. A study of compact object mergers as short gamma-ray burst progenitors. *The Astrophysical Journal*, 648(2):1110, 2006.
- [9] Francois Foucart. A brief overview of black hole-neutron star mergers. *Frontiers in Astronomy and Space Sciences*, 7:46, 2020.
- [10] Marica Branchesi. Multi-messenger astronomy: gravitational waves, neutrinos, photons, and cosmic rays. In *Journal of Physics: conference series*, volume 718, page 022004. IOP Publishing, 2016.
- [11] Eli Waxman and John Bahcall. High energy neutrinos from cosmological gamma-ray burst fireballs. *Physical Review Letters*, 78(12):2292, 1997.
- [12] Christopher S Kochanek and Tsvi Piran. Gravitational waves and γ -ray bursts. *arXiv preprint astro-ph/9305015*, 1993.
- [13] Albert Einstein and Nathan Rosen. On gravitational waves. *Journal of the Franklin Institute*, 223(1):43–54, 1937.
- [14] Joseph Weber. *General Relativity and gravitational waves*. Courier Corporation, 2004.

- [15] Benjamin P Abbott, Richard Abbott, TD Abbott, MR Abernathy, Fausto Acernese, Kendall Ackley, Carl Adams, Thomas Adams, Paolo Addesso, RX Adhikari, et al. Observation of gravitational waves from a binary black hole merger. *Physical review letters*, 116(6):061102, 2016.
- [16] Pawan Kumar. Gamma-ray burst energetics. *The Astrophysical Journal*, 523(2):L113, 1999.
- [17] Maria Grazia Bernardini, Carlo Luciano Bianco, Pascal Chardonnet, Federico Fraschetti, Remo Ruffini, and She-Sheng Xue. Theoretical interpretation of the luminosity and spectral properties of grb 031203. *The Astrophysical Journal*, 634(1):L29, 2005.
- [18] Donald Q Lamb and Daniel E Reichart. Gamma-ray bursts as a probe of the very high redshift universe. *The Astrophysical Journal*, 536(1):1, 2000.
- [19] J Wei, B Cordier, S Antier, P Antilogus, J-L Atteia, A Bajat, S Basa, V Beckmann, MG Bernardini, Samuel Boissier, et al. The deep and transient universe in the svom era: new challenges and opportunities-scientific prospects of the svom mission. *arXiv preprint arXiv:1610.06892*, 2016.
- [20] Bing Zhang and Peter Meszaros. Gamma-ray bursts: progress, problems & prospects. *International Journal of Modern Physics A*, 19(15):2385–2472, 2004.
- [21] Jim Hinton and Edna Ruiz-Velasco. Multi-messenger astronomy with very-high-energy gamma-ray observations. In *Journal of Physics: Conference Series*, volume 1468, page 012096. IOP Publishing, 2020.
- [22] R Abbott, TD Abbott, S Abraham, F Acernese, K Ackley, C Adams, RX Adhikari, VB Adya, C Affeldt, M Agathos, et al. Search for gravitational waves associated with gamma-ray bursts detected by fermi and swift during the ligo–virgo run o3a. *The Astrophysical Journal*, 915(2):86, 2021.
- [23] B Cordier, Jianyan Wei, J-L Atteia, S Basa, A Claret, F Daigne, J Deng, Y Dong, O Godet, A Goldwurm, et al. The svom gamma-ray burst mission. *arXiv preprint arXiv:1512.03323*, 2015.
- [24] O Godet, J Paul, JY Wei, S-N Zhang, J-L Atteia, S Basa, D Barret, A Claret, B Cordier, J-G Cuby, et al. The chinese-french svom mission: studying the brightest astronomical explosions. In *Space Telescopes and Instrumentation 2012: Ultraviolet to Gamma Ray*, volume 8443, page 84431O. International Society for Optics and Photonics, 2012.
- [25] D Götz, J Osborne, B Cordier, J Paul, P Evans, A Beardmore, Adrian Martindale, Richard Willingale, P O’Brien, S Basa, et al. The microchannel x-ray telescope for the gamma-ray burst mission svom. In *Space Telescopes and Instrumentation 2014: Ultraviolet to Gamma Ray*, volume 9144, pages 613–624. SPIE, 2014.

- [26] A Cucchiara, SB Cenko, JS Bloom, A Melandri, A Morgan, S Kobayashi, RJ Smith, DA Perley, W Li, JL Hora, et al. Constraining gamma-ray burst emission physics with extensive early-time, multiband follow-up. *The Astrophysical Journal*, 743(2):154, 2011.
- [27] Maria Grazia Bernardini, Raffaella Margutti, Jirong Mao, Elena Zaninoni, and Guido Chincarini. The x-ray light curve of gamma-ray bursts: clues to the central engine. *Astronomy & Astrophysics*, 539:A3, 2012.
- [28] Emily M Levesque, Edo Berger, Lisa J Kewley, and Megan M Bagley. The host galaxies of gamma-ray bursts. i. interstellar medium properties of ten nearby long-duration gamma-ray burst hosts. *The Astronomical Journal*, 139(2):694, 2010.
- [29] ZG Dai and Tan Lu. Gamma-ray burst afterglows: effects of radiative corrections and non-uniformity of the surrounding medium. *Monthly Notices of the Royal Astronomical Society*, 298(1):87–92, 1998.
- [30] Charlotte H Feldman, Richard Willingale, James Pearson, Valentin Aslanyan, Tony Crawford, Paul Houghton, Jon Sykes, Christopher Bicknell, Julian Osborne, Paul O’Brien, et al. Calibration of a fully populated lobster eye optic for svom. In *Space Telescopes and Instrumentation 2020: Ultraviolet to Gamma Ray*, volume 11444, page 114441K. International Society for Optics and Photonics, 2020.
- [31] Francesco Ceraudo, Aline Meuris, Eric Doumayrou, Luc Dumaye, Alain Goetschy, Tony Lavanant, Michel Lortholary, Isabelle Le Mer, François Nico, Frédéric Pinsard, et al. Characterization of the detection chain of the micro-channel x-ray telescope. *Nuclear Instruments and Methods in Physics Research Section A: Accelerators, Spectrometers, Detectors and Associated Equipment*, 973:164164, 2020.
- [32] Sidney Singer. The vela satellite program for detection of high-altitude nuclear detonations. *Proceedings of the IEEE*, 53(12):1935–1948, 1965.
- [33] Ray W Klebesadel, Ian B Strong, and Roy A Olson. Observations of gamma-ray bursts of cosmic origin. *The Astrophysical Journal*, 182:L85, 1973.
- [34] L Woltjer. Supernova remnants. *Annual Review of Astronomy and Astrophysics*, 10(1):129–158, 1972.
- [35] Hans Albrecht Bethe. Supernova mechanisms. *Reviews of Modern Physics*, 62(4):801, 1990.
- [36] John T Gosling. The solar flare myth. *Journal of Geophysical Research: Space Physics*, 98(A11):18937–18949, 1993.
- [37] Wm A Wheaton, MP Ulmer, Wm A Baity, DW Datlowe, MJ Elcan, LE Peterson, Ray W Klebesadel, Ian B Strong, TL Cline, and UD Desai. The direction and spectral variability of a cosmic gamma-ray burst. *The Astrophysical Journal*, 185:L57, 1973.

- [38] Neil Gehrels, Carl E Fichtel, Gerald J Fishman, James D Kurfess, and Volker Schönfelder. The compton gamma ray observatory. *Scientific American*, 269(6):68–77, 1993.
- [39] GJ Fishman, CA Meegan, RB Wilson, WS Paciesas, TA Parnell, RW Austin, JR Rehage, and JL Matteson. Batse: The burst and transient source experiment on the gamma ray observatory. In *Proc. GRO Science Workshop, GSFC*, volume 2, 1989.
- [40] C. A. Meegan, G. J. Fishman, R. B. Wilson, W. S. Paciesas, G. N. Pendleton, J. M. Horack, M. N. Brock, and C. Kouveliotou. Spatial distribution of γ -ray bursts observed by BATSE. , 355(6356):143–145, January 1992.
- [41] William S Paciesas, Charles A Meegan, Geoffrey N Pendleton, Michael S Briggs, Chryssa Kouveliotou, Thomas M Koshut, John Patrick Lestrade, Michael L McCollough, Jerome J Brainerd, Jon Hakmila, et al. The fourth batse gamma-ray burst catalog (revised). *The Astrophysical Journal Supplement Series*, 122(2):465, 1999.
- [42] Gerald J Fishman, Charles A Meegan, Robert B Wilson, Martin N Brock, John M Horack, Chryssa Kouveliotou, Sethanne Howard, William S Paciesas, Michael S Briggs, Geoffrey N Pendleton, et al. The first batse gamma-ray burst catalog. *The Astrophysical Journal Supplement Series*, 92:229–283, 1994.
- [43] Amir Shahmoradi and Robert J Nemiroff. Short versus long gamma-ray bursts: a comprehensive study of energetics and prompt gamma-ray correlations. *Monthly Notices of the Royal Astronomical Society*, 451(1):126–143, 2015.
- [44] Martin J Rees and P Mészáros. Unsteady outflow models for cosmological gamma-ray bursts. *arXiv preprint astro-ph/9404038*, 1994.
- [45] P Mészáros, Martin J Rees, and H Papathanassiou. Spectral properties of blast wave models of gamma-ray burst sources. *arXiv preprint astro-ph/9311071*, 1993.
- [46] MA Aloy, H-T Janka, and E Müller. Relativistic outflows from remnants of compact object mergers and their viability for short gamma-ray bursts. *Astronomy & Astrophysics*, 436(1):273–311, 2005.
- [47] Helmut Wiedemann. Synchrotron radiation. In *Particle Accelerator Physics*, pages 647–686. Springer, 2003.
- [48] G Boella, RC Butler, GC Perola, L Piro, L Scarsi, and JAM Bleeker. BeppoSAX, the wide band mission for x-ray astronomy. *Astronomy and Astrophysics Supplement Series*, 122(2):299–307, 1997.
- [49] E Costa, M Feroci, L Piro, MN Cinti, F Frontera, G Zavattini, L Nicastro, E Palazzi, D Dal Fiume, M Orlandini, et al. Grb 970228. *International Astronomical Union Circular*, 6576:1, 1997.

- [50] E etal Costa, F Frontera, J Heise, M al Feroci, F Fiore, MN Cinti, D Dal Fiume, L Nicastro, M Orlandini, E Palazzi, et al. Discovery of an x-ray afterglow associated with the γ -ray burst of 28 february 1997. *Nature*, 387(6635):783–785, 1997.
- [51] Mario Vietri. The afterglow of gamma-ray bursts: the cases of grb 970228 and grb 970508. *The Astrophysical Journal*, 488(2):L105, 1997.
- [52] J Van Paradijs, PJ Groot, T Galama, C Kouveliotou, RG Strom, J Telting, RGM Rutten, GJ Fishman, CA Meegan, M Pettini, et al. Transient optical emission from the error box of the γ -ray burst of 28 february 1997. *Nature*, 386(6626):686–689, 1997.
- [53] MR Metzger, SG Djorgovski, SR Kulkarni, CC Steidel, KL Adelberger, DA Frail, E Costa, and F Frontera. Spectral constraints on the redshift of the optical counterpart to the γ -ray burst of 8 may 1997. *Nature*, 387(6636):878–880, 1997.
- [54] GR Ricker, J-L Atteia, GB Crew, JP Doty, EE Fenimore, M Galassi, C Graziani, K Hurley, JG Jernigan, N Kawai, et al. The high energy transient explorer (hete): mission and science overview. In *AIP Conference Proceedings*, volume 662, pages 3–16. American Institute of Physics, 2003.
- [55] Jens Hjorth, Jesper Sollerman, Palle Møller, Johan PU Fynbo, Stan E Woosley, Chryssa Kouveliotou, Nial R Tanvir, Jochen Greiner, Michael I Andersen, Alberto J Castro-Tirado, et al. A very energetic supernova associated with the γ -ray burst of 29 march 2003. *Nature*, 423(6942):847–850, 2003.
- [56] Krzysztof Z Stanek, T Matheson, PM Garnavich, P Martini, P Berlind, N Caldwell, P Challis, WR Brown, R Schild, K Krisciunas, et al. Spectroscopic discovery of the supernova 2003dh associated with grb 030329. *The Astrophysical Journal Letters*, 591(1):L17, 2003.
- [57] Neil Gehrels, Guido Chincarini, P ea Giommi, KO Mason, JA Nousek, AA Wells, NE White, SD Barthelmy, DN Burrows, LR Cominsky, et al. The swift gamma-ray burst mission. *The Astrophysical Journal*, 611(2):1005, 2004.
- [58] Scott D Barthelmy, Louis M Barbier, Jay R Cummings, Ed E Fenimore, Neil Gehrels, Derek Hullinger, Hans A Krimm, Craig B Markwardt, David M Palmer, Ann Parsons, et al. The burst alert telescope (bat) on the swift midex mission. *Space Science Reviews*, 120(3):143–164, 2005.
- [59] David N Burrows, JE Hill, JAea Nousek, JA Kennea, A Wells, JP Osborne, AF Abbey, A Beardmore, K Mukerjee, ADT Short, et al. The swift x-ray telescope. *Space science reviews*, 120(3):165–195, 2005.
- [60] Peter WA Roming, Thomas E Kennedy, Keith O Mason, John A Nousek, Lindy Ahr, Richard E Bingham, Patrick S Broos, Mary J Carter, Barry K Hancock, Howard E

- Huckle, et al. The swift ultra-violet/optical telescope. *Space Science Reviews*, 120(3):95–142, 2005.
- [61] Bing Zhang. Gamma-ray bursts in the swift era. *Chinese Journal of Astronomy and Astrophysics*, 7(1):1, 2007.
- [62] Rubén Salvaterra, M Della Valle, S Campana, G Chincarini, S Covino, P D’Avanzo, A Fernández-Soto, Cristiano Guidorzi, F Mannucci, R Margutti, et al. Grb 090423 at a redshift of $z = 8.1$. *Nature*, 461(7268):1258–1260, 2009.
- [63] A Cucchiara, AJ Levan, Derek B Fox, Nial R Tanvir, TN Ukwatta, Edo Berger, T Krühler, A Küpcü Yoldaş, XF Wu, K Toma, et al. A photometric redshift of $z = 9.4$ for grb 090429b. *The Astrophysical Journal*, 736(1):7, 2011.
- [64] Gamma-ray bursts. <https://annalisadecia.com/site/grb/>.
- [65] Paolo D’Avanzo. Short gamma-ray bursts: A review. *Journal of High Energy Astrophysics*, 7:73–80, 2015.
- [66] Ravi Kumar Kopparapu, Chad Hanna, Vicky Kalogera, Richard O’Shaughnessy, Gabriela Gonzalez, Patrick R Brady, and Stephen Fairhurst. Host galaxies catalog used in ligo searches for compact binary coalescence events. *The Astrophysical Journal*, 675(2):1459, 2008.
- [67] Ehud Nakar. Short-hard gamma-ray bursts. *Physics Reports*, 442(1-6):166–236, 2007.
- [68] David Eichler, Mario Livio, Tsvi Piran, and David N Schramm. Nucleosynthesis, neutrino bursts and γ -rays from coalescing neutron stars. *Nature*, 340(6229):126–128, 1989.
- [69] Krzysztof Belczynski, Rosalba Perna, Tomasz Bulik, Vassiliki Kalogera, Natalia Ivanova, and Donald Q Lamb. A study of compact object mergers as short gamma-ray burst progenitors. *The Astrophysical Journal*, 648(2):1110, 2006.
- [70] Benjamin P Abbott, Richard Abbott, TD Abbott, F Acernese, C Adams, T Adams, P Addesso, RX Adhikari, VB Adya, C Affeldt, et al. Multi-messenger observations of a binary neutron star merger. *Astrophys. J. Lett.*, 848(2):L12, 2017.
- [71] Peter F Michelson, William B Atwood, and Steven Ritz. Fermi gamma-ray space telescope: high-energy results from the first year. *Reports on Progress in Physics*, 73(7):074901, 2010.
- [72] Charles Meegan, Giselher Lichti, PN Bhat, Elisabetta Bissaldi, Michael S Briggs, Valerie Connaughton, Roland Diehl, Gerald Fishman, Jochen Greiner, Andrew S Hoover, et al. The fermi gamma-ray burst monitor. *The Astrophysical Journal*, 702(1):791, 2009.

- [73] Aous A Abdo, Markus Ackermann, Marco Ajello, J Ampe, B Anderson, WB Atwood, Magnus Axelsson, R Bagagli, Luca Baldini, Jean Ballet, et al. The on-orbit calibration of the fermi large area telescope. *Astroparticle Physics*, 32(3-4):193–219, 2009.
- [74] Markus Ackermann, Marco Ajello, William B Atwood, Luca Baldini, J Ballet, Guido Barbiellini, D Bastieri, J Becerra Gonzalez, R Bellazzini, E Bissaldi, et al. 2fhl: the second catalog of hard fermi-lat sources. *The Astrophysical Journal Supplement Series*, 222(1):5, 2016.
- [75] Gene CK Leung, J Takata, CW Ng, AKH Kong, PHT Tam, CY Hui, and KS Cheng. Fermi-lat detection of pulsed gamma-rays above 50 gev from the vela pulsar. *The Astrophysical Journal Letters*, 797(2):L13, 2014.
- [76] Aous A Abdo, Markus Ackermann, M Arimoto, K Asano, William B Atwood, Magnus Axelsson, Luca Baldini, Jean Ballet, DL Band, Guido Barbiellini, et al. Fermi observations of high-energy gamma-ray emission from grb 080916c. *Science*, 323(5922):1688–1693, 2009.
- [77] A Goldstein, P Veres, E Burns, MS Briggs, R Hamburg, D Kocevski, CA Wilson-Hodge, RD Preece, S Poolakkil, OJ Roberts, et al. An ordinary short gamma-ray burst with extraordinary implications: Fermi-gbm detection of grb 170817a. *The Astrophysical Journal Letters*, 848(2):L14, 2017.
- [78] V Savchenko, C Ferrigno, E Kuulkers, ANGELA Bazzano, E Bozzo, S Brandt, J Chenevez, TJ-L Courvoisier, R Diehl, A Domingo, et al. Integral detection of the first prompt gamma-ray signal coincident with the gravitational-wave event gw170817. *The Astrophysical Journal Letters*, 848(2):L15, 2017.
- [79] Junaid Aasi, BP Abbott, Richard Abbott, Thomas Abbott, MR Abernathy, Kendall Ackley, Carl Adams, Thomas Adams, Paolo Addesso, RX Adhikari, et al. Advanced ligo. *Classical and quantum gravity*, 32(7):074001, 2015.
- [80] Fet al Acernese, M Agathos, K Agatsuma, D Aisa, N Allemandou, A Allocca, J Amarni, P Astone, G Balestri, G Ballardini, et al. Advanced virgo: a second-generation interferometric gravitational wave detector. *Classical and Quantum Gravity*, 32(2):024001, 2014.
- [81] Christoph Winkler, G Di Cocco, N Gehrels, A Giménez, S Grebenev, W Hermsen, JM Mas-Hesse, F Lebrun, N Lund, GGC Palumbo, et al. The integral mission. *Astronomy & Astrophysics*, 411(1):L1–L6, 2003.
- [82] Bing Zhang. The delay time of gravitational wave—gamma-ray burst associations. *Frontiers of Physics*, 14(6):1–11, 2019.

- [83] Werner Hofmann and Hess Collaboration. The high energy stereoscopic system (hess) project. In *AIP Conference Proceedings*, volume 515, pages 500–509. American Institute of Physics, 2000.
- [84] Bradley M Peterson. *An introduction to active galactic nuclei*. Cambridge University Press, 1997.
- [85] Felix Aharonian, AG Akhperjanian, U Barres De Almeida, AR Bazer-Bachi, B Behera, M Beilicke, W Benbow, K Bernlöhr, C Boisson, O Bolz, et al. Hess very-high-energy gamma-ray sources without identified counterparts. *Astronomy & Astrophysics*, 477(1):353–363, 2008.
- [86] M Ackermann, M Ajello, Luca Baldini, G Barbiellini, MG Baring, K Bechtol, R Bellazzini, RD Blandford, ED Bloom, Eea Bonamente, et al. Constraining the high-energy emission from gamma-ray bursts with fermi. *The Astrophysical Journal*, 754(2):121, 2012.
- [87] Ciro Bigongiari. The magic telescope. *arXiv preprint astro-ph/0512184*, 2005.
- [88] Clemens Hoischen, A Blazer, Elisabetta Bissaldi, Matthias Fülling, Tania Garrigoux, Daniel Gottschall, Markus Holler, Alison Mitchell, Paul O’Brien, Robert Parsons, et al. Grb observations with hess ii. *arXiv preprint arXiv:1708.01088*, 2017.
- [89] Vikas Chand, Ankush Banerjee, Rahul Gupta, Partha Sarathi Pal, Jagdish C Joshi, Bin-Bin Zhang, R Basak, PHT Tam, Vidushi Sharma, SB Pandey, et al. Peculiar prompt emission and afterglow in the hess-detected grb 190829a. *The Astrophysical Journal*, 898(1):42, 2020.
- [90] Quentin Piel, Markus Böttcher, Cornelia Arcaro, Halim Ashkar, and Elisabetta Bissaldi. Grb observations with hess. 2019.
- [91] B. Zhang. *The Physics of Gamma-Ray Bursts*. Cambridge University Press, 2018.
- [92] Andreja Gomboc. Unveiling the secrets of gamma ray bursts. *Contemporary Physics*, 53(4):339–355, 2012.
- [93] P Meszaros. The fireball model of gamma-ray bursts. *Progress of Theoretical Physics Supplement*, 143:33–49, 2001.
- [94] Tsvi Piran. Gamma-ray bursts and the fireball model. *Physics Reports*, 314(6):575–667, 1999.
- [95] David Eichler and Amir Levinson. A compact fireball model of gamma-ray bursts. *The Astrophysical Journal*, 529(1):146, 2000.
- [96] L Binette, MICHAEL A Dopita, and IR Tuohy. Radiative shock-wave theory. ii-high-velocity shocks and thermal instabilities. *The Astrophysical Journal*, 297:476–491, 1985.

- [97] Stan E Woosley. Gamma-ray bursts from stellar mass accretion disks around black holes. *The Astrophysical Journal*, 405:273–277, 1993.
- [98] Jelena Petrovic, Norbert Langer, S-C Yoon, and Alexander Heger. Which massive stars are gamma-ray burst progenitors? *Astronomy & Astrophysics*, 435(1):247–259, 2005.
- [99] SE Woosley and JS Bloom. The supernova–gamma-ray burst connection. *Annu. Rev. Astron. Astrophys.*, 44:507–556, 2006.
- [100] N Mirabal, JP Halpern, D An, JR Thorstensen, and DM Terndrup. Grb 060218/sn 2006aj: a gamma-ray burst and prompt supernova at $z=0.0335$. *The Astrophysical Journal*, 643(2):L99, 2006.
- [101] Paolo A Mazzali, Jinsong Deng, Nozomu Tominaga, Keiichi Maeda, Ken’ichi Nomoto, Thomas Matheson, Koji S Kawabata, Krzysztof Z Stanek, and Peter M Garnavich. The type ic hypernova sn 2003dh/grb 030329. *The Astrophysical Journal*, 599(2):L95, 2003.
- [102] D Hullinger, L Barbier, S Barthelmy, J Cummings, E Fenimore, N Gehrels, H Krimm, M Koss, C Markwardt, D Palmer, et al. Grb 060505 bat refined analysis. *GRB Coordinates Network*, 5142:1, 2006.
- [103] Neil Gehrels, JP Norris, SD Barthelmy, J Granot, Y Kaneko, C Kouveliotou, CB Markwardt, P Mészáros, E Nakar, JA Nousek, et al. A new γ -ray burst classification scheme from grb 060614. *Nature*, 444(7122):1044–1046, 2006.
- [104] Nanae Domoto, Masaomi Tanaka, Shinya Wanajo, and Kyohei Kawaguchi. Signatures of r-process elements in kilonova spectra. *The Astrophysical Journal*, 913(1):26, 2021.
- [105] DM Coward, EJ Howell, Tsvi Piran, Giulia Stratta, Marica Branchesi, Omer Bromberg, Bruce Gendre, RR Burman, and Dafne Guetta. The swift short gamma-ray burst rate density: implications for binary neutron star merger rates. *Monthly Notices of the Royal Astronomical Society*, 425(4):2668–2673, 2012.
- [106] E Sterl Phinney. The rate of neutron star binary mergers in the universe-minimal predictions for gravity wave detectors. *The Astrophysical Journal*, 380:L17–L21, 1991.
- [107] CN Leibler and E Berger. The stellar ages and masses of short gamma-ray burst host galaxies: investigating the progenitor delay time distribution and the role of mass and star formation in the short gamma-ray burst rate. *The Astrophysical Journal*, 725(1):1202, 2010.
- [108] SJeana Smartt, T-W Chen, A Jerkstrand, M Coughlin, E Kankare, SA Sim, M Fraser, C Inserra, K Maguire, KC Chambers, et al. A kilonova as the electromagnetic counterpart to a gravitational-wave source. *Nature*, 551(7678):75–79, 2017.

- [109] DA Perley, BD Metzger, J Granot, NR Butler, T Sakamoto, Enrico Ramirez-Ruiz, AJ Levan, JS Bloom, AA Miller, A Bunker, et al. Grb 080503: implications of a naked short gamma-ray burst dominated by extended emission. *The Astrophysical Journal*, 696(2):1871, 2009.
- [110] Rodrigo Fernández and Brian D Metzger. Electromagnetic signatures of neutron star mergers in the advanced ligo era. *Annual Review of Nuclear and Particle Science*, 66:23–45, 2016.
- [111] MG Bernardini, R Margutti, G Chincarini, C Guidorzi, and J Mao. Gamma-ray burst long lasting x-ray flaring activity. *Astronomy & Astrophysics*, 526:A27, 2011.
- [112] Wei-Hong Gao and Yi-Zhong Fan. Short-living supermassive magnetar model for the early x-ray flares following short grbs. *Chinese Journal of Astronomy and Astrophysics*, 6(5):513, 2006.
- [113] David N Burrows, Patrizia Romano, Abraham Falcone, Shiho Kobayashi, Bing Zhang, Alberto Moretti, Paul T O’Brien, Michael R Goad, Sergio Campana, Kim L Page, et al. Bright x-ray flares in gamma-ray burst afterglows. *Science*, 309(5742):1833–1835, 2005.
- [114] YQ Xue, XC Zheng, Yuexing Li, William N Brandt, Bryna Zhang, Bruce Luo, B-B Zhang, Franz E Bauer, H Sun, Bret D Lehmer, et al. A magnetar-powered x-ray transient as the aftermath of a binary neutron-star merger. *Nature*, 568(7751):198–201, 2019.
- [115] Xueying Shao and He Gao. Gamma-ray burst prompt emission spectrum and e_p evolution patterns in the icmart model. *arXiv preprint arXiv:2201.03750*, 2022.
- [116] Gor Oganessian, Lara Nava, Giancarlo Ghirlanda, and Annalisa Celotti. Detection of low-energy breaks in gamma-ray burst prompt emission spectra. *The Astrophysical Journal*, 846(2):137, 2017.
- [117] David Gruber, Adam Goldstein, Victoria Weller von Ahlefeld, P Narayana Bhat, Elisabetta Bissaldi, Michael S Briggs, Dave Byrne, William H Cleveland, Valerie Connaughton, Roland Diehl, et al. The fermi gbm gamma-ray burst spectral catalog: four years of data. *The Astrophysical Journal Supplement Series*, 211(1):12, 2014.
- [118] D Band, J Matteson, L Ford, B Schaefer, D Palmer, B Teegarden, T Cline, M Briggs, W Paciesas, G Pendleton, et al. Batse observations of gamma-ray burst spectra. i-spectral diversity. *The Astrophysical Journal*, 413:281–292, 1993.
- [119] MS Briggs, DL Band, RM Kippen, RD Preece, C Kouveliotou, J Van Paradijs, GH Share, RJ Murphy, SM Matz, A Connors, et al. Observations of grb 990123 by the compton gamma ray observatory. *The Astrophysical Journal*, 524(1):82, 1999.
- [120] Richard Willingale, RLC Starling, Andrew P Beardmore, Nial R Tanvir, and Paul T O’Brien. Calibration of x-ray absorption in our galaxy. *Monthly Notices of the Royal Astronomical Society*, 431(1):394–404, 2013.

- [121] S Campana, CC Thöne, A de Ugarte Postigo, G Tagliaferri, A Moretti, and S Covino. The x-ray absorbing column densities of swift gamma-ray bursts. *Monthly Notices of the Royal Astronomical Society*, 402(4):2429–2435, 2010.
- [122] PA Evans, AP Beardmore, KL Page, JP Osborne, PT O’Brien, R Willingale, RLC Starling, DN Burrows, O Godet, L Vetere, et al. Methods and results of an automatic analysis of a complete sample of swift-xrt observations of grbs. *Monthly Notices of the Royal Astronomical Society*, 397(3):1177–1201, 2009.
- [123] Bing Zhang, Y. Z. Fan, Jarosław Dyks, Shiho Kobayashi, P. Mészáros, David N. Burrows, J A Nousek, and N. C. Gehrels. Physical processes shaping gamma-ray burst x-ray afterglow light curves: Theoretical implications from the swift x-ray telescope observations. *The Astrophysical Journal*, 642:354 – 370, 2005.
- [124] David Branch and GA Tammann. Type ia supernovae as standard candles. *Annual review of astronomy and astrophysics*, 30(1):359–389, 1992.
- [125] PS Cowperthwaite, Edo Berger, VA Villar, BD Metzger, M Nicholl, R Chornock, PK Blanchard, W f Fong, R Margutti, M Soares-Santos, et al. The electromagnetic counterpart of the binary neutron star merger ligo/virgo gw170817. ii. uv, optical, and near-infrared light curves and comparison to kilonova models. *The Astrophysical Journal Letters*, 848(2):L17, 2017.
- [126] E Troja and L Piro. Gw170817/grb170817a: Updated results from the full chandra dataset. *The Astronomer’s Telegram*, 11245:1, 2018.
- [127] Arvind Balasubramanian, Alessandra Corsi, Kunal P Mooley, Murray Brightman, Gregg Hallinan, Kenta Hotokezaka, David L Kaplan, Davide Lazzati, and Eric J Murphy. Continued radio observations of gw170817 3.5 yr post-merger. *The Astrophysical Journal Letters*, 914(1):L20, 2021.
- [128] Arnaud Albert, Michel André, Marco Anghinolfi, M Ardid, J-J Aubert, J Aublin, T Avgitas, B Baret, J Barrios-Martí, S Basa, et al. Search for high-energy neutrinos from binary neutron star merger gw170817 with antares, icecube, and the pierre auger observatory. *arXiv preprint arXiv:1710.05839*, 2017.
- [129] Benjamin P Abbott, Robert Abbott, TD Abbott, F Acernese, K Ackley, C Adams, T Adams, P Addesso, RX Adhikari, VB Adya, et al. Gravitational waves and gamma-rays from a binary neutron star merger: Gw170817 and grb 170817a. *The Astrophysical Journal Letters*, 848(2):L13, 2017.
- [130] Benjamin P Abbott, R Abbott, TD Abbott, S Abraham, F Acernese, K Ackley, C Adams, VB Adya, C Affeldt, M Agathos, et al. Prospects for observing and localizing gravitational-wave transients with advanced ligo, advanced virgo and kagra. *Living reviews in relativity*, 23(1):1–69, 2020.

- [131] O Godet, J Paul, JY Wei, S-N Zhang, J-L Atteia, S Basa, D Barret, A Claret, B Cordier, J-G Cuby, et al. The chinese-french svom mission: studying the brightest astronomical explosions. In *Space Telescopes and Instrumentation 2012: Ultraviolet to Gamma Ray*, volume 8443, page 84431O. International Society for Optics and Photonics, 2012.
- [132] Stéphane Schanne, Bertrand Cordier, Jean-Luc Atteia, Olivier Godet, Cyril Lachaud, and Karine Mercier. The eclairs grb-trigger telescope on-board the future mission svom. 08 2015.
- [133] Olivier Godet, Guillaume Nasser, B Cordier, P Mandrou, D Barret, H Triou, R Pons, C Amoros, S Bordon, O Gevin, et al. The x-/gamma-ray camera eclairs for the gamma-ray burst mission svom. In *Space Telescopes and Instrumentation 2014: Ultraviolet to Gamma Ray*, volume 9144, pages 625–639. SPIE, 2014.
- [134] Nicolas Dagoneau, Stéphane Schanne, Jean-Luc Atteia, Diego Götz, and Bertrand Cordier. Ultra-long gamma-ray bursts detection with svom/eclairs. *Experimental Astronomy*, 50(1):91–123, 2020.
- [135] Maria Grazia Bernardini, Fei Xie, P Sizun, F Piron, Y Dong, J-L Atteia, S Antier, F Daigne, O Godet, B Cordier, et al. Scientific prospects for spectroscopy of the gamma-ray burst prompt emission with svom. *Experimental Astronomy*, 44(1):113–127, 2017.
- [136] Sarah Antier-Farfar. Detection of gamma-ray bursts with the eclairs instrument onboard the space mission svom. Technical report, Univ. Paris-Saclay, 2016.
- [137] Yongwei Dong, Bobing Wu, Yanguo Li, Yongjie Zhang, and Shuangnan Zhang. Svom gamma ray monitor. *Science China: Physics, Mechanics and Astronomy*, 53, 07 2009.
- [138] D. Götz et al. The Microchannel X-ray Telescope on Board the SVOM Satellite. *PoS, SWIFT10:074*, 2015.
- [139] Xuewu Fan et al. The Visible Telescope onboard the Chinese-French SVOM satellite. In Makenzie Lystrup, Marshall D. Perrin, Natalie Batalha, Nicholas Siegler, and Edward C. Tong, editors, *Space Telescopes and Instrumentation 2020: Optical, Infrared, and Millimeter Wave*, volume 11443, pages 139 – 154. International Society for Optics and Photonics, SPIE, 2020.
- [140] CG Wynne. Ritchey-chretien telescopes and extended field systems. *The Astrophysical Journal*, 152:675, 1968.
- [141] Y. Xu, L. P. Xin, J. Wang, X. H. Han, Y. L. Qiu, M. H. Huang, and J. Y. Wei. A real-time automatic validation system for optical transients detected by GWAC. *Publications of the Astronomical Society of the Pacific*, 132(1011):054502, apr 2020.
- [142] JY Wei, XH Han, C Wu, N Leroy, S Antier, LP Xin, XM Meng, L Huang, Y Xu, HB Cai, et al. Ligo/virgo g270580: Observations of initial skymap by project mini-gwac of svom. *GRB Coordinates Network*, 20490:1, 2017.

- [143] et al. Fuentes-Fernández. Optical design of colibrí: A fast follow-up telescope for transient events. *Journal of Astronomical Instrumentation*, 09(01):2050001, 2020.
- [144] M Tarenghi and RN Wilson. The eso ntt (new technology telescope): the first active optics telescope. In *Active telescope systems*, volume 1114, pages 302–313. International Society for Optics and Photonics, 1989.
- [145] Joel Vernet, H Dekker, S d’Odorico, L Kaper, P Kjaergaard, F Hammer, S Randich, F Zerbi, PJ Groot, J Hjorth, et al. X-shooter, the new wide band intermediate resolution spectrograph at the eso very large telescope. *Astronomy & Astrophysics*, 536:A105, 2011.
- [146] Alwyn Wootten and A Richard Thompson. The atacama large millimeter/submillimeter array. *Proceedings of the IEEE*, 97(8):1463–1471, 2009.
- [147] Zakaria Meliani and Rony Keppens. Dynamics and stability of relativistic gamma-ray-bursts blast waves. *Astronomy & Astrophysics*, 520:L3, 2010.
- [148] A Meli and JJ Quenby. Particle acceleration in ultra-relativistic oblique shock waves. *Astroparticle Physics*, 19(5):649–666, 2003.
- [149] Dimitrios Giannios. Prompt emission spectra from the photosphere of a grb. *Astronomy & Astrophysics*, 457(3):763–770, 2006.
- [150] Volker Beckmann and Chris R Shrader. The agn phenomenon: open issues. *arXiv preprint arXiv:1302.1397*, 2013.
- [151] Walter HG Lewin, Edward PJ van den Heuvel, and Jan van Paradijs. *X-ray Binaries*, volume 26. Cambridge University Press, 1997.
- [152] Jeffrey E McClintock and Ronald A Remillard. Black hole binaries. *arXiv preprint astro-ph/0306213*, 2003.
- [153] Edward L Robinson. The structure of cataclysmic variables. *Annual review of astronomy and astrophysics*, 14(1):119–142, 1976.
- [154] SJ Kenyon and LW Hartmann. Spectral energy distributions of t tauri stars-disk flaring and limits on accretion. *The Astrophysical Journal*, 323:714–733, 1987.
- [155] Alberto Moretti, S Campana, D Lazzati, and G Tagliaferri. The resolved fraction of the cosmic x-ray background. *The Astrophysical Journal*, 588(2):696, 2003.
- [156] B Cordier, D Götz, and C Motch. The svom mission, a pathfinder for theseus. *arXiv preprint arXiv:1802.01681*, 2018.
- [157] Bertrand Cordier, Francois Desclaux, Jacques Foliard, and Stephane Schanne. Svom pointing strategy: how to optimize the redshift measurements? In *AIP conference proceedings*, volume 1000, pages 585–588. American Institute of Physics, 2008.

- [158] Nicholas H Crisp, Peter CE Roberts, Sabrina Livadiotti, Vitor Toshiyuki Abrao Oiko, Steve Edmondson, SJ Haigh, Claire Huyton, LA Sinpetru, KL Smith, SD Worrall, et al. The benefits of very low earth orbit for earth observation missions. *Progress in Aerospace Sciences*, 117:100619, 2020.
- [159] R Giacconi, E Kellogg, P Gorenstein, H Gursky, and H Tananbaum. An x-ray scan of the galactic plane from uhuru. *The Astrophysical Journal*, 165:L27, 1971.
- [160] JA Gledhill. Aeronomic effects of the south atlantic anomaly. *Reviews of Geophysics*, 14(2):173–187, 1976.
- [161] SD Barthelmy, P Butterworth, T Lo Cline, N Gehrels, F Marshall, To Takeshima, Vo Connaughton, RM Kippen, C Kouveliotou, and Co Ro Robinson. The grb coordinates network (gcn): A status report. In *AIP Conference Proceedings*, volume 428, pages 99–103. American Institute of Physics, 1998.
- [162] MGF Kirsch, UG Briel, D Burrows, S Campana, G Cusumano, K Ebisawa, MJ Freyberg, M Guainazzi, F Haberl, K Jahoda, et al. Crab: the standard x-ray candle with all (modern) x-ray satellites. In *UV, X-Ray, and Gamma-Ray Space Instrumentation for Astronomy XIV*, volume 5898, pages 22–33. SPIE, 2005.
- [163] Richard Pio. Euler angle transformations. *IEEE Transactions on automatic control*, 11(4):707–715, 1966.
- [164] Pierre Manil, Yannick Jan, François Nunio, Fernando Lomello, Axel Arhancet, Mickaël Lacroix, Damien Bachet, and Jean Lapresle. Structural optimization, additive manufacturing and vibration testing of titanium alloy supports based on the space detector svom-mxt. In *Advances in Optical and Mechanical Technologies for Telescopes and Instrumentation IV*, volume 11451, pages 526–544. SPIE, 2021.
- [165] Francesco Ceraudo. *Characterization and performance optimization of the focal plane of the Microchannel X-ray Telescope on-board the space astronomy mission SVOM*. PhD thesis, Université Paris-Saclay, 2019.
- [166] B Aschenbach. X-ray telescopes. *Reports on Progress in Physics*, 48(5):579, 1985.
- [167] Hans Wolter. Mirror systems with grazing incidence as image-forming optics for x-rays. *Mirror systems with grazing incidence as image-forming optics for X-rays Transl. into ENGLISH from Ann. Phys.(Leipzig)*, 10:94–114, 1975.
- [168] Baozhong Mu, Hongying Liu, Huijun Jin, Xiajun Yang, Fangfang Wang, Wenbin Li, Hong Chen, and Zhanshan Wang. Optimization of geometrical design of nested conical wolter-i x-ray telescope. *Chinese Optics Letters*, 10(10):103401–103401, 2012.
- [169] Wujun Mi, Peter Nillius, Mark Pearce, and Mats Danielsson. A stacked prism lens concept for next-generation hard x-ray telescopes. *Nature Astronomy*, 3(9):867–872, 2019.

- [170] David N Burrows, JE Hill, JAea Nousek, JA Kennea, A Wells, JP Osborne, AF Abbey, A Beardmore, K Mukerjee, ADT Short, et al. The swift x-ray telescope. *Space science reviews*, 120(3):165–195, 2005.
- [171] JRP Angel. Lobster eyes as x-ray telescopes. In *Space Optics Imaging X-Ray Optics Workshop*, volume 184, pages 84–85. SPIE, 1979.
- [172] Charlotte H Feldman, Richard Willingale, James Pearson, Valentin Aslanyan, Tony Crawford, Paul Houghton, Jon Sykes, Christopher Bicknell, Julian Osborne, Paul O’Brien, et al. Calibration of a fully populated lobster eye optic for svom. In *Space Telescopes and Instrumentation 2020: Ultraviolet to Gamma Ray*, volume 11444, page 114441K. International Society for Optics and Photonics, 2020.
- [173] The photonis company. <https://www.photonis.com/careers-our-facilities/photonis-france>.
- [174] JM Le Duigou, K Mercier, F Gonzalez, D Götz, and A Meuris. Optical models of mxt using zemax. In *International Conference on Space Optics—ICSO 2016*, volume 10562, page 105620T. International Society for Optics and Photonics, 2017.
- [175] Andrew G Peele, Kaushal D Vora, B-Y Shew, B Loechl, Erol C Harvey, and Jason P Hayes. Production issues for high aspect ratio lobster-eye optics using liga. *Microsystem technologies*, 13(5):511–515, 2007.
- [176] Francesco Ceraudo, Aline Meuris, Eric Doumayrou, Clément Raux, Modeste Donati, François Visticot, Marin Prieur, Diana Renaud, Frédéric Pinsard, and Diego Götz. First characterization of the focal plane of the micro-channel x-ray telescope on board the svom mission and preparation of radiation tests to predict its performances in low-earth orbit. In *2018 IEEE Nuclear Science Symposium and Medical Imaging Conference Proceedings (NSS/MIC)*, pages 1–7. IEEE, 2018.
- [177] Norbert Meidinger, Stefan Bonerz, Rouven Eckhardt, Jakob Englhauser, Robert Hartmann, Günther Hasinger, Peter Holl, Norbert Krause, Gerhard Lutz, Rainer Richter, et al. First measurements with a frame store pn-ccd x-ray detector. *Nuclear Instruments and Methods in Physics Research Section A: Accelerators, Spectrometers, Detectors and Associated Equipment*, 512(1-2):341–349, 2003.
- [178] Francesco Ceraudo. Characterization and performance optimization of the focal plane of the micro-channel x-ray telescope on-board the space astronomy mission svom. Technical report, Universite de Paris-Saclay, 2019.
- [179] Miguel Masmano, Ismael Ripoll, Alfons Crespo, and Vicent Brocal. Xtratum hypervisor for leon3, volume 2: User manual, 2011.
- [180] Jiri Gaisler and Edvin Catovic. Multi-core processor based on leon3-ft ip core (leon3-ft-mp). In *DASIA 2006-Data Systems in Aerospace*, volume 630, 2006.

- [181] Koichi Onoue and Tomoyuki Nishita. Virtual sandbox. In *11th Pacific Conference on Computer Graphics and Applications, 2003. Proceedings.*, pages 252–259. IEEE, 2003.
- [182] G Ann Campbell and Patroklos P Papapetrou. *SonarQube in action*. Manning Publications Co., 2013.
- [183] The panter x-ray test facility. <https://www.mpe.mpg.de/heg/panter>.
- [184] Martin C Weisskopf and Leon Van Speybroeck. The advanced x-ray astrophysics facility (axaf). *Optics and Photonics News*, 7(4):16, 1996.
- [185] Joachim Trümper. The rosat mission. *Advances in Space Research*, 2(4):241–249, 1982.
- [186] F Jansen, D Lumb, BXMM Altieri, J Clavel, M Ehle, C Erd, C Gabriel, M Guainazzi, P Gondoin, R Much, et al. Xmm-newton observatory-i. the spacecraft and operations. *Astronomy & Astrophysics*, 365(1):L1–L6, 2001.
- [187] Kazuhisa Mitsuda, Mark Bautz, Hajime Inoue, Richard L Kelley, Katsuji Koyama, Hideyo Kunieda, Kazuo Makishima, Yoshiaki Ogawara, Robert Petre, Tadayuki Takahashi, et al. The x-ray observatory suzaku. *Publications of the Astronomical Society of Japan*, 59(sp1):S1–S7, 2007.
- [188] Peter Predehl, G Hasinger, H Böhringer, U Briel, H Brunner, E Churazov, M Freyberg, P Friedrich, E Kendziorra, D Lutz, et al. erosita. In *Space Telescopes and Instrumentation II: Ultraviolet to Gamma Ray*, volume 6266, pages 194–203. SPIE, 2006.
- [189] Miranda Bradshaw, Vadim Burwitz, Gisela Hartner, Carlo Pellicciari, Andreas Langmeier, Yingyu Liao, Peter Friedrich, Giuseppe Valsecchi, Nicolas Barrière, Maximilien J Collon, et al. Developments in testing x-ray optics at mpe’s panter facility. In *Optics for EUV, X-Ray, and Gamma-Ray Astronomy IX*, volume 11119, pages 385–404. SPIE, 2019.
- [190] Satandlight: a simulation toolkit for space telescopes. <https://svom.pages.in2p3.fr/SatAndLight/>, 2020.
- [191] B Raja Sekhar and KMM Prabhu. Radix-2 decimation-in-frequency algorithm for the computation of the real-valued fft. *IEEE transactions on signal processing*, 47(4):1181–1184, 1999.
- [192] Deyun Wei, Qiwen Ran, and Yuanmin Li. A convolution and correlation theorem for the linear canonical transform and its application. *Circuits, Systems, and Signal Processing*, 31(1):301–312, 2012.
- [193] A Moretti. A new measurement of the cosmic x-ray background. In *AIP Conference Proceedings*, volume 1126, pages 223–226. American Institute of Physics, 2009.
- [194] Edward Anders and Mitsuru Ebihara. Solar-system abundances of the elements. *Geochimica et Cosmochimica Acta*, 46(11):2363–2380, 1982.

- [195] Catalogue xrt results for grb 091018. https://www.swift.ac.uk/xrt_live_cat/00373172/.
- [196] Joanne E Hill, David N Burrows, John A Nousek, Anthony F Abbey, Richard M Ambrosi, Heinrich W Brauning, Wolfgang Burkert, Sergio Campana, Chaitanya Cheruvu, Giancarlo Cusumano, et al. Readout modes and automated operation of the swift x-ray telescope. In *X-Ray and Gamma-Ray Instrumentation for Astronomy XIII*, volume 5165, pages 217–231. SPIE, 2004.
- [197] P d’Avanzo, R Salvaterra, MG Bernardini, L Nava, S Campana, S Covino, V d’Elia, G Ghirlanda, G Ghisellini, A Melandri, et al. A complete sample of bright swift short gamma-ray bursts. *Monthly Notices of the Royal Astronomical Society*, 442(3):2342–2356, 2014.
- [198] George Helou, BF Madore, M Schmitz, MD Bicay, X Wu, and J Bennett. The nasa/ipac extragalactic database. In *Databases & On-Line Data in Astronomy*, pages 89–106. Springer, 1991.
- [199] Alberto Fernandez-Soto, Kenneth M Lanzetta, Hsiao-Wen Chen, Sebastian M Pascarelle, and Noriaki Yahata. On the compared accuracy and reliability of spectroscopic and photometric redshift measurements. *The Astrophysical Journal Supplement Series*, 135(1):41, 2001.
- [200] Daniel A Perley, T Krühler, S Schulze, A de Ugarte Postigo, J Hjorth, Edo Berger, SB Cenko, R Chary, A Cucchiara, R Ellis, et al. The swift gamma-ray burst host galaxy legacy survey. i. sample selection and redshift distribution. *The Astrophysical Journal*, 817(1):7, 2016.
- [201] François Ochsenbein, Patricia Bauer, and James Marcout. The vizier database of astronomical catalogues. *Astronomy and Astrophysics Supplement Series*, 143(1):23–32, 2000.
- [202] Joshua S Bloom, Shrinivas R Kulkarni, and S George Djorgovski. The observed offset distribution of gamma-ray bursts from their host galaxies: a robust clue to the nature of the progenitors. *The Astronomical Journal*, 123(3):1111, 2002.
- [203] Arne A Henden and Ronald H Kaitchuck. Astronomical photometry. *New York: Van Nostrand Reinhold*, 1982.
- [204] Narciso Benitez. Bayesian photometric redshift estimation. *The Astrophysical Journal*, 536(2):571, 2000.
- [205] C Weaver, T Brennan, M Schubel, J Styblova, J Haislip, D Reichart, M Nysewander, A Lacluyze, K Ivarsen, JA Crain, et al. Short-hard grb070714b: Prompt observations. *GRB Coordinates Network*, 6657:1, 2007.

- [206] Fabian Knust, Jochen Greiner, HJ Van Eerten, P Schady, DA Kann, T-W Chen, Corentin Delvaux, John F Graham, S Klose, T Krühler, et al. Long optical plateau in the afterglow of the short grb 150424a with extended emission-evidence for energy injection by a magnetar? *Astronomy & Astrophysics*, 607:A84, 2017.
- [207] Nikhil Anand, Mustafa Shahid, and Lekshmi Resmi. Merger delay time distribution of extended emission short grbs. *Monthly Notices of the Royal Astronomical Society*, 481(4):4332–4341, 2018.
- [208] P Minaev, A Pozanenko, and GRB IKI FuN. Grb 211211a: redshift estimation and spi-acs/integral detection. *GRB Coordinates Network*, 31230:1, 2021.
- [209] A Tsvetkova, D Frederiks, A Lysenko, D Svinkin, A Ridnaia, M Ulanov, and AY Lien. Grb 211227a: Konus-wind detection and joint konus-wind+ swift-bat spectral analysis. *GRB Coordinates Network*, 31544:1, 2022.
- [210] PA Evans, AP Beardmore, KL Page, JP Osborne, PT O’Brien, R Willingale, RLC Starling, DN Burrows, O Godet, L Vetere, et al. Methods and results of an automatic analysis of a complete sample of swift-xrt observations of grbs. *Monthly Notices of the Royal Astronomical Society*, 397(3):1177–1201, 2009.
- [211] Charles Meegan, Giselher Lichti, PN Bhat, Elisabetta Bissaldi, Michael S Briggs, Valerie Connaughton, Roland Diehl, Gerald Fishman, Jochen Greiner, Andrew S Hoover, et al. The fermi gamma-ray burst monitor. *The Astrophysical Journal*, 702(1):791, 2009.
- [212] RL Aptekar, DD Frederiks, SV Golenetskii, VN Ilynskii, EP Mazets, VN Panov, ZJ Sokolova, MM Terekhov, LO Sheshin, TL Cline, et al. Konus-w gamma-ray burst experiment for the ggs wind spacecraft. *Space Science Reviews*, 71(1):265–272, 1995.
- [213] Patrick L Nolan, AA Abdo, Markus Ackermann, Marco Ajello, A Allafort, E Antolini, WB Atwood, Magnus Axelsson, Luca Baldini, Jean Ballet, et al. Fermi large area telescope second source catalog. *The Astrophysical Journal Supplement Series*, 199(2):31, 2012.
- [214] Brian D Metzger and Edo Berger. What is the most promising electromagnetic counterpart of a neutron star binary merger? *The Astrophysical Journal*, 746(1):48, 2012.
- [215] J Aasi, J Abadie, BP Abbott, R Abbott, TD Abbott, M Abernathy, T Accadia, F Acernese, C Adams, T Adams, et al. Prospects for observing and localizing gravitational-wave transients with advanced ligo and advanced virgo. *Living Reviews in Relativity*, 19, 2016.
- [216] Laura Gosset. *Etude et optimisation des performances de l’instrument MXT, télescope X à micro-canaux, embarqué à bord de la mission spatiale d’astronomie SVOM*. PhD thesis, Université Paris-Saclay, 2019.